PRECURSOR DAMAGE EVOLUTION AND STRESS CORROSION CRACK INITIATION OF COLD-WORKED ALLOY 690 IN PWR PRIMARY WATER

Technical Milestone Report: M2LW-16OR0402034
September 2016

Z. Zhai, M. B. Toloczko, K. Kruska, N. R. Overman
M. J. Olszta and S. M. Bruemmer
Pacific Northwest National Laboratory

Research Project:
Stress Corrosion Crack Initiation of Nickel-Base Alloys in LWR Environments
Project Manager: S. M. Bruemmer
Pacific Northwest National Laboratory

Conducted for:
Office of Nuclear Energy, U.S. Department of Energy
Light Water Reactor Sustainability Program
Materials Aging and Degradation Pathway
Pathway Manager: K. J. Leonard
Oak Ridge National Laboratory

Table of Contents

Project Background

Objective

This research project addresses one of the least understood aspects of stress corrosion cracking (SCC) for light-water reactor (LWR) pressure boundary components - crack initiation. The focus of the work is to investigate important material (composition, processing, microstructure) and environmental (water chemistry, temperature, electrochemical potential, stress) effects on the SCC susceptibility of corrosion-resistant, nickel-base alloys. The primary objectives are to identify mechanisms controlling crack nucleation, investigate the transition to long crack growth in these alloys under realistic LWR conditions and help establish the framework to effectively model and mitigate SCC initiation processes.

Approach

Alloy 600 materials were selected for the first phase of SCC initiation experimentation followed by testing on the more resistant alloy 690 materials. For both alloys, material variants known to influence SCC response are being examined including cold work (forged, rolled and tensile strained), banded/inhomogeneous microstructures (plate versus extruded pipe), grain boundary precipitation (heat-to-heat variations and changes due to thermal treatments) and surface grinding (various depths of damage). Materials and material conditions have been identified and obtained from ongoing research projects where stress corrosion crack growth has been characterized, thus creating an important link between SCC initiation and propagation behavior. Detailed examinations have been performed using optical and electron microscopy to establish key bulk and surface microstructural features that may act as initiation precursors. Dedicated test systems with continuous in-situ detection of crack formation were designed and constructed enabling SCC initiation experimentation of a range of alloy 600 and 690 materials. After SCC testing in high temperature autoclave systems, surface and near-surface characterizations were conducted to document nano-to-microscale initiation precursors leading to macroscopic stress corrosion cracks. A fundamental understanding of how the near-surface microstructure is altered during high-temperature water exposure is essential to develop an improved predictive methodology for SCC initiation of both alloy 600 and alloy 690.

Focus of Current Report

This report reviews recent SCC initiation testing on cold-worked (CW) alloy 690 materials in high-temperature, simulated PWR primary water. It follows earlier milestone reports [1-6] that described corrosion-structure characterizations and prior SCC initiation tests on both alloy 600 and alloy 690. Microstructural characterization activities performed on SCC initiation specimens from recently completed blunt notch compact tension (BNCT) tests and ongoing constant load tensile (CLT) tests are summarized and discussed in detail in this report. All tests are being conducted on alloy 690 materials in the CW condition that has been shown to increase SCC susceptibility in SCC crack-growth experiments [7-11]. The evolution of precursor damage at grain boundaries during long-term testing leading to the nucleation of intergranular (IG) cracks at the surface in highly CW alloy 690 materials have been documented. A direct correlation has been discovered between cavity distributions along grain boundaries reaching the surface and crack nucleation during both BNCT and CLT experiments. Preliminary observations reveal a strong effect of the %CW, applied stress, dynamic straining and grain boundary (GB) carbide microstructure on cavity formation and IG cracking during tests in 360°C PWR primary water.

Alloy 690 Materials and Microstructure Characterizations

This chapter summarizes the alloy 690 materials investigated in this report along with microstructural characterization results. Most initial examinations were conducted on these heats as part of a Nuclear Regulatory Commission (NRC) project at PNNL investigating SCC crack growth behavior [7, 8]. Because alloy 690 shows a strong increase in SCC crack-growth rate (CGR) with cold work, it was determined to assess the susceptibility to SCC initiation in CW alloy 690 materials. The current research focuses on three alloy 690 control rod drive mechanism (CRDM) heats and three plate/bar heats that are being tested for SCC initiation response at various cold work levels. Grain boundary microstructures were characterized in detail for these heats in both the as-received and CW conditions. Heat-to-heat comparison was made focusing on the distribution of permanent damage induced during cold work. In addition, the effect of cold work on many of these materials was also evaluated by hardness and electron backscatter diffraction (EBSD) measurements.

Examinations of As-Received Alloy 690 Microstructures

Three alloy 690 CRDM heats from three different manufacturers have been evaluated as listed in Table 1. All materials are in a thermally treated (TT) condition with semi-continuous GB carbide coverage as shown in the scanning electron microscope (SEM) backscatter electron (BSE) images in Figure 1. Grain size images in Figure 2 show that the Valinox and Doosan materials have a grain size of ~90 μm while the Sumitomo CRDM has a smaller average grain size of ~35 μm with significant twinning.

Table 1. Composition, heat treatment and mechanical properties for the as-received alloy 690TT CRDM materials.

Source/Manufacturer and Heat #	Dimension (mm)	Composition, wt%	Heat Treatments and Room Temp. Mechanical Properties
Valinox/Valinox RE243 Tube 2360	112 OD x 34 wall	Ni-28.9Cr-10.4Fe-0.02C-0.3Mn-0.35Si-0.14Al-0.23Ti-0.024N-0.008P-0.0005S	1122°C/~1 min, WQ + 716-725°C/10.5h, Air Cool YS = 255 MPa, HV = 157 kgf/mm^2
EPRI/ Sumitomo E67074C Tube	127 OD x 33 wall	Ni-29.8Cr-9.8Fe-0.02C-0.29Mn-0.23Si-0.03Cu-0.0002S	Anneal + 725°C/10h/Air Cool YS and HV not measured
EPRI/ TK-VDM (Doosan) 133454 Bar	152 OD solid bar	Ni-29.1Cr-8.9Fe-0.020C-0.26Mn-0.29Si-0.26Al-0.32Ti-0.01Cu-0.02N-0.005P-<0.002S-0.002B	1045°C/4 hr/WQ + 720°C/10h/Air Cool YS = 263 MPa, HV = 165 kgf/mm^2

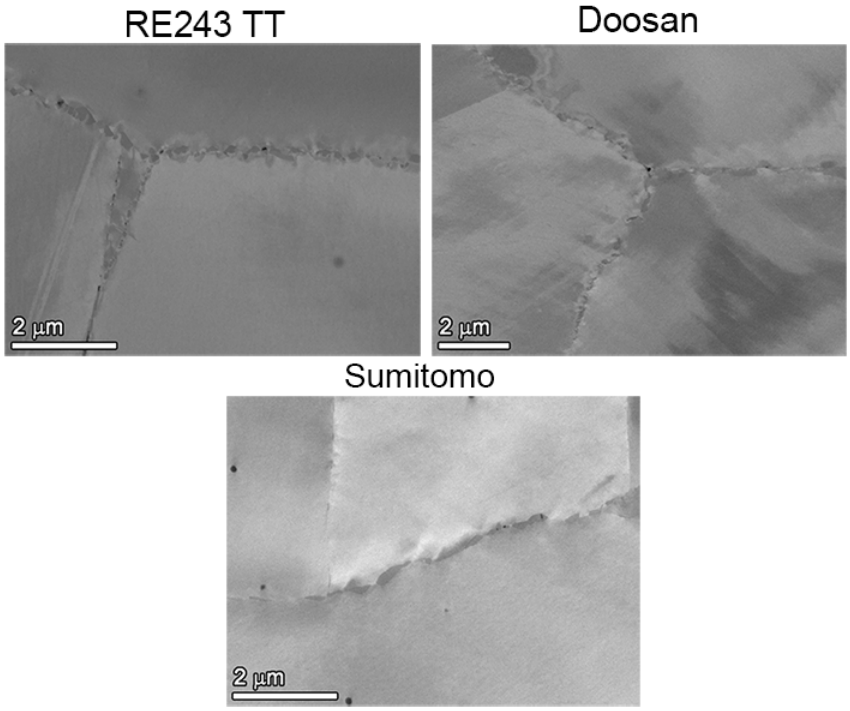

Figure 1. SEM-BSE images illustrating the GB microstructures for the three alloy 690TT CRDM materials in the as-received condition.

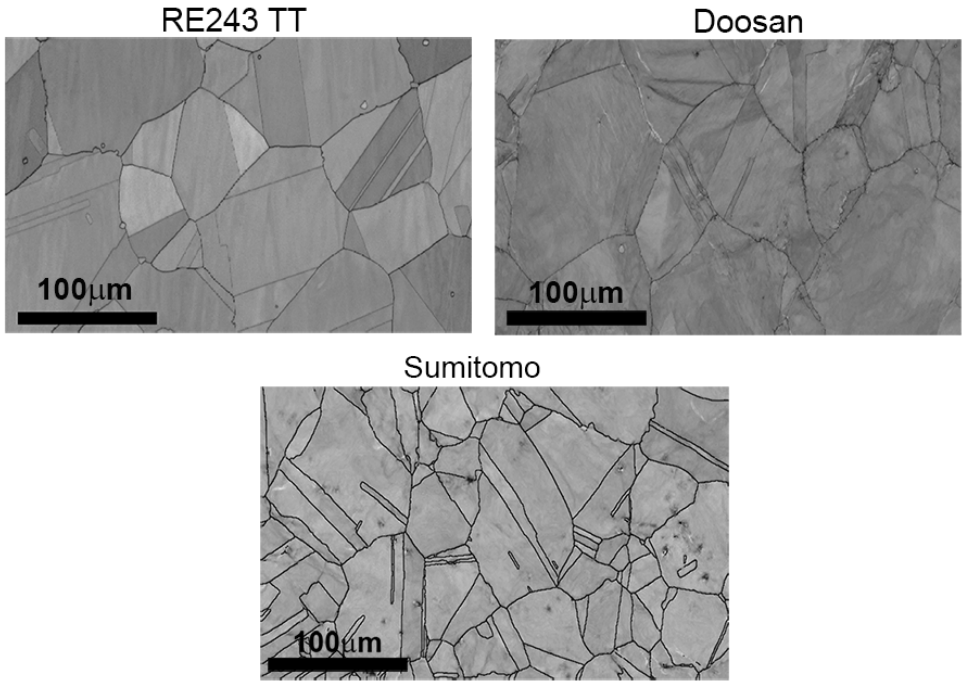

Figure 2. SEM EBSD pattern quality maps showing the general microstructure and grain size for the three alloy 690TT CRDM materials in the as-received condition.

Three alloy 690 plate/bar materials from three manufacturers have also been evaluated with specifications given in Table 2. Carbide precipitation was limited to a few isolated GBs in the mill-annealed (MA) GEG B25K heat, while the MA ANL NX3297HK12 and the TT TK-VDM 114092 heats exhibited a moderate distribution of IG carbides as shown in Figure 3. SEM-EBSD pattern quality images in Figure 4 show that the grain size is ~15 μm for the GEG material, ~50 μm for the ANL material and ~30 μm for the TK-VDM material. This information on the CRDM and bar/plate heats is summarized in Table 3.

Table 2. Composition, heat treatment, and mechanical properties for the alloy 690 bar/plate materials covered in this report.

Source/Manufacturer and Heat #	Composition, wt%	Heat Treatments and Room Temp. Mechanical Properties
ANL/ Special Metals NX3297HK12	Ni-29.5Cr-9.9Fe-0.03C-0.20Mn-0.07Si-0.01Cu-<0.001S	1038°C/2 hr/AC YS not measured, HV = 173 kgf/mm^2
GEG/ Allvac B25K	Ni-29.3Cr-9.2Fe-0.034C-0.22Mn-0.06Si-0.26Al-0.37Ti-<0.01Cu-0.03N-0.006P-<0.0003S-<0.001B	996°C/20 min/AC YS = 294 MPa, HV = 173 kgf/mm^2
EPRI/TK-VDM 114092	Ni-29.5Cr-9.5Fe-0.020C-0.25Mn-0.26Si-0.32Al-0.36Ti-<0.01Cu-0.003P-<0.002S	1030°C/1 hr/WQ + 715°C/10 hr/AC YS = 285 MPa, HV = 155 kgf/mm^2

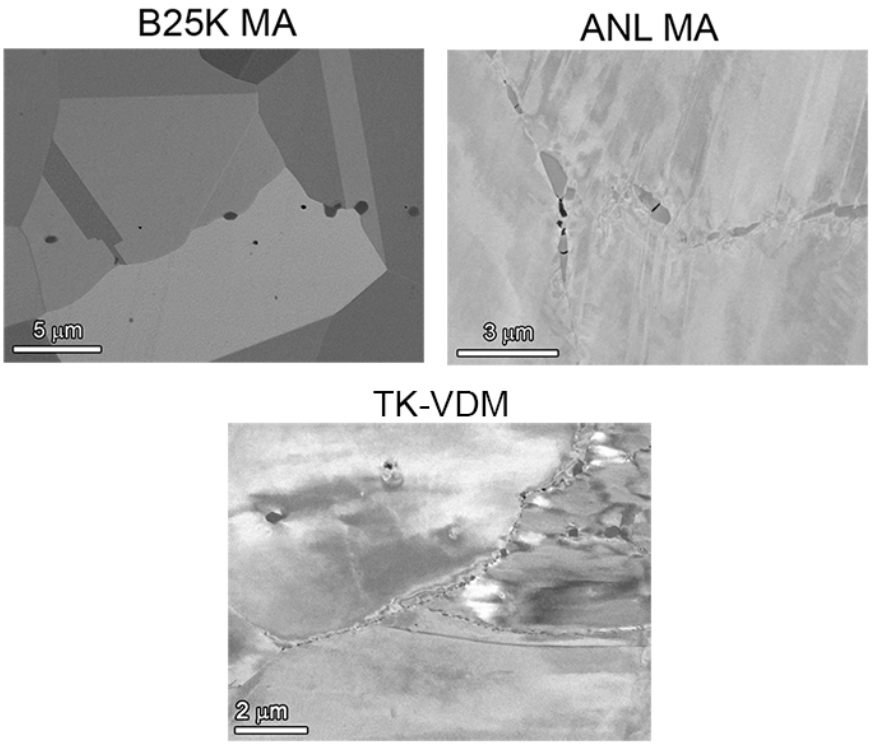

Figure 3. SEM-BSE images illustrating differences in the grain boundary carbide microstructures for each of the alloy 690 plate/bar materials in the as-received condition.

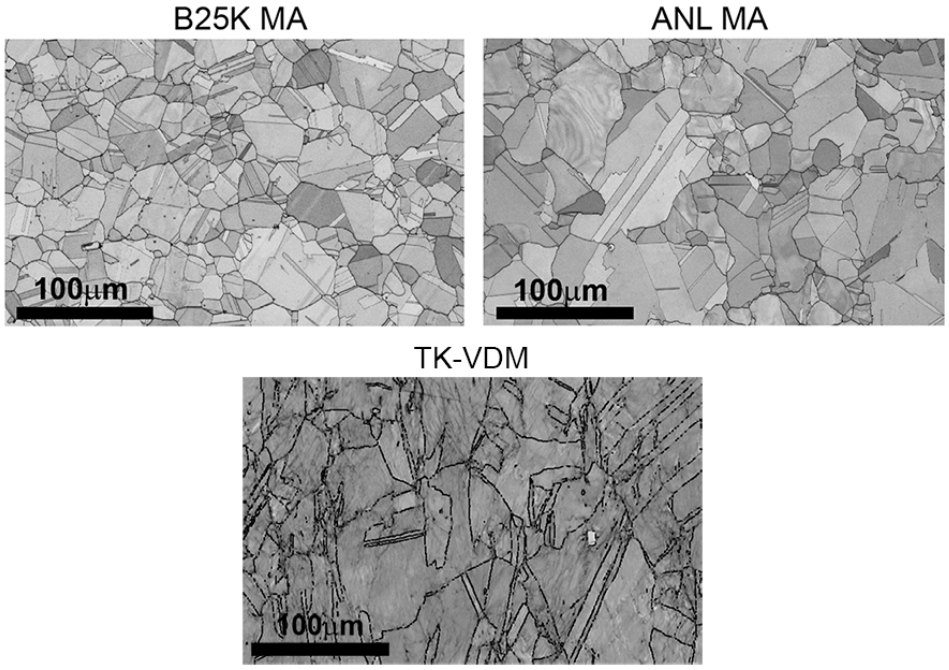

Figure 4. SEM EBSD pattern quality maps showing the grain size for the three alloy 690 plate/bar materials.

Table 3. Summary of grain size and carbide distributions for materials selected for SCC initiation testing.

Material	Grain Size (μm)	Carbide Location, Size	GB Carbide Density
CRDM Materials			
Valinox RE243 TT	~90	IG, 50–200 nm	Semi-continuous, spacing ~100 nm
Doosan 133454 TT	~90	IG, 1–5 μm	Semi-continuous, spacing ~0.5–2 μm
Sumitomo E67074C TT	~35-40	IG, 50–300 nm	Semi-continuous, spacing ~100 nm
Plate/Bar Materials			
GEG B25K MA	~10-15	TG and isolated IG, 1–3 μm	Low
ANL HK3297HK12 MA	~20-25	IG, 0.5–3 μm	Semi-continuous, spacing ~0.2–2 μm
TK-VDM 114092 TT	~35-40	IG, 50-200 nm	Semi-continuous, spacing ~0.1–0.5 μm

Characterization of Permanent Damage in Cold Worked Alloy 690 Materials

Scanning and transmission electron microscopy (TEM) were utilized to examine permanent damage induced during cold work on the alloy 690 materials. SEM was used to obtain a global perspective of the damage throughout the sample, whereas TEM provided a more detailed, localized examination. There is evidence that deformation tends to be localized at GBs, particularly for materials with a semi-continuous distribution of small carbides. The damage induced by cold work generally falls into two categories: (1) nano-size voids at GB precipitate interfaces and (2) cracking of the precipitates themselves. It should be noted that identification of a void versus a crack through SEM imaging was often challenging in the TT samples due to their high GB carbide coverage. For example, a void between two overlapping carbides may easily appear as a crack. In addition, titanium nitride (TiN) particles can be very dark during SEM-BSE imaging making them difficult to distinguish from voids. As a result, comparisons were routinely made between SEM secondary (SE) and BSE image pairs to better discriminate these fine features.

Cold Work Damage in CRDM Materials

All of the CRDM materials that were used for cold-work studies on SCC growth have been examined for permanent GB damage, from which materials for the SCC initiation testing were selected. Using the counting methodology adopted in a NRC NUREG report prepared by PNNL [7], the number of cracks and voids were counted from at least 10 GBs (properly oriented to the deformation plane) across each sample. A summary of the degree of damage for the CRDM materials is provided in Table 4. Examples of damage microstructures for the alloy 690 CRDM RE243 heat are provided in the following paragraphs.

Table 4. Summary of carbide microstructures and damage morphologies in CW alloy 690 TT CRDM materials.

Material	AR GB Carbide Microstructure		Cold Work Induced GB Damage	
	Location, Size	Density, Spacing	Density of Cracked GB Precipitates	IG Void Density
Valinox RE243 12%CF*	IG, 50–200 nm	Semi-continuous, spacing ~100 nm	None–Low	Low
Valinox RE243 17%CR			Low	Low
Valinox RE243 21%CF*			Low	Low–Moderate
Valinox RE243 31%CR			Low	Moderate
Valinox RE243 31%CF*			Low	Moderate
Sumitomo E67074C 13%CF	IG, 50–200 nm	Semi-continuous, spacing ~100 nm	None–Low	Low
Sumitomo E67074C 21%CF*			Low	Low–Moderate
Sumitomo E67074C 31%CF*			Low	Moderate
Doosan 133454 21%CF*	IG, 1–5 µm	Semi-continuous, spacing ~0.5–2 µm	Low	Low–Moderate
Doosan 133454 31%CF*			Low	Moderate

CF = cold-forged, CR = cold-rolled.
* Materials tested for SCC initiation.

The 17%CR CRDM alloy 690TT material showed significant strain contrast in SEM images, and limited TEM exams documented the expected high dislocation densities. Isolated nano-size voids and cracked carbides were observed in this material as illustrated in Figures 5 and 6. SEM exams indicated that the most common permanent damage in this material was small, well-spaced voids. Only a few cracked carbides were found, however a TEM sample prepared via focused ion beam (FIB) milling (Figure 6) revealed two cracks as well as a void along a GB with a high density of carbides. It can be difficult to discriminate between the formation of a crack or void in the scanning TEM image, but examination of the Cr-K elemental map from energy dispersive x-ray spectroscopy (EDS) shows that the cracks disrupt two continuous carbides. A secondary point of note in the Cr elemental map in Figure 6 is the overlap of two carbides in this section. Because TEM samples have a finite thickness, overlap of carbides on the GBs is expected. Unfortunately, this brings into question as to whether observations on overlapping, faceted carbides signify a crack or a void. Often in SEM and TEM images, there are high contrast objects between carbides that appear angled, and thus complicate the identification. The easiest determination of void formation is seen by its shape and relationship to adjacent carbides in both Figures 5 and 6.

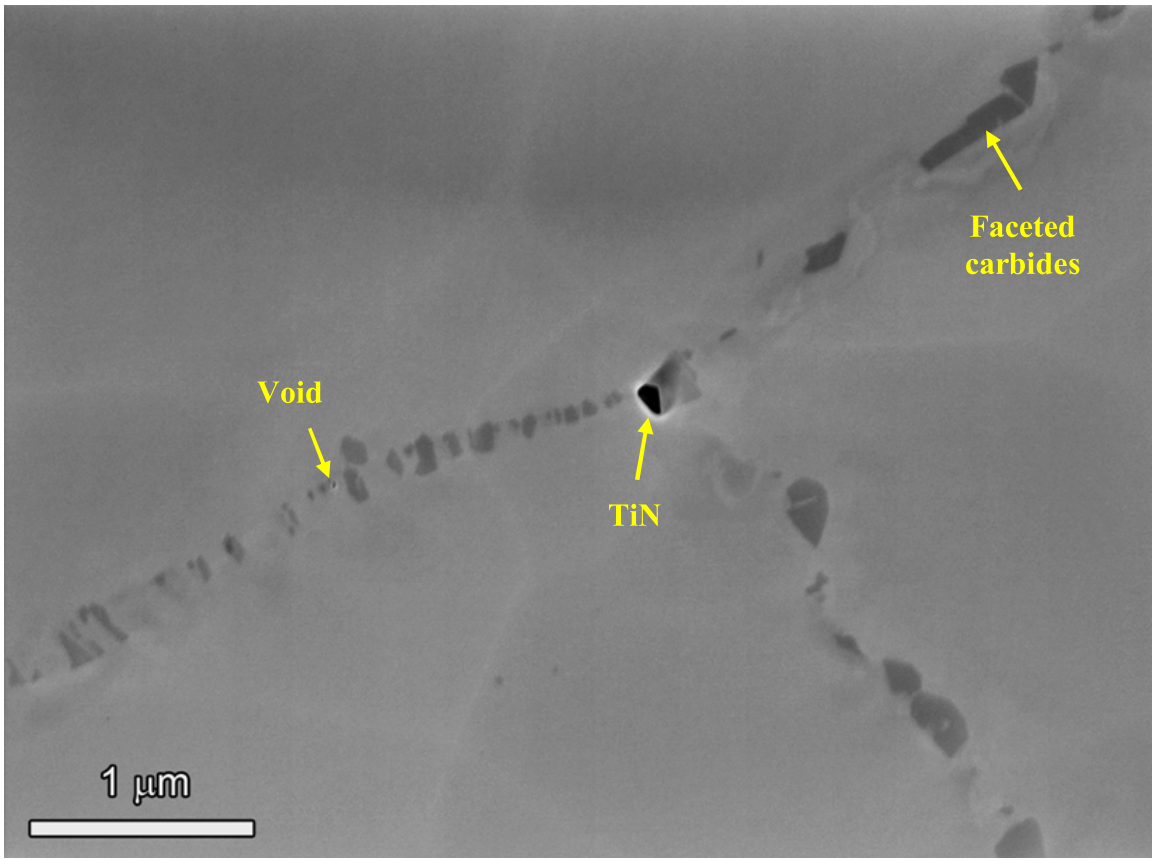

Figure 5. SEM-BSE micrograph illustrating representative image of $M_{23}C_6$ damage microstructure in the 17%CR Valinox CRDM alloy 690TT (heat RE243).

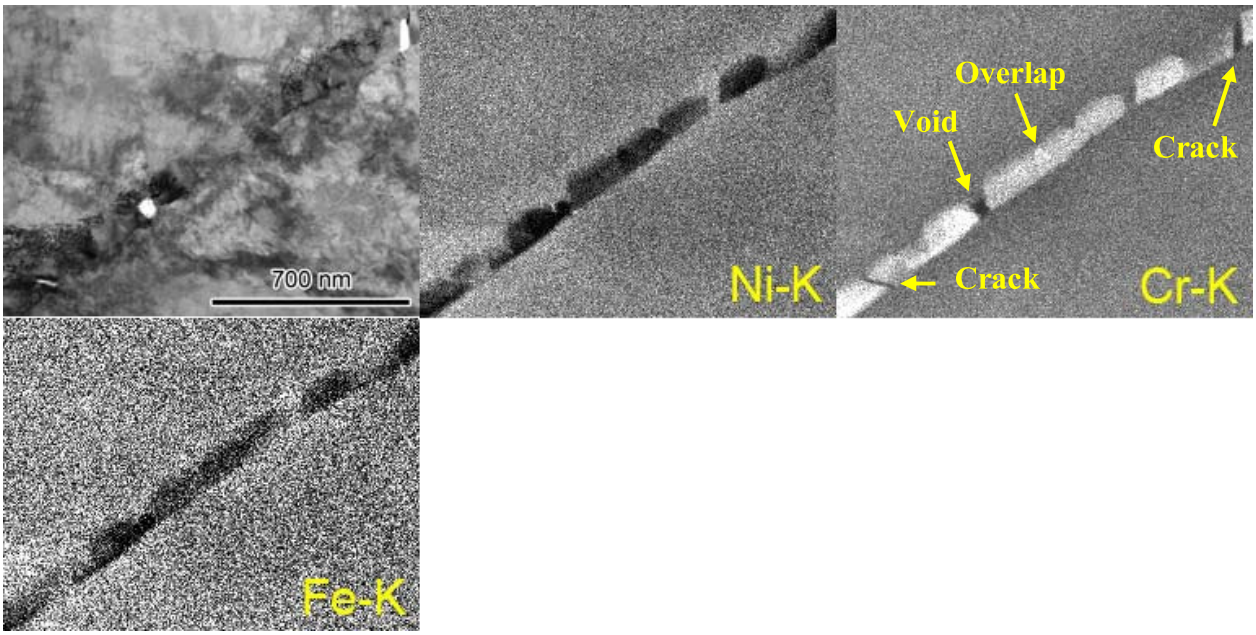

Figure 6. TEM EDS elemental maps illustrating damage in the 17%CR Valinox CRDM alloy 690TT (heat RE243).

The 31%CR CRDM alloy 690TT exhibited an extremely high dislocation density and a much larger amount of localized permanent damage at GBs as compared to the 17%CR alloy 690TT material. SEM analyses identified a large number of voids in cellular carbide regions (Figure 7) and a somewhat lower density along discrete carbide regions (Figures 8 and 9). Cellular carbide regions typically exhibited an array of various sized voids adjacent to $M_{23}C_6$ interfaces within the boundary migrated area. A much lower density of cracked carbides than voids were present in these structures. More importantly, there also appeared to be more voids than cracked carbides along boundaries with discrete $M_{23}C_6$ particles. As previously discussed, differentiating between the sporadic TiN particles, cracked carbides and voids can be difficult. Examples of highly damaged GB regions are presented in Figure 8 and a high density of local "dark" features can be seen resulting from low BSE yield. After careful examination (often comparing BSE and SE images), it was determined that most of the small (<75 nm) equiaxed and the elongated features (formed at the interfaces of faceted carbides) were voids. These cavities appear to abruptly change in shape as the void grows between faceted carbides as seen in Figures 7, 8(b) and 8(c).

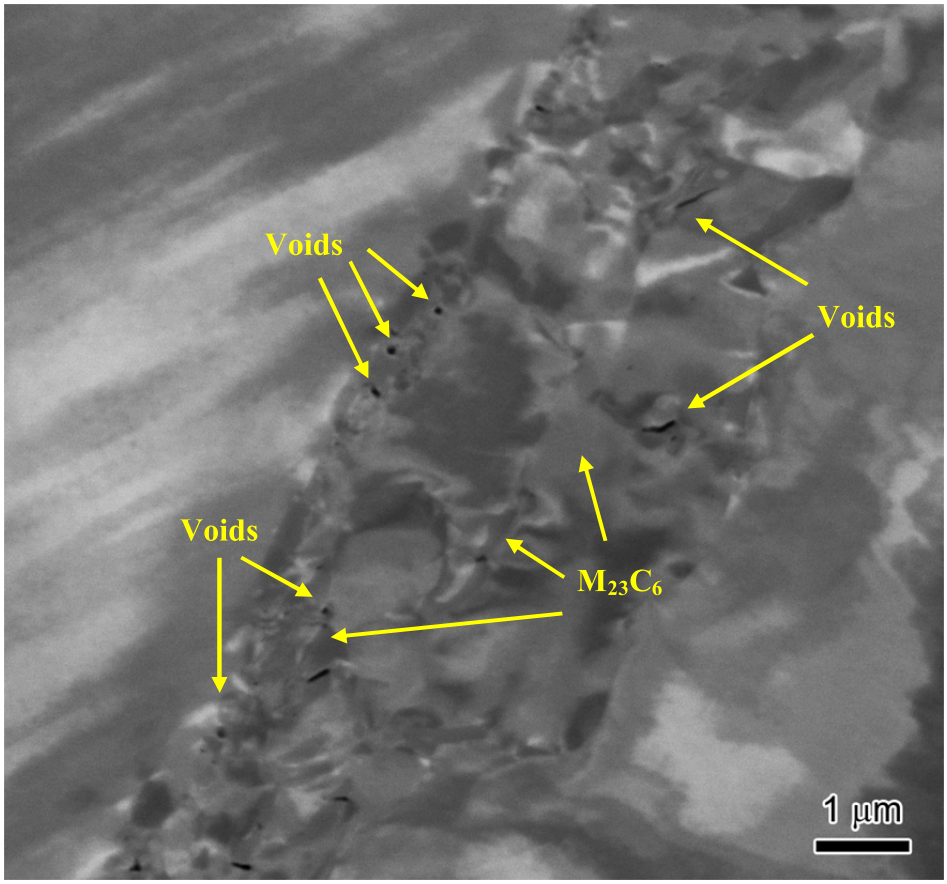

Figure 7. Low magnification SEM-BSE image showing CR-induced void formation within a cellular carbide microstructure region in the 31%CR Valinox CRDM alloy 690TT material (heat RE243). The strain contrast in this BSE image masks the appearance of the $M_{23}C_6$ carbides, but the voids between carbides are readily apparent.

SEM pair images are taken because of the different information gathered from each. SE contrast in Figure 9(a, c and e) very easily distinguishes between voids/cracks and TiN particles. The increased surface area around a void or crack provides a higher secondary yield, whereas the TiN particles do not have this contrast. Figure 9(a) highlights this perfectly, as a void and a TiN particle appear close together in the middle of the micrograph. At a certain point though, SE contrast is not as useful for imaging cracks versus voids as BSE contrast illustrated in Figure 9(b). In the upper left hand corner, the $M_{23}C_6$ carbide appears to be continuous but in the SE image the slight crack is tight enough that the additional surface area does not provide extra contrast. The complimentary BSE contrast in Figure 9(b) identifies that this is indeed a crack. Similar comparisons can be seen in the remaining image pairs in Figure 9(c-d) and (e-f).

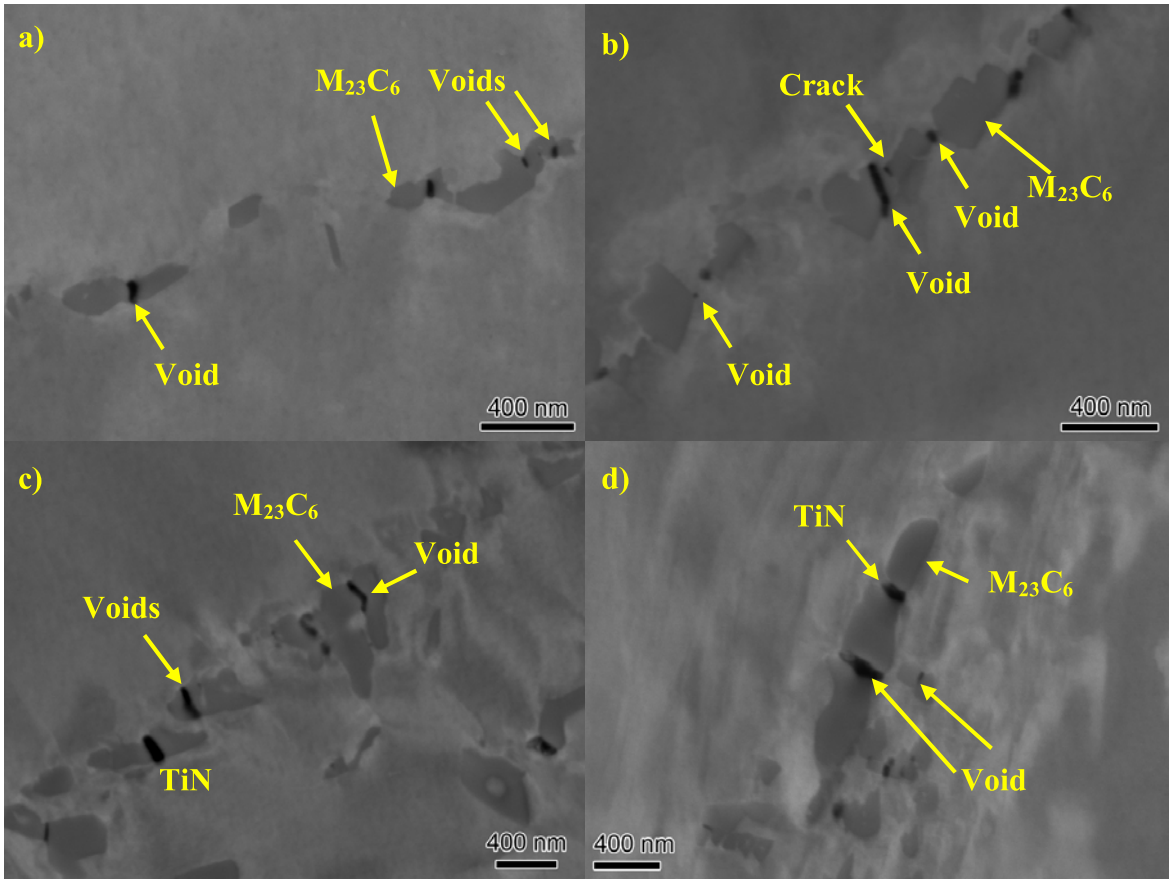

Figure 8. High magnification SEM-BSE micrographs illustrating IG carbide damage microstructures in the 31%CR Valinox CRDM alloy 690TT (heat RE243).

As a result of SEM and limited TEM examinations on the 31%CR alloy 690TT material, general conclusions can be made about the cold rolling induced damage microstructure. A significant difference in the permanent damage distributions is seen between the cellular and discrete carbide regions although both show a moderate density of small voids and a limited number of cracked carbides. It is important to note that most GBs in the TT material have a semi-continuous distribution of discrete carbides. As a result, the primary cold work induced damage is the presence of small voids at IG carbide interfaces. Along with this permanent damage, cold work also produces extremely high dislocation densities and localized strains at the boundaries.

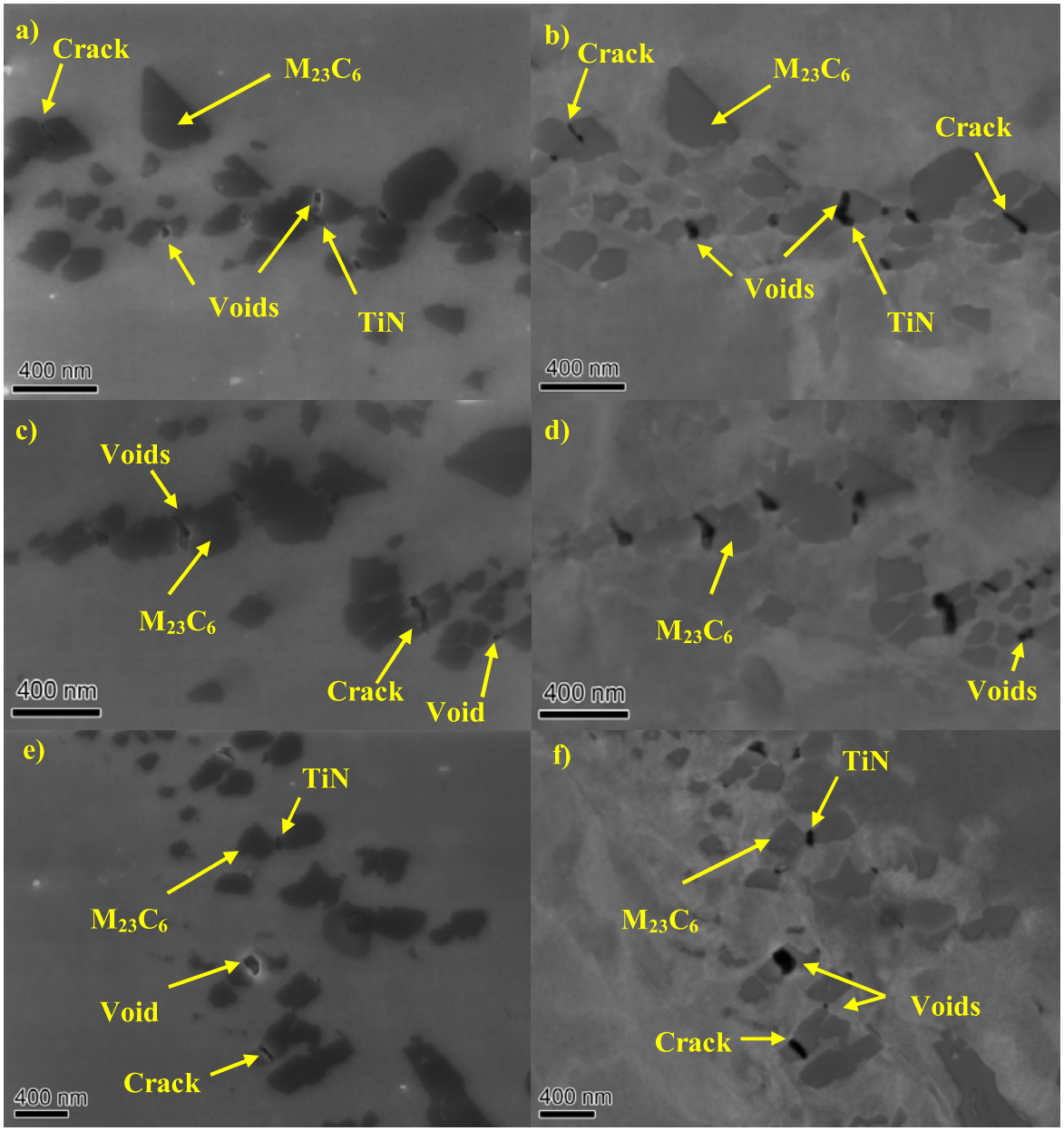

Figure 9. High magnification SEM-SE (a, c, e)/BSE (b, d, f) pair micrographs showing carbide damage microstructures in the 31%CR Valinox CRDM alloy 690TT (heat RE243).

Figure 10 illustrates the effect of increasing cold work damage on the same alloy 690 CRDM heat, ranging from 12% to 31%. At lower cold work levels (12% and 17%), there are no cracks and only a few sporadic voids observed on carbides along the GB length. At 21% cold work there is a low density of cracked carbides observed, but the increase in void density as compared to the 17% is apparent. Finally at levels of 30-31% cold work, the void density definitely increases, although the crack density (carbides and nitrides) at GBs does not change significantly compared to the lower CW materials.

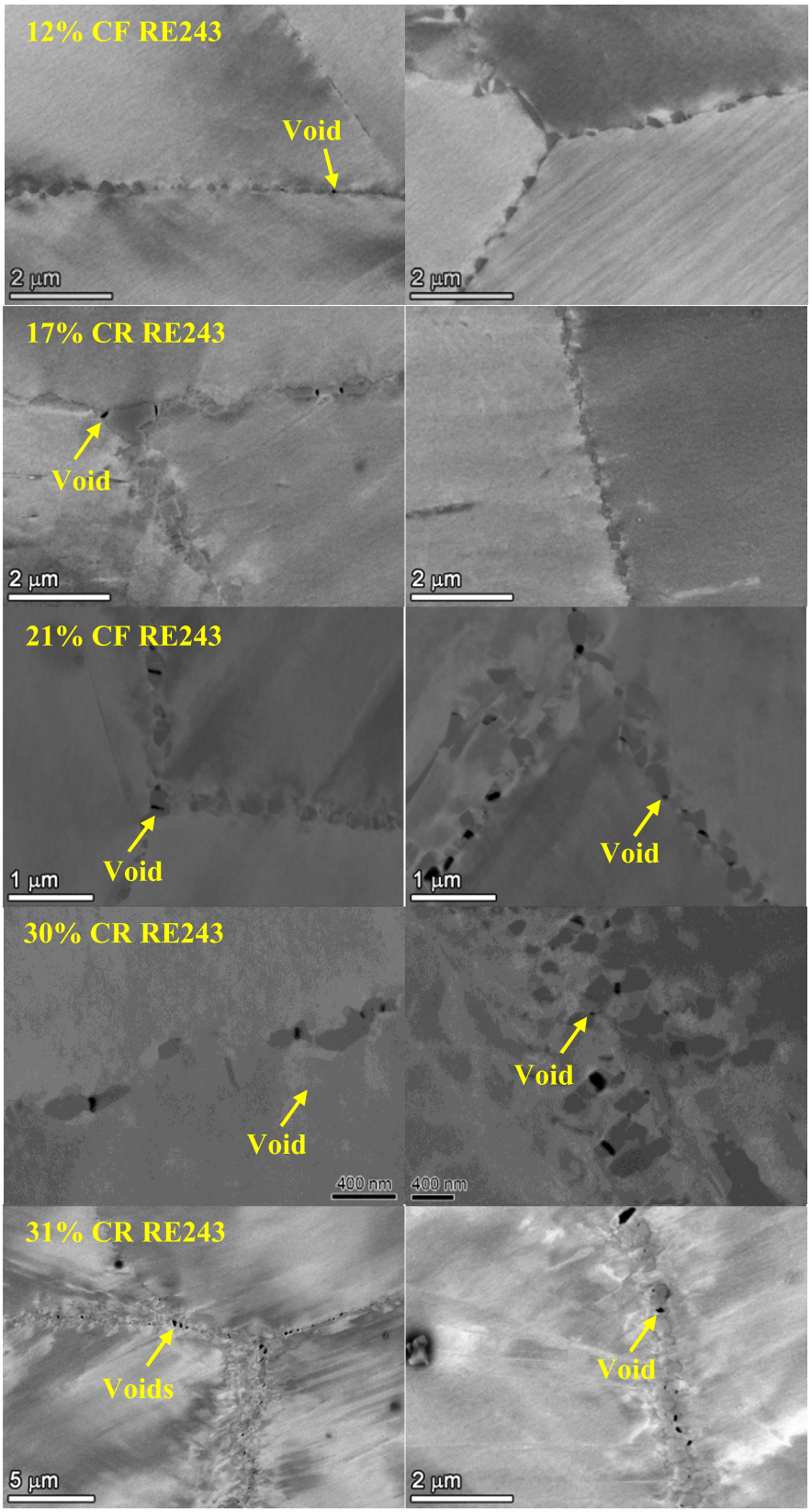

Figure 10. High magnification SEM-BSE images showing the evolution in GB damage with increasing cold work in the Valinox CRDM alloy 690TT.

Only limited GB characterizations have been performed on the Sumitomo and Doosan CRDM materials. Examples of GB damage are shown in Figure 11 for these materials with a low-to-moderate degree of cold work. In general, similar permanent damage structures were discovered in the Sumitomo CRDM heat as for the Valinox material at the same cold work level. This is consistent with their comparable GB carbide microstructures as summarized in Table 4. For the Doosan CRDM material exhibiting bulkier carbides with wider spacing, the voids/cracks were also observed to be larger and more separated. However, the permanent damage was clearly observed to increase with the cold work level in all three CRDM alloy 690TT materials.

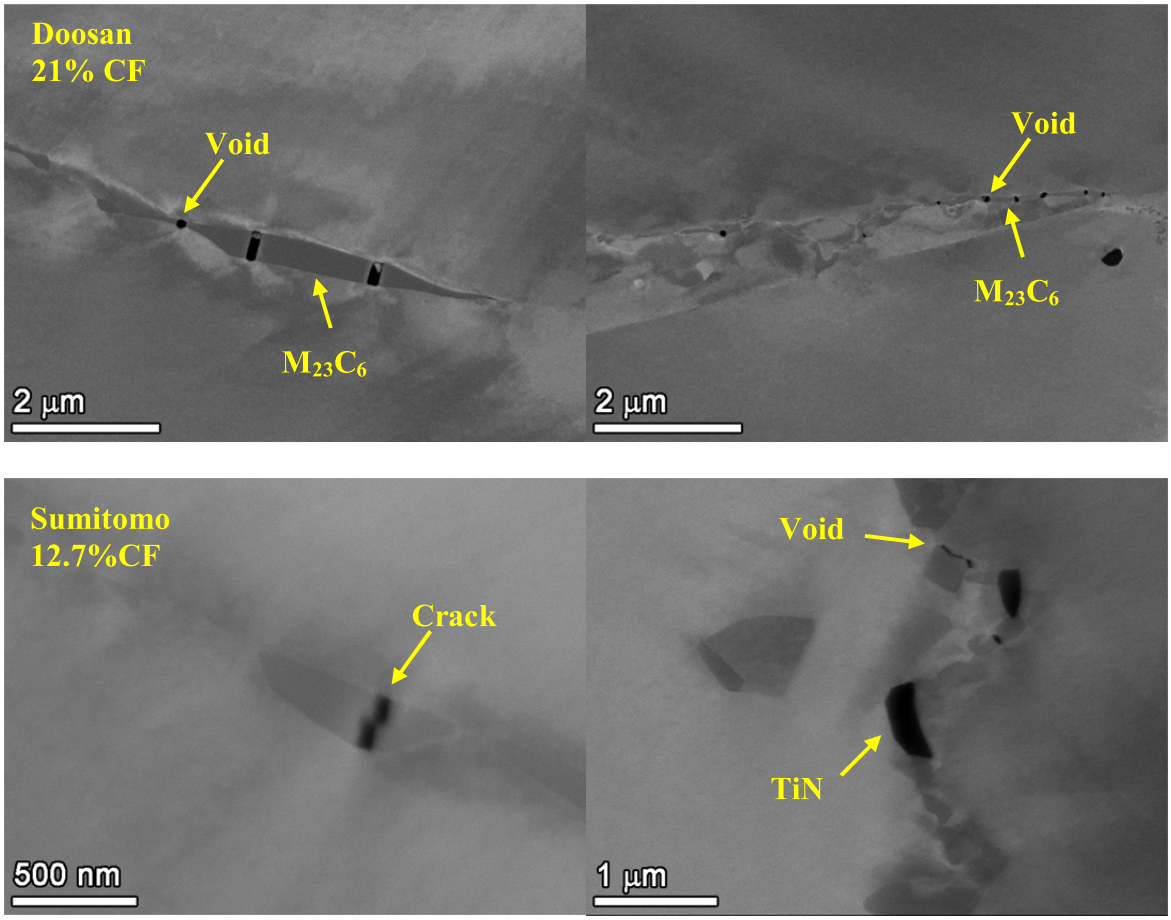

Figure 11. High magnification SEM-BSE images showing carbide damage microstructures for the Doosan and Sumitomo CRDM alloy 690TT materials.

Cold Work Damage in Plate/Bar Materials

A summary of the carbide and GB damage structures for the plate and bar materials is provided in Table 5. Although in the MA condition, the 26%CR ANL alloy 690 had a moderate-to-high density of IG $M_{23}C_6$ carbides. Even though the density of the carbides in the ANL alloy 690 was lower than that of the CRDM TT materials, the 26%CR ANL alloy 690 exhibited the highest density of permanent damage among the various CW materials. Additionally, there appear to be a higher density of TiN at GBs in the ANL material and many more TiN inclusions in the matrix. Examples of the various types of cold rolling induced damage in the ANL material are presented in Figures 12 and 13. A high density of small (50–75 nm) voids can be seen in Figure 12(a, b and d), typically forming at an IG carbide interface. Lastly, cracks through $M_{23}C_6$ carbides are identified in Figures 12(b and d) and 13. Without question, the 26%CR ANL cross-sections revealed the highest density of IG cracked carbides among CW materials along with a high density of voids slightly greater than for the ~30%CW alloy 690TT CRDM materials. TiN precipitates could often be identified in these samples as opposed to voids due to the faceted nature on the interface with the matrix. In Figure 13(d–e), the IG TiN precipitates are often found between Cr-rich carbides.

Table 5. Summary of carbide microstructures and damage morphologies in CW alloy 690 plate and bar materials.

Material	**AR GB Carbide Microstructure**		**Cold Work Induced GB Damage**	
	Location, Size	**Density, Spacing**	**Density of Cracked GB Precipitates**	**IG Void Density**
ANL MA 26%CR*	IG, 0.5–3 μm	Semi-continuous, spacing ~0.2–2 μm	Moderate	Moderate–High
GEG MA 20%CR	Primarily TG, 1–3 μm	Low density, unevenly distributed	None–Low	None–Low
TK-VDM 114092 22%CF	IG, 50–200 nm	Semi-continuous, spacing ~0.2–0.5 μm	Low	Low–Moderate
TK-VDM 114092 32%CF*			Low	Moderate

CF = cold-forged, CR = cold-rolled.
* Materials tested for SCC initiation.

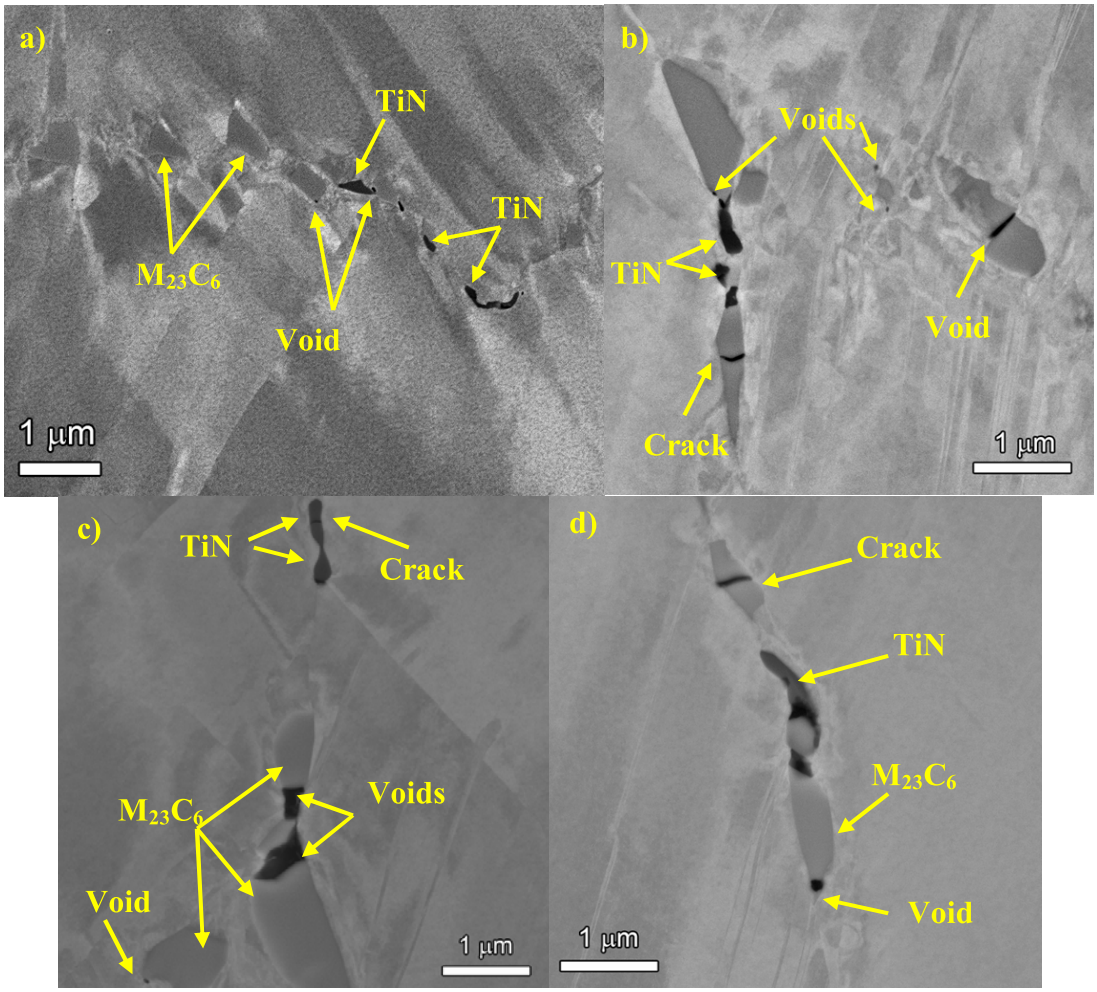

Figure 12. SEM-BSE micrographs illustrating GB damage microstructure in the 26%CR ANL alloy 690.

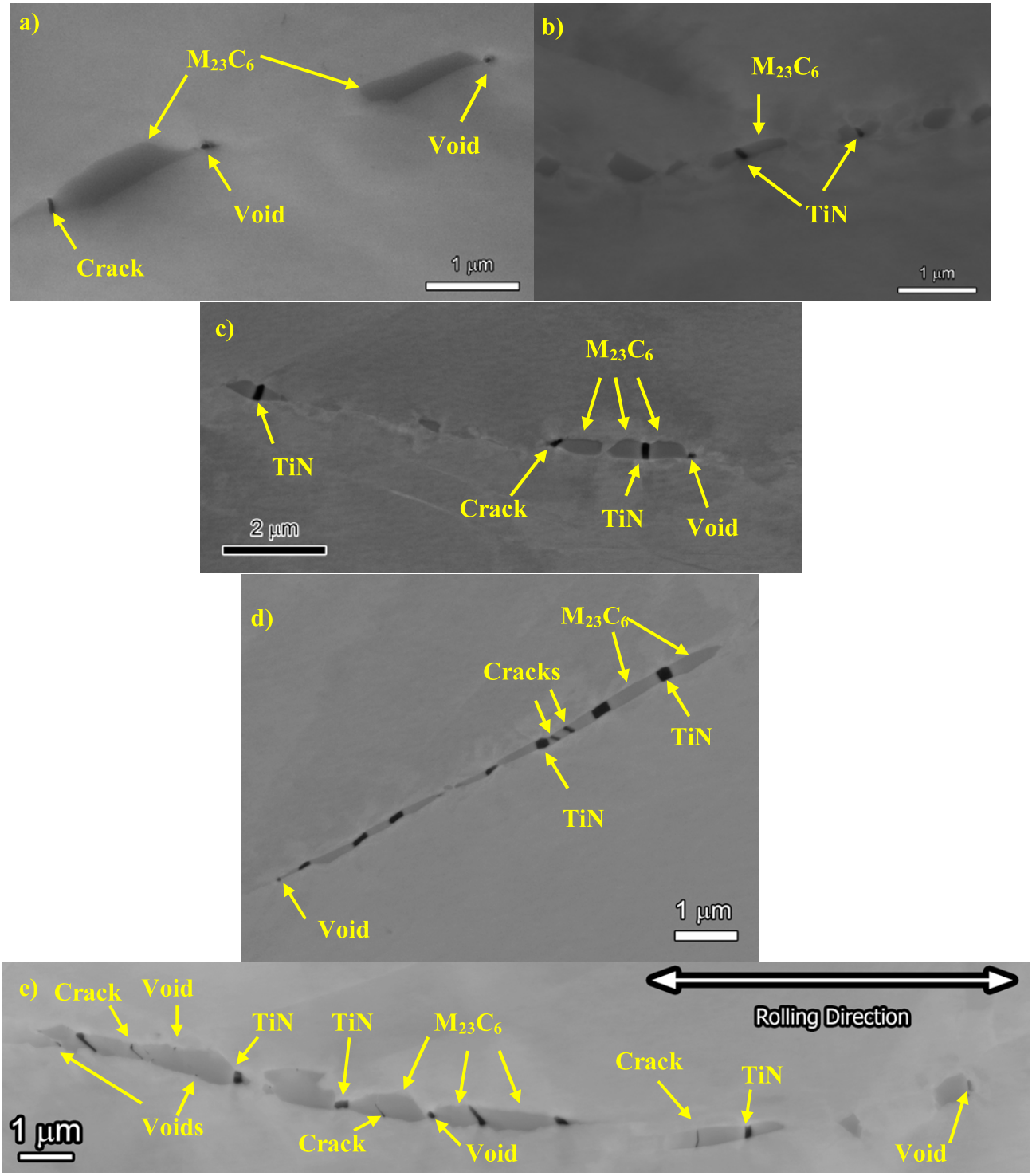

Figure 13. SEM-BSE micrographs illustrating general carbide damage microstructure in the 26%CR ANL alloy 690.

As noted earlier, the 20%CR GEG alloy 690 material had a significantly different microstructure with a much lower density of IG carbides and nitrides along with many transgranular (TG) carbides. This resulted in a much lower density of IG cracked carbides and voids for most GBs. However, isolated boundary regions exhibited closely spaced carbides and more extensive permanent damage. Representative images for these isolated regions with cracked carbides and voids are presented in Figures 14, 15 and 16. They illustrate the presence of both cracks and voids associated with $M_{23}C_6$ carbides in local regions. Figure 14 shows cracks and voids on an irregularly shaped, elongated carbide. Figure 15 shows various IG carbides with both equiaxed shapes and irregular shapes with sharper facets, as well as an equiaxed, IG TiN particle. Voids are observed between the carbide and nitride in Figure 15(a) and on the irregularly shaped carbide in Figure 15(b). Figure 15(c) highlights cracks in another irregularly shaped carbide. Lastly, voids can be identified among a cluster of equiaxed carbides in Figure 16. As well, a void is observed between an equiaxed TiN and $M_{23}C_6$ precipitate at the bottom of the figure. Although characterizations have not yet been performed on the 12.4% and 18.3%CF conditions being used for the SCC initiation tests, the general morphology of the permanent damage is believed to be similar to what has been observed in the 20%CR condition except with lower densities of cracks and voids.

In summary, the low density of IG carbides in most GBs for the GEG material resulted in a much lower distribution of cracked carbides and voids than for the 26% ANL material. Only local GB regions on the order of 10 μm in length had semi-continuous IG precipitates and more extensive permanent damage. These regions appeared to be associated with compositional banding that was oriented perpendicular to the rolling direction.

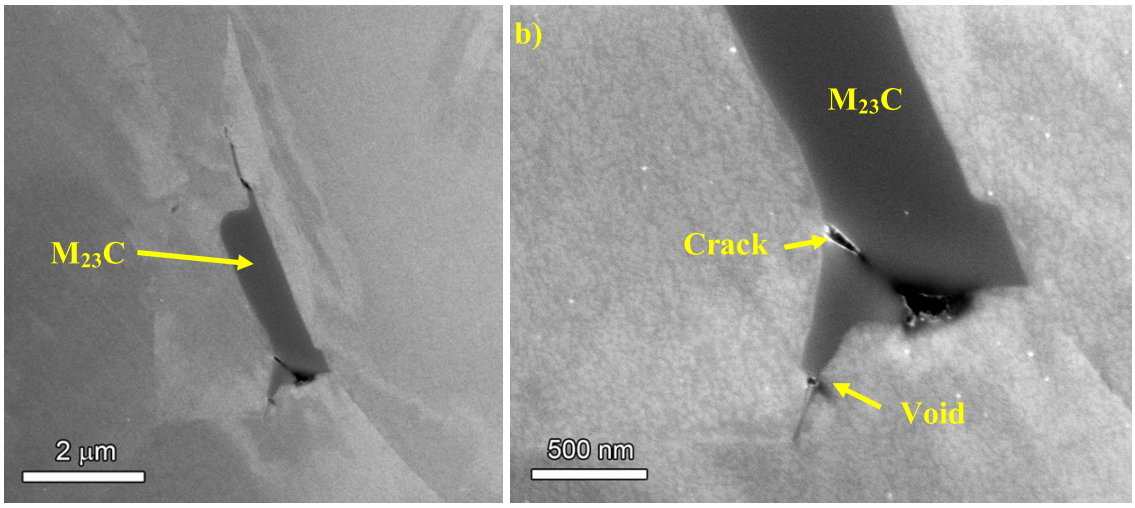

Figure 14. SEM-BSE (left) and SE (right) micrographs illustrating general carbide damage microstructure in the 20%CR GEG alloy 690.

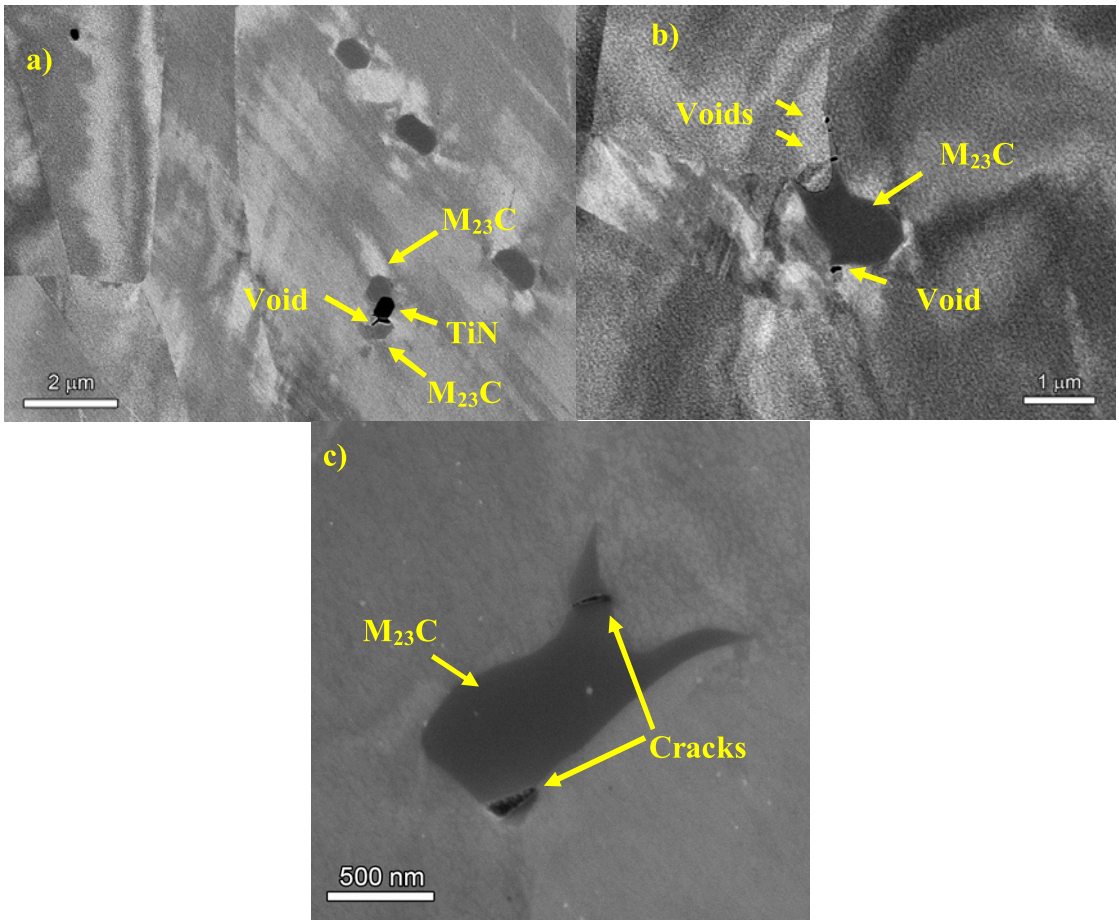

Figure 15. SEM-BSE micrographs illustrating general carbide damage microstructure in the 20%CR GEG alloy 690.

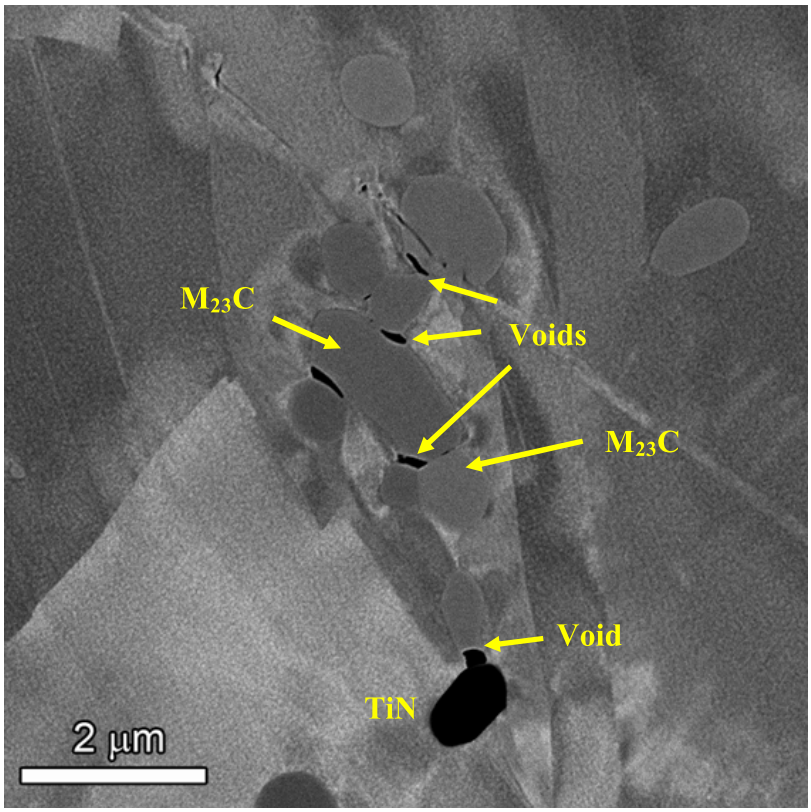

Figure 16. SEM-BSE micrograph showing void damage near carbides in the 20%CR GEG alloy 690.

Only limited examinations were performed on the CW TK-VDM plate material. Consistent with its TT condition a semi-continuous distribution of GB carbides was present, however the cold work-induced void distribution was somewhat lower than seen in the CRDM materials with the same cold work level. This is illustrated in Figure 17 and is considered to be associated with slightly non-uniform spacing between the GB carbides (Table 3).

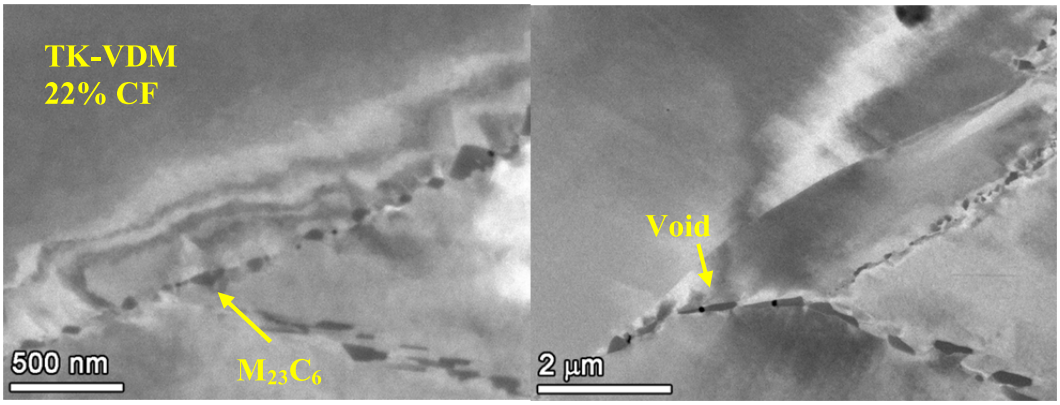

Figure 17. High magnification SEM-BSE micrographs showing carbide damage microstructures in the 22%CF TK-VDM plate alloy 690TT.

Summary of Hardness and EBSD Measurements

To assist in understanding of cold work effect on material properties, EBSD mapping was used to estimate residual plastic strains and hardness mapping was employed to indicate strength levels in the alloy 690 materials. These measurements assessed the material response over a region of many grains and were performed on the compact tension (CT) specimens used for SCC propagation tests in the crack growth plane.

EBSD samples were prepared by mechanically polishing through a series of successively finer grits of diamond paste followed by a final polish on colloidal silica (0.05 μm). The EBSD analyses were conducted using a JEOL 7600F field emission gun (FEG)-scanning electron microscope (SEM) equipped with a Nordlys camera interfaced with the Oxford/HKL Channel 5 software package. Maps were collected at 8x8 binning using a step size of 0.5 μm with a magnification of 250X for all conditions. Such a map required ~5.5 hours to image and contained on average ~750,000 data points. The map size and detail were necessary to accurately describe the spatial distribution of boundary misorientations within the sample. Processing the data with the Channel 5 software reveals the grain size, types of boundaries, degree of crystal misorientation between individual pixels. In this study, the phase was limited to austenitic stainless steel, which provides an analogue for alloy 690 since both materials possess the same crystal structure and have nearly identical lattice parameters. Results focus on the overall crystal orientation and strain of the alloy 690 austenite phase and do not consider orientation relationships of the small precipitates.

Two methods are used to effectively demonstrate the strain distribution within the various alloy 690 conditions. The first is mapping to provide visual clues as to the local accumulation of strain represented by misorientation. All maps were generated within the Channel 5 software module Tango including pattern quality maps, inverse pole figure maps and local misorientation maps, all of which make use of the crystallographic orientation data at each pixel position. The second analysis method is a numerical calculation of the density of low angle misorientation boundaries. This approach provides a global estimate of the accumulated strain within the region of interest called the integrated misorientation density (IMD). The IMD is the sum of normalized density of misorientation boundaries weighted by the magnitude of the misorientation within a designated range of misorientation angles. The upper limit of the misorientation range is defined as the threshold strain beyond which the density of low angle boundaries may be too high to resolve, or pattern quality degrades to the point that Kikuchi patterns cannot be identified. In this study, the upper limit was set at 5° at which the limiting density of misorientation boundaries was not reached and the pattern quality was sufficient for analyses. Meanwhile, 0.3° was chosen as the lower limit to minimize the impact of random noise on measured misorientations. The IMD values for the investigated alloy 690 samples are listed in Table 6. More detailed information on the EBSD approach and specific measurements are reported in a prior NRC report [8].

Hardness testing was conducted after SEM and EBSD microstructural exams where a 0.05 μm colloidal silica final polish was required. This surface condition provided an ideal platform for hardness testing. Hardness experiments were carried out using a CM-700AT Clark Microhardness Tester equipped with a FutureTech FM-ARS9000 fully automated hardness testing system. The automated Vickers hardness system was chosen for its ability to rapidly perform and measure large indentation arrays that can then be converted to hardness contour

plots. Contour plots are especially useful for evaluating materials that have the potential to exhibit hardness gradients due to microstructural or compositional variability. They have been extremely informative for evaluating weld metals, dissimilar metal welds and heat affected zone regions. For this work on alloy 690 materials, the contour plots were generated to ensure uniformity of the base metal and particularly in CW materials where through-thickness differences in deformation can be produced. These effects were minimized since measurements were made along the CT specimen crack growth plane and thus from a constant thickness location within the CW plate, bar or tube material.

Vickers microindentation testing was performed using a 300 g load, 0.225 mm indent spacing and 12 s dwell time. Parameters were chosen based on the response for the as-received, lowest strength materials. The 0.225 mm indent spacing was chosen to maintain >2.5*d* spacing while maximizing the number of hardness data points acquired. Basing the pattern spacing on the as-received (lowest strength material) ensured that the indentation load and spacing for subsequent measurements could be held constant.

A tabulated summary of hardness data for the CW alloy 690 materials pertinent to this study is given in Table 6. For reference, the as-received materials in the non-CW condition exhibited Vickers hardness values between 150 and 180 kgf/mm^2. Once again, more specific information on these measurements are reported previously [8, 12].

Table 6. Measured hardness and IMD values for the CW alloy 690 samples.

Crack Growth Specimen ID	Sample Information	Average IMD	Average HV (kgf/mm^2)
CT104	Valinox RE243 TT + 12%CF*	0.058	222.3
CT054	Valinox RE243 TT + 17%CR	0.050	249.1
CT100	Valinox RE243 TT + 21%CF*	0.089	275.2
CT038	Valinox RE243 TT + 31%CR	0.160	314.7
CT099	Valinox RE243 TT +31%CF*	0.157	302.0
CT103	Sumitomo TT + 13%CF	0.064	242.2
CT098	Sumitomo TT + 31%CF*	0.187	317.8
CT037	GEG MA + 20%CR	0.180	321.3
CT102	Doosan TT + 21%CF*	0.104	285.2
CT036	ANL MA + 26%CR*	0.170	310.1
CT094	TK-VDM TT + 32%CF*	0.160	328.5

* Materials tested for SCC initiation.

Examples of the EBSD pattern quality and local misorientation maps are presented for lightly CW CT samples from two alloy 690TT CRDM heats (Valinox RE243 and Sumitomo) in Figure 18 along with hardness maps. The Valinox RE243 specimen showed a slightly lower hardness (by ~10%) than the similar CW Sumitomo sample. Local misorientation distributions for the two were also slightly different with the Sumitomo material showing typical near-boundary misorientation accumulation, while the Valinox RE243 material exhibiting pockets of intragranular misorientation.

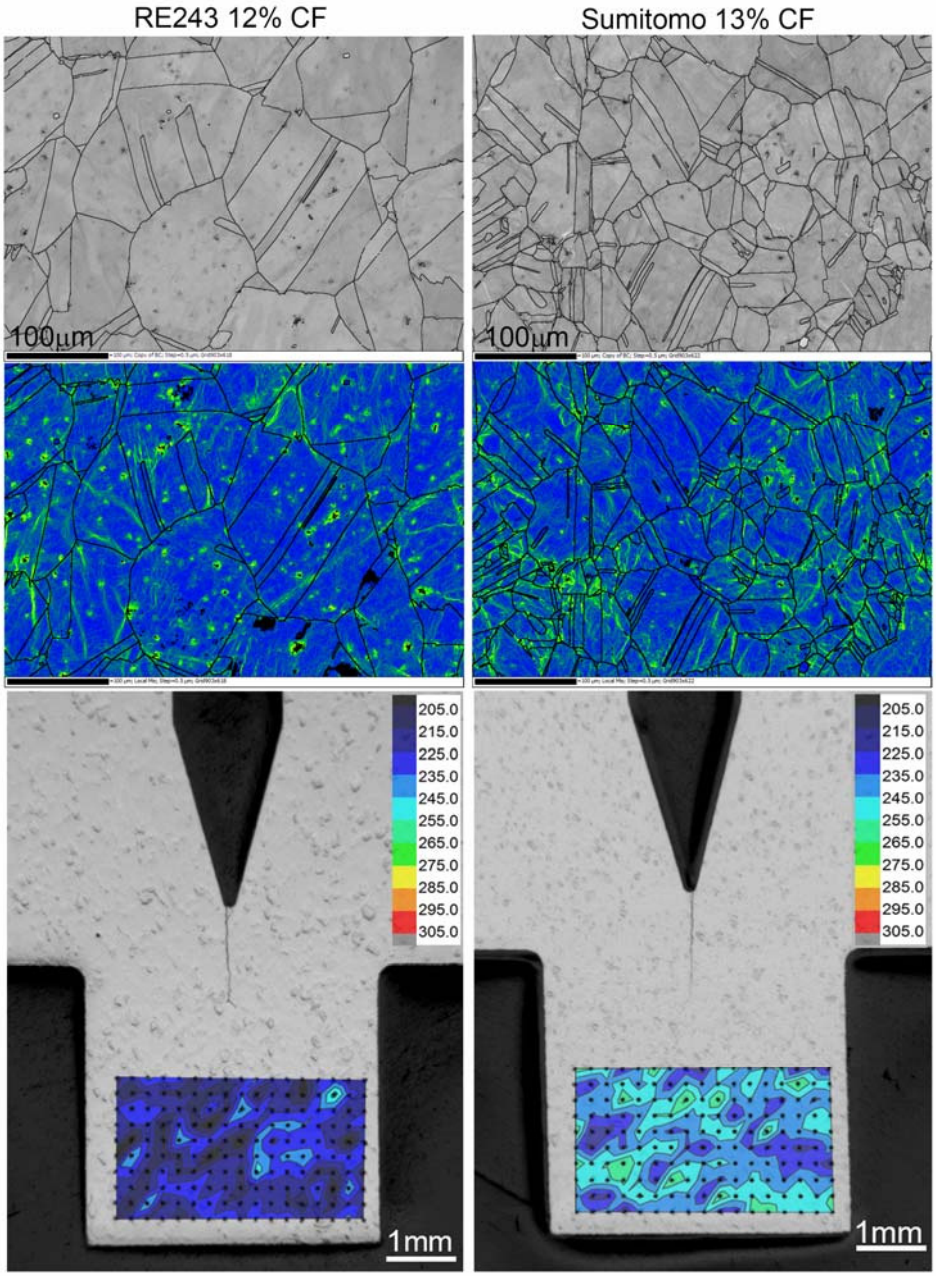

Figure 18. EBSD pattern quality images (top), IMD maps (center) and hardness contour overlays (bottom) for the most lightly cold worked samples CT103 and CT104. The 13%CF Sumitomo sample is slightly harder, whereas the Valinox sample exhibited unique intragranular pockets of elevated misorientation density.

As expected, drastic increases in misorientation and hardness are identified in the 31%CF Valinox and Sumitomo alloy 690 CRDM materials as shown in Figure 19. As noted earlier, the Sumitomo heat has a smaller grain size than the Valinox heat. This may be a factor in the lower average hardness and IMD values for the 31%CF Valinox specimen in comparison to the 31%CF Sumitomo specimen.

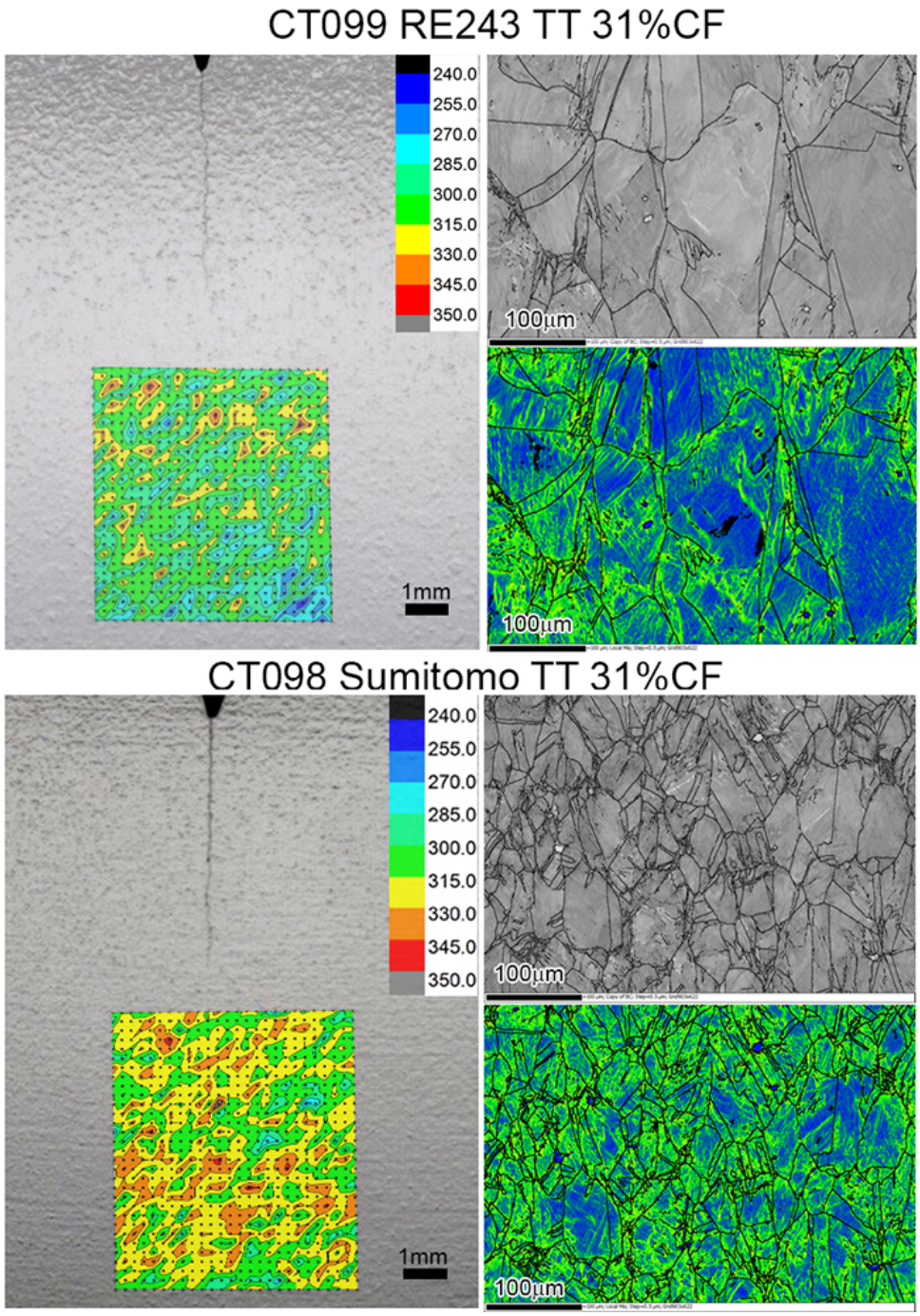

Figure 19. Hardness and EBSD results for the 31%CF Valinox specimen (CT099) compared to the 31%CF Sumitomo TT specimen (CT098). Grain size differences were readily apparent, likely causing the visible hardness and local misorientation distribution differences.

Blunt-Notch SCC Initiation Testing on CW Alloy 690 CRDM Materials

Chapter Overview

Previous SCC initiation testing in simulated PWR primary water revealed that a stable chromia layer forms over exposed GBs suggesting that alloy 690 would be highly resistant to a stress corrosion dominated SCC nucleation and initiation mechanism [2, 13]. It was therefore decided to evaluate dynamic straining as a means to accelerate the formation of precursor surface cracks. The first tests were performed on 31%CF blunt notch compact tension (BNCT) specimens from two alloy 690TT CRDM (Sumitomo and Valinox) heats. These specimens were subjected to several load cycles with 100 h load ramps that were designed to produce ~1% plastic strain in the vicinity of the notch. This resulted in a significant increase in the DCPD-measured CGRs due to sharp increase in the depth of cracks within 2500 h in both specimens. Post-test examination revealed significant creep cavitation and cracking in the bulk of these specimens with detailed results reported previously [3, 4]. In order to better understand how the loading ramps employed in these blunt notch tests could produce such extensive creep cavitation and cracking, a second series of blunt notch experiments were started in late 2014. Once again, the 31%CF Valinox CRDM and 31%CF Sumitomo CRDM materials were selected along with these same heats in the ~21%CF condition. In an effort to affect the degree of creep cavity formation, the decision was made to limit the strain level to 0.5% for each ramp. No crack initiation was detected by DCPD during the cyclic loading ramps, and the test was continued at constant load condition with moderate stress intensity (K) until DCPD-indicated initiation occurred at ~10400 h in the two 31%CF specimens. The tests were ended for the four specimens in April 2016 after a total exposure of ~11800 h. During the testing period, periodic inspections were conducted on the notch surface of the specimens to look for initiation precursor microstructures, especially for the small cracks that had not yet been detected by DCPD. Meanwhile, a slice was removed from all specimens at each test interruption and at the conclusion of the test to document GB cavity distributions. Microstructural characterization results on the BNCT specimens are summarized in this chapter, providing a comprehensive overview on the evolution of precursor damage and small IG cracks over time.

Experimental

Materials and Specimen Preparation

Mechanisms controlling crack initiation in CW alloy 690 have been evaluated using BNCT specimens tested at GE Global Research Center under a PNNL subcontract. Two alloy 690 CRDM heats (Valinox heat RE243 and Sumitomo heat E67074C) in 21%CF and 31%CF conditions were tested. Standard 0.5T CT specimens were used (Figure 20), but the notch tip was "wet ground" to a ~0.75 mm radius using a diamond wheel and given a final polish at PNNL to a 1 μm diamond finish. This created a well-controlled surface closely matching the surface condition for the constant load tensile specimens. Crack initiation can be better resolved by SEM examinations of the notch for the polished surface and compared to in-situ direct current potential drop (DCPD) measurements. All specimens were fabricated in S-L orientation such that the normal vector to crack propagation plane was parallel with the forging direction.

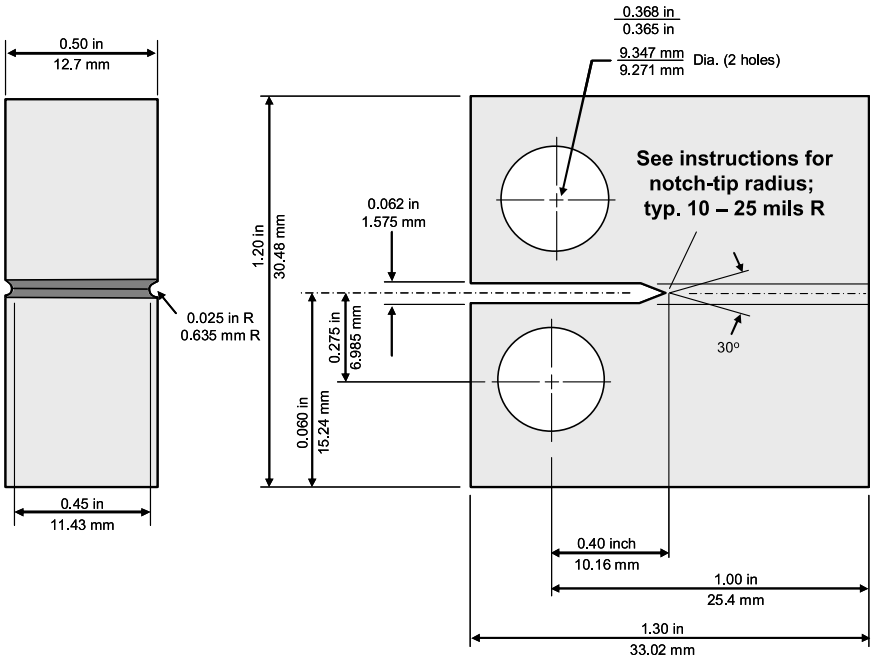

Figure 20. Dimensions of the 0.5T BNCT specimen. The notch radius is ~0.75mm for all specimens.

Test Methods and DCPD Measurements

The 1st phase of SCC initiation testing was performed in 2014 on two 31%CF alloy 690 CRDM specimens c672 (Valinox RE243) and c673 (Sumitomo E67074C). The BNCT specimens went through 4 load ramps between a K (actually a "pseudo K" assuming a tight crack rather than a blunt notch) of 27.5 and 44 MPa√m designed to produced ~1% plastic strain near the notch. Crack initiation was detected by DCPD at ~2050 h for c672 and at 2200 h for c673. Post-test characterization revealed a few large IG cracks emanating from the notch tip and many small IG creep cracks in the bulk for both specimens. More details on this test were described in previous reports [3, 4].

In order to better understand how loading conditions affect creep cavity and crack nucleation in CW alloy 690, 2nd-phase SCC initiation testing was performed from late 2014 to early 2016 on 21% and 31%CF materials from the same two heats. One specimen was machined for each material and cold work combination, i.e. c703 for the 31%CF and c707 for the 21%CF from Valinox RE243, and c704 for the 31%CF and c708 for the 21%CF from Sumitomo E67074C. The tests were again conducted in 360°C simulated PWR primary water with 600 ppm of boron, 1 ppm of lithium, and a dissolved hydrogen content of 26 cc/kg (at the Ni/NiO stability line). The two 31%CF specimens (c703 and c704) were tested in one system, while the two 21%CF specimens (c707 and c708) were in a second system. Measured DCPD response for the 31%CF specimens is summarized in Figure 21 and for the 21%CF specimens in Figure 22. The general experimental approach was the same for all specimens. They were equilibrated for several weeks in 360°C PWR primary water followed by initial observation at a *K* level of 27.5 MPa√m for ~1000 hours. The *K* level was slowly increased to 36 MPa√m over ~200 hours at ~1500 hours, and specimens were held at this higher *K* for a period of time that increased for each subsequent loading ramp. This higher *K* value was chosen to produce 0.5% plastic strain at the blunt notch tip as estimated by finite element modeling (FEM). After establishing that no DCPD-indicated crack growth was occurring at constant *K*, a loading ramp was reapplied by first quickly dropping load back to a *K* level of 27.5 MPa√m and then slowly increasing load to 36 MPa√m over ~200 hours. This sequence was repeated a few times for the specimens. After a final loading ramp at ~4000 hours, constant *K* conditions were again established and held for the remainder of the test. A small increase in load of 1 MPa√m was applied at ~8400 hours to 37 MPa√m. Detailed DCPD responses for the four specimens under constant *K* are shown in Figures 23-26. In the two 31%CF specimens, an obvious increase in DCPD-based CGR response at ~10400 hours indicating crack initiation and growth at constant *K*. Meanwhile, the DCPD response for the two 21%CF specimens remained low and invariant through the entire constant *K* period until the conclusion of the test. The measured CGR of the BNCT specimens showing in the test plots is an indicator of the rate of nucleation and growth of multiple small cracks.

The tests were stopped at ~5400 hours and ~10000 hours, then ended at ~11700 h as documented in Figures 21 and 22. At each test interruption and at the conclusion of the test, detailed characterizations were performed on the notch surface, and a ~1/4 section of the CT specimens was removed from one side for detailed cross-section characterizations. The applied load was adjusted each time based on the new specimen dimensions to reapply and maintain the same applied *K* after interruptions.

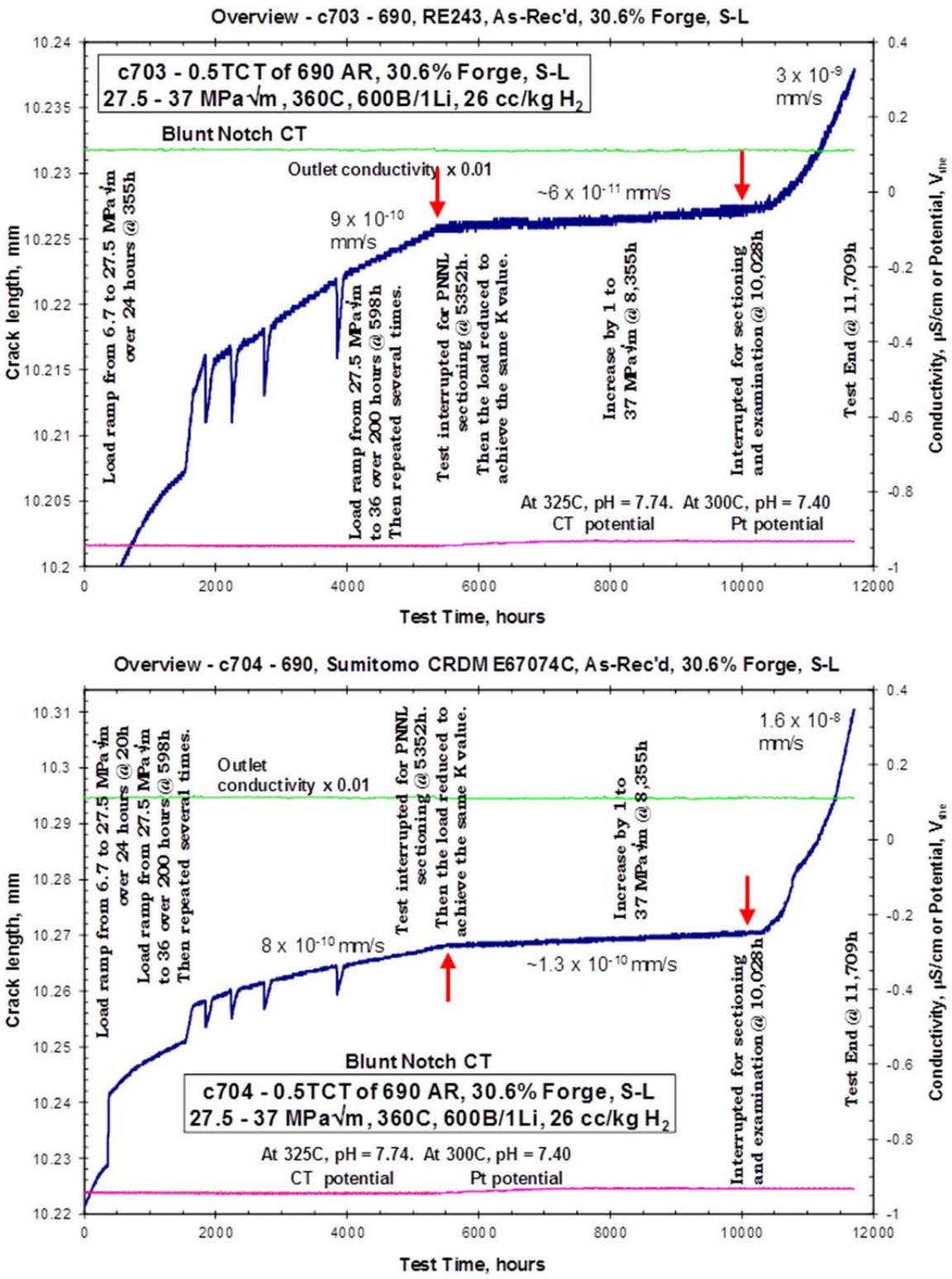

Figure 21. Overall crack length versus time response for the 31%CF Valinox CRDM (c703) and 31%CF Sumitomo CRDM (c704) BNCT specimens. The red arrows indicate the test interruptions at ~5352 h and 10028 h.

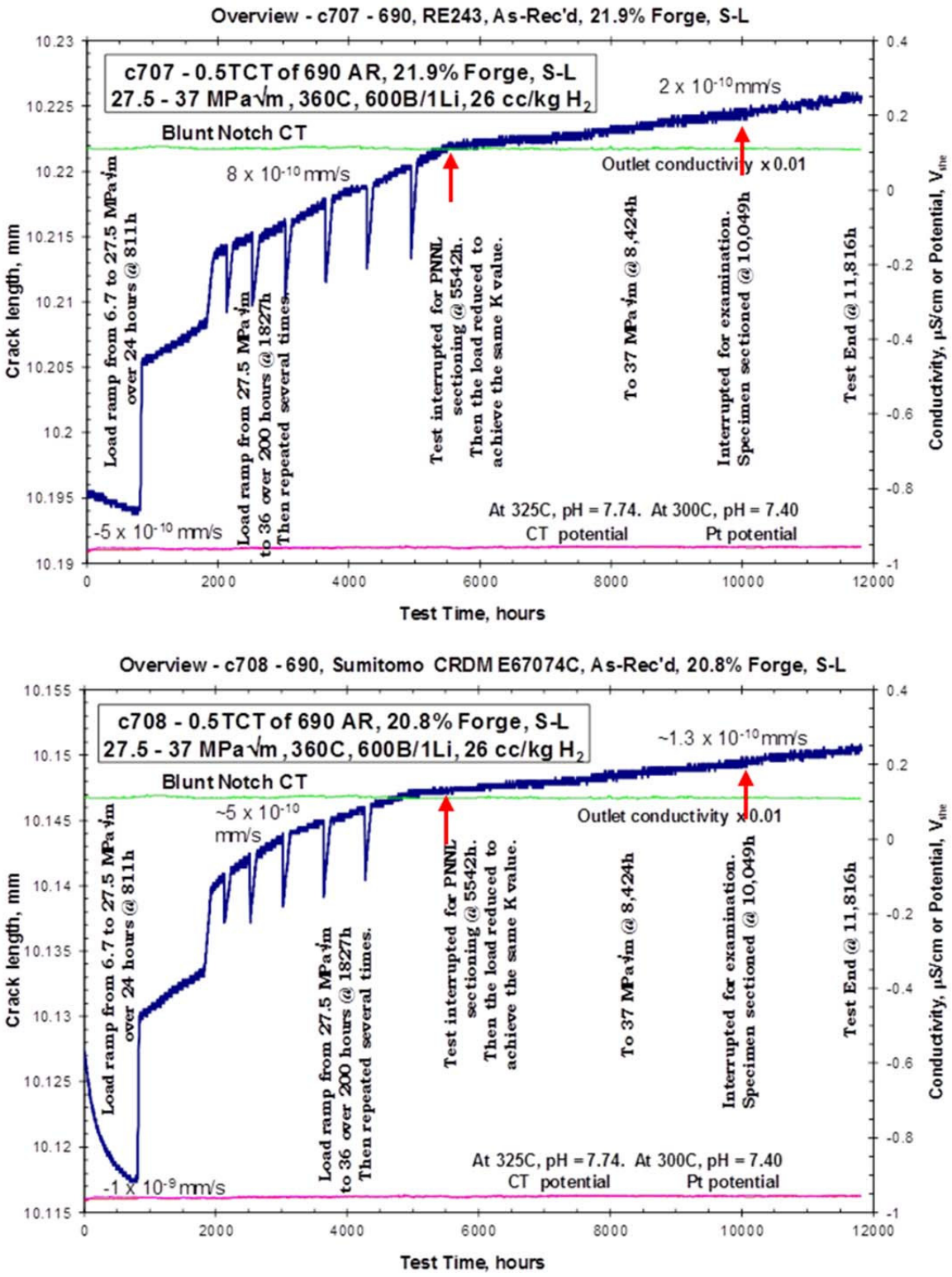

Figure 22. Overall crack length versus time response for the 21%CF Valinox CRDM (c707) and 21%CF Sumitomo CRDM (c708) BNCT specimens. The red arrows indicate the test interruptions at ~5542 h and 10049 h.

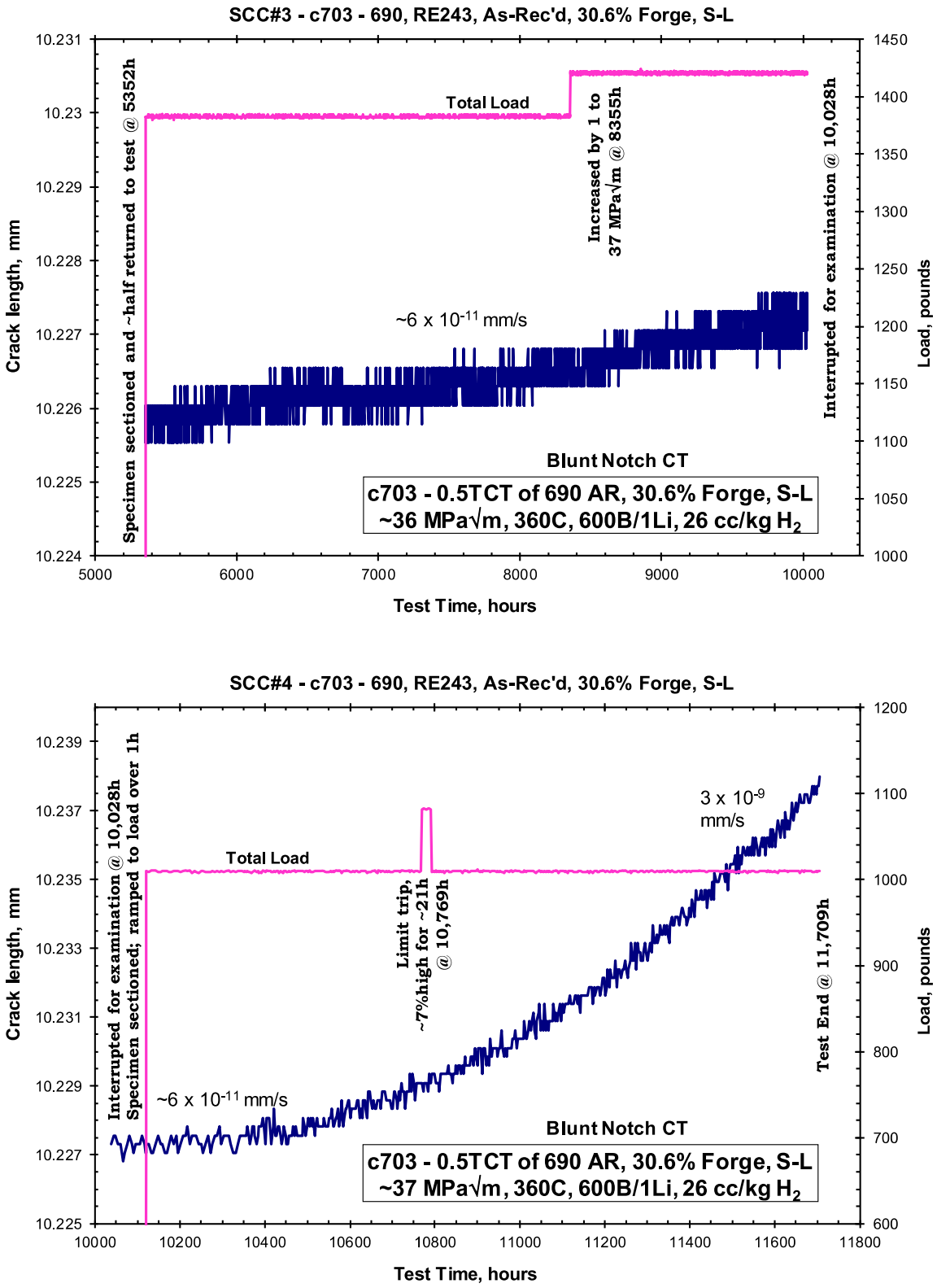

Figure 23. Constant *K* crack length versus time response for 31%CF Valinox CRDM (c703) BNCT specimen during test resumed after interruptions.

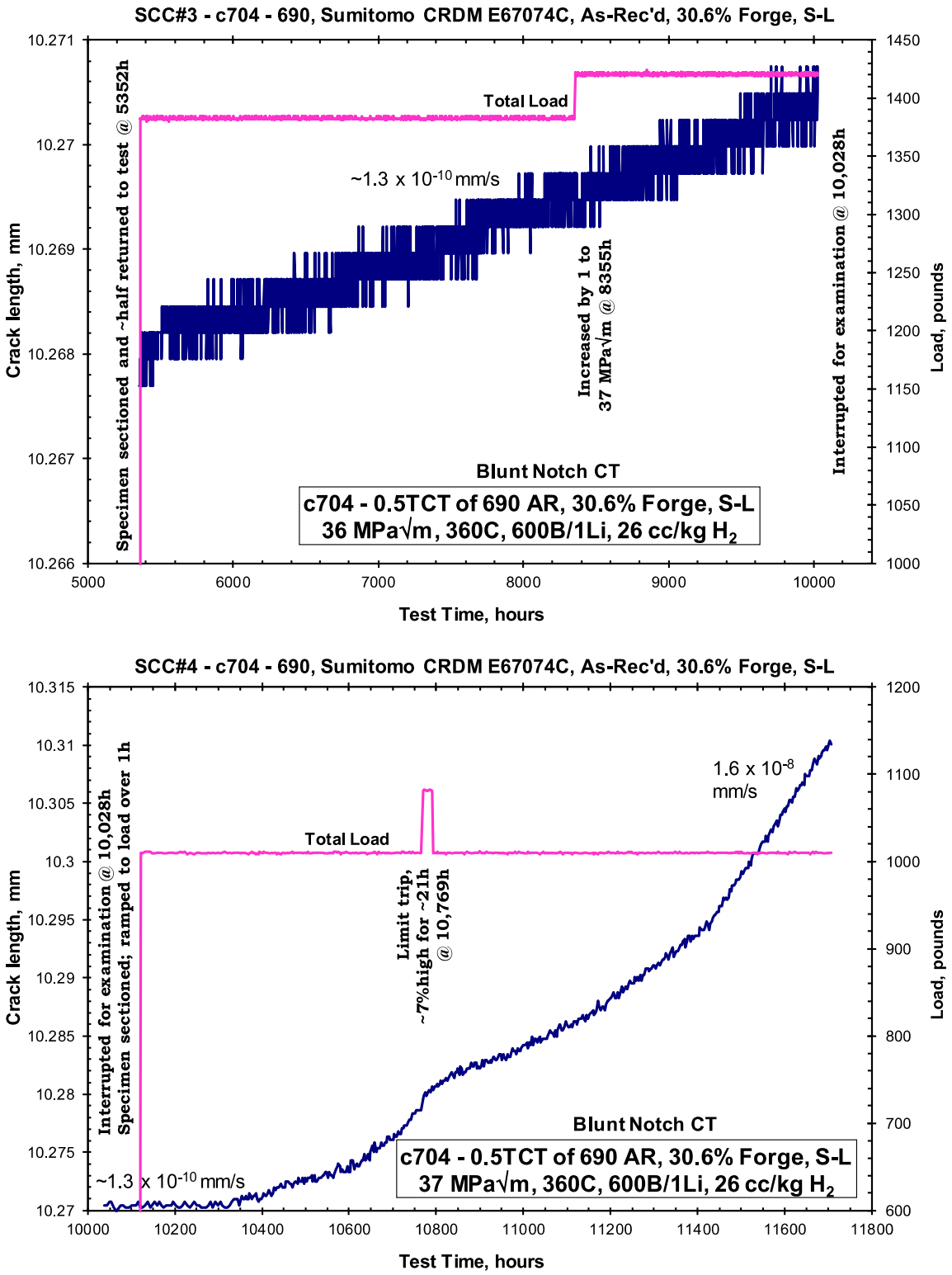

Figure 24. Constant *K* crack length versus time response for 31%CF Sumitomo CRDM (c704) BNCT specimen during test resumed after interruptions.

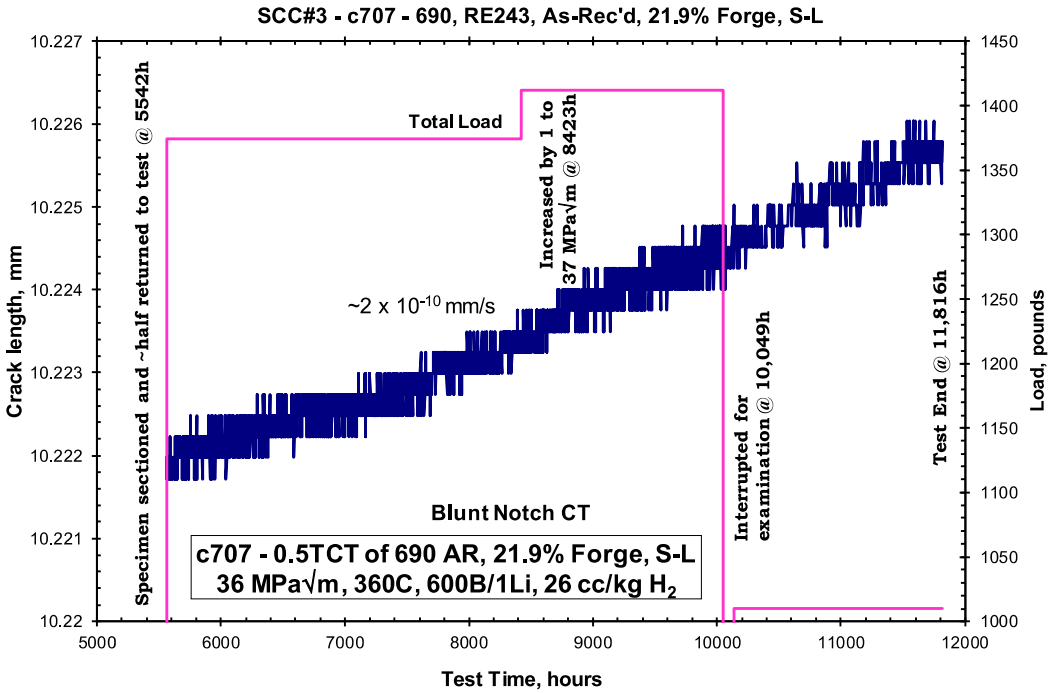

Figure 25. Constant *K* crack length versus time response for 21%CF Valinox CRDM (c707) BNCT specimen. The lower load after test interruption at 10049 h was calculated to maintain the same constant *K* on the specimen of which a section had been removed for SEM examinations.

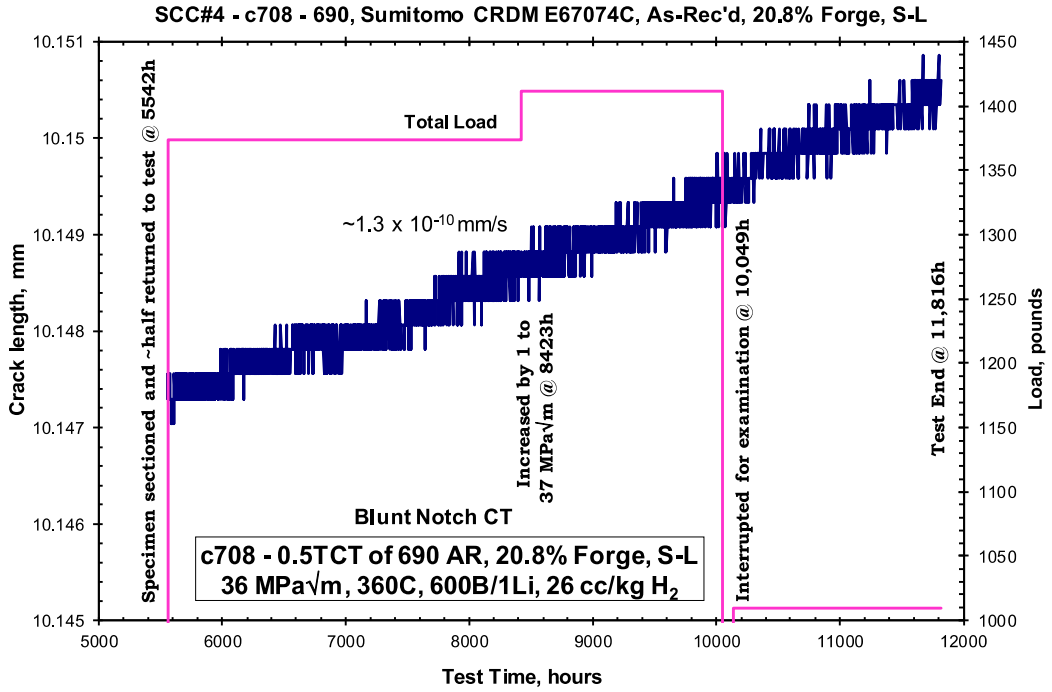

Figure 26. Constant *K* crack length versus time response for 21%CF Sumitomo CRDM (c708) BNCT specimen. The lower load after test interruption at 10049 h was calculated to maintain the same constant *K* on the specimen of which a section had been removed for SEM examinations.

Microstructural Characterizations

Microstructural examinations were conducted using a JEOL 7600 SEM and an FEI Quanta™ 3-dimension (3D) field emission gun FIB/SEM dual beam facility. The routine approach is to use Oxford Aztec software installed in the SEM to acquire montages of the entire surface at 200X magnification and areas of interest in cross-sections at 500X magnification of all the specimens with automated stage movement. In this way, morphology and location of SCC precursors and cracks can be quickly documented, enabling evolution of these features to be tracked over time. Examinations at higher resolution were also performed on selected damage structures. This involved high-kV (20–30keV) BSE imaging on the surface of specimens so that features covered by surface oxides can be revealed, as well as low-kV (5keV) imaging on highly polished cross-sections in order to capture damage characteristics at higher resolution. In addition, comparisons were routinely made in the SEM between BSE and SE imaging to better define local features.

Damage Characterizations

Evolution of Precursor Damage and Cracks on the Surface

Figures 27-28 provide an overview of the test and the SEM examination sequence on the two 31%CF specimens c703 and c704. As illustrated in the Figures 29-30, the entire notch surface of these two specimens was examined at 5352, 10028 and 11709 hours. In 30keV BSE mode, grain structures are revealed in SEM facilitating identification of IG damage and cracks. In order to better visualize the evolution of IG damage and cracks over time, obvious open IG cracks are highlighted in red and possible cracks with a darker contrast to normal GBs are highlighted in green. Higher magnification images were also taken at selected sites across the notch surface at each test interruption and at the conclusion of the test with examples shown in Figures 29 and 30 for c703 and c704, respectively.

In the 31%CF Valinox specimen c703, a number of isolated IG cracks were readily identified at GBs on the notch surface after the first test interruption at 5352 h (Figure 27). These cracks were probably nucleated during initial cyclic loading ramps. A gradual increase in the density of obvious cracks was observed in subsequent exposure that were all at constant load, suggesting nucleation of new cracks and growth of existing cracks had taken place under constant *K* condition. This is confirmed by higher magnification images in Figure 29 where obvious cracks were evidenced to form at IG damage precursors/possible cracks (sites A, B and C) as well as to grow larger from existing open IG cracks (site B). The 31%CF Sumitomo specimen c704 exhibited some isolated obvious IG cracks, and a high density of possible cracks after the test was interrupted at 5352 and 10028 h (Figure 28). In general at the first two test interruptions, the IG cracks in this specimen are more difficult to identify than those in the 31%CF Valinox specimen c703 because of their shorter surface length. This may have resulted due to the ~3X smaller grain size of the Sumitomo CRDM heat in comparison to the Valinox CRDM heat. However, the 31%CF Sumitomo specimen c704 exhibited much more extensive formation of large cracks at the conclusion of the test than the 31%CF Valinox specimen c703. As illustrated in Figure 30, many IG cracks have linked up across multiple grains in c704 while most IG cracks in c703 still confined in a single grain. This is also consistent with the DCPD response showing higher CGR in c704 as compared to c703 after initiation detection at ~10400 h.

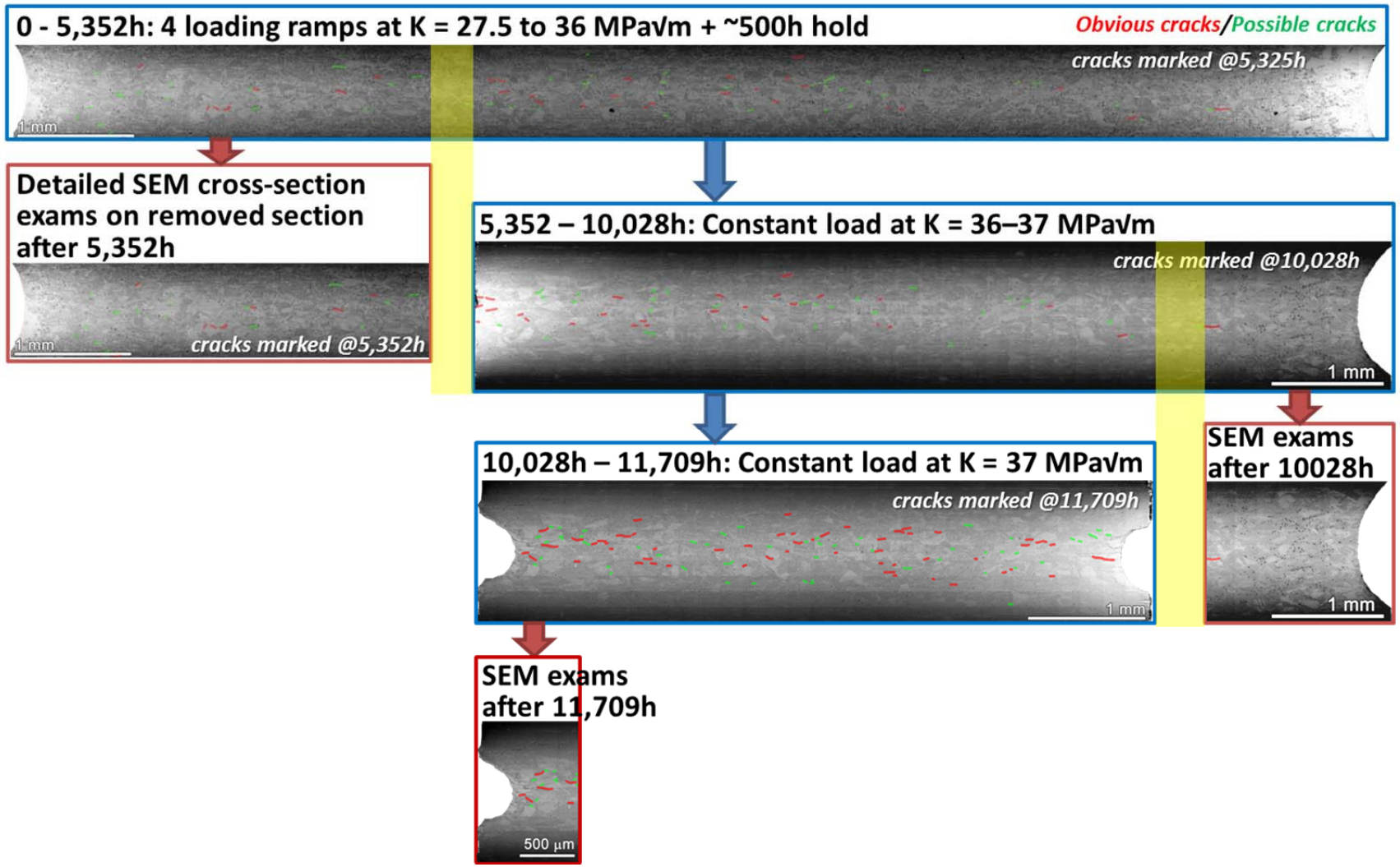

Figure 27. Test and SEM sequence for the 31%CF Valinox CRDM (c703) BNCT specimen viewed on notch surface, with obvious cracks marked in red and possible cracks marked in green. The sections outlined in blue are the parts tested during each test interval. The sections outlined in red are the parts removed for SEM examinations after test interruptions or at the conclusion of the test. The yellow bands indicate the material that was removed during sectioning.

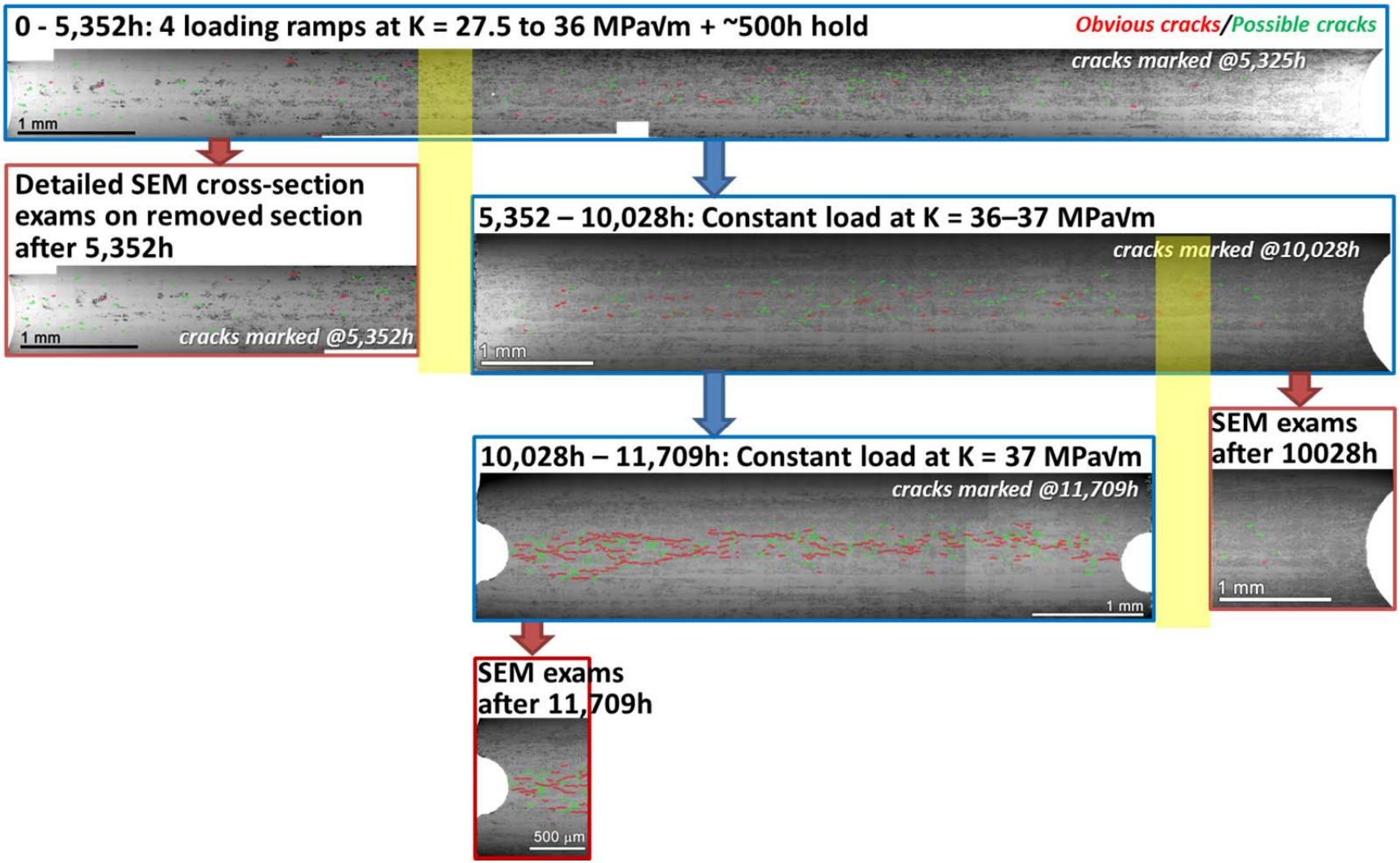

Figure 28. Test and SEM sequence for the 31%CF Sumitomo CRDM (c704) BNCT specimen viewed on notch surface, with obvious cracks marked in red and possible cracks marked in green. The sections outlined in blue are the parts tested during each test interval. The sections outlined in red are the parts removed for SEM examinations after test interruptions or at the conclusion of the test. The yellow bands indicate the material that was removed during sectioning.

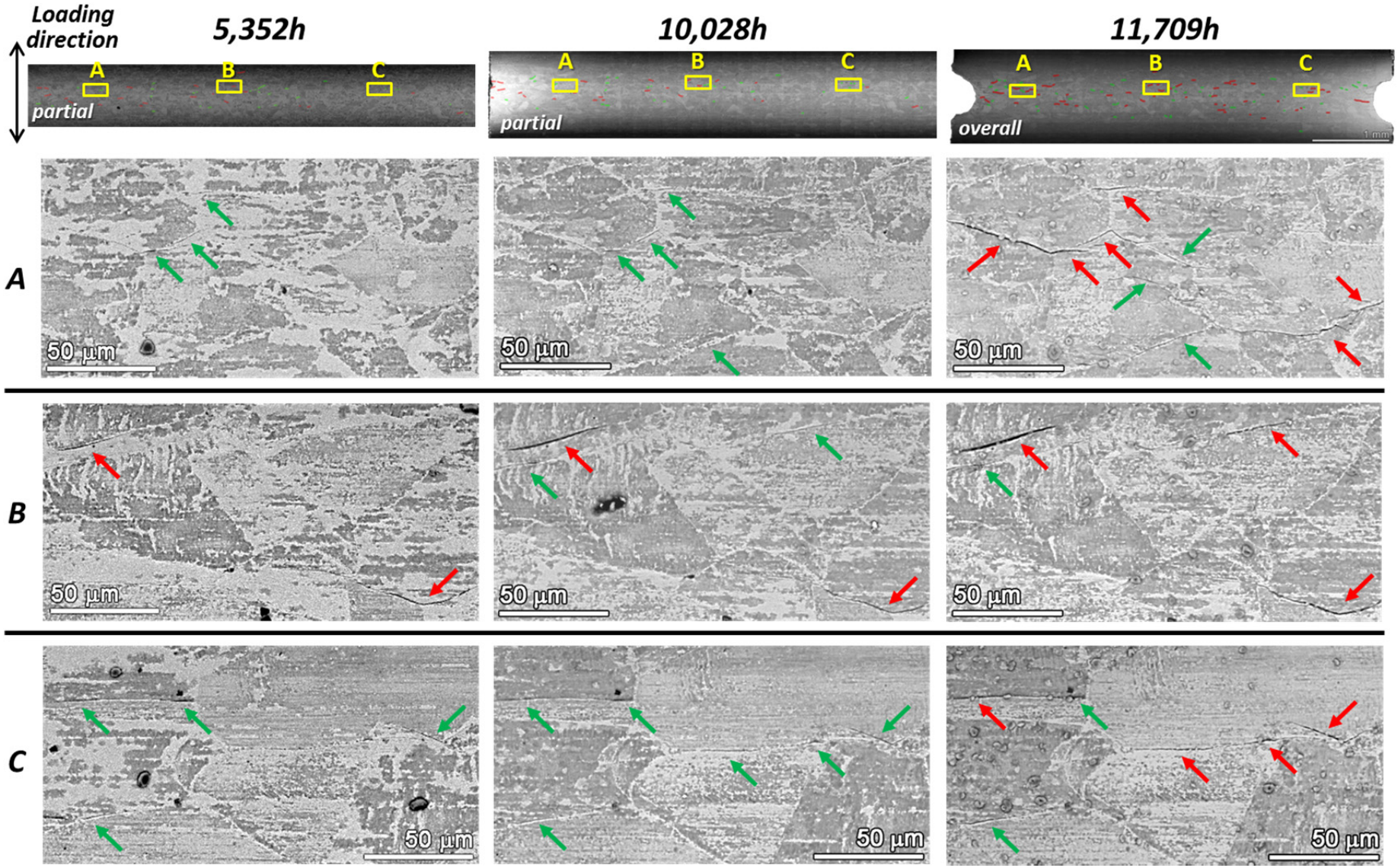

Figure 29. SEM-BSE images showing crack evolution at selected areas (marked in yellow boxes) on the notch surface of the 31%CF Valinox CRDM (c703) specimen. Obvious cracks are highlighted in red and possible cracks are highlighted in green.

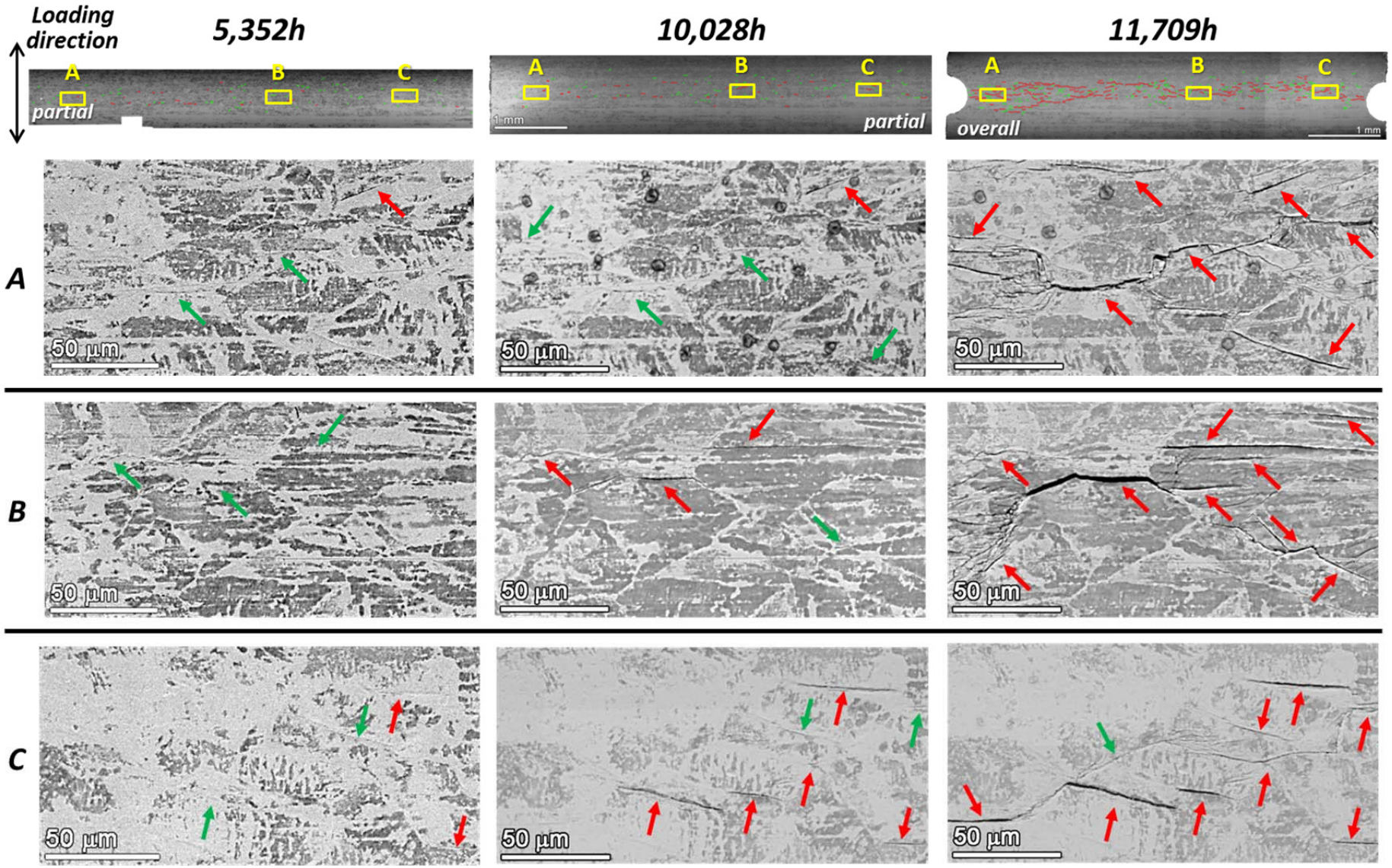

Figure 30. SEM-BSE images showing crack evolution at selected area (highlighted in yellow) on the notch surface of the 31%CF Sumitomo CRDM (c704) specimen. Obvious cracks are highlighted in red and possible cracks are highlighted in green.

The notch surface of the two 21%CF specimens c707 and c708 were also examined at each test interruption and at the conclusion of the test as illustrated in Figures 31-32. Damage evolution was examined in detail at selected sites with higher magnifications as shown in Figure 33 for c707 and Figure 34 for c708. In both specimens, the IG crack density is much lower than in the corresponding 31%CF specimen after the same exposure time. In particular, most of the obvious, open IG cracks in these two specimens were found at 5542 h after the initial cyclic loading ramps with little growth shown during subsequent constant *K* exposure. This can be clearly seen in Figure 33 where the large crack at site B remained invariant in appearance over the entire constant *K* exposure. A few possible cracks exhibited some growth and could be marked as obvious cracks at the conclusion of the test mainly because of a darker contrast shown (sites A and C). However, they still appear much shorter and narrower in comparison to those relatively large obvious cracks that were created during cyclic loading. Similar observations were discovered on the 21%CF Sumitomo specimen c708. The overview of IG damage evolution shown in Figure 32 suggested the density of possible cracks gradually increased over the constant *K* exposure. Nevertheless, a closer look on crack morphology at selected sites revealed that the change in the size and shape of obvious cracks formed during the initial cyclic loading was negligible as illustrated for sites B and C in Figure 34.

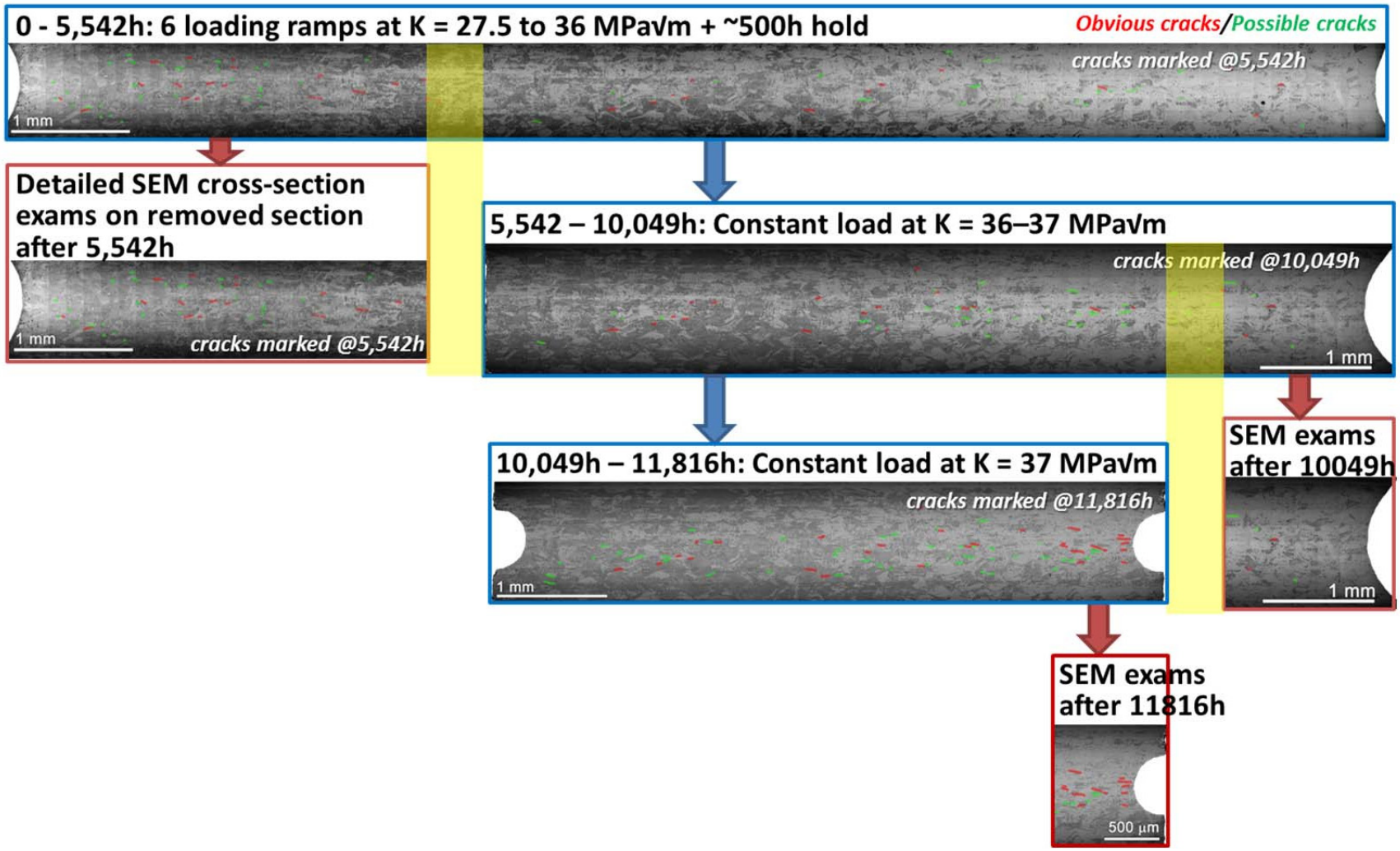

Figure 31. Test and SEM sequence for the 21%CF Valinox CRDM (c707) BNCT specimen viewed on notch surface, with obvious cracks marked in red and possible cracks marked in green. The sections outlined in blue are the parts tested during each test interval. The sections outlined in red are the parts removed for SEM examinations after test interruptions or at the conclusion of the test. The yellow bands indicate the material that was removed during sectioning.

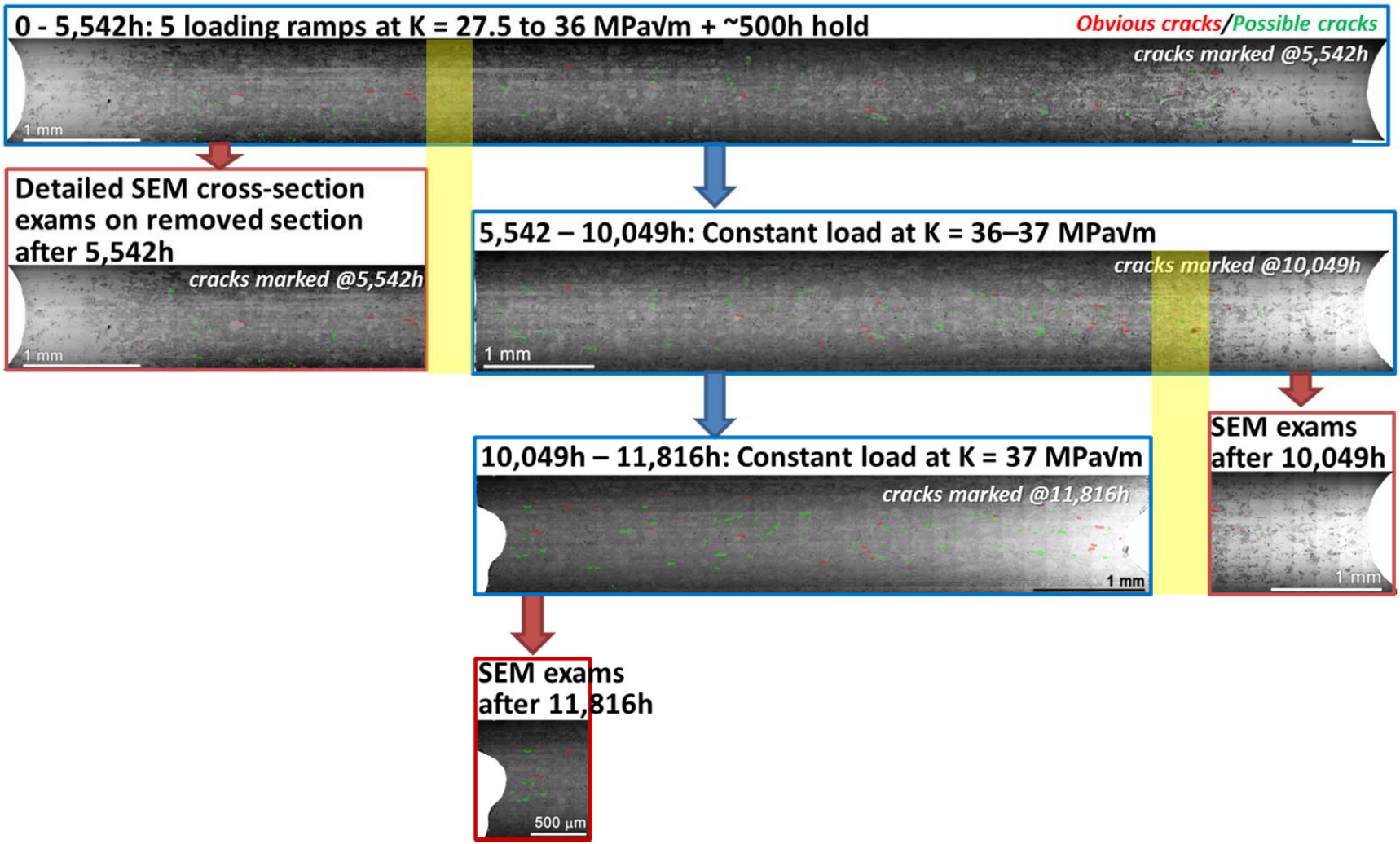

Figure 32. Test and SEM sequence for the 21%CF Sumitomo CRDM (c708) BNCT specimen viewed on notch surface, with obvious cracks marked in red and possible cracks marked in green. The sections outlined in blue are the parts tested during each test interval. The sections outlined in red are the parts removed for SEM examinations after test interruptions or at the conclusion of the test. The yellow bands indicate the material that was removed during sectioning.

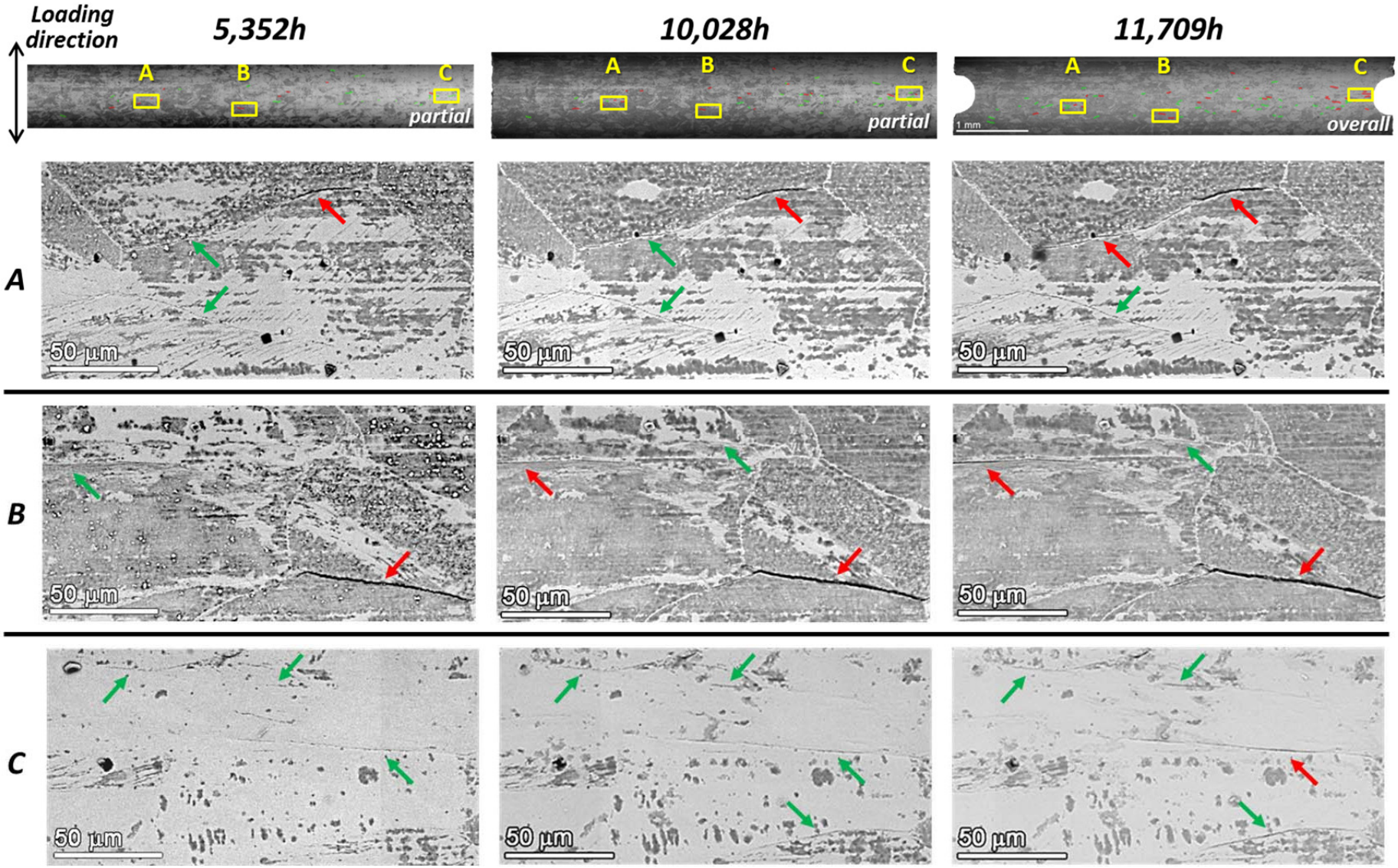

Figure 33. SEM-BSE images showing crack evolution at selected area (highlighted in yellow) on the notch surface of the 21%CF Valinox CRDM (c707) specimen. Obvious cracks are highlighted in red and possible cracks are highlighted in green.

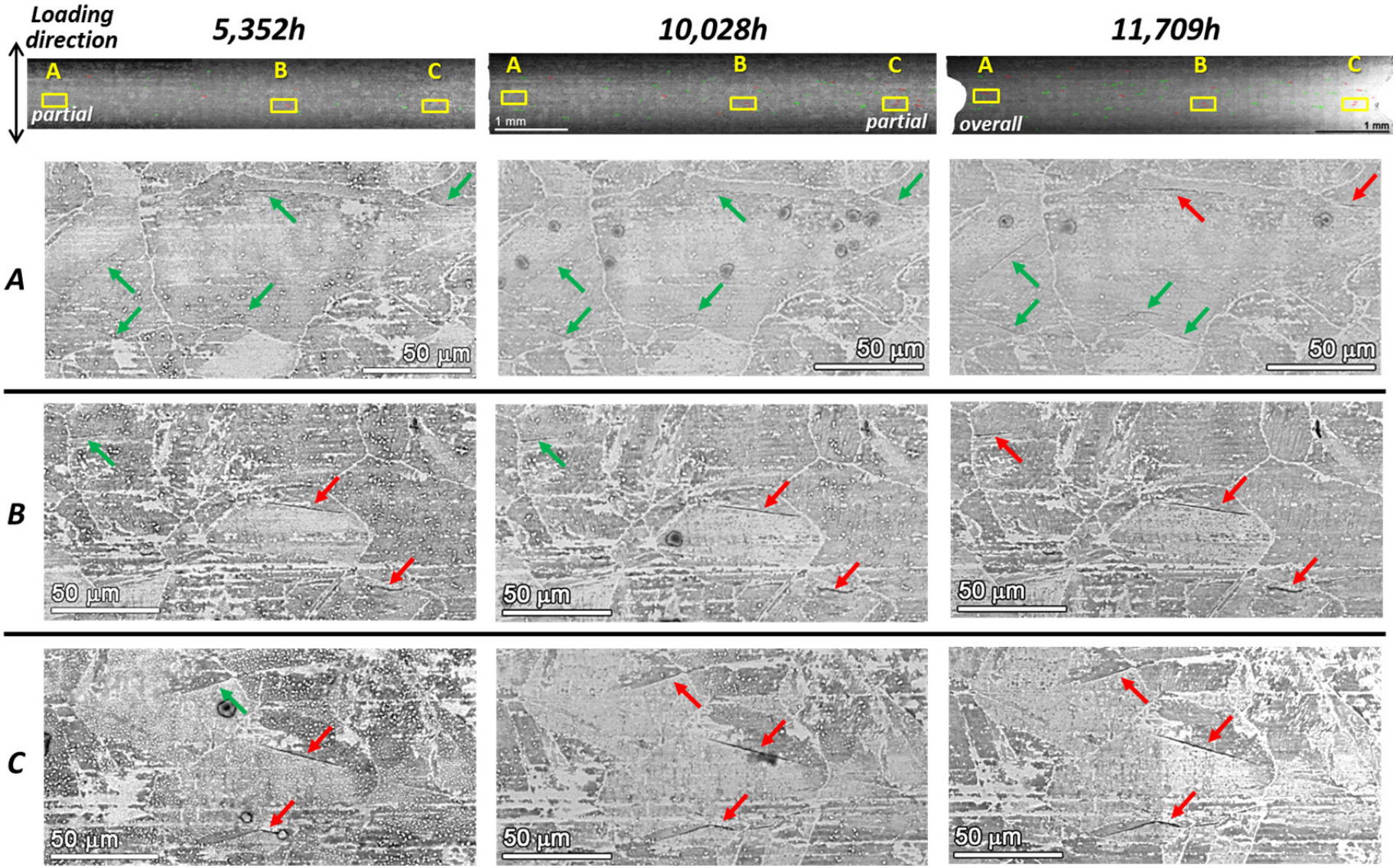

Figure 34. SEM-BSE images showing crack evolution at selected area (highlighted in yellow) on the notch surface of the 21%CF Sumitomo CRDM (c708) specimen. Obvious cracks are highlighted in red and possible cracks are highlighted in green.

Evolution of Precursor Damage and Cracks in Specimen Cross-Sections

GB cavities were observed in the region below the blunt notch surface on the cross-section slices removed after every test interruption for all test specimens. Although small discrete cavities can be difficult to differentiate from GB carbides in the low-magnification BSE montage images, aggregations of GB cavities are readily visible with a significantly darker contrast as highlighted in Figure 35. Higher magnification images presented later in Figures 36-39 show that a series of cavities with size >100 nm and spacing < 1 μm is required to become differentiable from the rest of the GB in the montage images. The overall evolution of GB cavities and development of IG cracks for the four BNCT specimens is summarized in Figures 36-39 with aggregations of GB cavities marked in yellow, SCC cracks marked in red and creep cracks marked in orange. The SCC cracks and creep cracks can be identified by observing crack walls at high resolutions where SCC cracks always exhibit penetrative oxidation while creep cracks exhibit none. In addition, examples at higher magnifications are also provided to show the morphology of typical aggregated GB cavities at the specific exposure time.

As shown in the montage images in Figures 36 and 37, a moderate density of GB cavities (probably produced during the initial cyclic loading ramps) is present beneath the notch in the two 31%CF BNCT specimens (c703 and c704) at 5352 h. With additional exposure time, a denser and broader distribution of GB cavities beneath the notch is clearly revealed indicative of continued cavity formation and growth under constant *K* condition. Consistent with the depth where the highest stress occurs based on FEM predictions, the cavity densities always tend to peak at ~200–300 μm below the notch tip. In addition, most of the cavities form at high-energy GBs that have a normal vector within 45^{o} of the loading direction suggesting an important role of applied stress on cavity nucleation and growth. Generally, shorter distributions of closely spaced cavities and more creep cracks were observed in the 31%CF Sumitomo specimen c704 whereas the 31%CF Valinox specimen c703 exhibited longer cavity distributions with fewer cracks. This corresponds well to the higher CGR indicated by DCPD in c704 than in c703. To the right of the montage images, typical cavity morphologies are shown in higher resolutions revealing that cavities nucleate at the GB carbide interface. When viewed with the progress in exposure time, it appears that the cavities in both specimens can grow from these discrete nucleation sites on a single boundary to form a semi-continuous cavity distribution and finally link up into creep cracks.

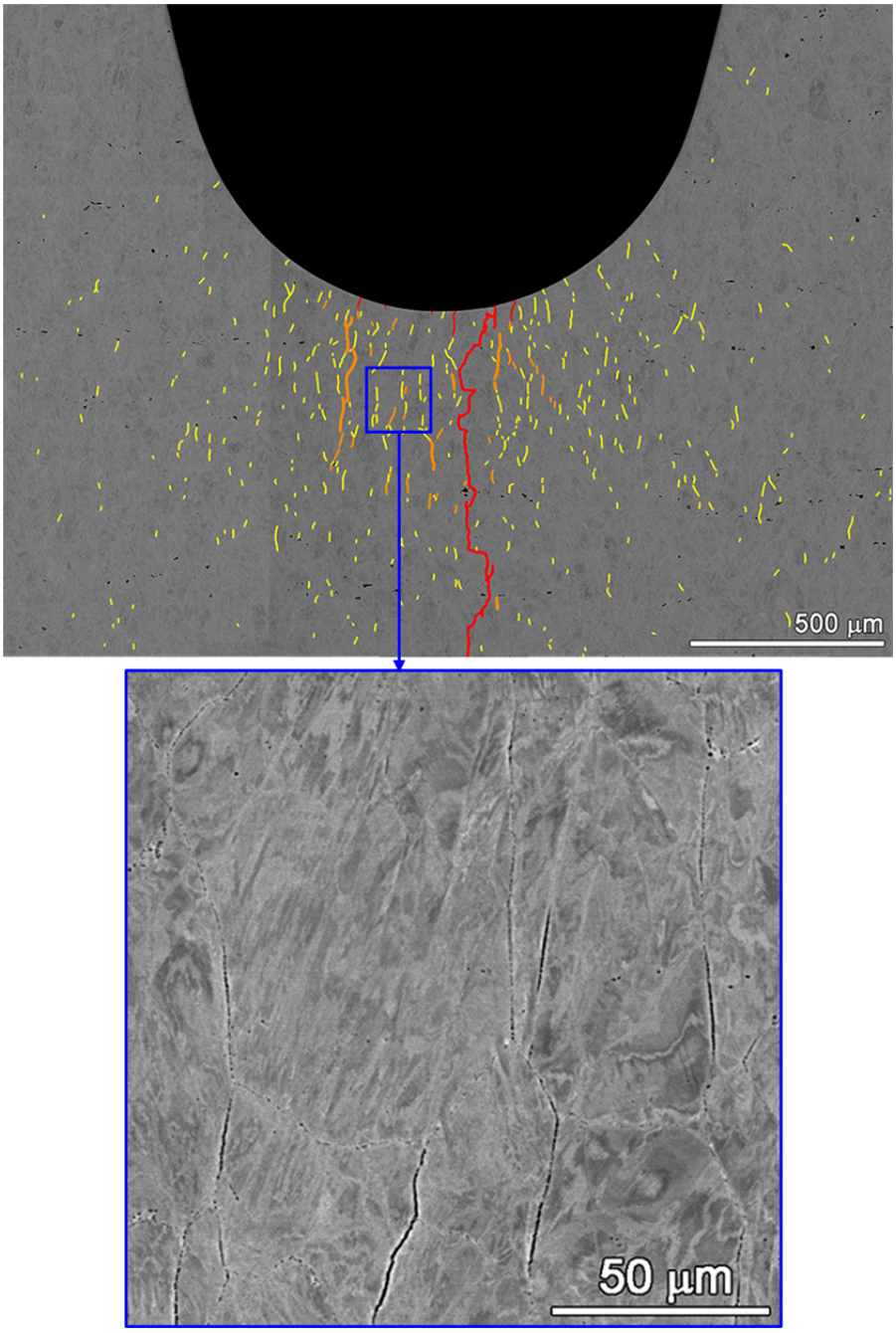

Figure 35. Upper image presents an overview of GB cavity aggregations (yellow highlight) and crack (red/orange highlight) distributions in a cross-section of the 31%CF Sumitomo CRDM BNCT specimen c704 at 11709 h. Lower image is from a selected area at higher magnification to illustrate the typical morphology of the cavity aggregations and cracks.

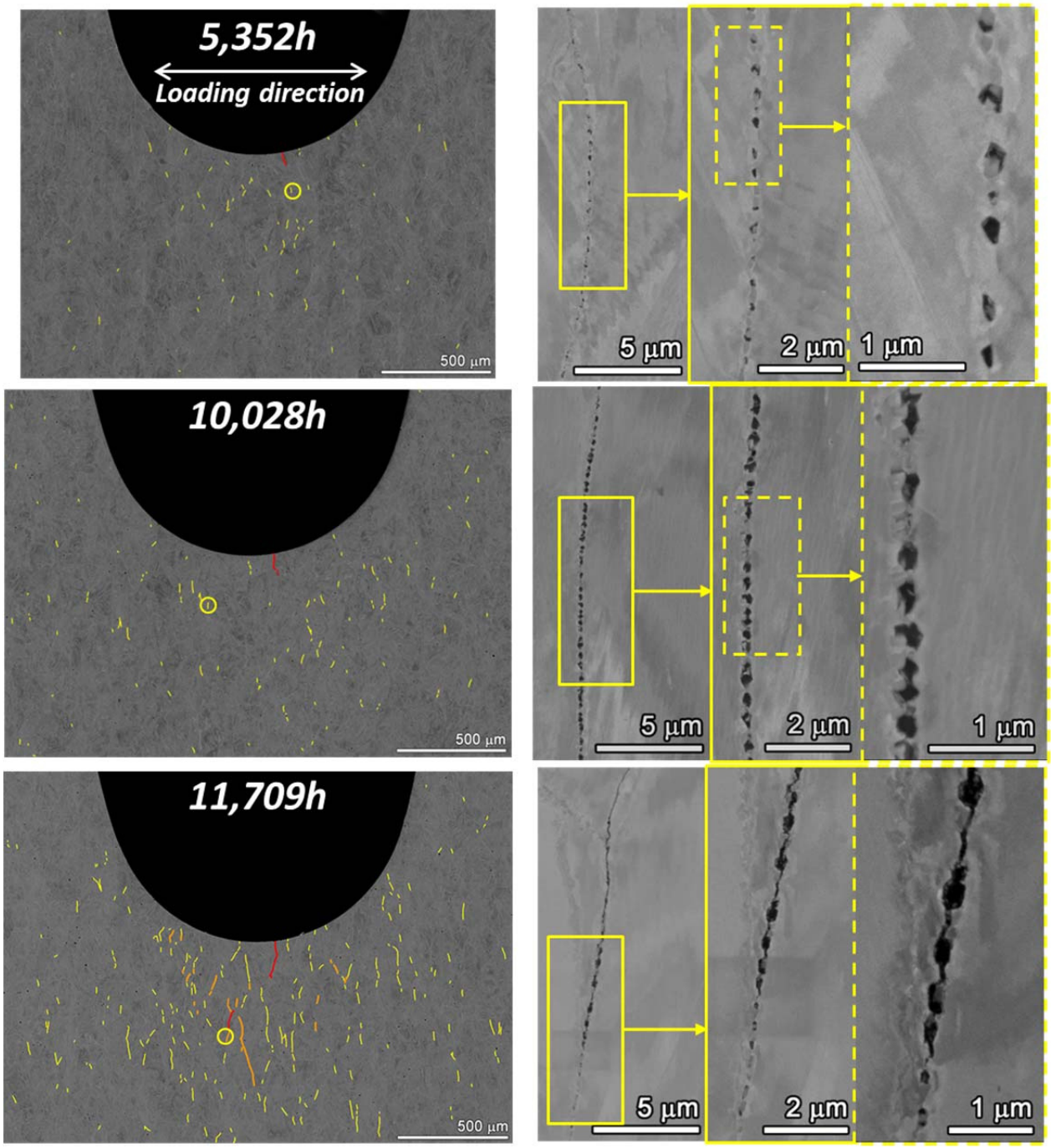

Figure 36. SEM-BSE montage images of the 31%CF Valinox specimen c703 cross-sections at 5352, 10028 and 11709 hours where obvious aggregations of GB cavities are highlighted in yellow, accompanied with higher-magnification BSE images at selected locations (marked in circle in the montage images) showing the morphology of GB cavities.

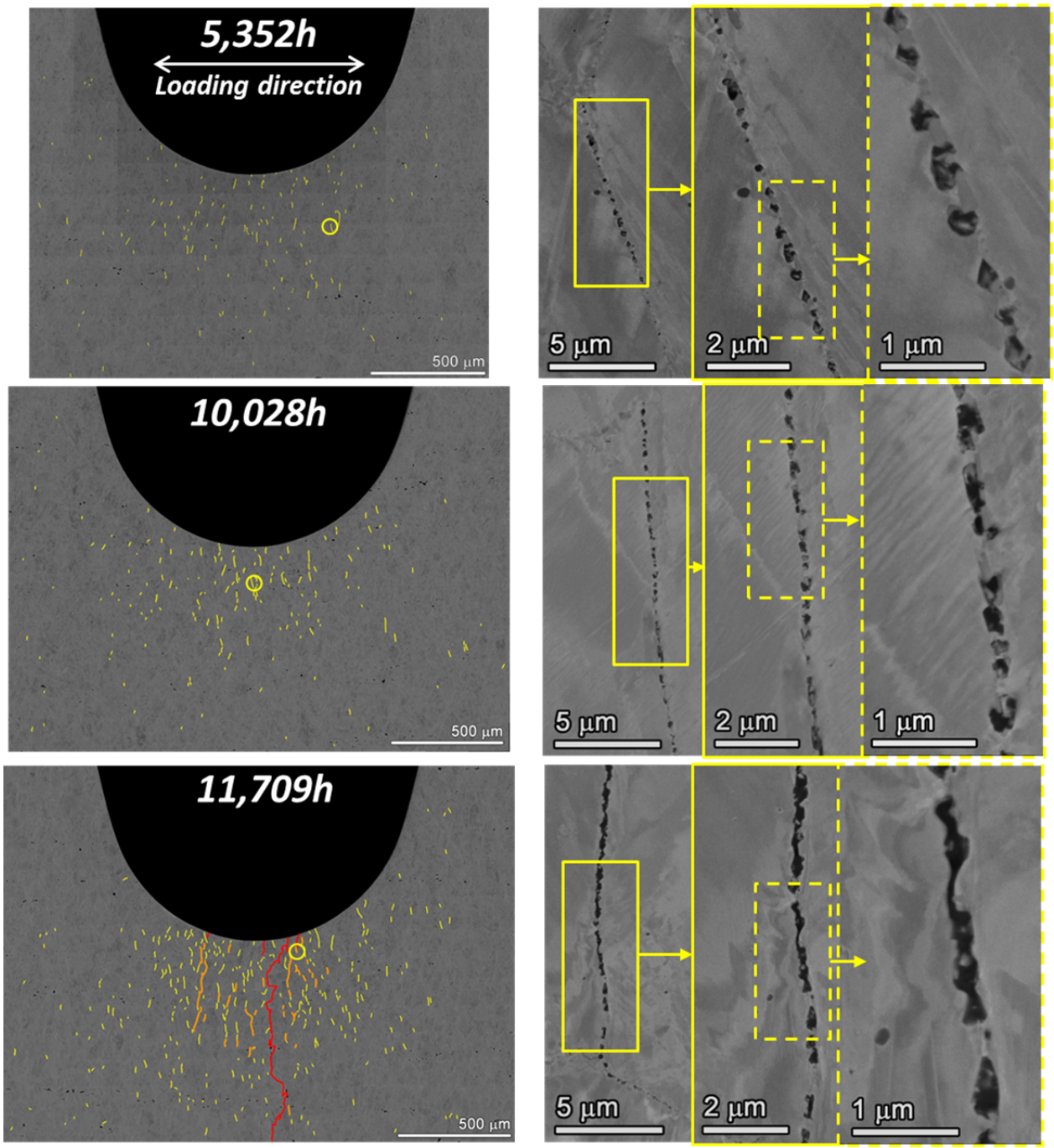

Figure 37. SEM-BSE montage images of the 31%CF Sumitomo specimen c704 cross-sections at 5352, 10028 and 11709 hours where obvious aggregations of GB cavities are highlighted in yellow. This is accompanied with higher-magnification BSE images at selected locations (marked in circle in the montage images) showing the morphology of GB cavities.

As shown in Figures 38 and 39, a few isolated GB cavity distributions were evidenced in the cross-sections for the two 21%CF BNCT specimens (c707 and c708) after 5542 h. Although the cavity density is much lower than for the 31%CF materials, it again suggests that some cavities were formed during the initial cyclic loading ramps. Interestingly, unlike the almost invariant appearance of the notch surface throughout the test shown in the previous section (Figures 31-34), a very gradual but steadily growing trend can be seen over time in the GB cavity distribution for these two 21%CF specimens. This can be clearly viewed from the high-resolution images in both specimens illustrating a continued increase in the number and size of GB cavities. Although no significant IG cracks were discovered after the full test time of 11816 h, it is suspected that GB cavities in these two moderately CW specimens would continue to develop and eventually lead to crack initiation as already observed in the two 31%CF specimens. However, more investigation is needed on the kinetics of cavity nucleation and growth in materials with lower levels of cold work. In the attempt to tackle this problem, quantitative analyses of cavity size and density evolution over time have been started on the four BNCT specimens and the results will be reported in the future.

In addition, a slightly higher density of cavities is observed in the 21%CF Sumitomo specimen c708 than in the 21%CF Valinox specimen c707. This is similar to the trend observed in the two 31%CF BNCT specimens. It is suspected that this difference in cavity distribution is associated with microstructures but further investigation is needed to elucidate the main influencing factors.

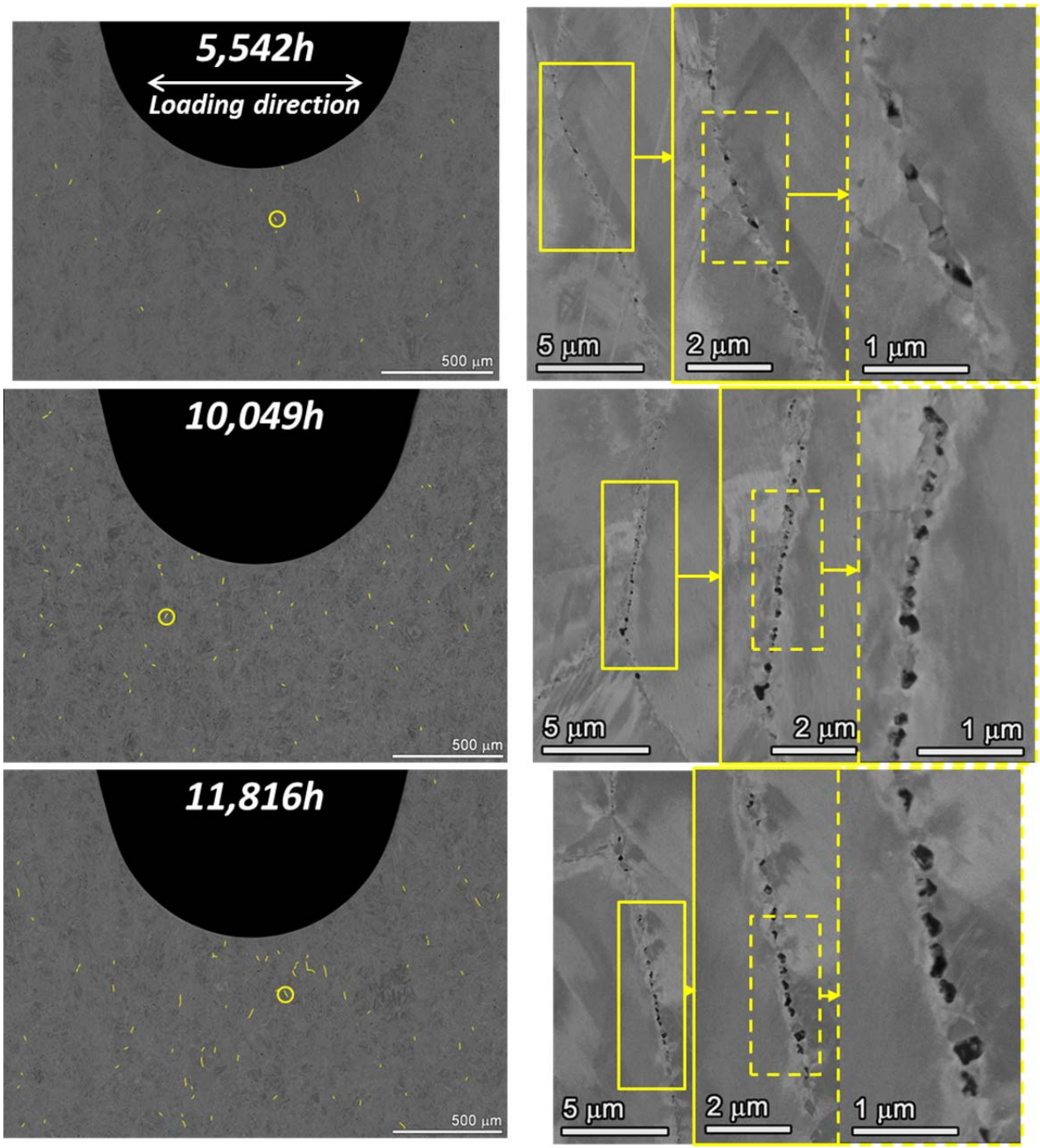

Figure 38. SEM-BSE montage images of the 21%CF Valinox specimen c707 cross-sections at 5352, 10028 and 11709 hours where obvious aggregations of GB cavities are highlighted in yellow. This is accompanied with higher-magnification BSE images at selected locations (marked in circle in the montage images) showing the morphology of GB cavities.

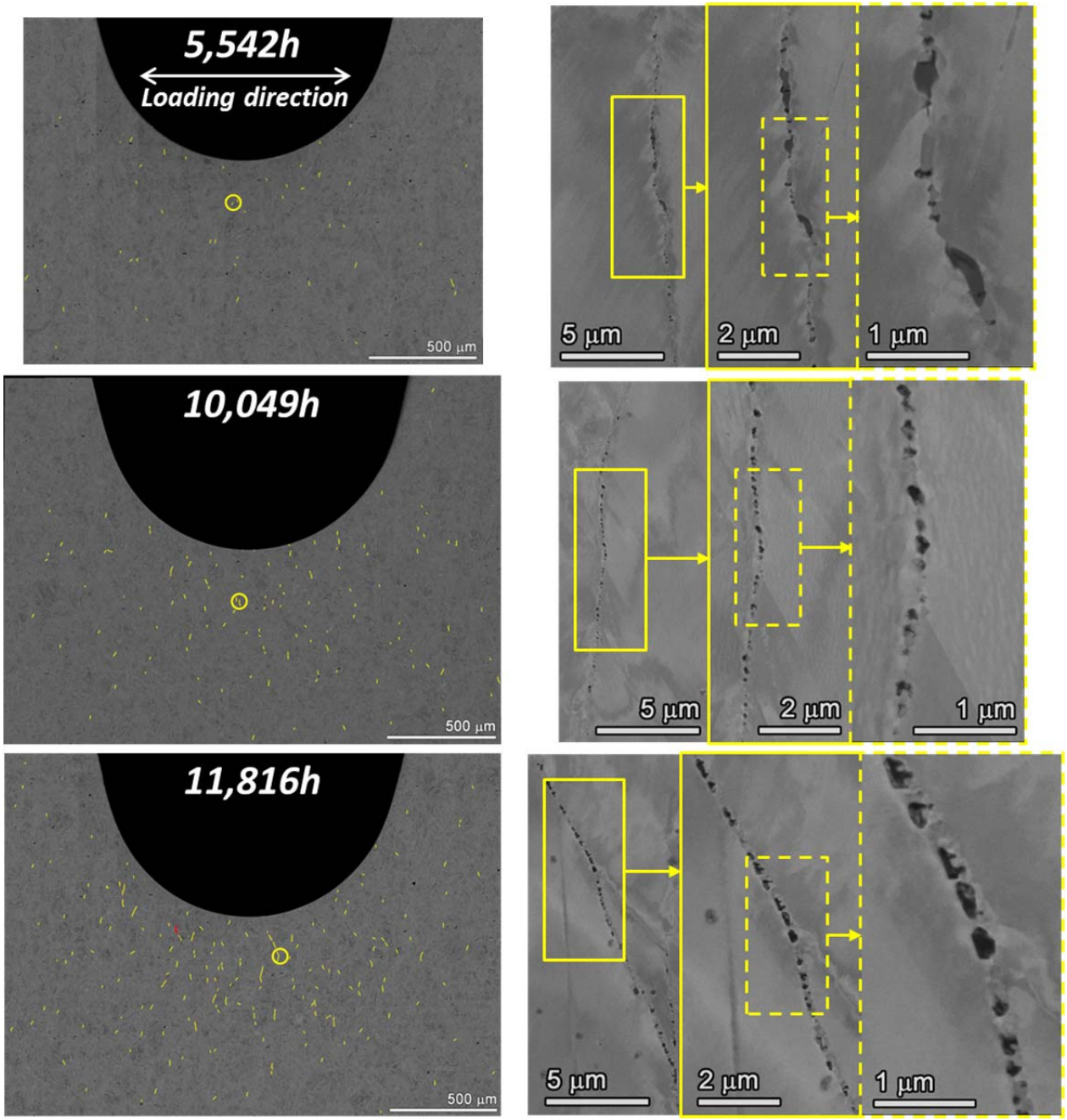

Figure 39. SEM-BSE montage images of the 21%CF Sumitomo specimen c708 cross-sections at 5352, 10028 and 11709 hours where obvious aggregations of GB cavities are highlighted in yellow. This is accompanied with higher-magnification BSE images at selected locations (marked in circle in the montage images) showing the morphology of GB cavities.

Detailed Examinations of Precursor Damage and Cracks

Characterization results in the prior sections have shown that GB cavity formation and growth had taken place in all BNCT specimens during testing. In order to better understand the role of cavity on IG crack nucleation and growth, detailed serial polishing steps were conducted on slices removed mid-test and at the conclusion of the tests. Observations are summarized below for each individual specimen.

31%CF Valinox CRDM BNCT Specimen c703

An example of the serial polishing and SEM examinations performed on c703 slices after 5352 h is provided in Figure 40. An area of the surface containing cracks along what appears to be incoherent twin boundaries is shown in Figure 40(a) together with cross-section locations examined after the 1^{st}-4^{th} polishing sequences. The subsurface features of crack B in the 1^{st}-2^{nd} polish locations are presented in Figure 40(c) showing limited IG penetration to less than 1 μm deep. Only a few isolated cavities were found ahead of the crack and their distribution appears to be too small to have any impact on the growth of the crack. The IG penetration disappeared at the 3^{rd} location, which corresponds to the end of crack B on the notch surface shown in Figure 40(a). In contrast, crack A that appears to be much shorter than crack B on the surface exhibited much greater depth in cross-sections. As shown in Figure 40(d), the crack starts at ~20 μm below the surface at the 1^{st} and the 4^{th} polish locations, but exhibits significant corrosion/oxidation along the crack walls and must be an SCC crack connected to the notch surface. At the 2^{nd} and the 3^{rd} polish locations, the SCC crack can be seen to extend to the surface confirming water ingress into the crack causing the observed crack wall corrosion structures and was linked to the 1^{st} and the 4^{th} locations. A schematic is therefore established showing the estimated depth profile of this crack with the greatest depth of ~80 μm observed near the 2^{nd} location (Figure 40b). Different from the semi-elliptical shape of the cracks found in alloy 600 constant load tensile specimens [4], the depth profile of cracks nucleated in the blunt notch specimen are irregular. This appears to be related to the development of GB cavity distributions below the blunt notch surface that are associated with the formation of SCC cracks (Figures 41 and 42). In addition, a series of cavities are present ahead of the corroded SCC crack tip of which the size and density tend to decrease with distance from the tip (Figure 40d). It is particularly interesting to note that this trend occurred at both ends of the SCC crack that is not directly linked to the notch surface in the 4^{th} polish location (Figure 42).

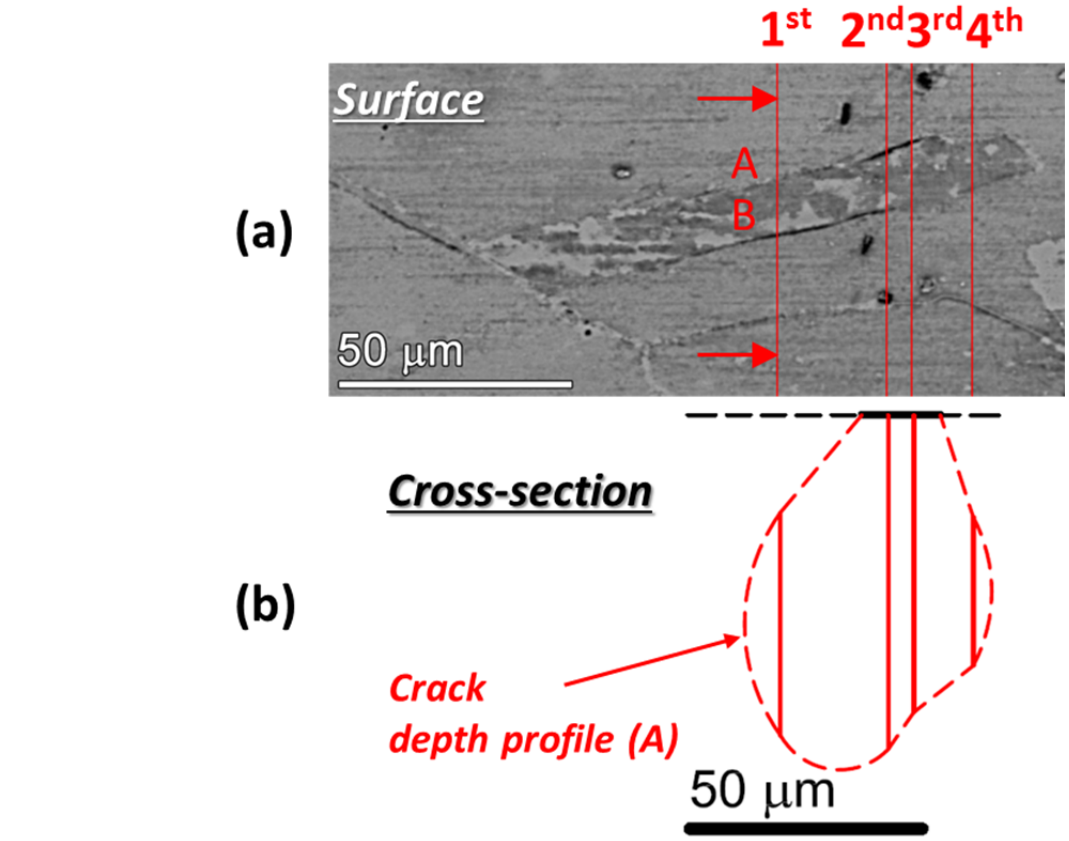
1st 2nd 3rd 4th
(a)
Surface
A
B
50 μm
Cross-section
(b)
Crack
depth profile (A)
50 μm

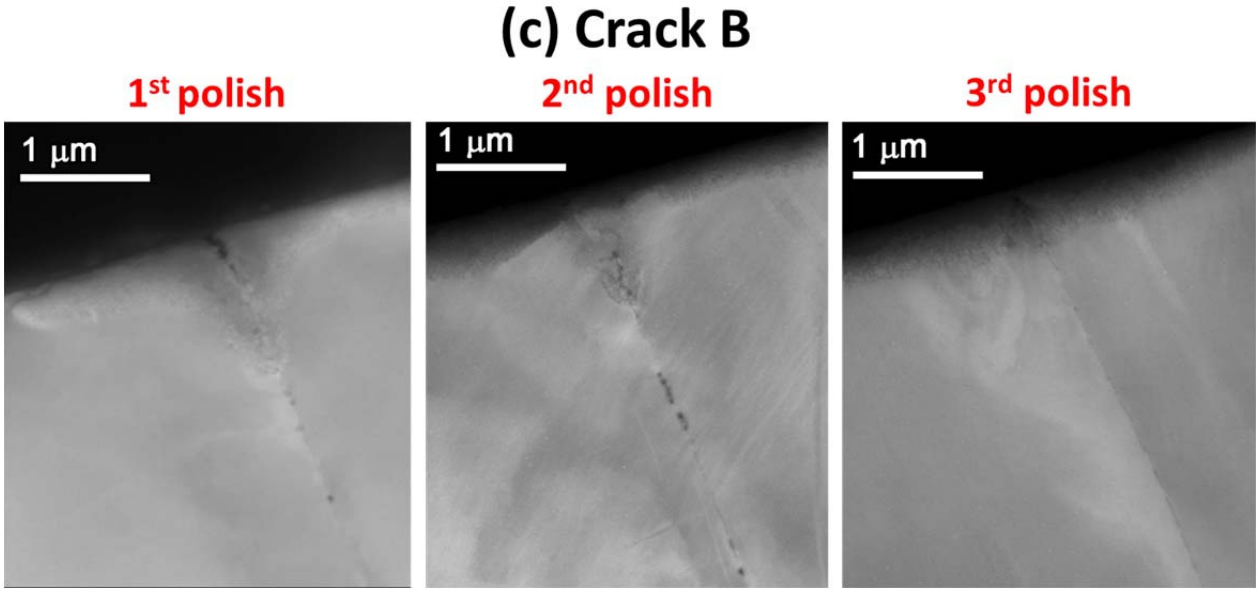
(c) Crack B
1st polish
2nd polish
3rd polish
1 μm
1 μm
1 μm

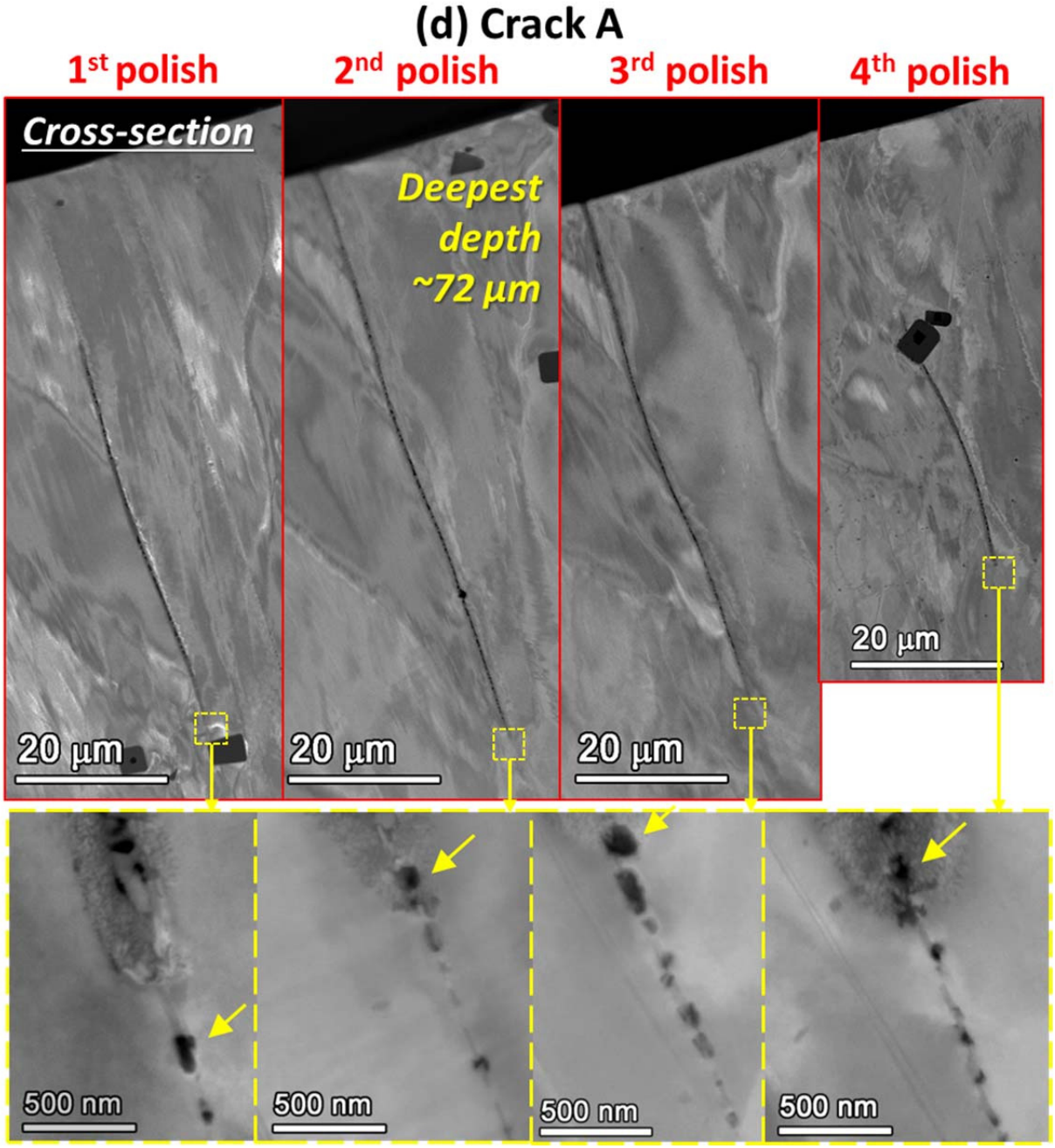

Figure 40. Serial polishing and SEM examinations on a slice removed from the 31%CF Valinox specimen c703 after 5352 h: (a) blunt notch surface region showing the position where cracks A and B were intersected by four serial polishing, (b) schematic of the depth profile of crack A based on cross-section observations, and high-resolution SEM-BSE images showing the morphology of (c) crack B and (d) crack A and cavities ahead of the crack tip in the cross-section after each polishing.

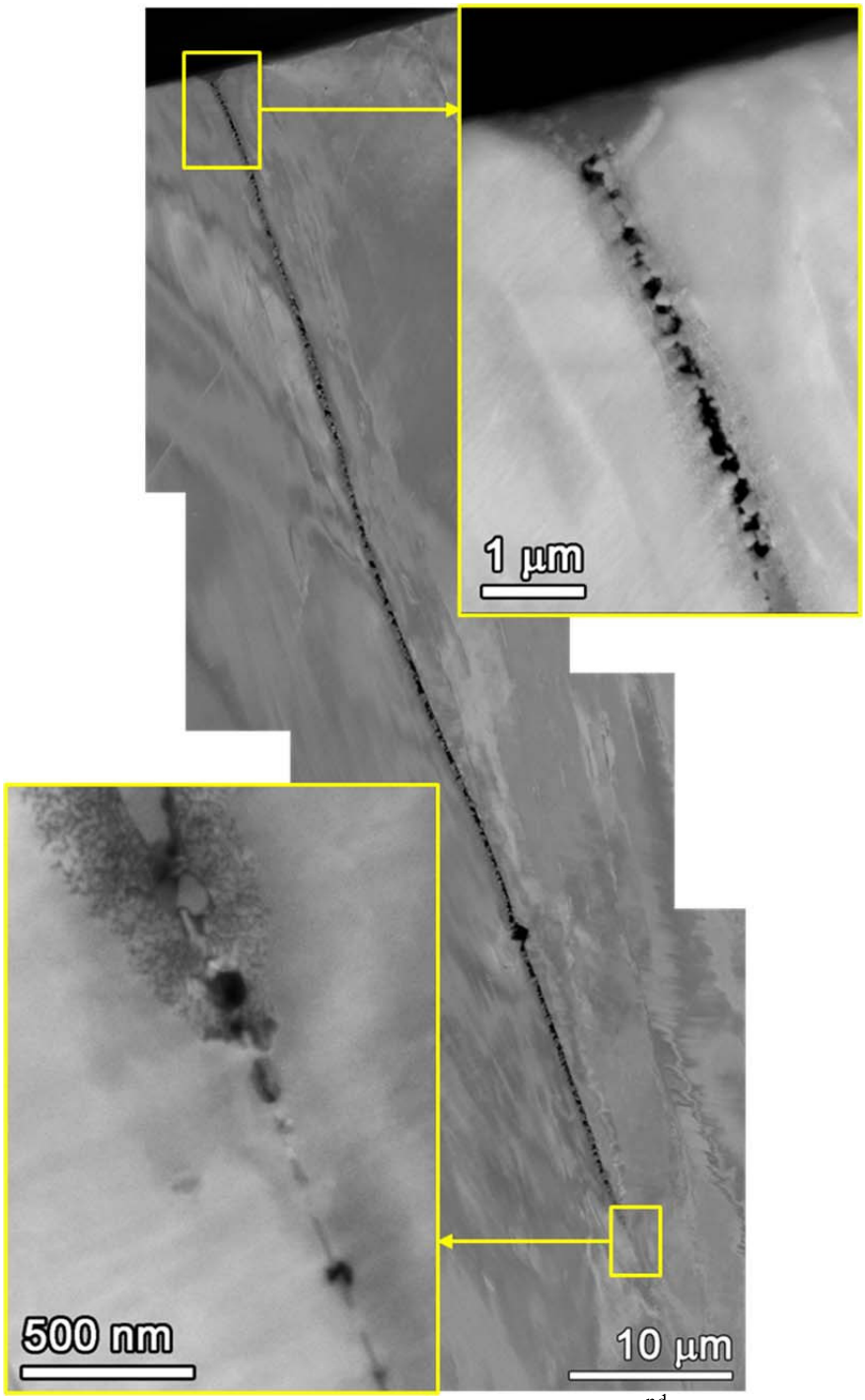

Figure 41. Detailed SEM examinations of the SCC crack in the 2nd polish cross-section from Figure 40 for the 31%CF Valinox specimen c703. Evidence of cavities is seen near the surface and immediately ahead of the SCC crack.

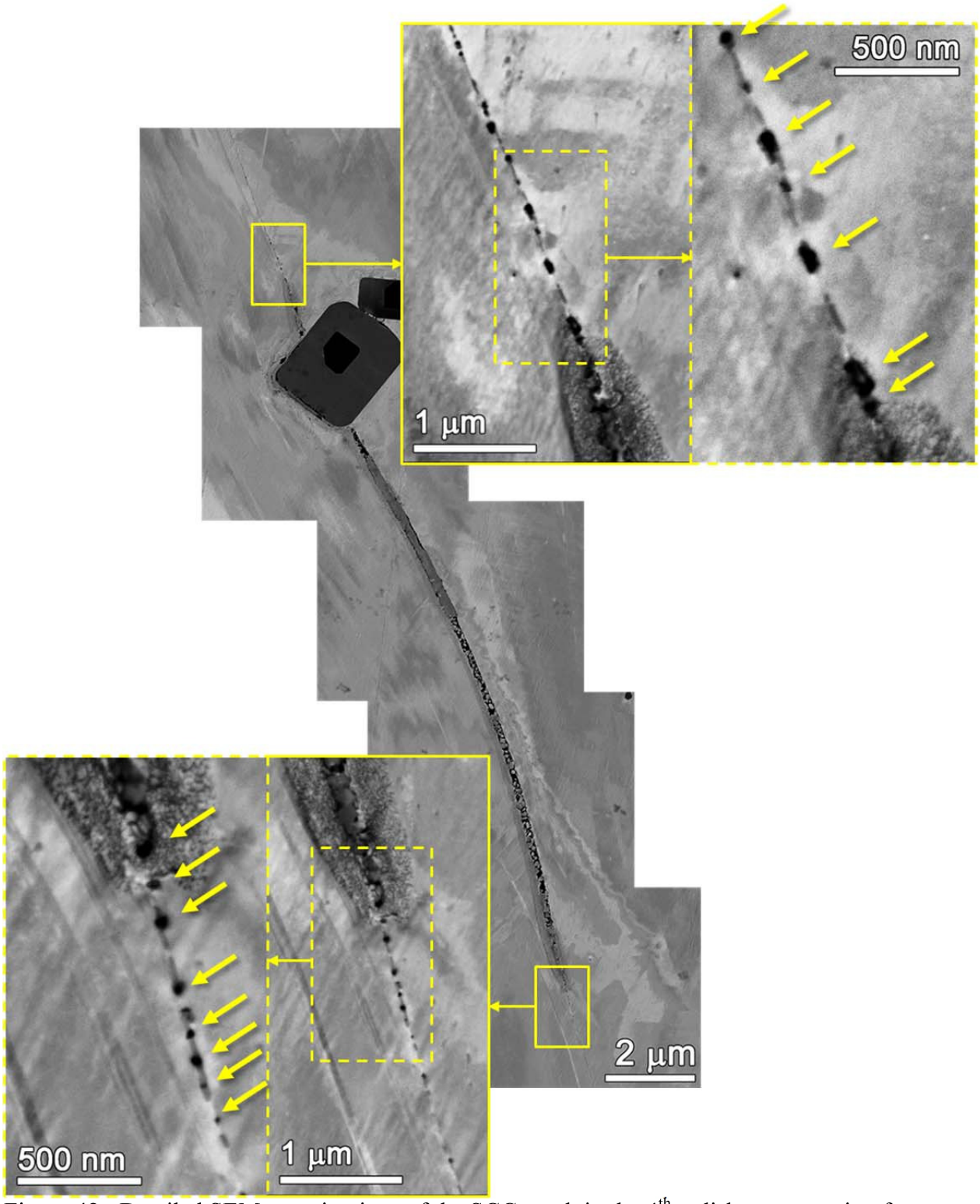

Figure 42. Detailed SEM examinations of the SCC crack in the 4th polish cross-section from Figure 40 for the 31%CF Valinox specimen c703. Evidence of cavities is seen immediately ahead of the SCC crack at both ends.

Serial polishing and SEM examinations were also conducted on the slice removed from BNCF specimen c703 after 10028 h of exposure. This time a larger crack with a surface length of ~120 μm passing along a few high-energy GBs was encountered (Figure 43a). Observations at cross-sections also revealed that this crack had propagated along several neighboring grains and reaching a maximum depth of ~108 μm (Figures 43b and c). Significant oxidation/corrosion walls flanked the crack all the way till the tip indicating that this is a SCC crack. Again discrete GB cavities were found immediately ahead of the crack tip in all the cross-section planes. However, different from the crack A observed at 5352 h in Figures 40-42, no consistent trend in the cavity size or density distribution was revealed in the four consecutive observations. While more investigation on the role of cavities in crack growth is needed, this might suggest that this crack was no longer actively growing.

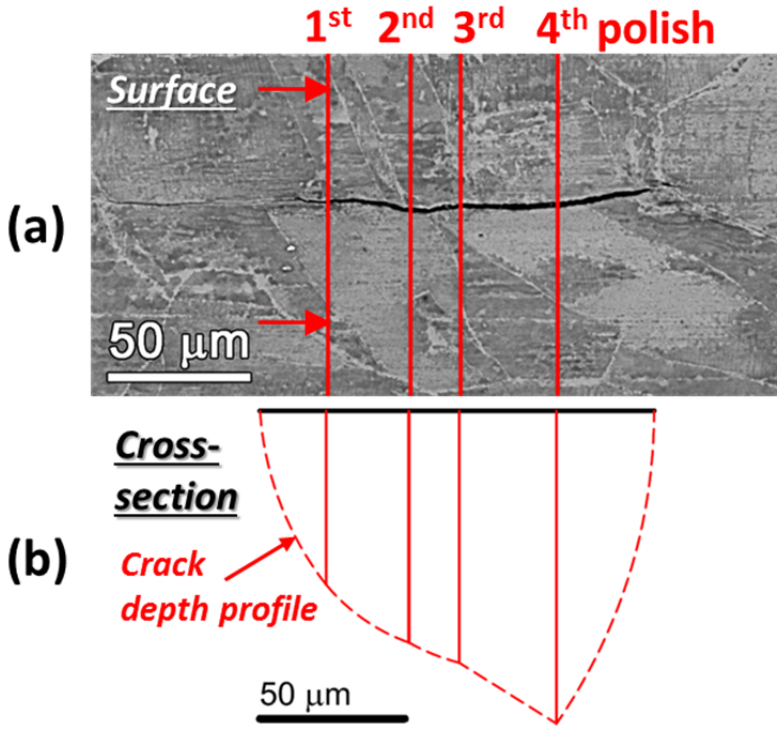

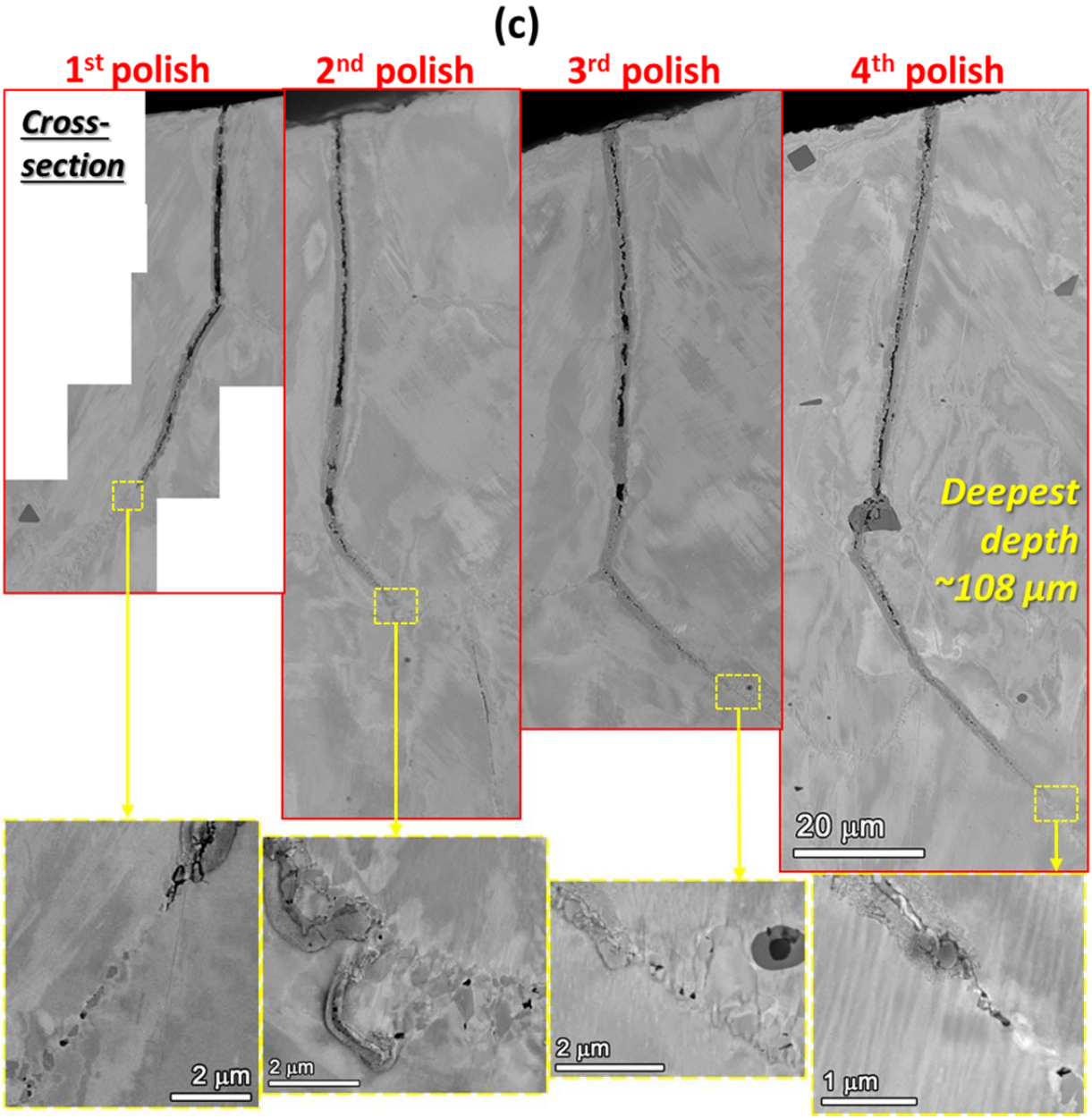

Figure 43. Serial polishing and SEM examinations on a slice removed from the 31%CF Valinox specimen c703 after 10028 h: (a) blunt notch surface region showing the position where the crack was intersected by four serial polishing, (b) schematic of the depth profile of the crack based on cross-section observations and (c) high-resolution SEM-BSE images showing the morphology of the crack and cavities ahead of the crack tip in the cross-section after each polishing.

The cross-section of a slice removed from the 31%CF Valinox BNCT specimen c703 after the conclusion of the test at 11709 h was also observed. Since the surface examinations (Figures 27 and 29) indicated that significant cracking had developed by this time, focus was shifted to characterize the detailed morphology of creep and SCC cracks in cross-section from the slice removed at the conclusion of the test. Two SCC cracks were found in the cross-section. Crack A was intersected by polishing at a location near the end of the crack as shown in Figure 44(a). Cross-section observations at the polished plane revealed that this crack grew from the surface and extended to a depth of ~200 µm with significant oxidation/corrosion along the crack walls all the way to the crack tip (Figure 44b). Considering this is the end portion of the crack and appear to be less open compared to the main portion to its left in Figure 44(a), the maximum depth of this crack is expected to be much deeper. In addition, GB cavities were again found ahead of the SCC crack among which the larger ones are located closer to the crack tip indicating the cavities were involved in crack propagation.

The other SCC crack (B) is located in the bulk with high-resolution images presented in Figure 45. Only the middle-section of this crack is flanked with oxidation/corrosion (Figure 45a), while no evidence of oxidation/corrosion was found in the upper or lower sections of this crack (Figures 45b and c). Interestingly, both ends showed cavities linking up along cracked GBs followed by discrete cavities suggesting that the subsurface crack was growing by connecting GB cavities. The above findings indicate that water probably made its way to the pre-existing creep crack through coalescence with cracks emanated from the surface, converting it to a SCC crack. In addition, slip bands and steps were present in the vicinity of the upper end of the creep crack as evidenced in Figure 45(c).

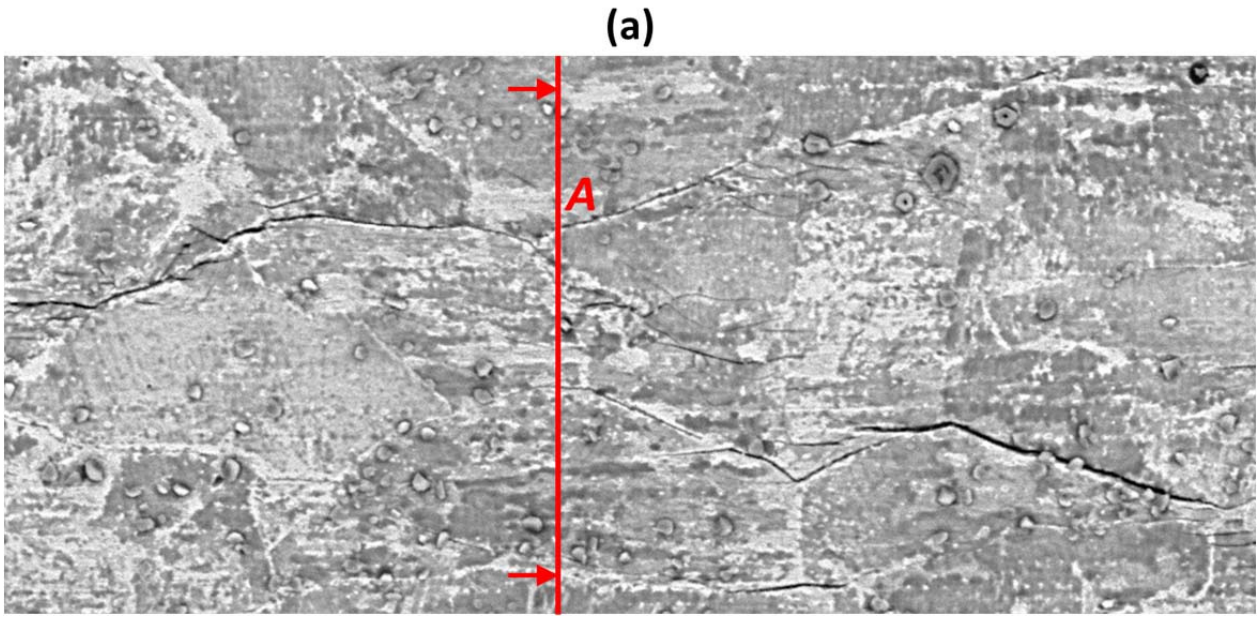

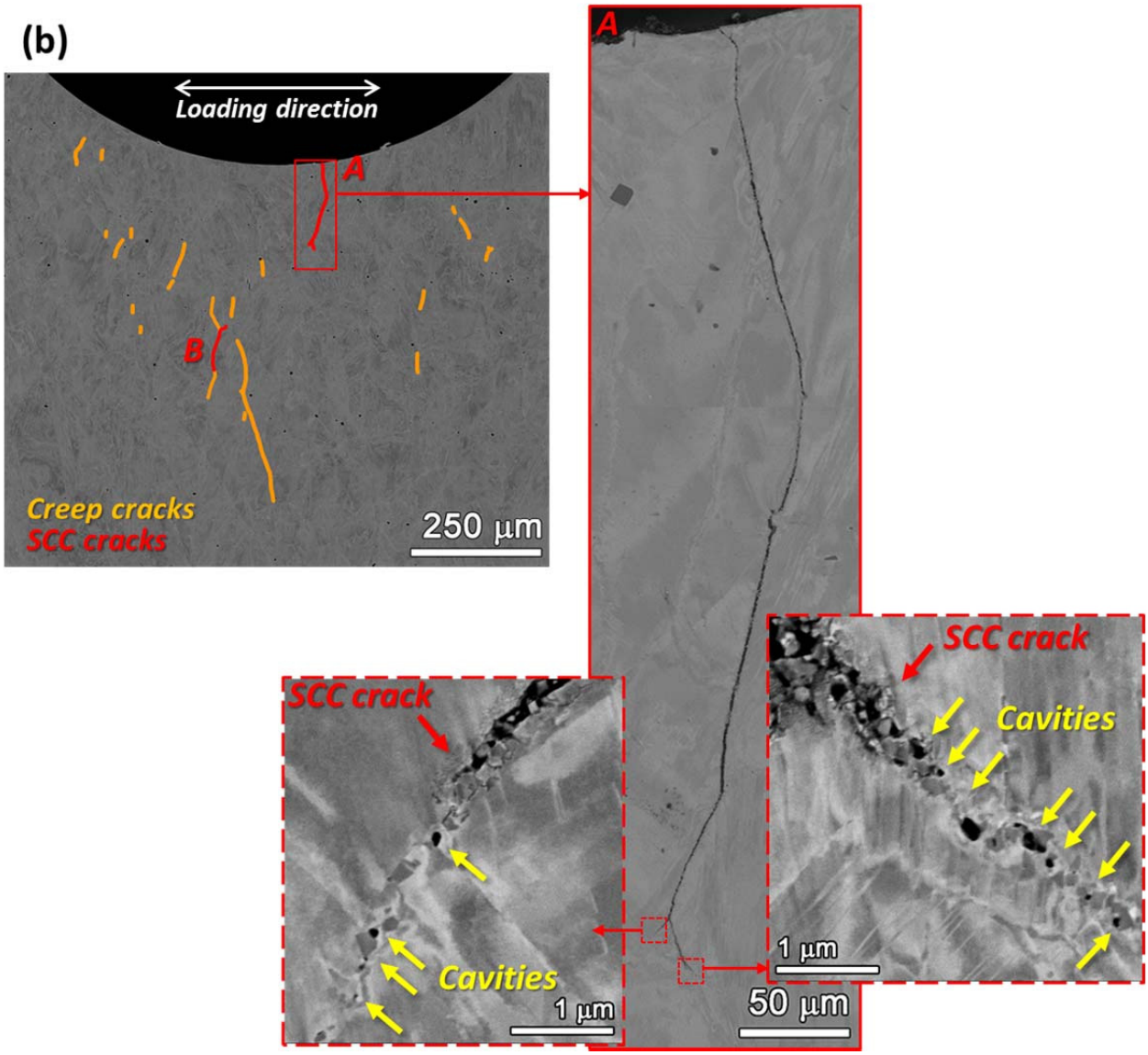

Figure 44. SEM examinations on a slice removed from the 31%CF Valinox specimen c703 after 11709 h: (a) blunt notch surface region showing the position where crack A was intersected by polishing and (b) high-resolution SEM-BSE images showing the morphology of crack A in the cross-section after polishing. Evidence of creep cavities is seen immediately ahead of the SCC crack tip.

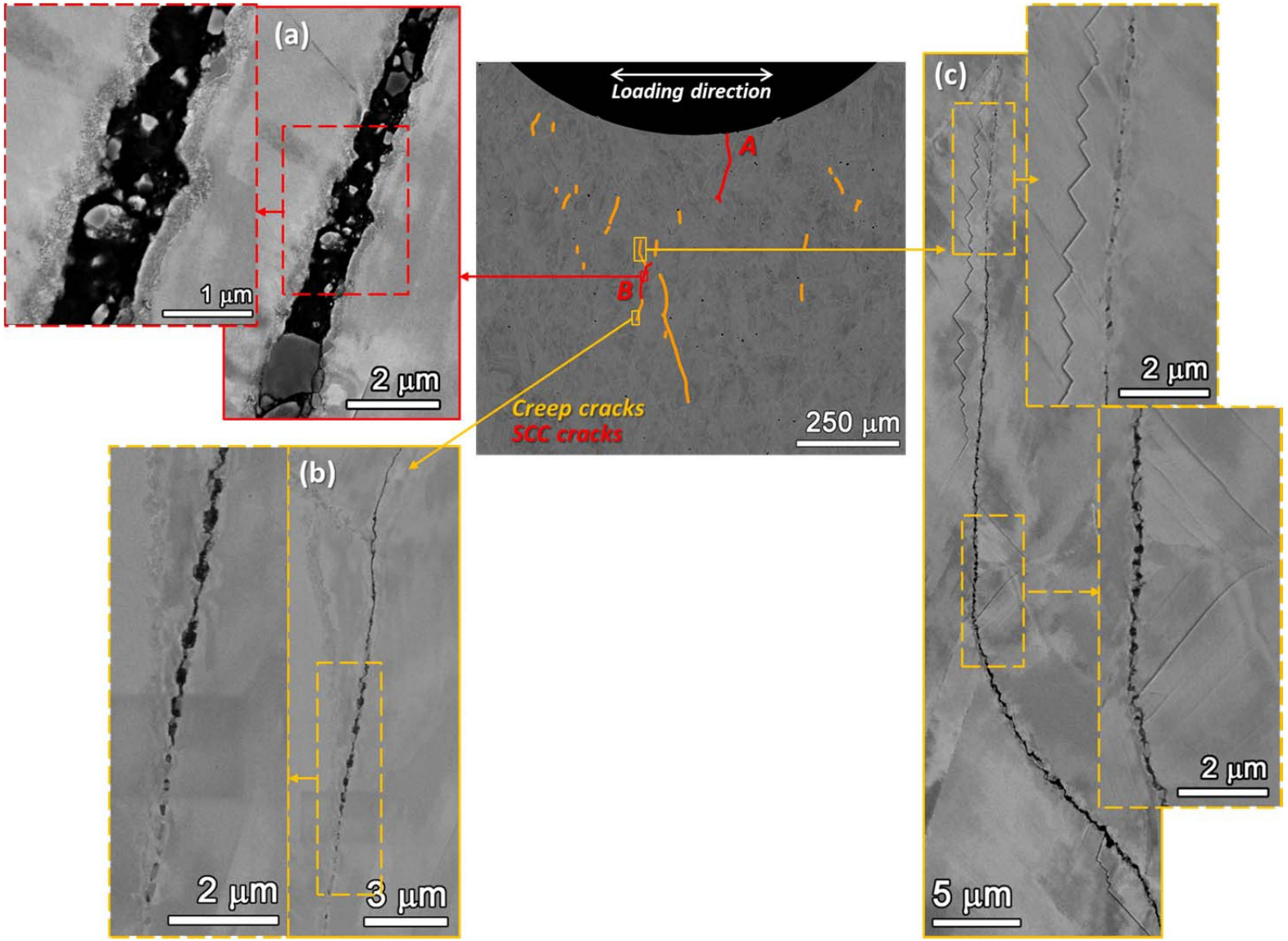

Figure 45. High-resolution SEM-BSE images showing the morphology of crack B in the cross-section of the slice removed from specimen c703 after 11709 h: (a) the SCC portion of crack B with evident oxidation/corrosion along the crack walls, (b) the lower portion and (c) the upper portion of crack B showing the crack ending in a series of cavities without any evidence of oxidation.

31%CF Sumitomo CRDM BNCT Specimen c704

Serial polish and SEM examinations did not encounter any conclusive observations of SCC cracks after 5352 and 10028 h of exposure in the 31%CF Sumitomo specimen c704 except some shallow IG crack precursors. This is not surprising because in comparison to c703, fewer obvious IG cracks often with shorter surface lengths were observed in c704.

As noted earlier, extensive cracking was observed in the low-resolution montage images of c704 by the time the test concluded at 11709 h (Figures 28 and 37). This can be more clearly viewed in Figure 46(a) where a few cracks emanating from the surface were intersected by polishing. The cross-section examination revealed that the largest SCC crack is located at position 5 with oxidation/corrosion along the crack walls extended to a depth of ~1.2 mm. In addition, substantiate creep cracks (highlighted in orange) without evidence of oxidation/corrosion were also found in the bulk. A comparison of the morphology of these two types of cracks is provided in Figure 46(b). High-magnification images revealed series of GB cavities at the tip of both the SCC and the creep cracks. In particular, the mature SCC crack where oxidation is present along the crack walls ended in what appears to be a creep crack, suggesting that the SCC was growing along a creep crack that had developed and linked to the surface well before significant SCC propagation took place.

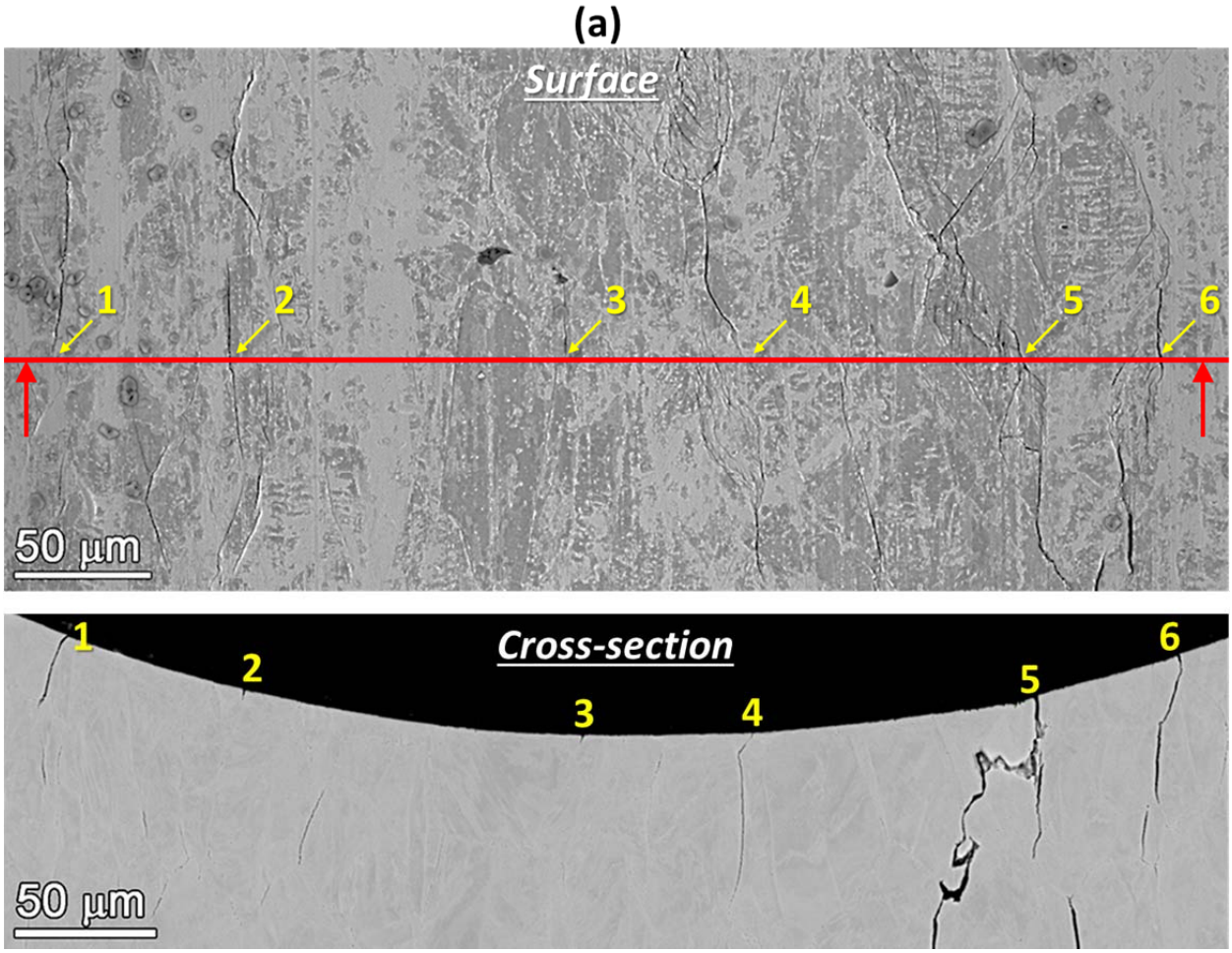

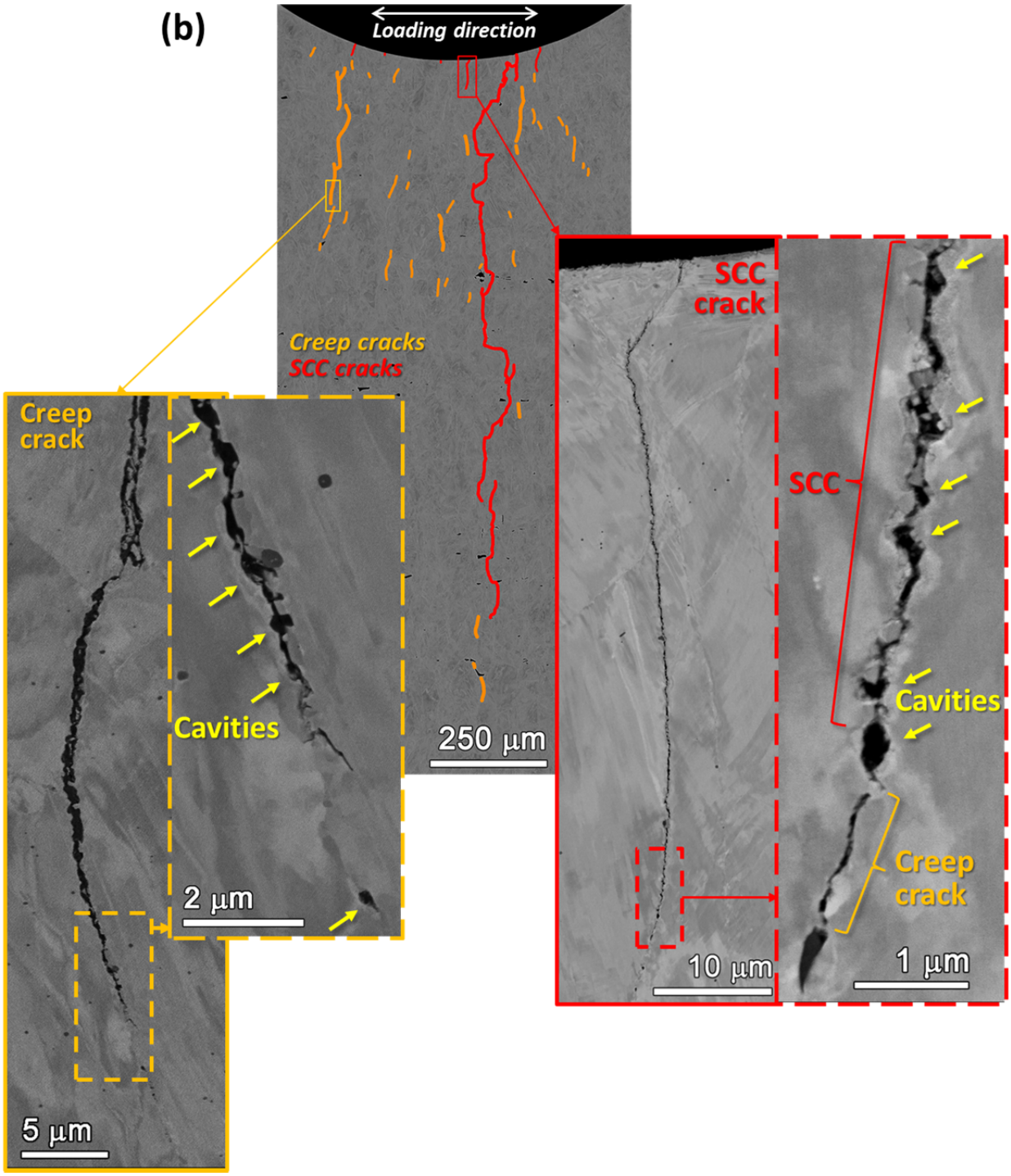

Figure 46. SEM examinations on a slice removed from the 31%CF Sumitomo specimen c704 after 11709 h: (a) low-resolution SEM-BSE images showing the surface (upper) and cross-section (lower) morphology of the cracks intersected by polishing, and (b) high-resolution SEM-BSE images showing the morphology of a creep crack (left) and a SCC crack (right, location 4 in Figure 46a) in the cross-section after polishing. Evidence of creep cavities is seen immediately ahead of the tip of both the creep crack and the SCC crack.

21%CF Valinox CRDM BNCT Specimen c707

A few small cracks were encountered during the serial polish and higher-resolution SEM examinations in the slices removed from the 21%CF Valinox specimen c707 after 5542 and 10049 h. While most of these features only had a very shallow depth less than 1 µm (Figure 47), the deepest SCC cracks encountered after the two test interruptions are shown in Figure 48. Both cracks exhibited significant oxidation/corrosion along the crack walls suggesting they must be SCC cracks. The crack observed at 5542 h has a depth of ~3 µm and had propagated along what appeared to be an incoherent twin boundary with two small cavities observed in the crack path. This incoherent twin boundary joined a high-angle GB not far ahead the crack tip where a series of cavities was present. The crack observed at 10049 h has a greater depth of ~11 µm with a cavity at the crack tip and few more immediately ahead of the tip. Although these cavities are generally smaller than those found ahead of the crack tips in the two 31%CF specimens, they probably played a role in IG crack nucleation for the 21%CF materials. Serial SEM characterizations are ongoing on the slice removed from c707 after the conclusion of the test at 11816 h.

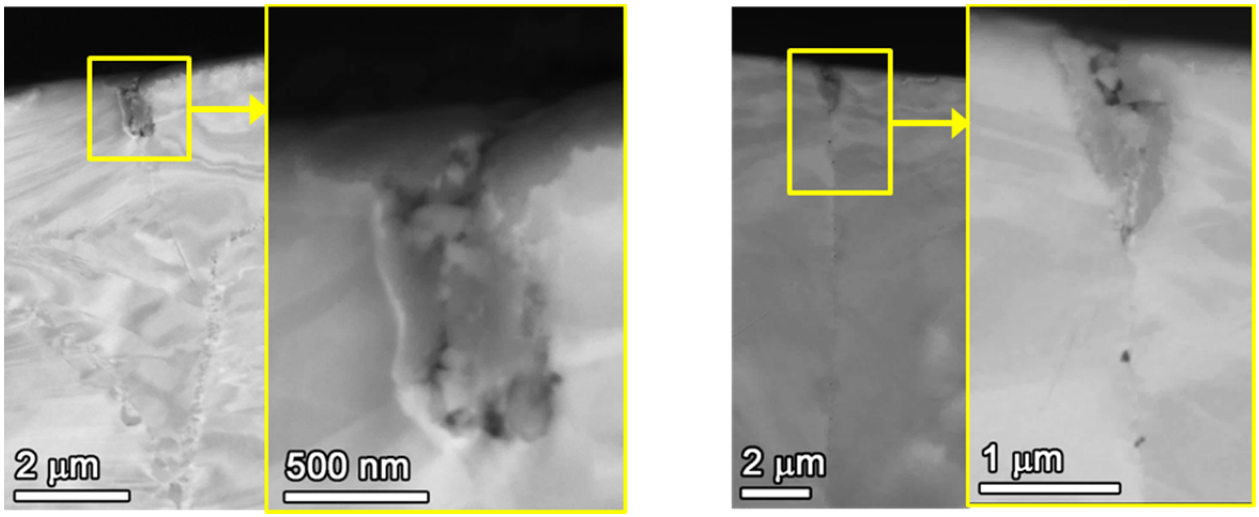

Figure 47. SEM-BSE images of the shallow IG crack precursors observed in the slices removed from the 21%CF Valinox CRDM specimen c707 after 5542 h and 10049 h.

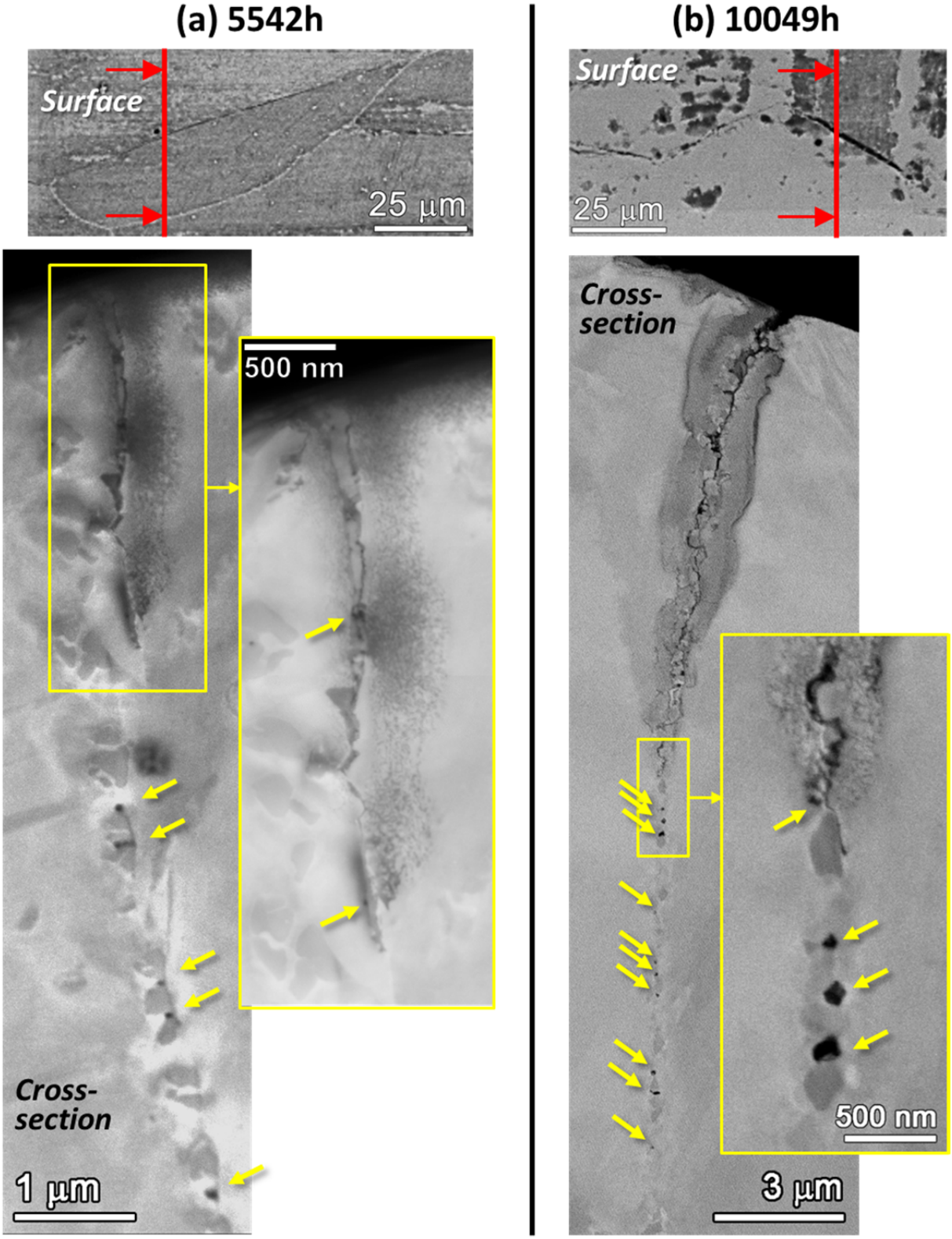

Figure 48. SEM examinations of the deepest SCC cracks in the 21%CF Valinox CRDM specimen c707 cross-section are presented after 5542 h (a) and 10049 h (b) exposure times. Evidence of creep cavities (arrows) is seen immediately ahead of the crack tip.

21%CF Sumitomo CRDM BNCT Specimen c708

Similar to what has been observed in the 21%CF Valinox c707 cross-sections, serial polish and SEM examinations only revealed several shallow IG precursor cracks in the 21%CF Sumitomo c708 specimen. An example is provided in Figure 49, where a shallow IG crack at a high-energy GB was intersected at three locations in a slice removed after the second test interruption at 10049 h. Very limited penetration of no more than ~2 μm in depth was observed along with few small, discrete cavities ahead of the crack tip. The estimated depth profile was also established for this shallow precursor crack (Figure 49b) showing negligible depth with respect to its surface length. Serial SEM/FIB characterizations are ongoing on the slice removed from c708 after the conclusion of the test at 11816 h.

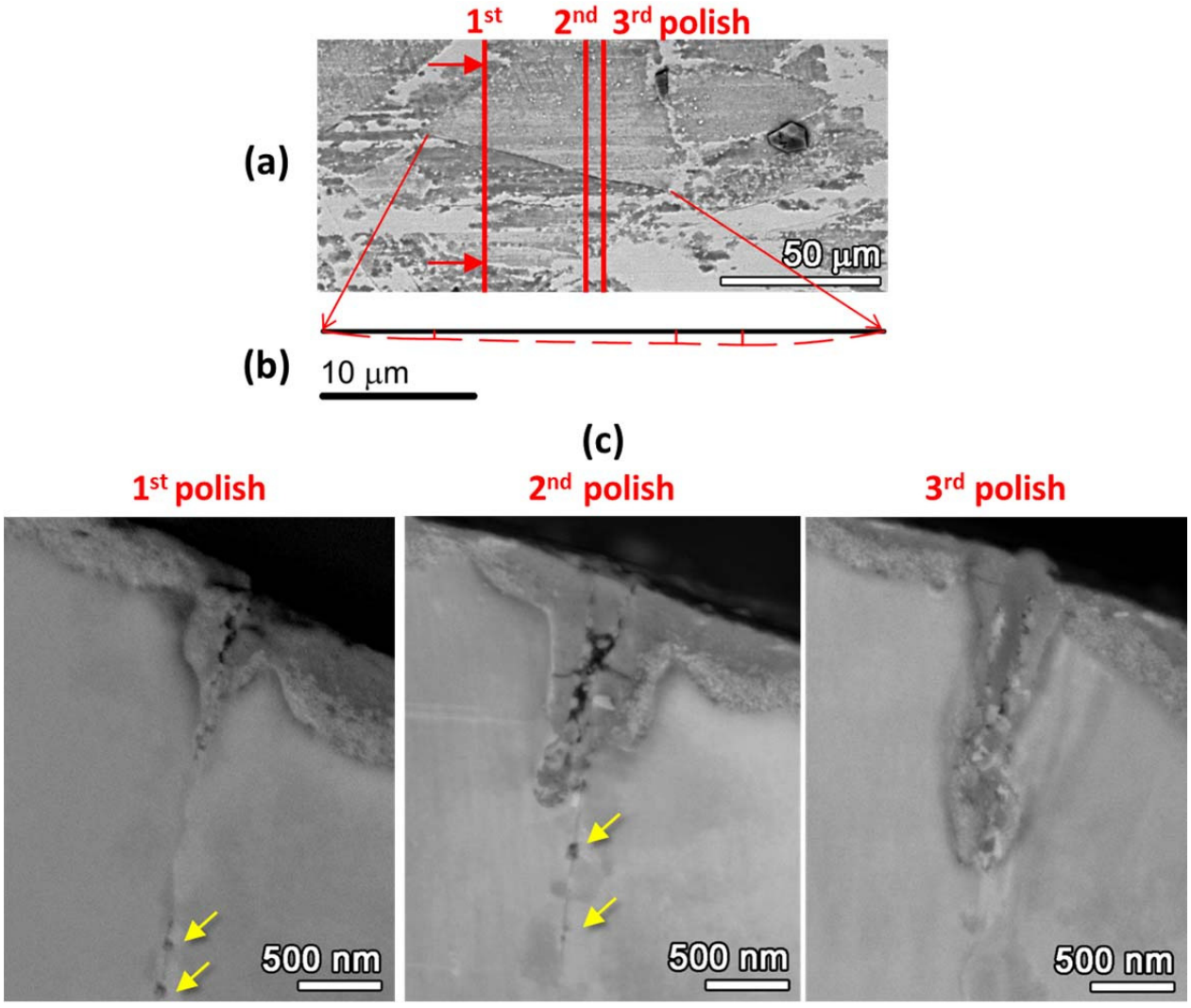

Figure 49. Serial polishing and SEM examinations on a slice removed from the 21%CF Sumitomo specimen c708 after 10049 h: (a) blunt notch surface region showing the position where the IG crack was intersected by three serial polishing, (b) schematic of the depth profile of the crack based on cross-section observations, and (c) high-resolution SEM-BSE images showing the morphology of the IG crack and cavities ahead of the crack tip in the cross-section after each polishing.

Discussion of Blunt Notch Test Results

The Sumitomo CRDM and Valinox CRDM alloy 690TT materials were tested for SCC initiation in both the 31%CF and 21%CF conditions. All specimens were loaded at moderate *K levels* for long times at constant load after several slow cyclic loading ramps. The two 31%CF specimens showed DCPD-indicated crack initiation and growth after 10400 h exposure. The 21%CF specimens only exhibited isolated small IG surface cracks and showed no apparent DCPD change throughout the test. Insights on the evolution of GB damage precursors and IG cracks were obtained by detailed surface and cross-section SEM examinations conducted at test interruptions and at the conclusion of the test. At the first interruption after the initial cyclic loading ramps, a number of isolated IG cracks were found on all four specimens with a much higher density in the 31%CF materials than in the 21%CF materials. Nano-size GB cavities were observed in the cross-sections beneath the notch surface in all specimens with a similar trend in cavity density as a function of cold work. As exposure progressed, an obvious increasing trend was observed in both surface IG cracks and GB cavities in the bulk for the two 31%CF specimens. The two 21%CF specimens exhibited a gradual increase in GB cavities, but little growth of IG cracks on the notch surface. This suggests that the formation of IG cracks has a strong dependence on cold work level and principally took place during initial cyclic loading ramps by dynamic straining. The subsequent constant *K* loading was found to increase the distribution and size of GB cavities in all specimens with a much larger effect on the 31%CF materials. Evidence indicates that GB cavities near the surface act as direct precursor for IG crack nucleation. The transition from small surface cracks to growing SCC cracks can be further accelerated when GB cavities in the bulk start to link up into creep cracks forming an interconnected network. This is likely the cause of the rapid crack growth in the two 31%CF specimens, highlighting the effect of creep on crack nucleation and propagation in CW alloy 690TT materials. However, critical creep rates to promote cavity formation and growth have not been fully established. New blunt notch test is under consideration to better assess the role of different loading conditions on cavity formation and growth that is believed to be important for key mechanistic aspects of the degradation in CW alloy 690 materials.

Constant Load SCC Initiation Testing on CW Alloy 690 Materials

Chapter Overview

While the blunt notch test revealed that GB cavities formed during both dynamic straining and constant *K* conditions are important for SCC initiation in CW alloy 690TT CRDM heats, the long-term damage evolution in CW alloy 690 under constant load is more relevant to service conditions. To enable this evaluation, constant load tensile (CLT) SCC initiation testing has been conducted on six commercial alloy 690 heats at various cold work levels in a 36-specimen test system. This chapter reviews the basic test approach and detailed characterizations performed on selected specimens after a test time of ~1 year in 360°C simulated PWR primary water. The applied stress for all tensile specimens was equivalent to the CW material yield stress therefore roughly scaled with the degree of cold work. IGSCC nucleation was observed for the first time under constant stress in highly CW alloy 690 and is again associated with the formation of GB creep cavities. Materials with a lower degree of cold work exhibited few IG damage precursors and no cracks. In the following sections, differences in the morphology of the precursor damage and cracks will be presented with regard to the % cold work and applied stress for each alloy 690 material. Comparison between heats will also be made in order to better understand the factors influencing GB cavity formation and crack initiation in CW alloy 690.

Constant Load SCC Initiation Testing

Materials, Specimens and Test Method

Experimentation was conducted in a 36-specimen test system with three strings each that can each accommodate up to 12 actively loaded and monitored specimens (Figure 50a). The set-up documentation of capabilities for this system was described in previous LWRS milestone reports [2, 3]. The validation of this test system design has benefited the NRC and EPRI justifying a jointly funded project to assess SCC initiation resistance of alloy 690/152/52 relative to alloy 600/182 that began in 2015.

Uniaxial tensile specimens, 1.2 inches (30.5 mm) long, were used for this test with dimensions shown in Figure 50(b). The relatively small specimen size was selected for multi-specimen testing and has the advantage of making DCPD more sensitive to changes in cross sectional area due to cracking. It also enables full characterization of the gauge surface by SEM in a reasonable period of time. The specimens were machined with the axis of the specimen parallel to the forging direction. This drives cracking to occur in the forging plane just as occurs during SCC CGR testing that has been performed by PNNL for the NRC using compact tension specimens. By varying the diameters of the tensile specimens, different stress levels can be achieved in the specimens in the loading strings to allow them all to be loaded at their yield stress (or any other target stress) for the applied load.

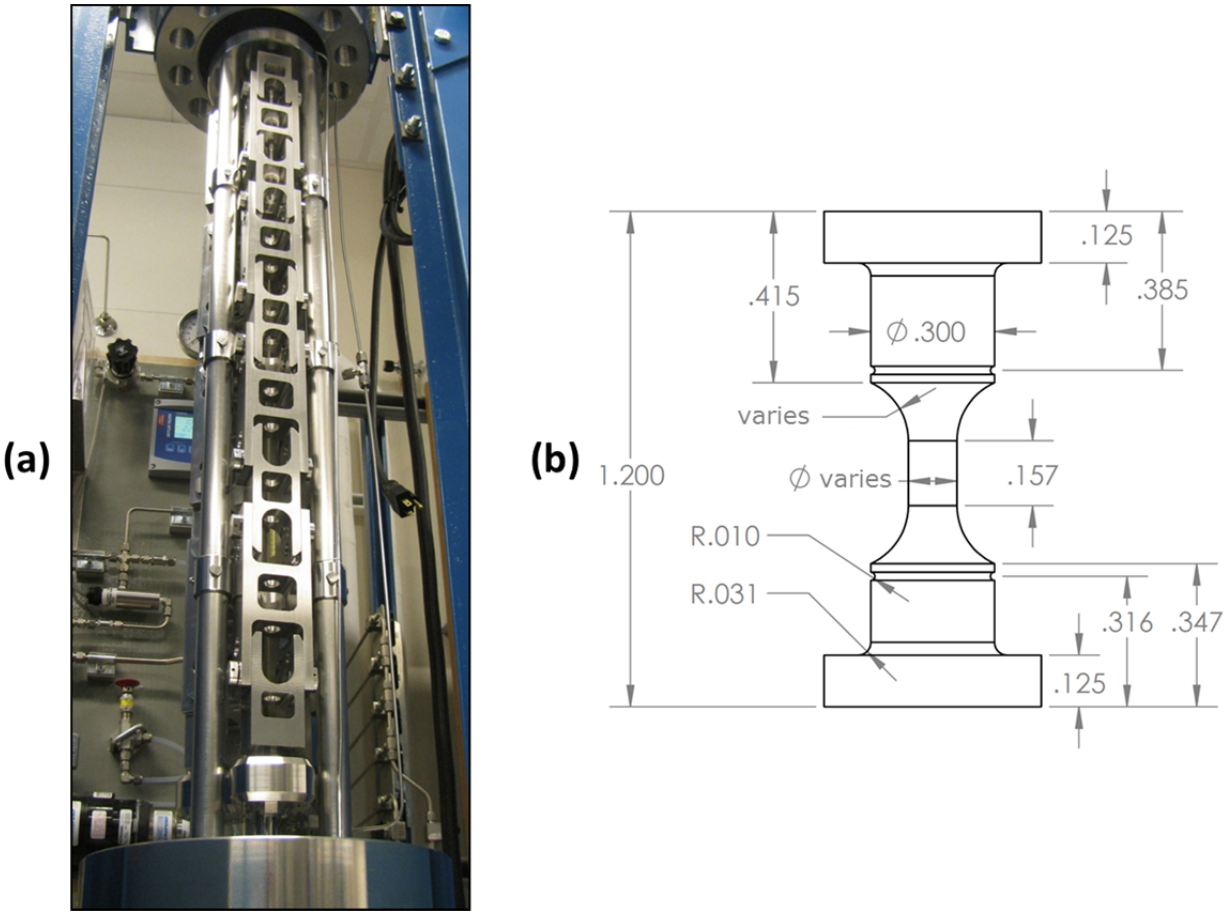

Figure 50. The 36-specimen crack initiation test system load train (a) and the dimensions (in inches) of the standard 1.2" tall tensile specimen (b) at PNNL.

Testing first began in October 2014 on the 21 alloy 690 specimens identified in Table 7. All testing has been performed at 360°C in simulated PWR primary water with 1000 ppm B, 2 ppm Li and 25 cc/kg H_2 (corresponding to the Ni/NiO stability line). Materials included four heats in the TT + 31%CF condition and three heats in the TT + 21%CF condition. The Sumitomo E67074C and Valinox RE243 are CRDM tubing, TK-VDM (Doosan) 133454 is a CRDM heat in rod form, and TK-VDM 114092 is a plate material. There are three specimens for each combination of heat and cold forge condition, and within each set of three, one has been polished to a 1 µm surface condition, whereas the other two have a ground "C" finish on the gauge emulating surface damage condition of in-service LWR components [4]. SCC crack growth testing has been conducted on most of these material conditions with high propagation rates observed for the 31%CF Sumitomo and Valinox materials and moderate propagation rates for all three heats in the 21%CF condition [7-9].

After ~2100 hours of operation, 15 additional CW alloy 690 specimens were inserted. These new alloy 690 specimens included the ANL (Special Metals) bar heat NX3297HK-12 in the mill-annealed (MA) + 26%CR condition, the GEG (Allvac) bar heat B25K in the MA + 18%CF and MA + 12%CF conditions, the TK-VDM 114092 plate in the TT + 21%CF condition, and the Valinox CRDM heat RE243 in the TT + 12%CF condition. Among these materials, only the 26%CR ANL material and the 12%CG Valinox material have been evaluated for SCC crack

growth, and only the 26%CR ANL exhibited high propagation rates. The B25K and TK-VDM heats were not examined in these CF conditions, however they did show moderate SCC growth rates with higher levels of cold work.

Three specimens were prepared for each combination of heat and cold work condition, but this time two of them were prepared with a 1 μm finish while the other one was in the ground "C" finish. Summary information on the 15 additional alloy 690 specimens is given in Table 8. Testing was restarted with all 36 specimens again loaded to their yield stress until a total exposure time of 9220 hours (~1.1 year) for the first 21 specimens and 7107 hours (~0.8 year) for the other 15 specimens. The test was then stopped and SEM characterizations were carried out to assess precursor damage on the surface of highly polished specimens before returning them for continued exposure.

Table 7. Summary of materials and applied stress (yield stress) for the first group of alloy 690 specimens in the 36-specimen test system

Specimen	Material	Material Condition	Surface Condition	Applied Stress, MPa
IN024 (CL)	Sumitomo CRDM	TT + 21%CF	1 μm Polish	590
IN025 (CL)	Sumitomo CRDM	TT + 21%CF	Ground C Finish	590
IN026 (CL)	Sumitomo CRDM	TT + 21%CF	Ground C Finish	590
IN027 (CL)	Valinox CRDM	TT + 21%CF	1 μm Polish	525
IN028 (CL)	Valinox CRDM	TT + 21%CF	Ground C Finish	525
IN029 (CL)	Valinox CRDM	TT + 21%CF	Ground C Finish	525
IN030 (CL)	Doosan CRDM	TT + 21.6%CF	1 μm Polish	555
IN031 (CL)	Doosan CRDM	TT + 21.6%CF	Ground C Finish	555
IN032 (CL)	Doosan CRDM	TT + 21.6%CF	Ground C Finish	555
IN033 (CL)	Sumitomo CRDM	TT + 31%CF	1 μm Polish	710
IN034 (CL)	Sumitomo CRDM	TT + 31 %CF	Ground C Finish	710
IN035 (CL)	Sumitomo CRDM	TT + 31%CF	Ground C Finish	710
IN036 (CL)	Valinox CRDM	TT + 31%CF	1 μm Polish	720
IN037 (CL)	Valinox CRDM	TT + 31%CF	Ground C Finish	720
IN038 (CL)	Valinox CRDM	TT + 31%CF	Ground C Finish	720
IN039 (CL)	Doosan CRDM	TT + 31%CF	1 μm Polish	685
IN040 (CL)	Doosan CRDM	TT + 31%CF	Ground C Finish	685
IN041 (CL)	Doosan CRDM	TT + 31%CF	Ground C Finish	685
IN042 (CL)	TK-VDM Plate	TT + 31.9%CF	1 μm Polish	700
IN043 (CL)	TK-VDM Plate	TT + 31.9%CF	Ground C Finish	700
IN044 (CL)	TK-VDM Plate	TT + 31.9%CF	Ground C Finish	700

CL = constant load

Table 8. Summary of materials and applied stress (yield stress) for the second group of alloy 690 specimens that were added to the 36-specimen test system

Specimen	Material	Material Condition	Surface Condition	Applied Stress, MPa
IN053 (CL)	ANL Flat Bar	MA + 26%CR	1 μm Polish	775
IN054 (CL)	ANL Flat Bar	MA + 26%CR	1 μm Polish	775
IN055 (CL)	ANL Flat Bar	MA + 26%CR	Ground C Finish	775
IN056 (CL)	GE B25K Bar	MA + 18.3%CF	1 μm Polish	550
IN057 (CL)	GE B25K Bar	MA + 18.3%CF	1 μm Polish	550
IN058 (CL)	GE B25K Bar	MA + 18.3%CF	Ground C Finish	550
IN059 (CL)	TK-VDM Plate	TT + 21%CR	1 μm Polish	675
IN060 (CL)	TK-VDM Plate	TT + 21%CR	1 μm Polish	675
IN061 (CL)	TK-VDM Plate	TT + 21%CR	Ground C Finish	675
IN062 (CL)	GE B25K Bar	MA + 12.4%CF	1 μm Polish	510
IN063 (CL)	GE B25K Bar	MA + 12.4%CF	1 μm Polish	510
IN064 (CL)	GE B25K Bar	MA + 12.4%CF	Ground C Finish	510
IN065 (CL)	Valinox CRDM	TT + 11.7%CF	1 μm Polish	365
IN066 (CL)	Valinox CRDM	TT + 11.7%CF	1 μm Polish	365
IN067 (CL)	Valinox CRDM	TT + 11.7%CF	Ground C Finish	365

CL = constant load

DCPD Response

Due to space limitations within the autoclave, only one (with 1 μm finish) out of each set of 3 duplicate CLT specimens could be instrumented for DCPD. The DCPD signal is sensitive not only to cracking but also to changes in length and diameter due to creep or tensile straining, as well as to resistivity change that occurs in alloy 690 when exposed at 360°C. DCPD values are presented as strain measurements because up to the point of crack initiation, strain more strongly affects the DCPD signal than cracking. However, it should be noted that resistivity changes affect the DPCD signal and create a higher strain rate than due to creep alone. DCPD-based strain response for 11 out of the 12 instrumented specimens for the final 3220 hours of testing is presented in Figures 51-54. The responses of the 11 specimens are similar with indicated non-referenced strain increases of 0.1-0.4% over this time period. Slightly higher strain rates can be seen for the 31%CF specimens in Figure 51 than for the lower cold-worked materials in Figures 52-54. This can be viewed more clearly in Figure 55 where the DCPD-indicated strain rate is plotted against applied stress. The variations in strain rates seem to scale with applied stress likely due to the contribution of creep. There is also a continually decreasing trend over time in the strain rate response of all the specimens consistent with a slowing resistivity evolution since material changes saturate after long exposures at 360°C.

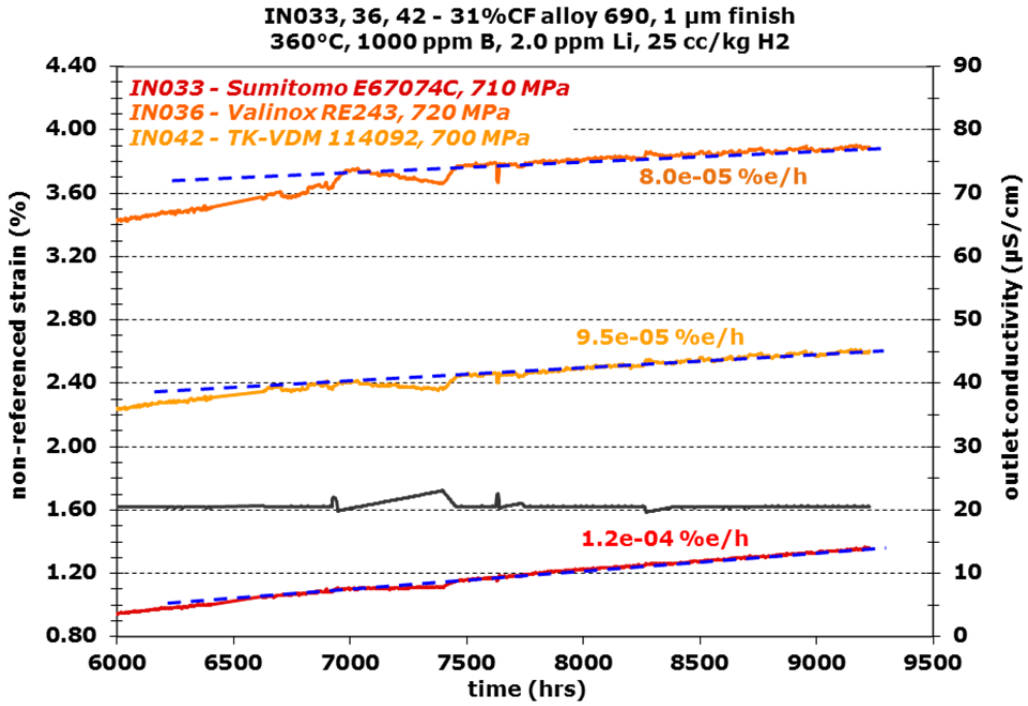

Figure 51. Non-referenced strain response for three heats of 31%CF alloy 690 undergoing long term constant load exposure at 360°C in the PNNL 36-specimen initiation test system. For each heat of material at this CW level, there are 3 CLT specimens in the test rig.

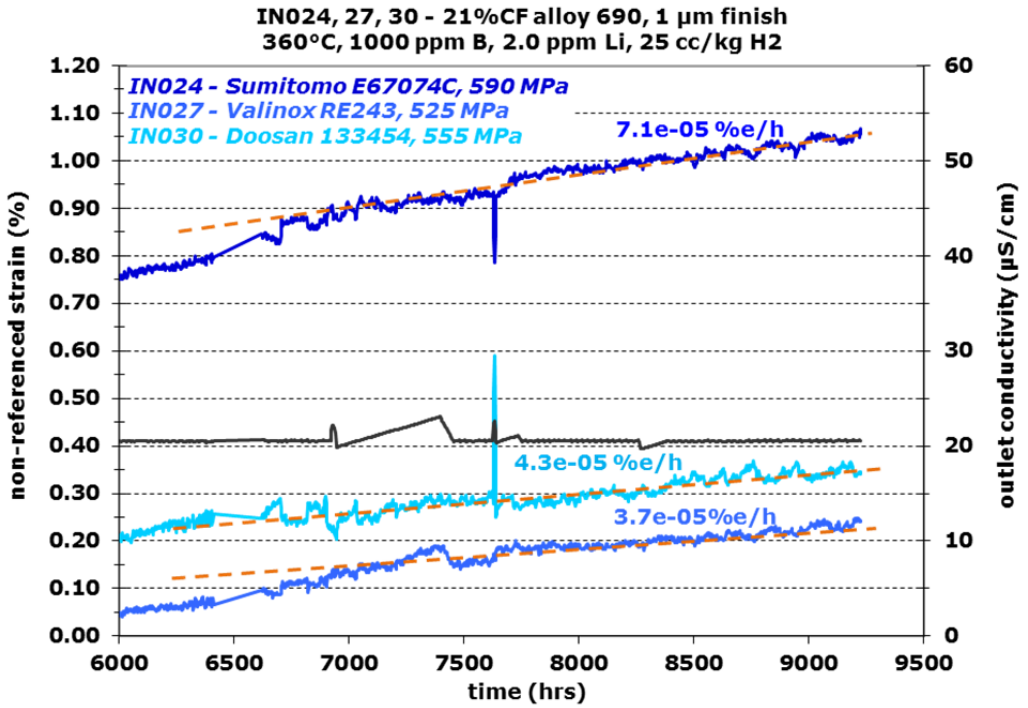

Figure 52. Non-referenced strain response for three heats of 21%CF alloy 690 undergoing long term constant load exposure at 360°C in the PNNL 36-specimen initiation test system. For each heat of material at this CW level, there are 3 CLT specimens in the test rig.

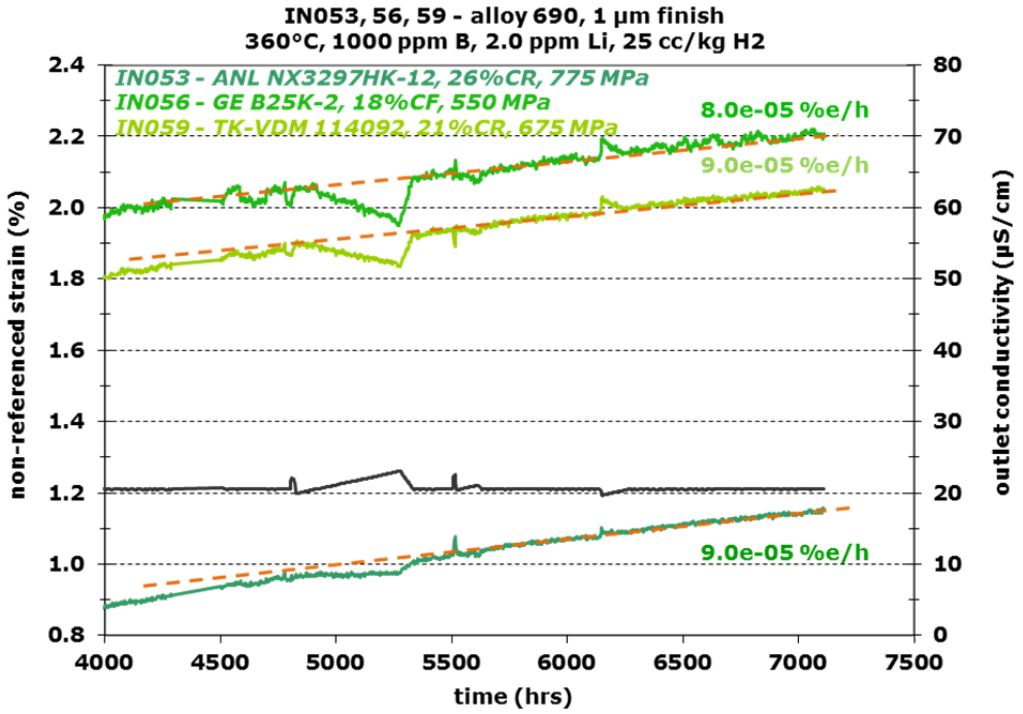

Figure 53. Non-referenced strain response for three heats of 18-26%CW alloy 690 undergoing long term constant load exposure at 360°C in the PNNL 36-specimen initiation test system. For each heat of material at this CW level, there are 3 CLT specimens in the test rig.

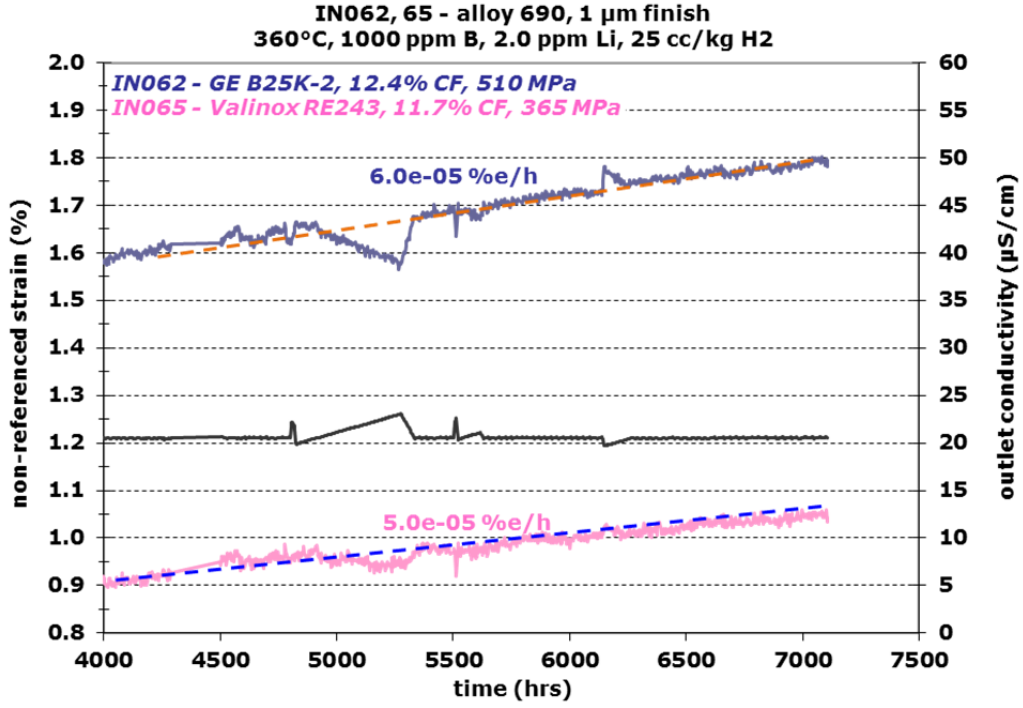

Figure 54. Non-referenced strain response for two heats of 12%CF alloy 690 undergoing long term constant load exposure at 360°C in the PNNL 36-specimen initiation test system. For each heat of material at this CW level, there are 3 CLT specimens in the test rig.

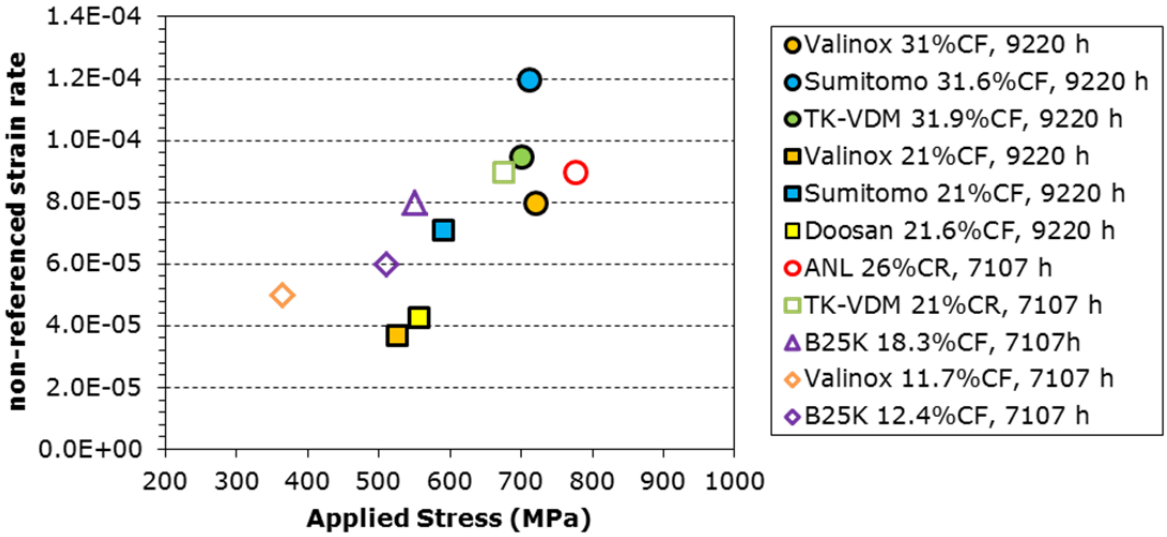

Figure 55. DCPD non-referenced strain rate over the latest ~2500 h as a function of applied stress in the tested alloy 690 CLT initiation specimens.

Measured Creep Strain in the Specimens

In the attempt to better quantify creep strain induced during high-temperature exposure, the gauge length and diameter of the specimens were measured prior to the test and after the test interruption. In order to reduce measurement error, 2-3 measurements were carried out for each dimension and the averaged values for the gauge length (measured between the grooves located above and below the fillet regions shown in Figure 50b) and the gauge diameter are listed in Table 9. The gauge diameter was not measured for a number of specimens that had been removed for destructive examinations and the corresponding cells are left blank in the table. The averaged creep strains were then calculated using equations below:

$$\text{Uniaxial creep strain based on gauge length: } \varepsilon_{\mathrm{cr,L}} = \frac{L-L_0}{L_0} - \varepsilon_{\mathrm{p}}$$

$$\text{Uniaxial creep strain based on gauge diameter: } \varepsilon_{\mathrm{cr,D}} = -\frac{D-D_0}{\nu_{cr} D_0} - \varepsilon_{\mathrm{p}}$$

where ε_{p} is the total amount of plastic strain accumulated during the loading processes to the yield stress as monitored using DCPD with values listed in Table 9. Only one specimen was monitored for each material and cold work combination, but the amount of plastic strain is assumed to be identical for the three duplicate specimens. ν_{cr} is the Poisson ratio with a value of 0.5 for volume-conservative creep deformation in the alloys. The calculated creep strains using these two methods are plotted against the applied stress as shown in Figures 56 and 57, where the specimens exposed for 9220 h are represented in closed symbols and those exposed for 7107 h are in open symbols. The creep strain calculated based on gauge length measurements are ~2-4% for most specimens while those calculated based on gauge diameter measurements are generally lower, within the range of ~1-3%. Surprisingly, for both estimates, the estimated creep strains are not obviously sensitive to the applied stress for the available data. Based on the observations of many GB cavities in the gauge section of these specimens that will be discussed in more detail later, it is likely that the gauge length measured along the stress axis is more sensitive to the existence of cavities, thus resulting in the higher values for creep strains.

Table 9. Summary of change in gauge length and gauge diameter of the 36 alloy 690 specimens.

Spec ID	Material Condition	ε_P (%)	Gauge length (in)		$\varepsilon_{cr,L}$ (%)	Gauge diameter (in)		$\varepsilon_{cr,D}$ (%)
			L_0	L		D_0	D	
IN024	Sumitomo CRDM TT + 21%CF	0.30	0.4817	0.5003	3.56	0.1257	0.1235	3.20
IN025		0.30	0.4810	0.5004	3.73	0.1256	0.1244	1.61
IN026		0.30	0.4810	0.4972	3.07	0.1249		
IN027	Valinox CRDM TT + 21%CF	0.20	0.4709	0.4928	4.45	0.1339	0.1309	4.21
IN028		0.20	0.4751	0.4971	4.43	0.1344	0.1337	0.77
IN029		0.20	0.4706	0.4942	4.81	0.1342		
IN030	Doosan CRDM TT + 21.6%CF	0.10	0.4728	0.4961	4.83	0.1300	0.1281	2.82
IN031		0.10	0.4822	0.4998	3.55	0.1291	0.1281	1.37
IN032		0.10	0.4893	0.5002	2.12	0.1313		
IN033	Sumitomo CRDM TT + 31%CF	0.45	0.4814	0.5004	3.49	0.1151		
IN034		0.45	0.4811	0.5007	3.61	0.1157		
IN035		0.45	0.4802	0.4994	3.55	0.1158	0.1151	0.76
IN036	Valinox CRDM TT + 31%CF	0.30	0.4820	0.5020	3.85	0.1149	0.1132	2.57
IN037		0.30	0.4838	0.5012	3.30	0.1151	0.1141	1.35
IN038		0.30	0.4813	0.4998	3.53	0.1152		
IN039	Doosan CRDM TT + 31%CF	0.22	0.4819	0.5007	3.68	0.1167	0.1160	0.98
IN040		0.22	0.4818	0.4987	3.29	0.1174	0.1160	2.08
IN041		0.22	0.4819	0.5007	3.67	0.1171		
IN042	TK-VDM Plate TT + 31.9%CF	1.10	0.4823	0.4990	2.36	0.1163	0.1132	4.15
IN043		1.10	0.4817	0.4996	2.62	0.1162	0.1141	2.51
IN044		1.10	0.4837	0.4971	1.67	0.1165		
IN053	ANL Flat Bar MA + 26%CR	0.00	0.5100	0.5195	1.86	0.1116	0.1084	5.79
IN054		0.00	0.4948	0.5152	4.12	0.1104	0.1067	6.70
IN055		0.00	0.4965	0.5112	2.95	0.1104		
IN056	GE B25K Bar MA + 18.3%CF	0.35	0.4899	0.5063	3.00	0.1295	0.1292	0.11
IN057		0.35	0.4953	0.5110	2.82	0.1295	0.1290	0.42
IN058		0.35	0.4944	0.5094	2.68	0.1300		
IN059	TK-VDM Plate TT + 21%CR	0.35	0.4853	0.5031	3.32	0.1179	0.1169	1.29
IN060		0.35	0.4872	0.5040	3.10	0.1184	0.1160	3.62
IN061		0.35	0.4864	0.5008	2.60	0.1170		
IN062	GE B25K Bar MA + 12.4%CF	0.25	0.4869	0.5038	3.22	0.1342	0.1328	1.76
IN063		0.25	0.4853	0.5050	3.81	0.1346	0.1346	-0.25
IN064		0.25	0.4842	0.5022	3.46	0.1346		
IN065	Valinox CRDM TT + 11.7%CF	0.50	0.4757	0.4878	2.04	0.1580	0.1561	1.84
IN066		0.50	0.4783	0.4894	1.82	0.1566	0.1561	0.07
IN067		0.50	0.4722	0.4908	3.43	0.1570		

Note: specimens IN024-IN044 were tested for 9220 hours, while *IN053-IN067 were tested for 7107 hours*.

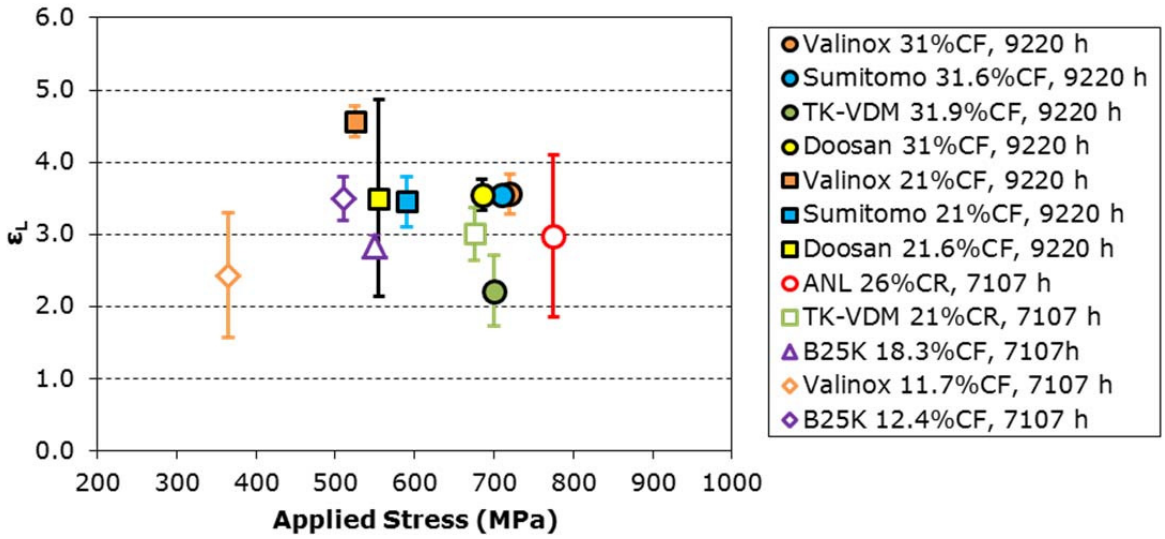

Figure 56. Uniaxial creep strain calculated based on gauge length measurements as a function of applied stress in the tested alloy 690 CLT initiation specimens.

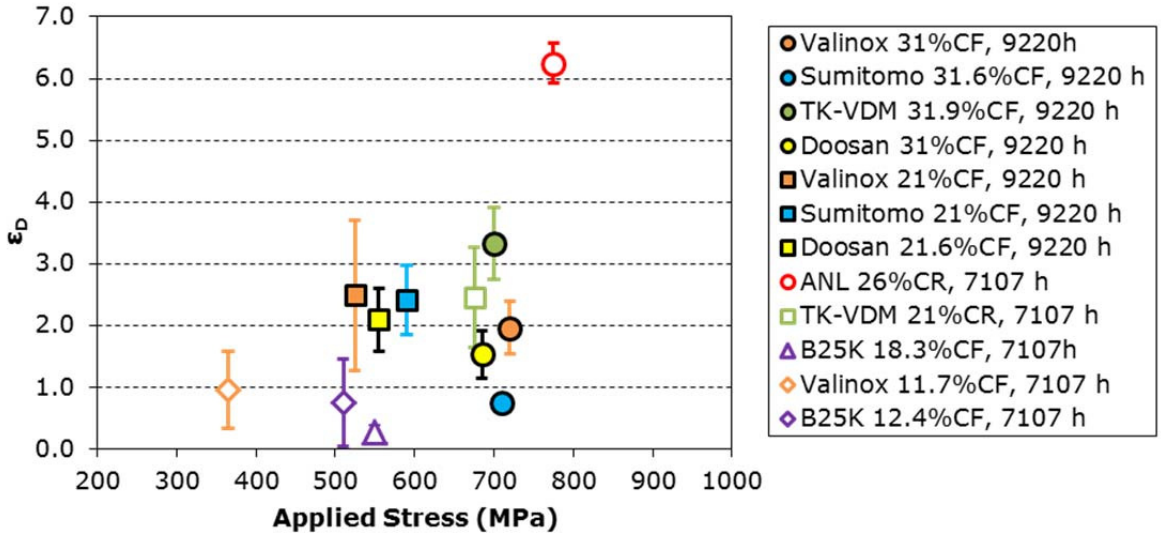

Figure 57. Uniaxial creep strain calculated based on gauge diameter measurements as a function of applied stress in the tested alloy 690 CLT initiation specimens.

Damage Characterizations

Precursor Damage and Crack Morphology on the Surface of the Polished Specimens

Microstructural examinations on the CLT specimens were also conducted using the same SEM and FIB systems that were used for the blunt notch specimens. Characterizations started by documenting the entire gauge surface of the 12 instrumented, highly polished specimens as listed in Table 10. In order to achieve this, four fiducial scribe marks (90° to one another) were made at the button ends of each specimen to keep track of the specimen orientation. Each of the four orientations was then mapped using low-magnification, high-keV BSE montage imaging followed by high-resolution SE/BSE imaging at specific sites of interest. Examples on one rotation randomly chosen for every specimen are summarized in Figures 58-59 for the 31%CF and 21%CF Sumitomo CRDM, Figures 60-62 for the 31%CF, 21%CF and 11.7%CF Valinox CRDM, Figures 63-64 for the 31%CF and 21.6%CF Doosan CRDM, Figures 65-66 for the 31.9%CF and 21%CR TK-VDM plate, Figure 67 for the 26%CR ANL flat bar heat and Figures 68-69 for the 18.3%CF and 12.4%CF GE bar materials. Obvious cracks are highlighted in red and possible cracks are highlighted in green whenever they can be readily identified on the surface. The obvious cracks usually appear as open or partially open IG cracks with a surface length greater than ~10 μm, whereas the possible cracks exhibit continuous dark contrast along GBs with a similar length but show no crack opening and may result from local corrosion.

Table 10. Constant load tensile specimens for surface examinations.

Specimen	Material	Material Condition	Surface Condition	Applied Stress, MPa	Exposure Time (h)
IN033 (CL)	Sumitomo CRDM	TT + 31%CF	1 μm Polish	710	9220
IN024 (CL)	Sumitomo CRDM	TT + 21 %CF	1 μm Polish	710	9220
IN036 (CL)	Valinox CRDM	TT + 31%CF	1 μm Polish	720	9220
IN027 (CL)	Valinox CRDM	TT + 21%CF	1 μm Polish	525	9220
IN065 (CL)	Valinox CRDM	TT + 11.7%CF	1 μm Polish	365	7107
IN039 (CL)	Doosan CRDM	TT + 31%CF	1 μm Polish	685	9220
IN030 (CL)	Doosan CRDM	TT + 21.6%CF	1 μm Polish	555	9220
IN042 (CL)	TK-VDM Plate	TT + 31.9%CF	1 μm Polish	700	9220
IN059 (CL)	TK-VDM Plate	TT + 21%CR	1 μm Polish	675	7107
IN056 (CL)	GE B25K Bar	MA + 18.3%CF	1 μm Polish	550	7107
IN062 (CL)	GE B25K Bar	MA + 12.4%CF	1 μm Polish	510	7107
IN053 (CL)	ANL Flat Bar	MA + 26%CR	1 μm Polish	775	7107

As shown in Figure 58, obvious small IG cracks of 20-150 μm long are widely distributed in the gauge section of the 31%CF Sumitomo CRDM specimen IN033. Similar to those found in the blunt notch specimens, the cracks in the CLT specimen also lie at 45-90^{o} to the loading direction. Examples of these cracks are also given at higher magnifications in the images taken at a randomly selected area (marked in yellow box) on the specimen. Small "possible" cracks were present throughout the entire gauge section shown, but were not marked because of their extremely high density. Although no initiation has been detected by DCPD, it is clear that crack nucleation had occurred in this highly CW alloy 690 material under constant load. The decision was therefore made to create shallow trenches using FIB to observe crack depth profiles in this specimen in a non-destructive manner and these results will be presented in the next section. In comparison to IN033, no obvious surface cracks were found for the 21%CF Sumitomo CRDM

specimen IN024. However, a few very short and tight IG features that appeared to be possible cracks were revealed (Figure 59). In addition, many high-energy GBs in this specimen showed a distinct "postage stamp" appearance where the GBs at the surface are decorated with what appear to be nano-sized, discrete holes or cavities.

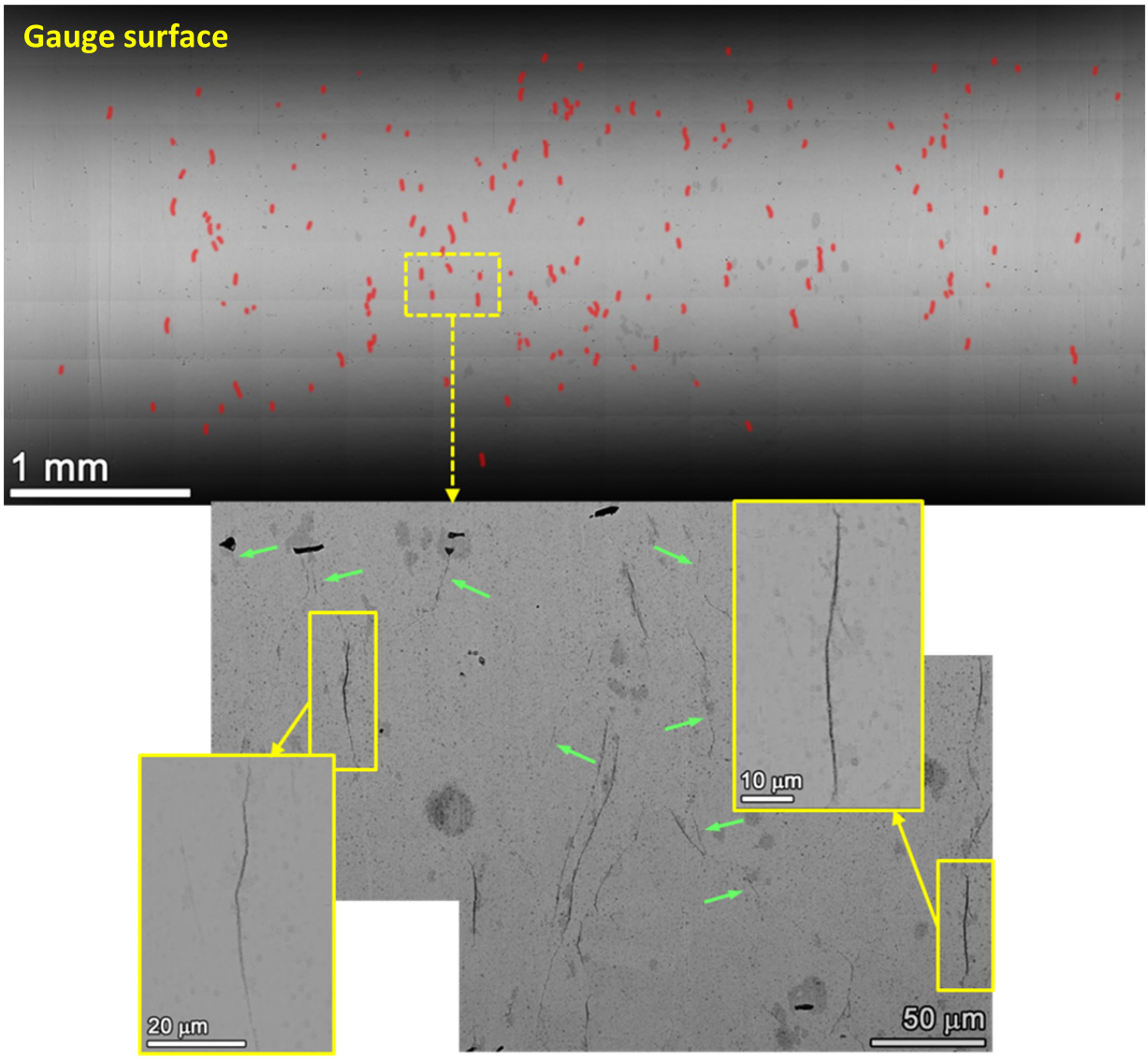

Figure 58. SEM-BSE montage images of the gauge surface are presented for one rotation of the 1 µm, 31%CF Sumitomo specimen IN033 after 9220 h of exposure. Obvious cracks are highlighted in red. Possible cracks are not highlighted in the upper low-resolution montage image because of their extremely high density in this specimen, but some of these possible cracks are marked with green arrows in the lower high-magnification images.

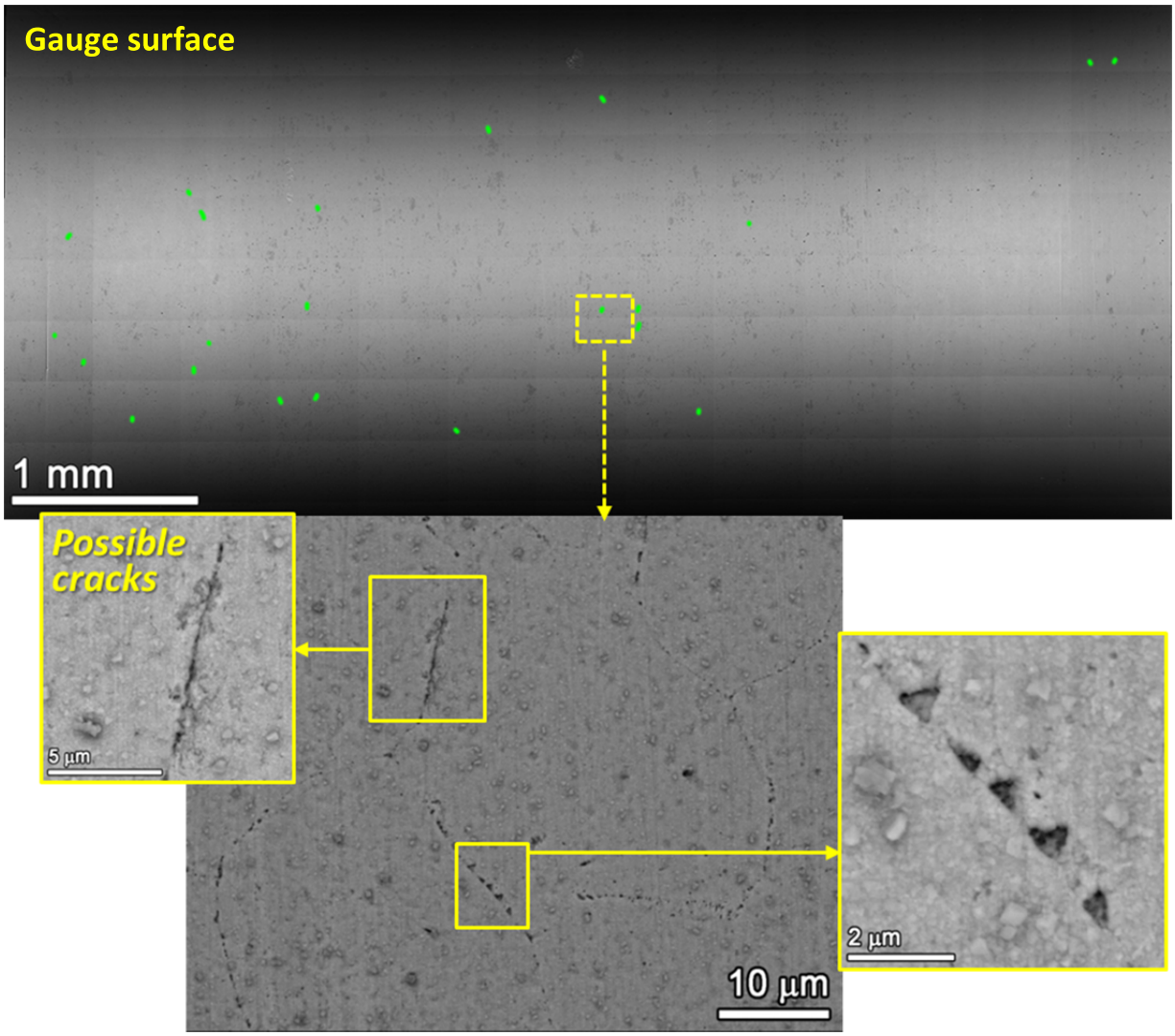

Figure 59. SEM-BSE montage images of the gauge surface are shown for one rotation of the 1 µm, 21%CF Sumitomo specimen IN033 after 9220 h of exposure. Possible cracks are highlighted in green and an example is shown in the high-magnification image. IG damage was also observed in the form of small holes or cavities along GBs intersecting the surface. No obvious cracks were found during the SEM surface examinations on this specimen.

A number of obvious cracks were also found in the 31%CF Valinox CRDM specimen IN036. Although the crack density is lower than for the 31%CF Sumitomo specimen IN033, the general morphology of the cracks appear similar with the largest one shown in the lower left of Figure 60, exhibiting a length of ~130 µm and a width of ~800 nm on the surface. On the other hand, no obvious or even what could be called possible cracks were observed in the 21%CF specimen IN027 (Figure 61) or the 11.7% specimen IN065 (Figure 62). However, very small holes or cavities were detected along a few high-energy GBs. The density of this damage was much lower than observed for the Sumitomo 21%CF specimen. A final observation was that isolated GBs intersecting the surface were decorated with dense spinels.

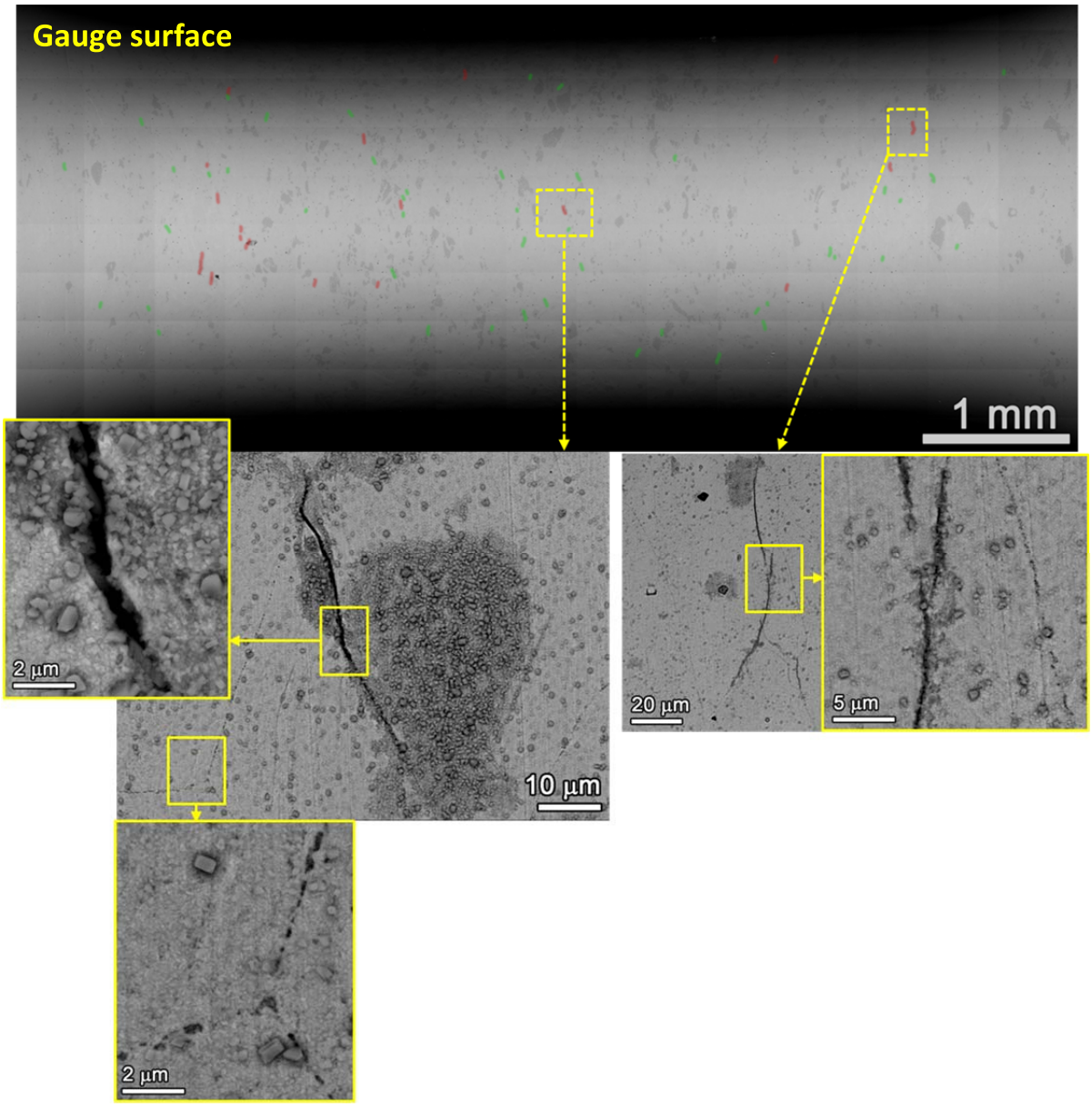

Figure 60. SEM-BSE montage images of the gauge surface are presented for one rotation of the 1 µm, 31%CF Valinox specimen IN036 after 9220 h of exposure. Obvious cracks are highlighted in red and possible cracks are highlighted in green.

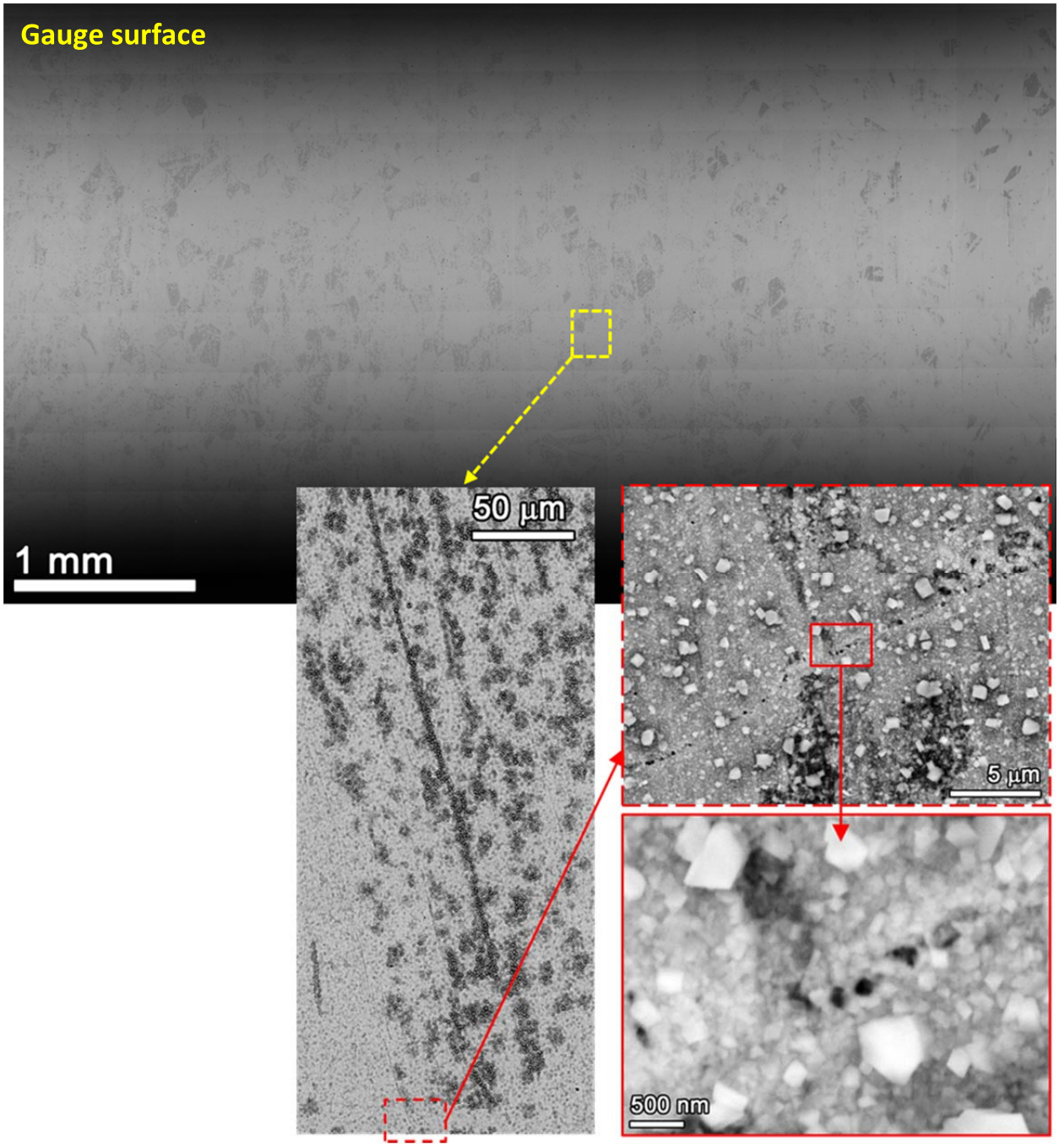

Figure 61. SEM-BSE montage images of the gauge surface are shown for one rotation of the 1 µm, 21%CF Valinox CRDM specimen IN027 after 9220 h of exposure. No definitive cracks on the surface were identified, however there was evidence for holes or cavities along a few GBs.

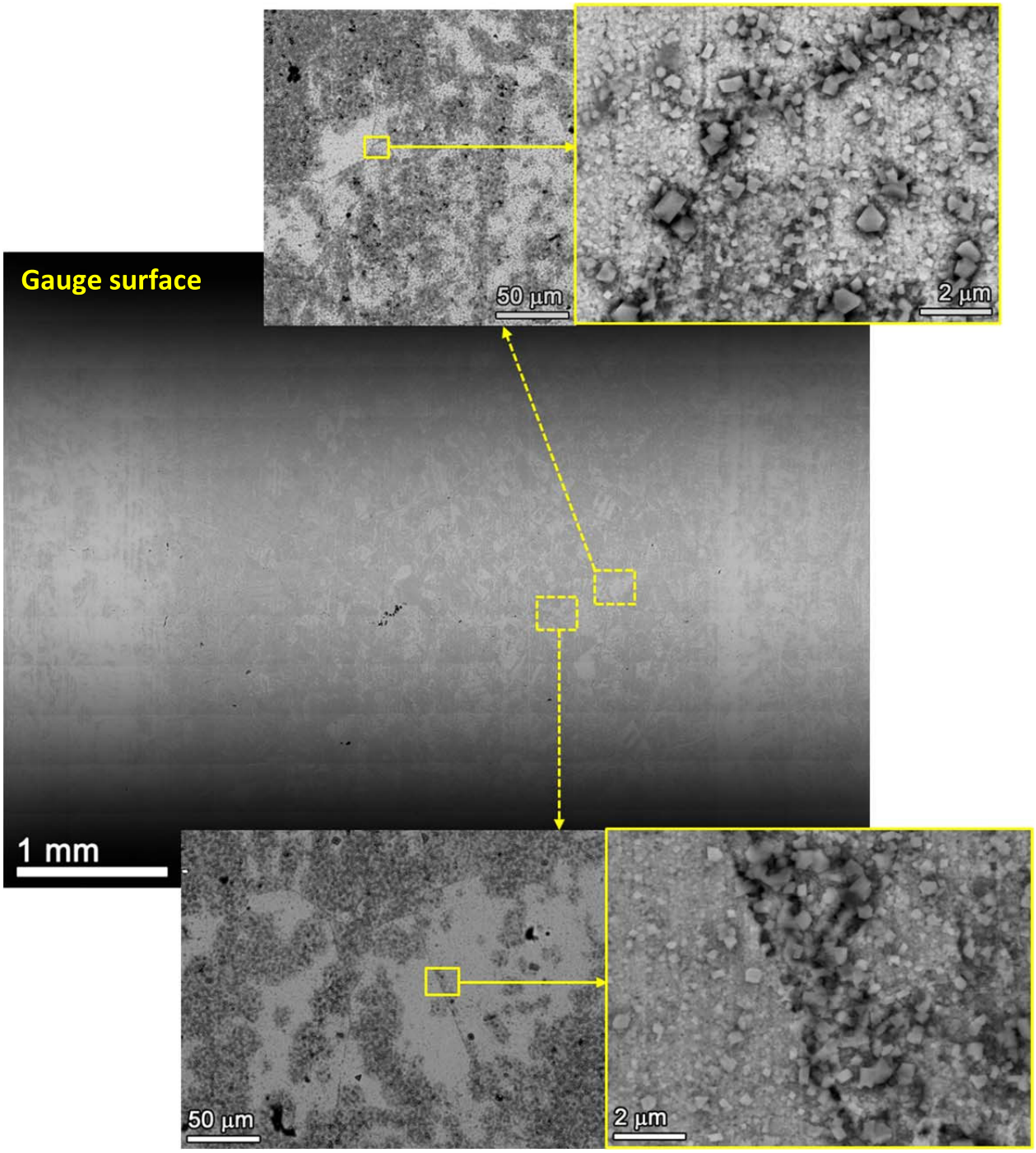

Figure 62. SEM-BSE montage images of the gauge surface are presented for one rotation of the 1 µm, 11.7%CF Valinox CRDM specimen IN065 after 7107 h of exposure. No definitive cracks on the surface were identified.

Obvious cracks were observed in the 31%CF Doosan CRDM specimen IN039 (Figure 63), but they are shorter and tighter in comparison to the cracks in the 31%CF Sumitomo specimen IN033 and the 31%CF Valinox specimen IN036. No cracks were resolved in the low-magnification montage image in the 21.6%CF Doosan CRDM specimen IN030, but higher-magnification images clearly revealed "postage stamp" GBs on the surface (Figure 64). Interestingly, the GB holes or cavities on this specimen surface appear to be larger and more rectangular in shape than those found in the 21%CF Sumitomo specimen IN024 and the 21%CF Valinox specimen IN027.

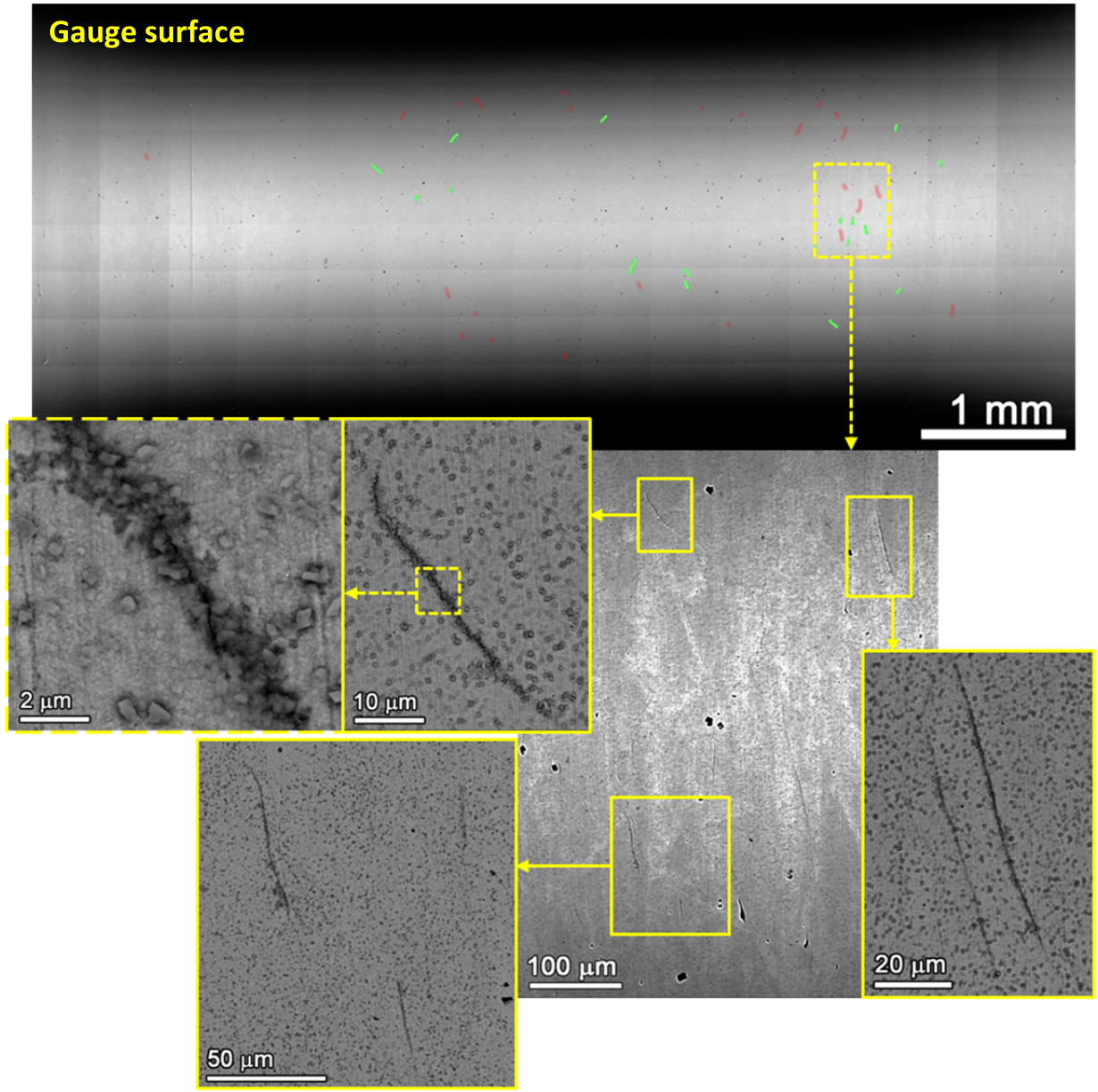

Figure 63. SEM-BSE montage images of the gauge surface are shown for one rotation of the 1 µm, 31%CF Doosan specimen IN036 after 9220 h of exposure. Obvious cracks are highlighted in red and possible cracks are highlighted in green.

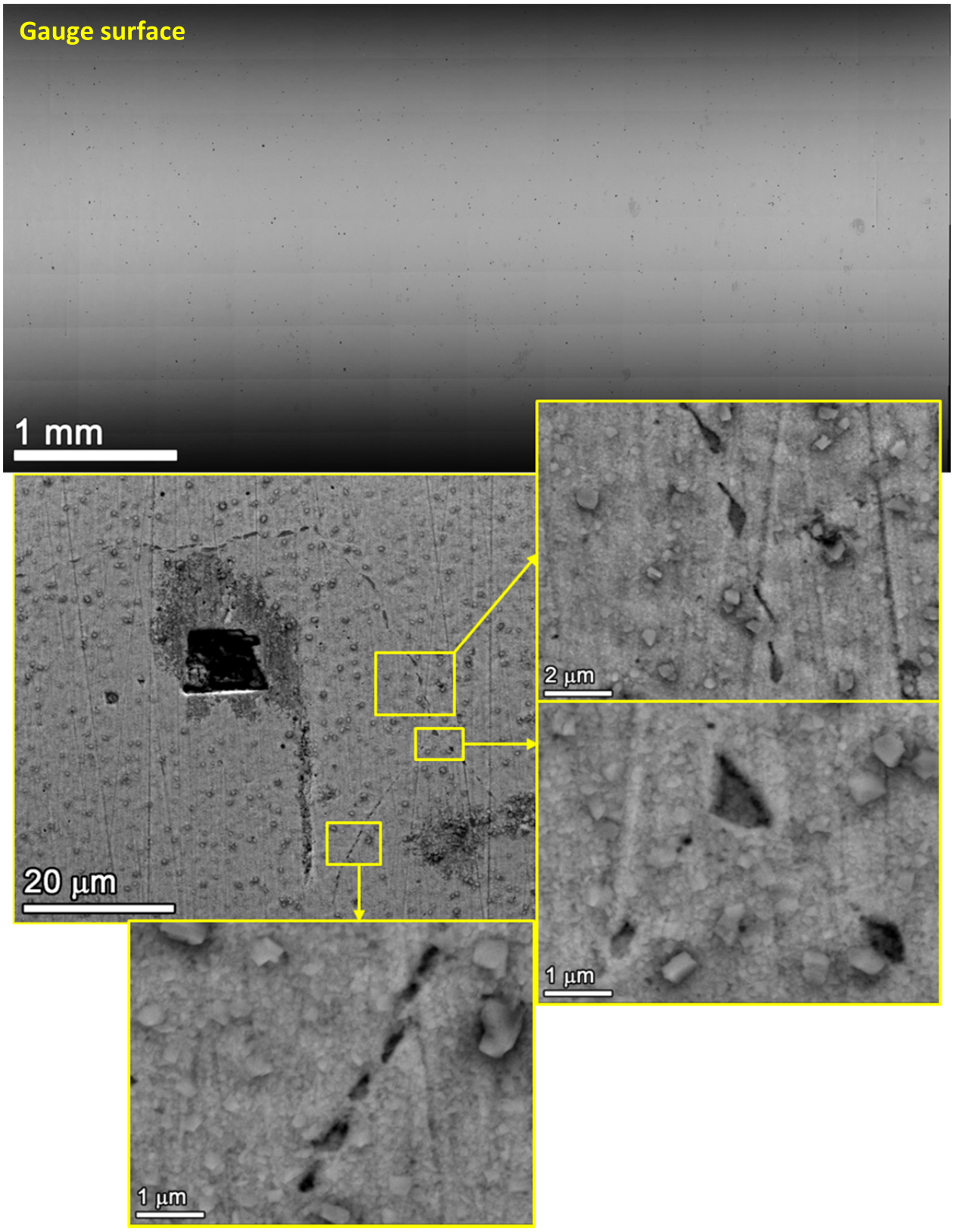

Figure 64. SEM-BSE montage images of the gauge surface are presented for one rotation of the 1 µm, 21.6%CF Doosan CRDM specimen IN030 after 9220 h of exposure.

A number of short IG damage features (possible cracks) were observed in the 31.9%CF TK-VDM plate specimen IN042 (Figure 65), but no obvious cracks as in the other three 31%CF specimens. In addition, a few "postage stamp" GBs were also observed in this specimen. The 21%CR TK-VDM plate specimen IN059 was tested in the second batch and had a shorter exposure time of ~7107 h. Surprisingly, the surface of this specimen is covered with a thick layer of oxide that obscured a clear identification of IG damage features (Figure 66).

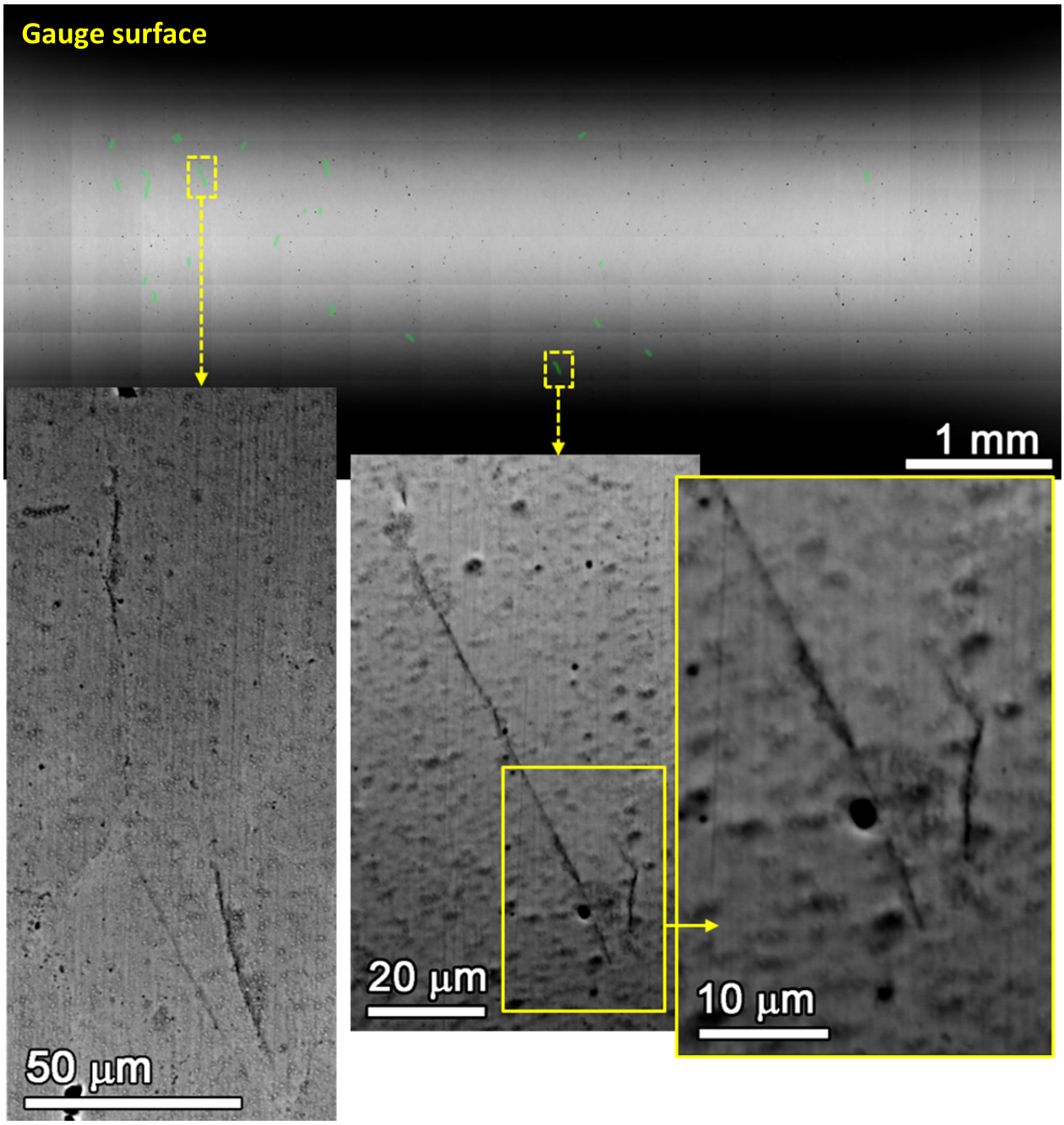

Figure 65. SEM-BSE montage images of the gauge surface of one rotation of the 1 µm, 31.9%CF TK-VDM plate specimen IN042 after 9220 h of exposure. Possible cracks are highlighted in green (no obvious crack were found).

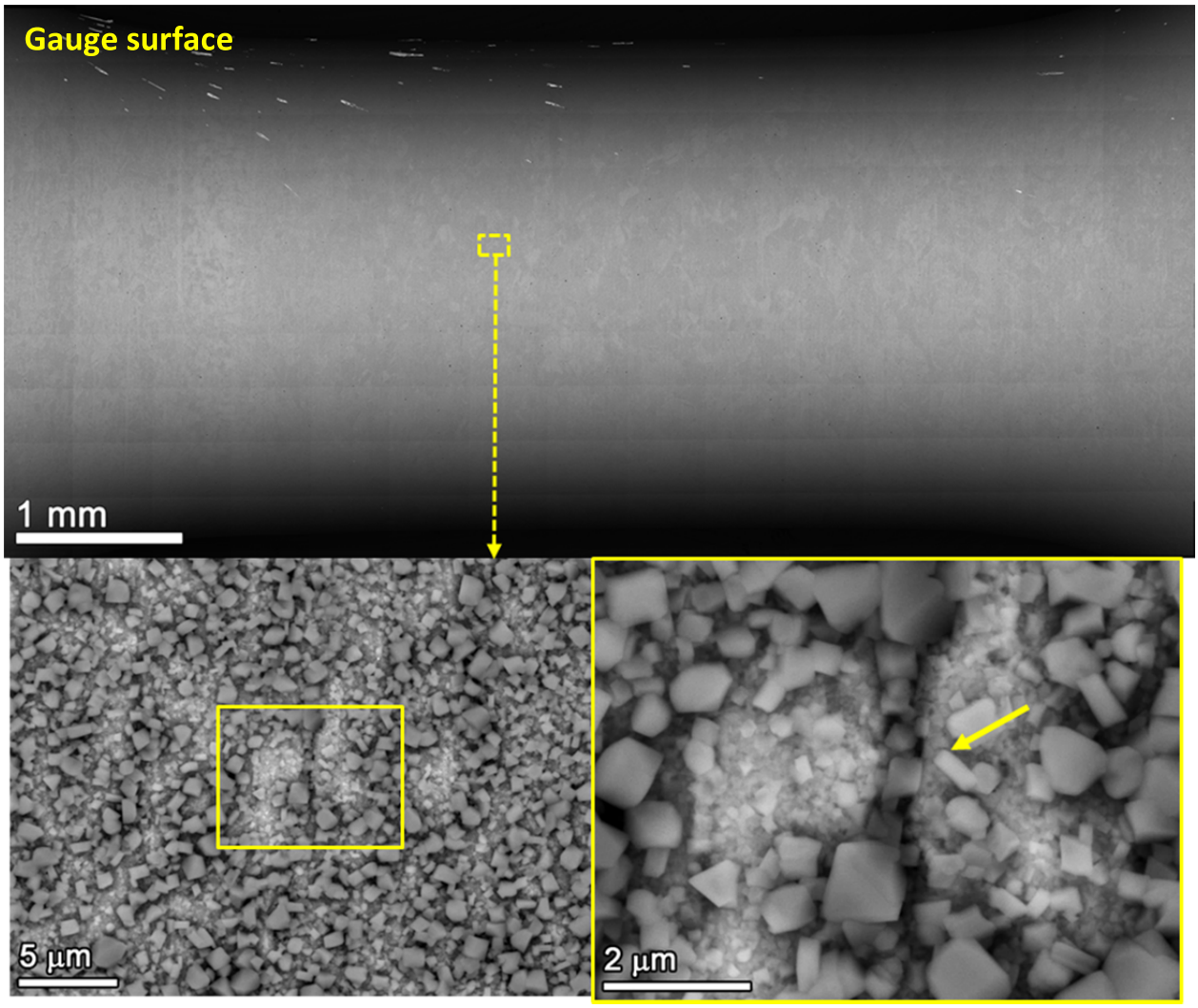

Figure 66. SEM-BSE montage images of the gauge surface are shown for one rotation of the 1 µm, 21%CR TK-VDM plate specimen IN059 after 7107 h of exposure. No surface cracks were detected, but a thick layer of oxide is present that obscured detailed observations of possible surface damage.

The 26%CR ANL flat bar specimen IN053 features a distinctively different surface morphology with extensive transgranular (TG) TiN second phase particles that appear to be favored sites for crack nucleation (Figure 67). These TiN particles are often present in stringers and are often cracked during initial cold rolling as described earlier in this report. The higher-magnification images in the lower right of Figure 67 reveal additional cracking and corrosion formed at single cracked TiN particles or along multiple TiN particles within a stringer. However, previous SCC initiation testing and microstructural characterizations indicated that the cracks associated with these TiN particles had remained shallow (a few micrometers) even after aggressive loading and an exposure time reaching ~10000 h [3]. Similar to the TK-VDM plate, obvious IG surface cracks were not identified on the gauge surface.

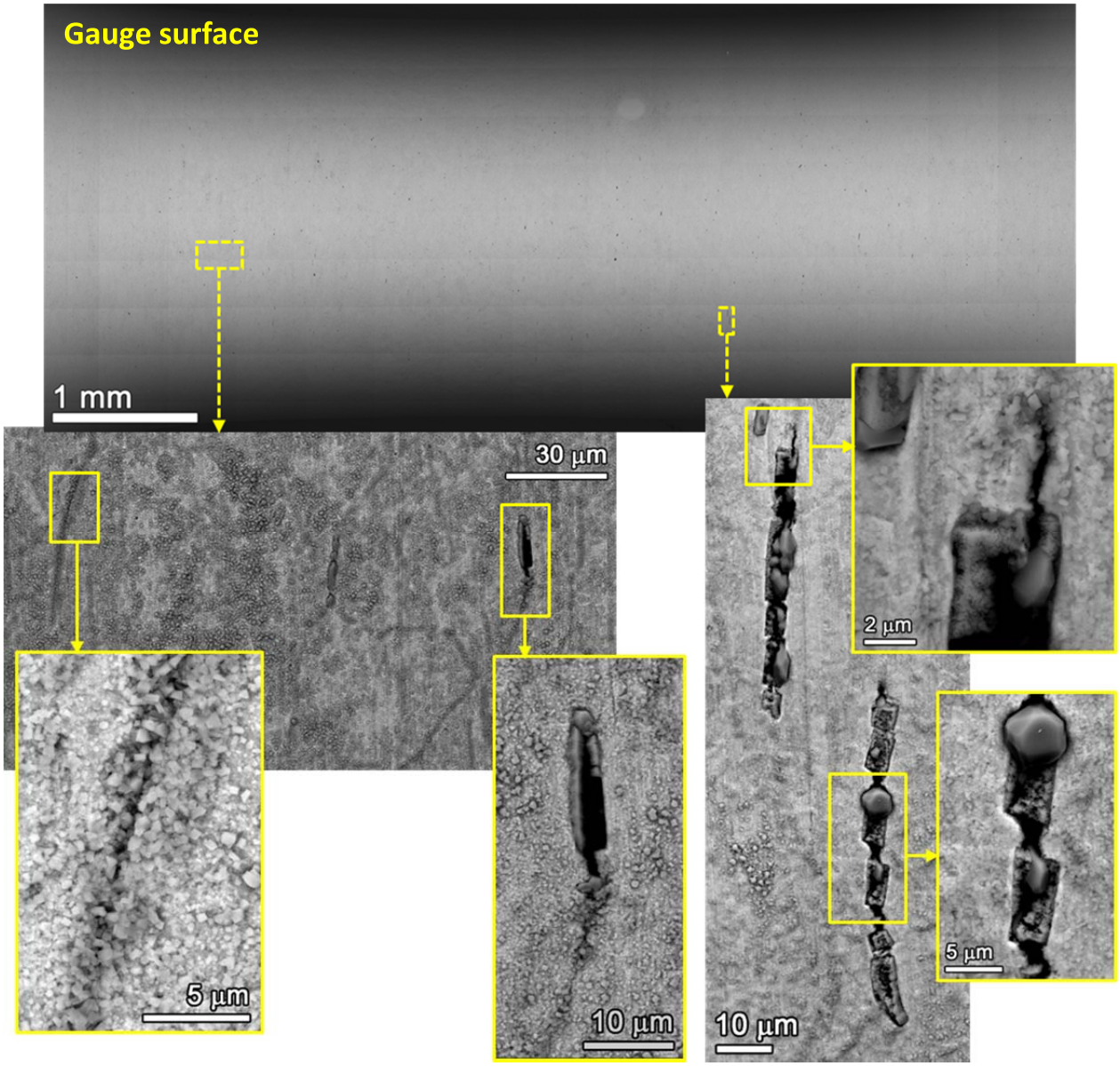

Figure 67. SEM-BSE montage images of the gauge surface are presented for one rotation of the 1 µm, 26%CR ANL plate specimen IN053 after 7107 h of exposure.

The gauge surface of the two GE B25K bar specimens IN056 (18.3%CF) and IN062 (12.6%CF) did not reveal any IG or TG damage features as illustrated in Figures 68 and 69. These specimens were also covered with a higher density of oxides that made imaging difficult even at higher magnifications.

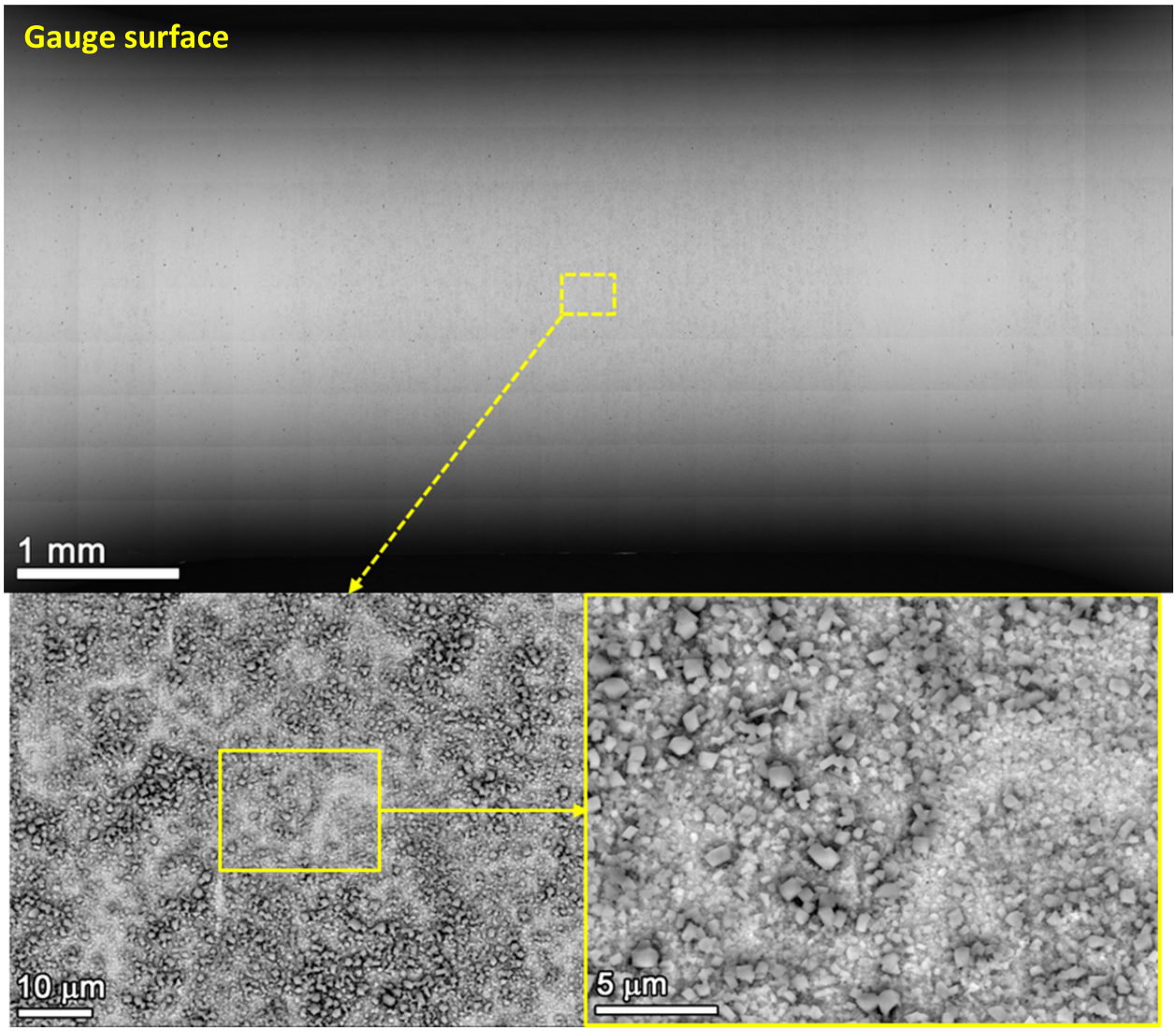

Figure 68. SEM-BSE montage images of the gauge surface are shown for one rotation of the 1 µm, 18.3%CF GE B25K bar specimen IN056 after 7107 h of exposure. No surface cracks were detected, but a relatively thick layer of oxide is present that obscure detailed observations of possible surface damage.

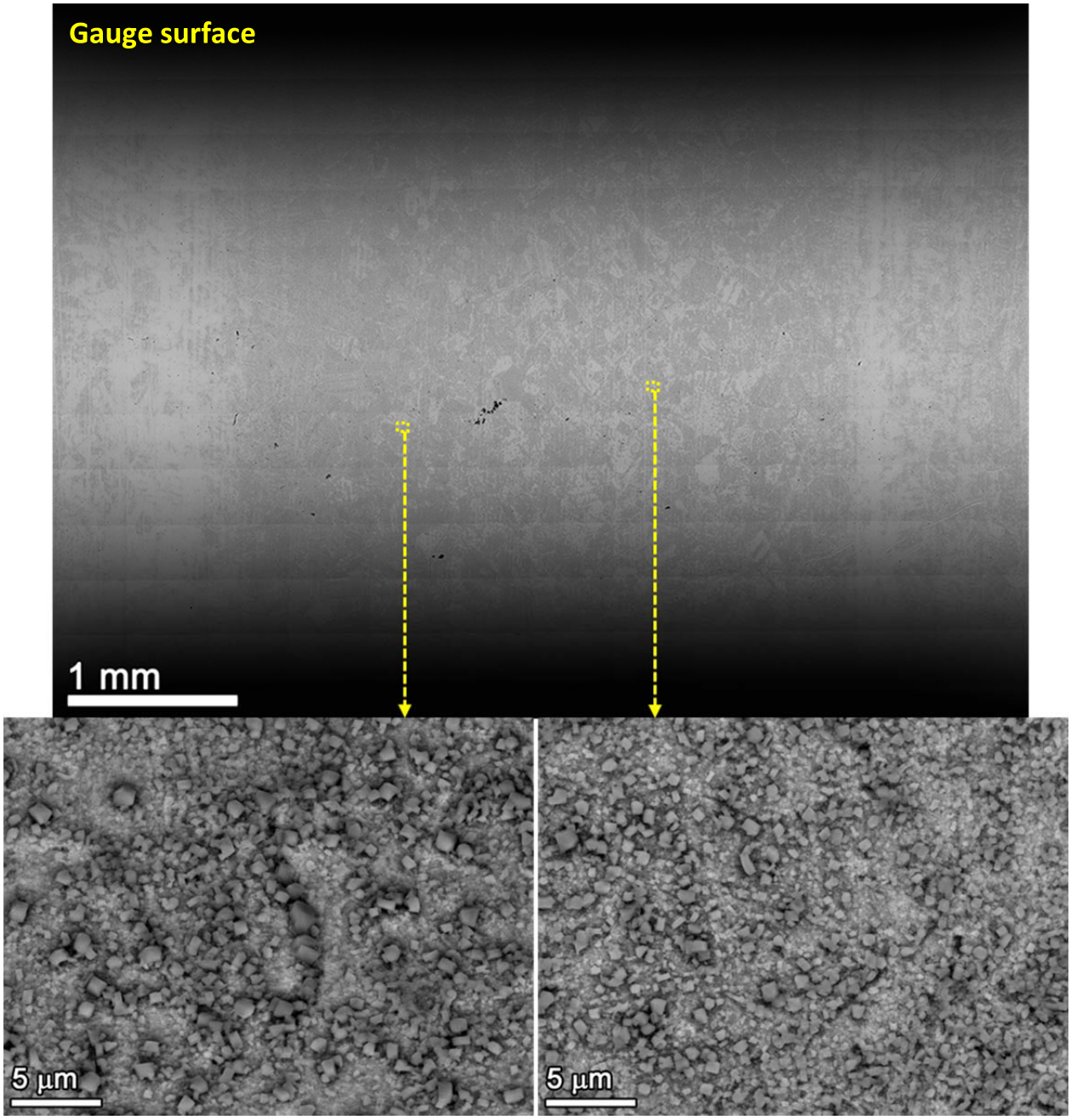

Figure 69. SEM-BSE montage images of the gauge surface are presented for one rotation of the 1 µm, 12.6%CF GE B25K bar specimen IN062 after 7107 h of exposure. No surface cracks were detected, but once again a thick layer of oxide is present that obscured detailed characterization of possible surface damage.

In summary, the density of surface cracks clearly decreased in every heat as the cold work level was dropped from ~30 to ~20% and the applied stress was reduced. While obvious and possible cracks can be mapped in all the ~30%CW specimens (Figures 58, 60, 63 and 65), no definitive cracks were found in any of the materials with a cold work level less than or equal to 21% except

the 21%CF Sumitomo specimen (Figure 59). The IG cracks that were consistently found in the highly polished 31%CF specimen in every heat have, for the first time, provided solid evidence that crack nucleation can take place in highly CW alloy 690 materials under constant load. Prior observations have been complicated by the application of dynamic straining in either slow-strain-rate tensile tests or blunt notch compact tension tests.

Another critical result is that the degree of surface cracking and the crack morphology differs among the various CRDM, bar and plate heats in the highly CW condition. In general, the three CRDM heats (Sumitomo, Valinox and Doosan) exhibit more IG cracks than the bar and plate materials, among which the Sumitomo CRDM heat (Figures 58 and 59) being the most susceptible to GB cavity formation and IG crack nucleation. The CRDM specimens also showed a large amount of distinct "postage stamp" features where high-energy GBs intersecting the surface are delineated by nano-size discrete holes or cavities (Figures 59, 60-62 and 64). One important difference for the Sumitomo and Valinox CRDM materials is the starting TT microstructural condition with a semi-continuous distribution of small and more uniform distribution of GB Cr carbides. This GB microstructure appears more susceptible to GB cavity formation in the CW condition. However, additional research is clearly needed to confirm the material issues controlling the observed behavior.

FIB Examination on Selected CLT Specimens

FIB trenching was employed for the 31%CF Sumitomo specimen IN033 and the 31%CF Valinox specimen IN036 to examine the cracks in profile. This has been proved to be an efficient and non-destructive characterization method for the specimens that can be returned to testing [3]. Trenches were first made to intersect IG cracks with various surface lengths to check the depth and subsurface morphology of these cracks. Quite surprisingly, results shown in Figures 70 and 71 revealed that many IG cracks had already exceeded 15 μm in depth (beyond the depth of the FIB trenches) at locations relatively far from the crack center so the depth observed in the trench is expected to be much shallower than at the crack center. Nano-sized GB cavities were usually present inside these deep cracks, whereas shallower and tighter cracks were found to end at GBs containing a distribution of similar cavities. In the attempt to better characterize IG depth evolution and cavity distribution, serial FIB milling was then performed on a few cracks with an example provided in Figure 72. As shown in Figure 72(a), a trench was produced examining a tight IG crack in IN033 on a high-energy GB exhibiting "postage stamp" appearance. GB cavities were readily visible beneath the surface in this section of the GB, and were linked to the onset of the IG cracking (Figure 72b). Cavities continued to be seen at the tip of the IG crack (Figure 72c) as it deepens along the GB. During the stages presented in Figure 72(d) where the crack depth extended beyond the bottom of the trench, GB cavities were sporadically found inside the crack suggesting they are directly associated with crack nucleation and propagation.

Serial FIB milling was also conducted on the 1 μm finish, 21%CF Sumitomo CRDM specimen IN024 to investigate subsurface morphology of the "postage stamp" GBs. As shown in Figure 73, the nano-sized holes observed on the surface are always linked to near-surface cavities that appeared to be oxidized. Meanwhile, isolated cavities were also frequently found along the GB beneath the surface during the FIB milling process. Therefore, the small holes or cavities along GBs on the surface are likely part of the distribution of sub-surface GB cavities extending to the surface.

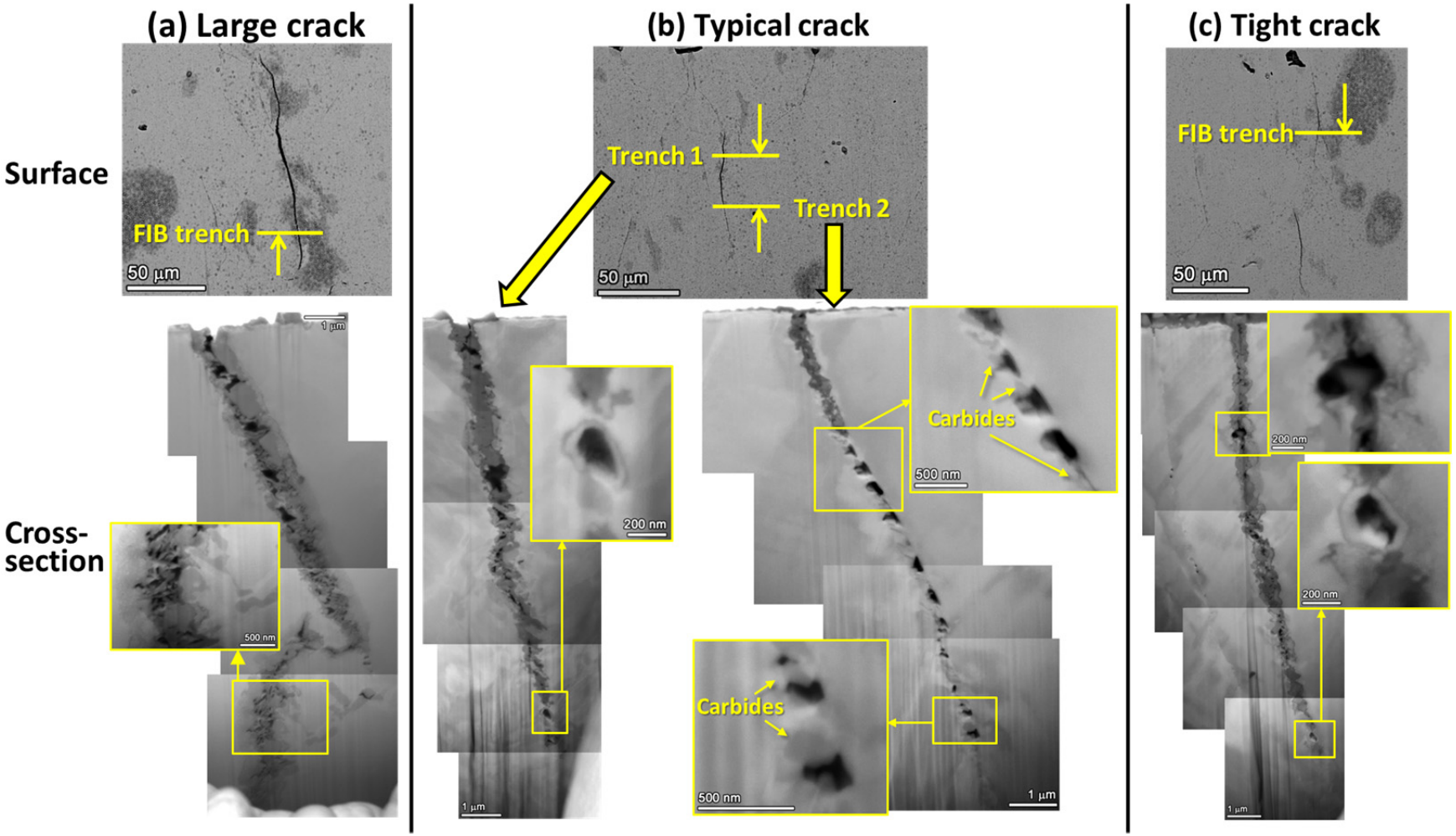

Figure 70. SEM-BSE images of the morphology of cracks in cross-sections created by FIB in the 1 µm finish, 31%CF Sumitomo CRDM specimen IN033.

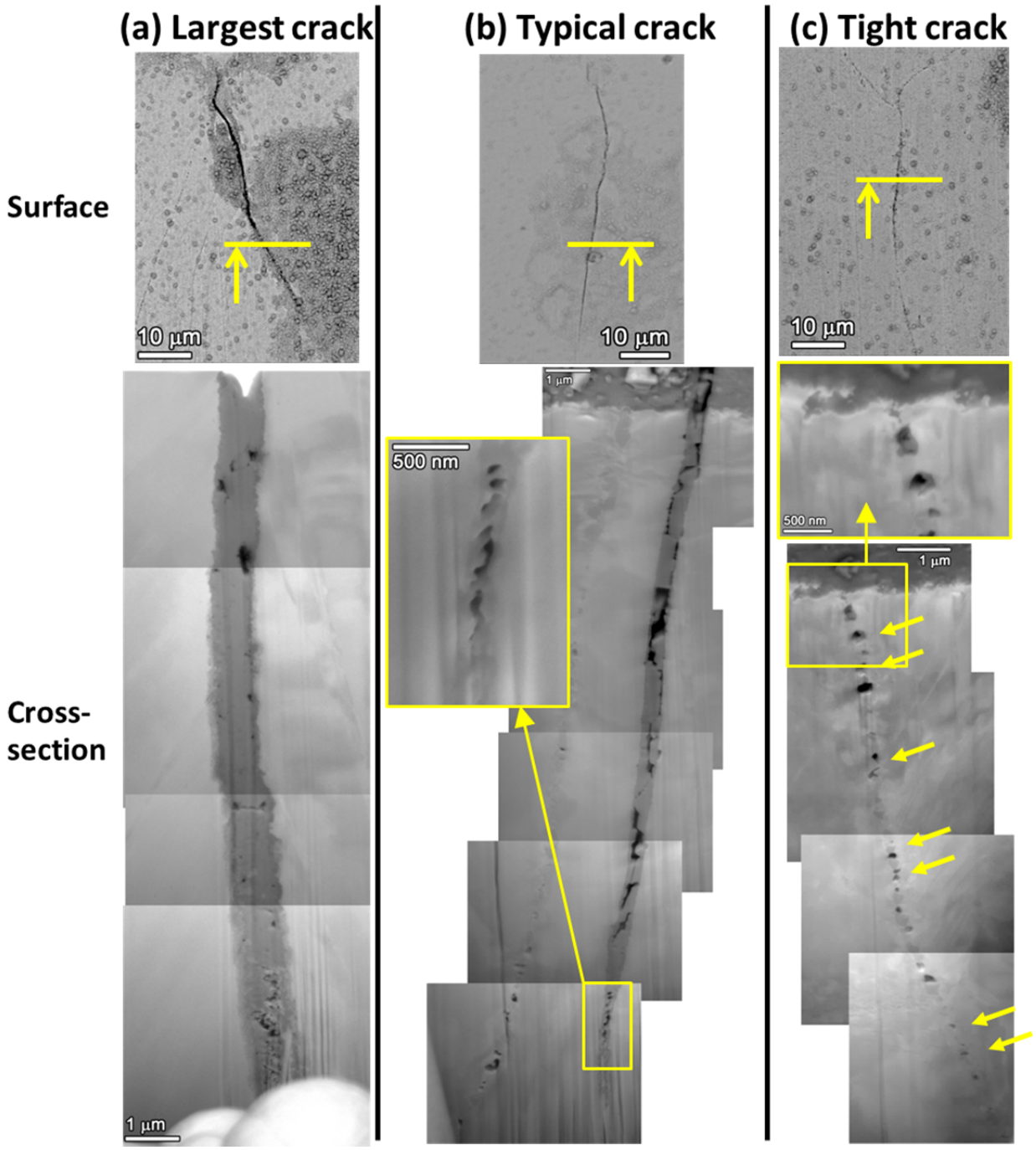

Figure 71. SEM-BSE images of the morphology of cracks in cross-sections created by FIB in the 1 µm finish, 31%CF Valinox CRDM specimen IN036.

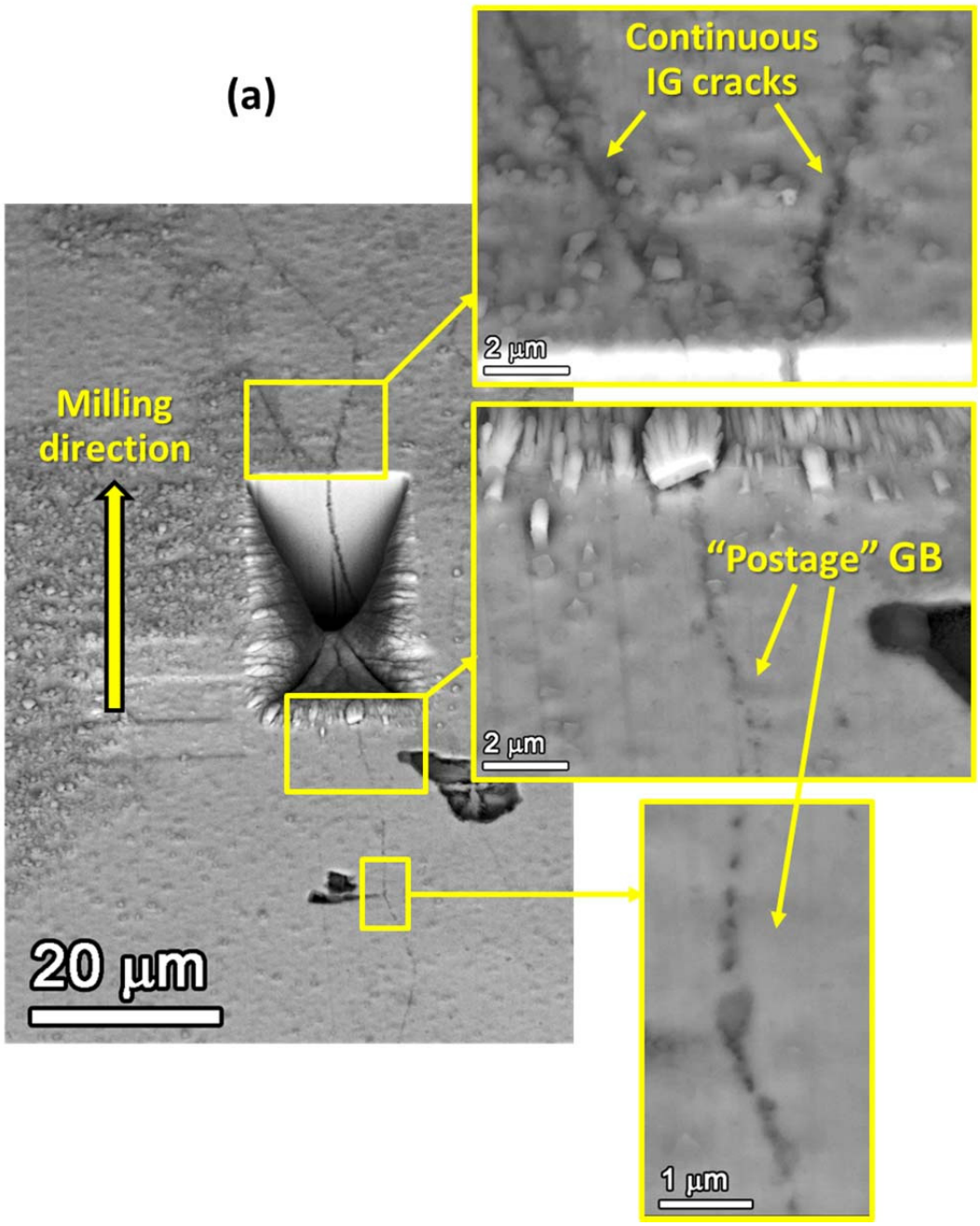
(a)
Continuous
IG cracks
2 µm
Milling
direction
"Postage" GB
2 µm
20 µm
1 µm

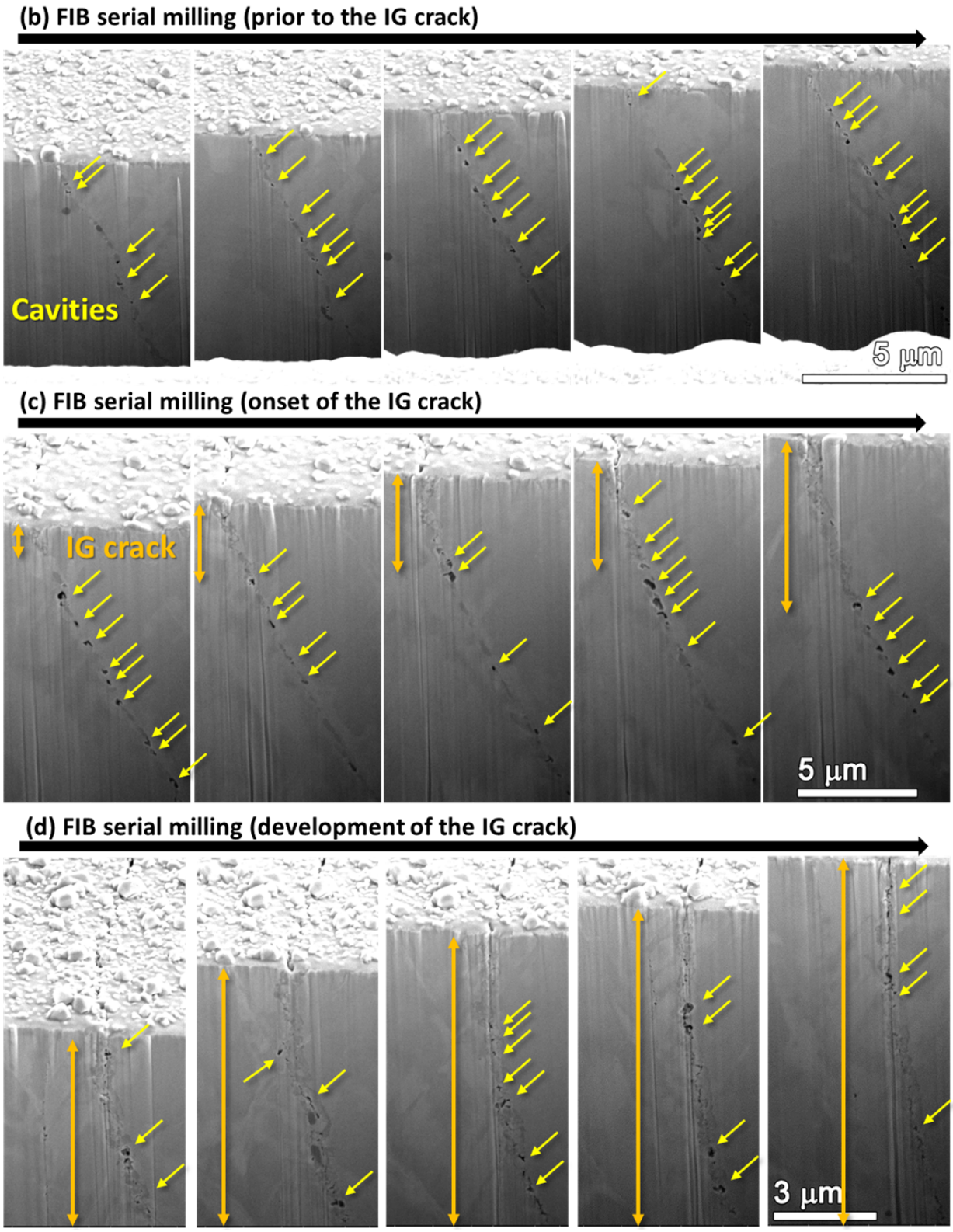

Figure 72. Serial FIB milling along a tight crack in IN033 with (a) view of the region after completion of FIB milling on the surface and (b, c and d) cross-sections revealed during serial FIB milling showing cavities (highlighted by arrows) and IG crack evolution along the milling direction.

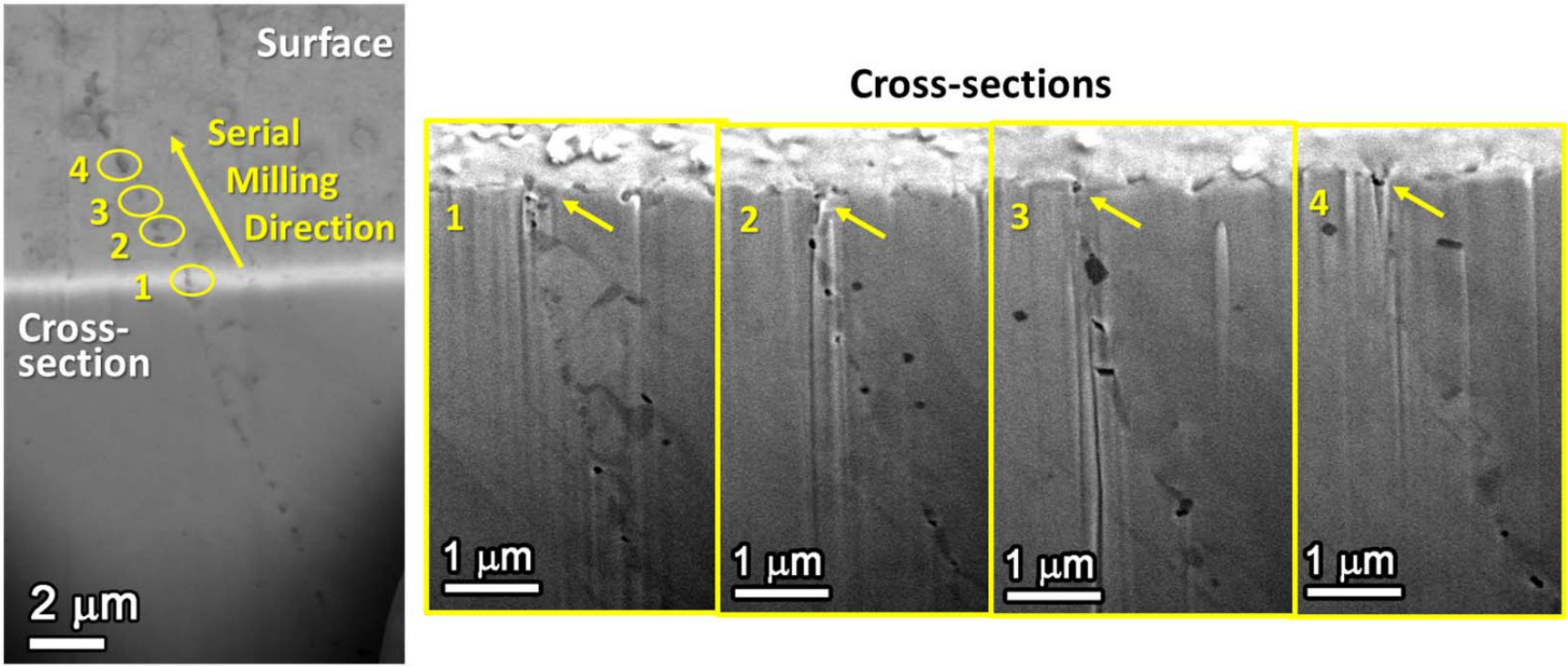

Figure 73. Serial FIB milling along a "postage" GB in IN024 showing the cross-sections intersected by FIB at the four locations marked on the gauge surface where nano-sized hole was observed.

GB Cavity Distributions in CLT Specimen Cross-Sections

Based on the results of surface examination and serial FIB milling, a thorough examination of GB cavity distribution in the bulk materials became of high interest. Since the highly polished specimens have the advantage to allow crack evolution on the gauge surface being tracked over time while the rough surface of the ground samples made it very difficult to identify cracks on the surface, decision was made to discontinue initiation testing and cross-section selected ground specimens. Thirteen specimens (Table 11) were removed including 12 ground specimens from each heat and cold work combination, as well as the 1 μm finish 31%CF Sumitomo CRDM specimen that showed the most extensive IG cracks on the gauge surface. These specimens were sectioned in half along the axial direction and the two halves were polished to a colloidal silica finish. High-keV BSE montage imaging was performed on the entire gauge cross-sections as indicated in Figure 74. Higher resolution images were then taken at a number of sites that appear to contain GB cavities based on indications from the montage images. These sites were near the mid-position of the gauge and were selected such that they are uniformly separated from each other across the entire thickness of the gauge section, allowing cavity morphology to be examined as a function of distance from the gauge surface. Meanwhile, similar cross-section characterizations were also performed in the higher CW specimens across the thickness of the long shoulder as indicated in Figure 74, covering an area of ~8×1 mm in size. This shoulder location is under a much lower stress (~15% of the yield stress) than the gauge section. In this way, an indication of applied stress effects on GB cavity formation and growth can be assessed within the same CLT specimen.

Table 11. CLT Specimens Removed for Destructive Examinations.

Specimen	Material	Material Condition	Surface Condition	Applied Stress, MPa	Exposure Time (h)
IN033 (CL)	Sumitomo CRDM	TT + 31%CF	1 μm Polish	710	9220
IN034 (CL)	Sumitomo CRDM	TT + 31 %CF	Ground C Finish	710	9220
IN026 (CL)	Sumitomo CRDM	TT + 21%CF	Ground C Finish	510	9220
IN038 (CL)	Valinox CRDM	TT + 31%CF	Ground C Finish	720	9220
IN029 (CL)	Valinox CRDM	TT + 21%CF	Ground C Finish	525	9220
IN067 (CL)	Valinox CRDM	TT + 11.7%CF	Ground C Finish	365	7107
IN041 (CL)	Doosan CRDM	TT + 31%CF	Ground C Finish	685	9220
IN032 (CL)	Doosan CRDM	TT + 21.6%CF	Ground C Finish	555	9220
IN044 (CL)	TK-VDM Plate	TT + 31.9%CF	Ground C Finish	700	9220
IN061 (CL)	TK-VDM Plate	TT + 21%CR	Ground C Finish	675	7107
IN055 (CL)	ANL Flat Bar	MA + 26%CR	Ground C Finish	775	7107
IN058 (CL)	GE B25K Bar	MA + 18.3%CF	Ground C Finish	550	7107
IN064 (CL)	GE B25K Bar	MA + 12.4%CF	Ground C Finish	510	7107

The GB cavity morphology as a function of distance to the gauge surface for the three Sumitomo CRDM specimens IN033 (31%CF, 1 μm finish), IN034 (31%CF, ground C finish) and IN026 (21%CF, ground C finish) are shown in Figures 75-77, respectively. Eight sites were chosen in each specimen where high magnification images were taken, providing a rough overview of the GB cavity distribution across the gauge diameter. In all three specimens, aggregations of dense GB cavities were found randomly distributed throughout the gauge thickness indicating creep damage had taken place uniformly in the gauge. Nevertheless, a decreasing trend in the size and

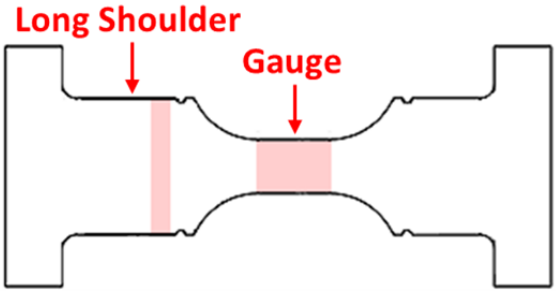

Figure 74. Schematic of the initiation tensile specimen cross-section illustrating the areas where montage images were taken (highlighted in shades).

density of GB cavities was clearly revealed with the decrease in cold work level, as well as with the change in surface condition for the 31%CF Sumitomo specimens. In the polished 31%CF specimen IN033, relatively large cavities (~200–500 nm in size) were frequently observed to aggregate at high-energy GBs extending to lengths of >50 μm (Figure 75). In comparison, the aggregation of cavities in the 31%CF ground C finish specimen IN034 were shorter, usually no more than 30 μm long, and the size of cavities were smaller (Figure 76). The cavities observed in the 21%CF ground C finish specimen IN026 were isolated and aggregations of cavities were only seen along short sections of GBs (<5 μm long) covering a few neighboring GB carbides. While most cavities in the two 31%CF specimens are spheroidal/oval, cavities in this 21%CF specimen appear to be smaller and more faceted or flat in shape (Figure 77). Since "mature" cavities tend to grow into spheroids to reduced surface energy, the irregular shape observed in IN026 might be an indication of ongoing slower creep evolution in this moderately CW material at a lower applied stress. The difference in the morphology and distribution of the GB cavities in these three specimens can be more clearly viewed in Figure 78(a), where high-resolution images on cavities near the gauge center in each specimen are shown at the same scale.

The more significant difference associated with surface finish was the distribution of cavities near the gauge surface. As shown in Figure 78(b), cavities extended to the surface where IG cracks were found in the polished 31%CF specimen IN033. By contrast, cavities were never observed in the nanocrystalline layer produced during grinding in the two ground specimens IN034 and IN026, but were found at some high-energy GBs immediately beneath this damage layer. More detailed examples are given in Figure 79 accompanied with a montage image near the gauge surface for one cross-section of the 31%CF ground C finish specimen IN034 showing locations at which the high-resolution observations were made. Three variations of typical near surface damage were evidenced: IG cavities on high-energy GBs immediately adjacent to the nanocrystalline layer (site 1), shallow cracks confined in the nanocrystalline layer (site 2) and a combination of the above two (site 3). In particular, cracks in the ground specimens were all observed to turn toward a direction parallel to the applied stress when reaching the interface between the damage layer and the bulk (Figure 80). Although industry experience suggests that surface CW layer is detrimental to SCC initiation resistance in alloy 600, it seems that in current study the surface damage layer delayed crack propagation into the bulk for CW alloy 690. Clearly, the damage layer blocked the formation of a semi-continuous distribution of GB cavities reaching the surface that promotes IG crack nucleation. SCC initiation testing has been restarted on the remaining polished and ground specimens, and the evolution of cracks in the ground samples will continue to be evaluated.

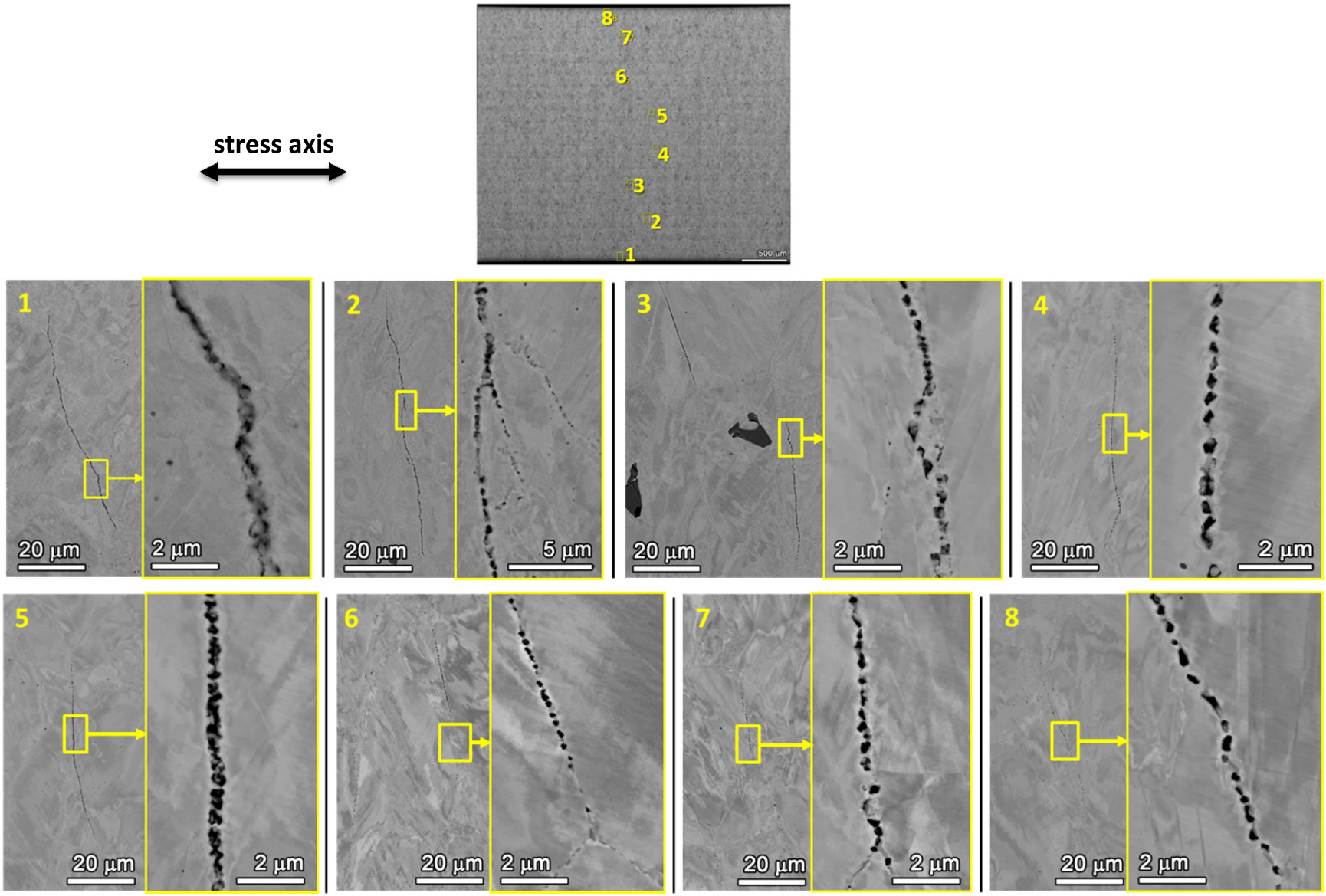

Figure 75. Morphology of GB cavities at selected sites across the gauge thickness in the polished 31%CF Sumitomo CRDM specimen IN033 after 9220 h of exposure.

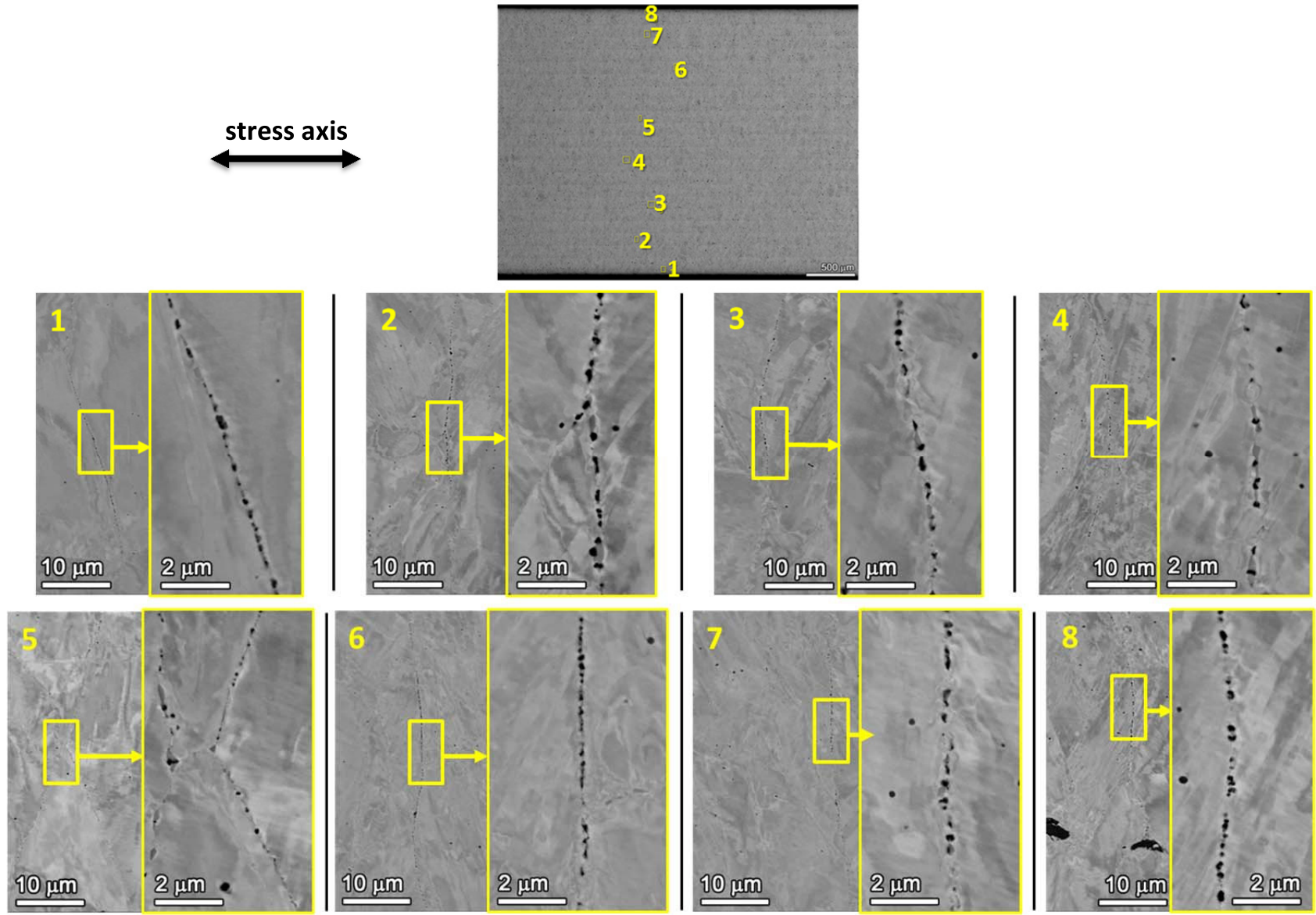

Figure 76. Morphology of GB cavities at selected sites across the gauge thickness in the ground 31%CF Sumitomo CRDM specimen IN034 after 9220 h of exposure.

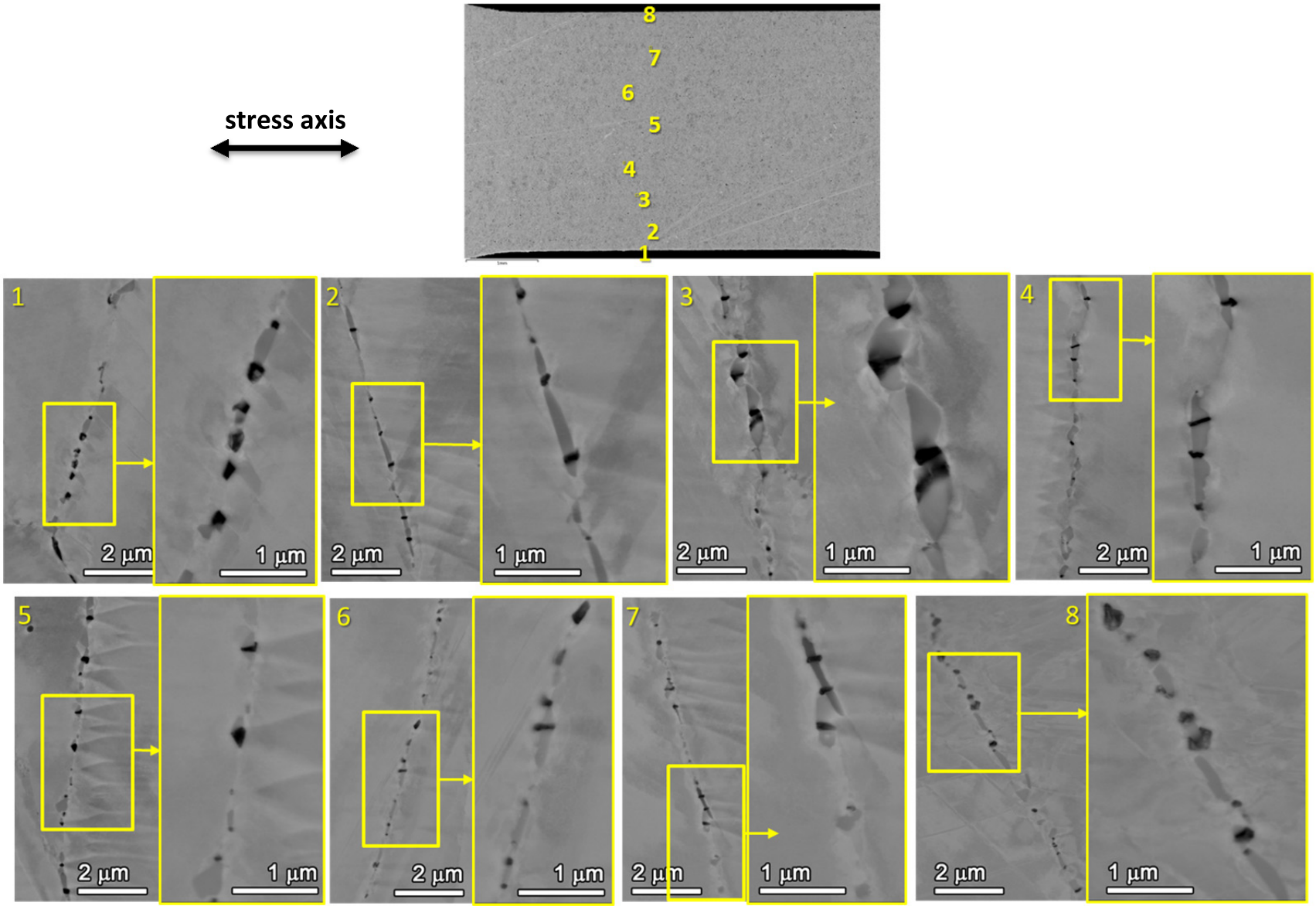

Figure 77. Morphology of GB cavities at selected sites across the gauge thickness in the ground 21%CF Sumitomo CRDM specimen IN026 after 9220 h of exposure.

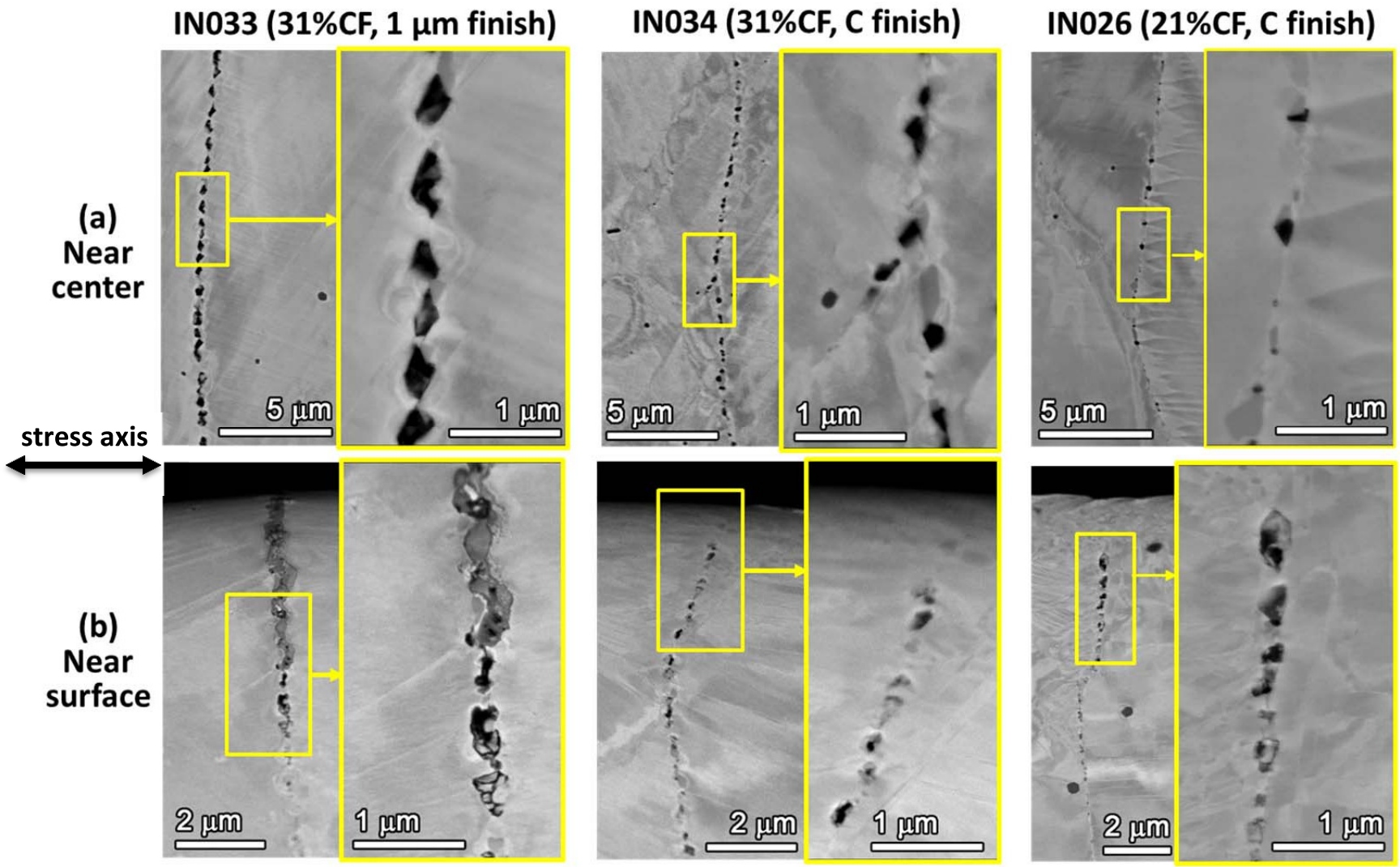

Figure 78. Comparison of the morphology of GB cavities in the three CW Sumitomo CRDM specimens IN033, IN034 and IN026 after 9220 h of exposure.

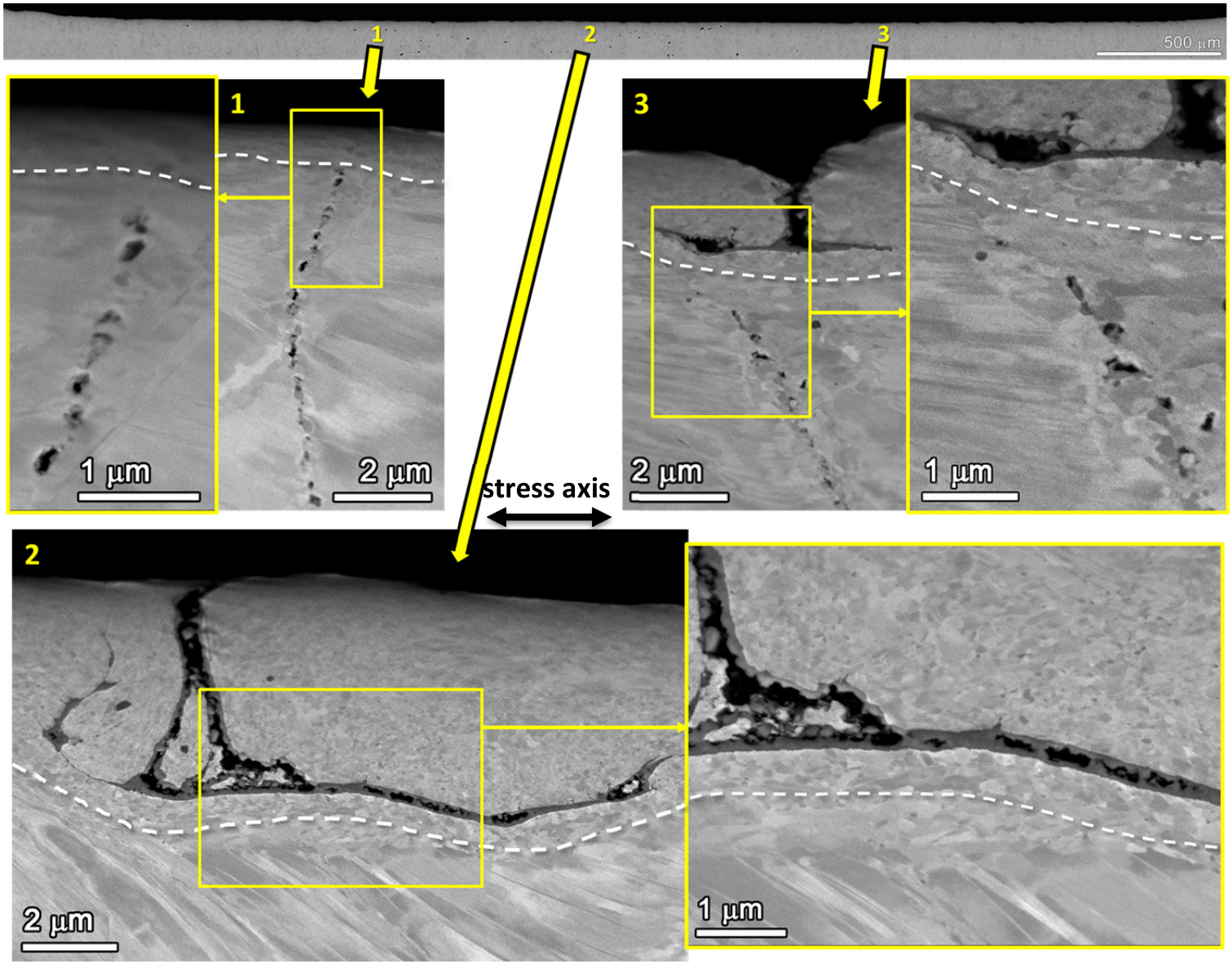

Figure 79. SEM-BSE images of typical morphology of near surface damage in one cross-section of the 31%CF Sumitomo CRDM ground specimen IN034. The interface between the nanocrystalline damage layer and the bulk is delineated by dashed curves.

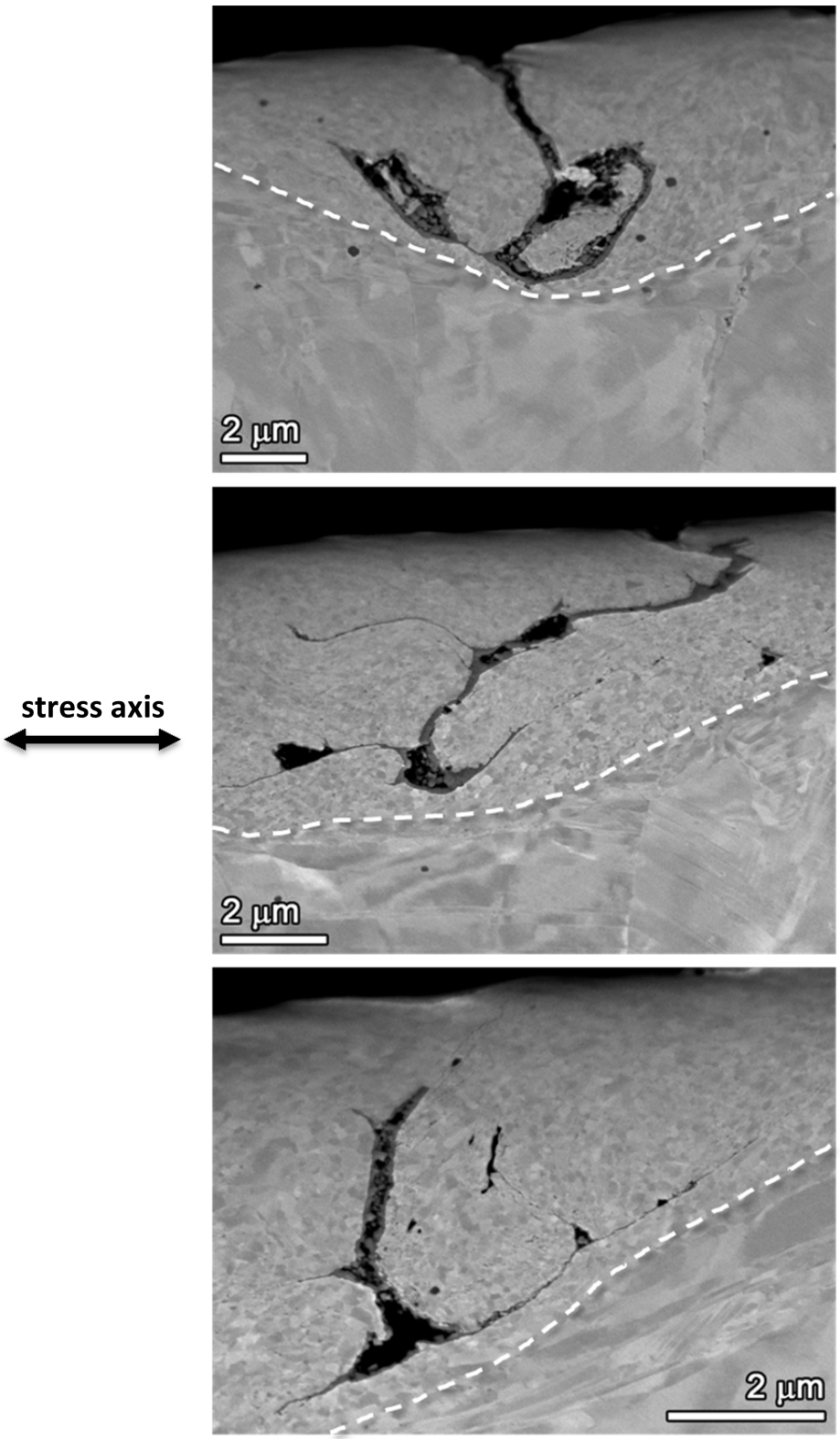

Figure 80. SEM-BSE images of near-surface cracks observed in the 31%CF Sumitomo ground specimen IN034 with the interface between the nanocrystalline damage layer and the bulk delineated by dashed curves. All cracks were confined within the damage layer induced by grinding.

A direct correlation was identified between surface IG cracks and near-surface GB cavities in the polished 31%CF specimen IN033 and many IG cracks were identified on the surface. As shown in Figure 81, every IG surface crack intersecting the polishing plane could be linked to a series of near-surface cavities along the same GB in cross-section. Two examples are shown at higher magnifications illustrating cavities ahead of two shallow cracks (one ~300 nm deep and one ~4 μm deep). In addition, serial polishing revealed a small crack of a surface length of ~50 μm with a depth of ~30 μm (Figure 82a). Additional smaller cracks were also intersected again confirming the presence of GB cavities ahead of the crack tip. Of particular interest is an oxidized cavity highlighted in Figure 82(c) where no direct connection to the surface can be seen. Higher SEM accelerating voltage (15 keV) was employed to image the same area and revealed a denser distribution of GB cavities below the observation plane with cracks linked to the surface. The oxidized cavity observed at 5 keV is most likely the result of water ingress through a complex 3D crack. Serial FIB milling and serial polish + SEM examinations are continuing to document 3D distributions of near-surface cavities and crack depth profiles to better understand nucleation and short crack growth processes.

As noted earlier, cavity distributions were also examined for the highly CW specimens in the long shoulder where the applied stress is ~15% to that in the gauge section. Results of this characterization for the two 31%CF Sumitomo specimens IN033 and IN034 are summarized in Figures 83 and 84, respectively. Representative images are compared between cavity morphology in the shoulder and in the gauge at the same magnifications. Obviously, the degree of GB cavitation in the shoulder is very low with only a few, sporadic cavities at high-energy GBs. In comparison, many GBs in the gauge section have a semi-continuous distribution of cavities reaching tens of micrometers in length. The sizes of the cavities in the gauge section are also much larger (usually >5X) than those observed in the shoulder. In fact, GB cavities in the shoulder are very similar in size and distribution to the permanent damage induced by cold work prior to testing (Figure 11). This indicated that the cavity formation and growth are negligible under this low applied stress even after up to 9,220 hours of exposure.

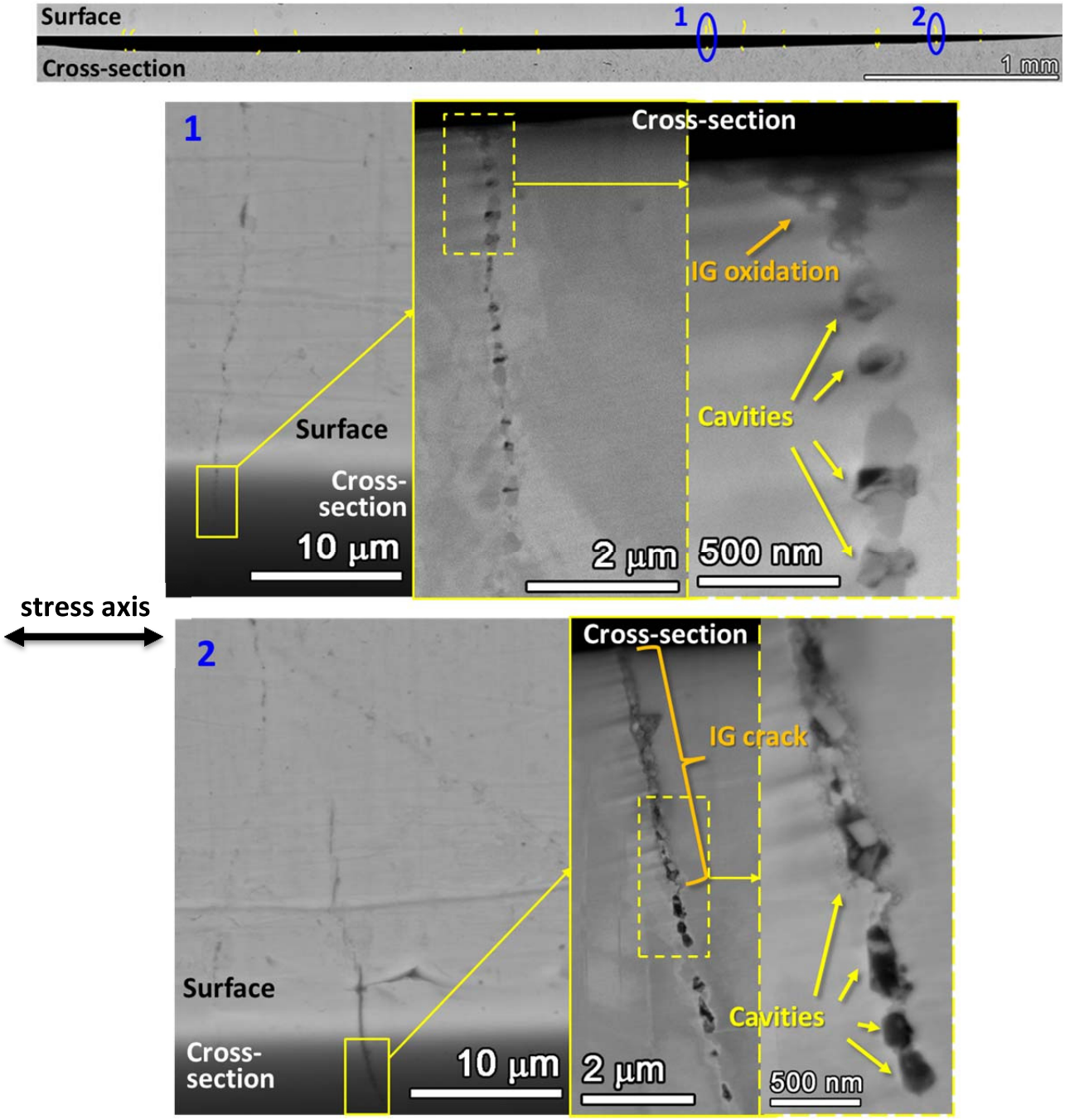

Figure 81. Comparison of the position of IG cracks identified on the surface and the GB cavities identified in cross-sections for the polished 31%CF Sumitomo specimen, accompanied with high-resolution BSE images highlighting the cross-section morphology below the identified IG cracks.

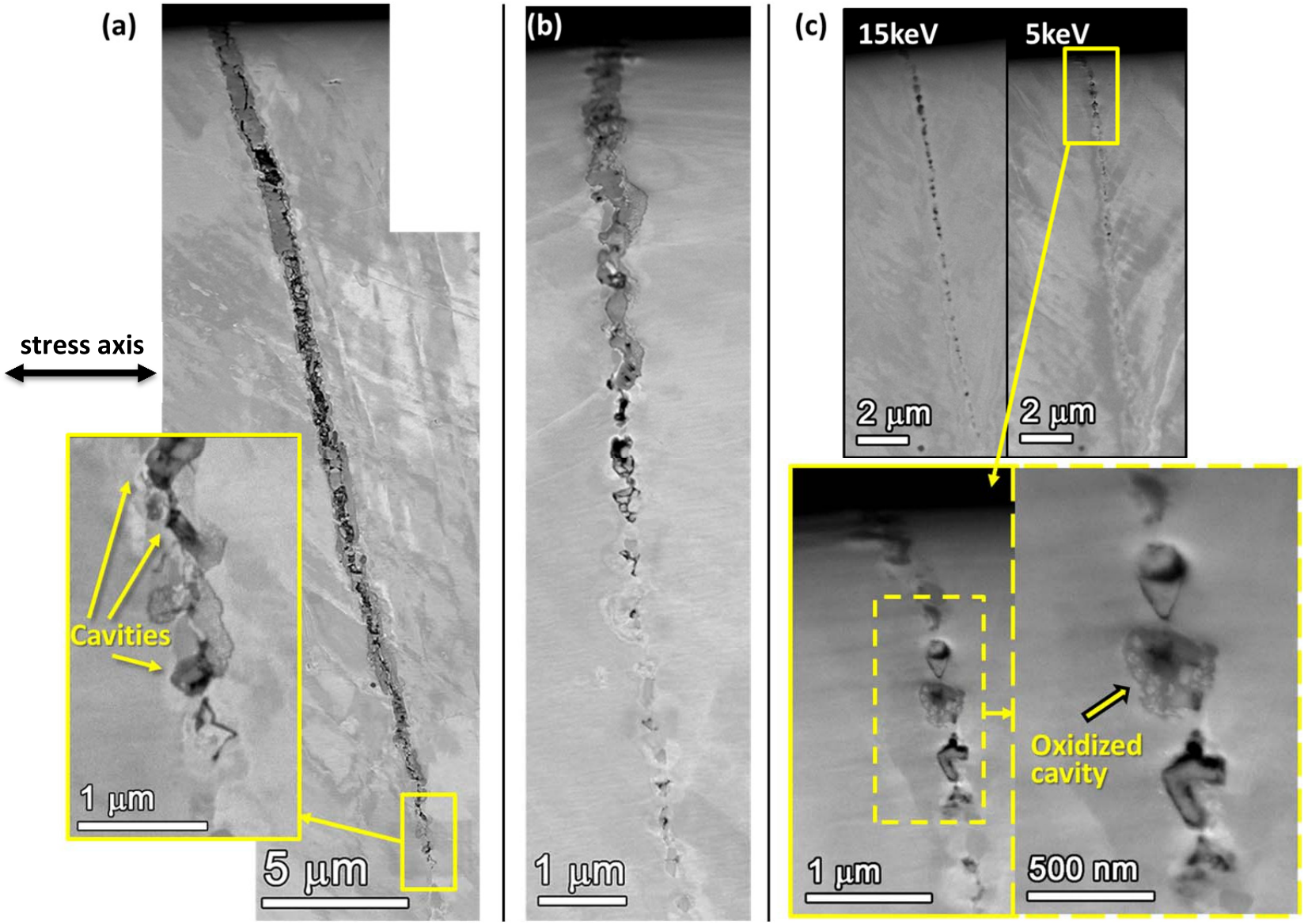

Figure 82. SEM-BSE images of examples of IG cracks intersected on the polished 31%CF Sumitomo specimen cross-section showing GB cavities ahead of crack tips. Unless otherwise stated, all images were taken with an acceleration voltage of 5 keV.

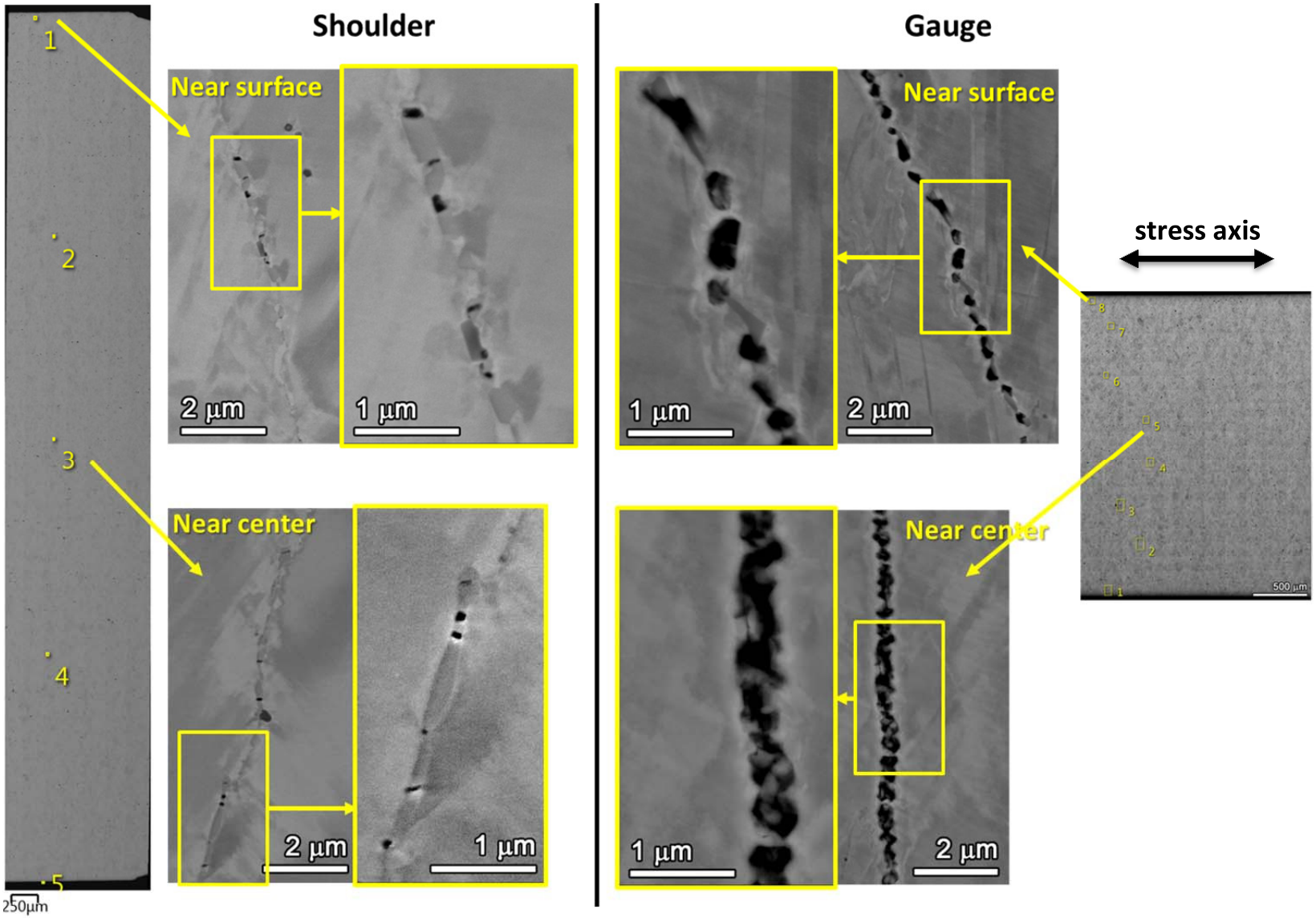

Figure 83. Morphology of the GB voids/cavities found in the shoulder (left) and the gauge (right) of the polished 31%CF Sumitomo CRDM specimen IN033 after 9220 h of exposure. The montage images of the shoulder and the gauge are shown at the same scale.

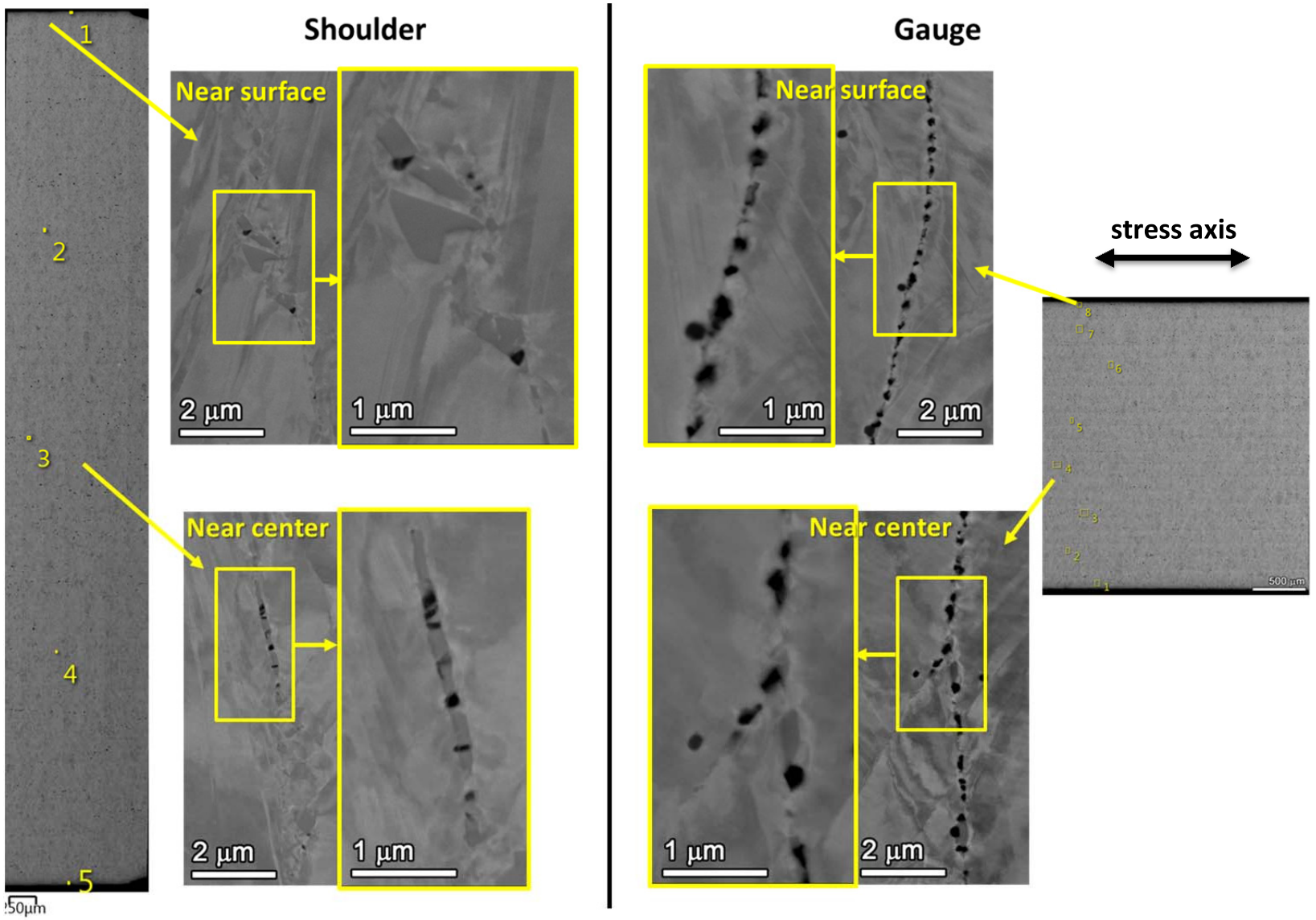

Figure 84. Morphology of the GB voids/cavities found in the shoulder (left) and the gauge (right) of the ground 31%CF Sumitomo CRDM specimen IN034 after 9220 h of exposure. The montage images of the shoulder and the gauge are shown at the same scale.

Three ground specimens from the Valinox CRDM heat with decreasing cold work levels were characterized for cavity distribution across the gauge thickness in the cross-sections. Similar to what was observed in the two 31%CF Sumitomo CRDM specimens IN033 and IN034, the 31%CF specimen IN038 exhibited semi-continuous aggregation of cavities at many high-energy GBs with a normal vector within 45^{o} of the loading direction (Figure 85). The cavities were randomly distributed throughout the entire gauge thickness. No cavities were observed in the thin nanocrystalline layer beneath the surface, but some were present at GBs immediately below this layer as illustrated at sites 1 and 8 in Figure 85. A sharp decrease in the size and density of GB cavities were discovered for 21%CF IN029 specimen versus the 31%CF specimen. Although a few cavities are present, they are too small and discrete in the 21%CF specimen to be resolved at magnifications lower than ~10,000X as shown in Figure 86. Because this cavity density is very low and some cavities were formed during initial cold work, it is difficult to tell whether constant load exposure had any influence on these cavities. Much more detailed characterizations would be required to enable a quantitative analysis of cavity formation and growth.

A further reduction in cold work from 21 to 11.7% resulted in only isolated GB cavities being detected. High-magnification examinations had been made on multiple sites in the gauge section of the 11.7%CF specimen IN067, but only two of them showed a few very small cavities as presented at sites 2 and 3 in Figure 87. Most high-energy GB exhibited semi-continuous distribution of carbides without any trace of cavities as those illustrated in images taken at site 4. Nevertheless, some shallow cracks were observed in the nanocrystalline damage layer (site 1 in Figure 87) in this specimen. These small, shallow cracks did not penetrate into the bulk similar to those observed in the ground specimens at higher cold work levels.

Microstructural examinations were also made in the shoulder of the 31%CF Sumitomo specimen IN038 (Figure 88). No indication of cavity formation or growth was identified that clearly occurred during the 360°C exposure at low stress, A limited distribution of small, discrete GB cavities were observed similar to the permanent damage produced by cold work.

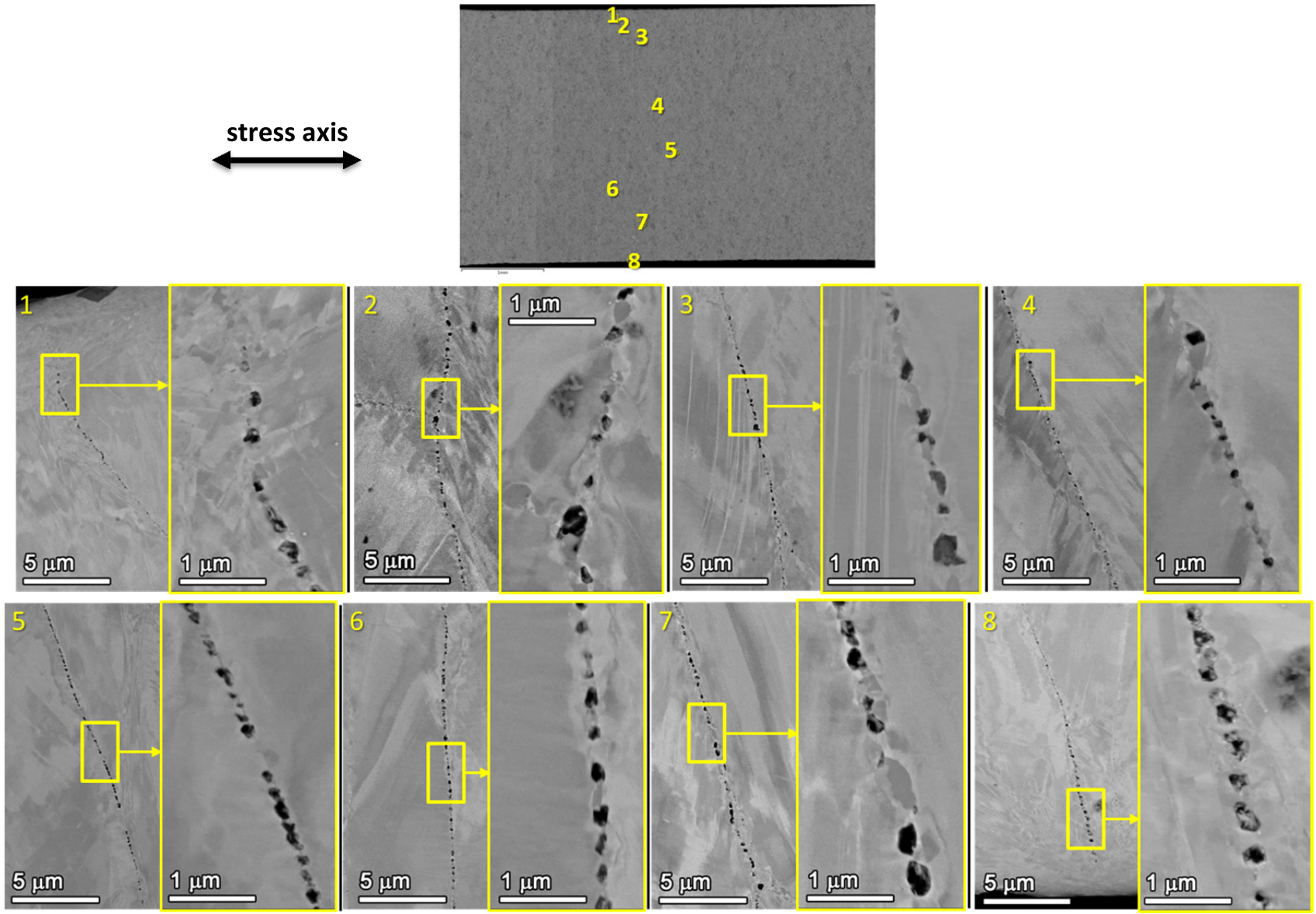

Figure 85. Morphology of GB cavities at selected sites across the gauge thickness in the ground 31%CF Valinox CRDM specimen IN038 after 9220 h of exposure.

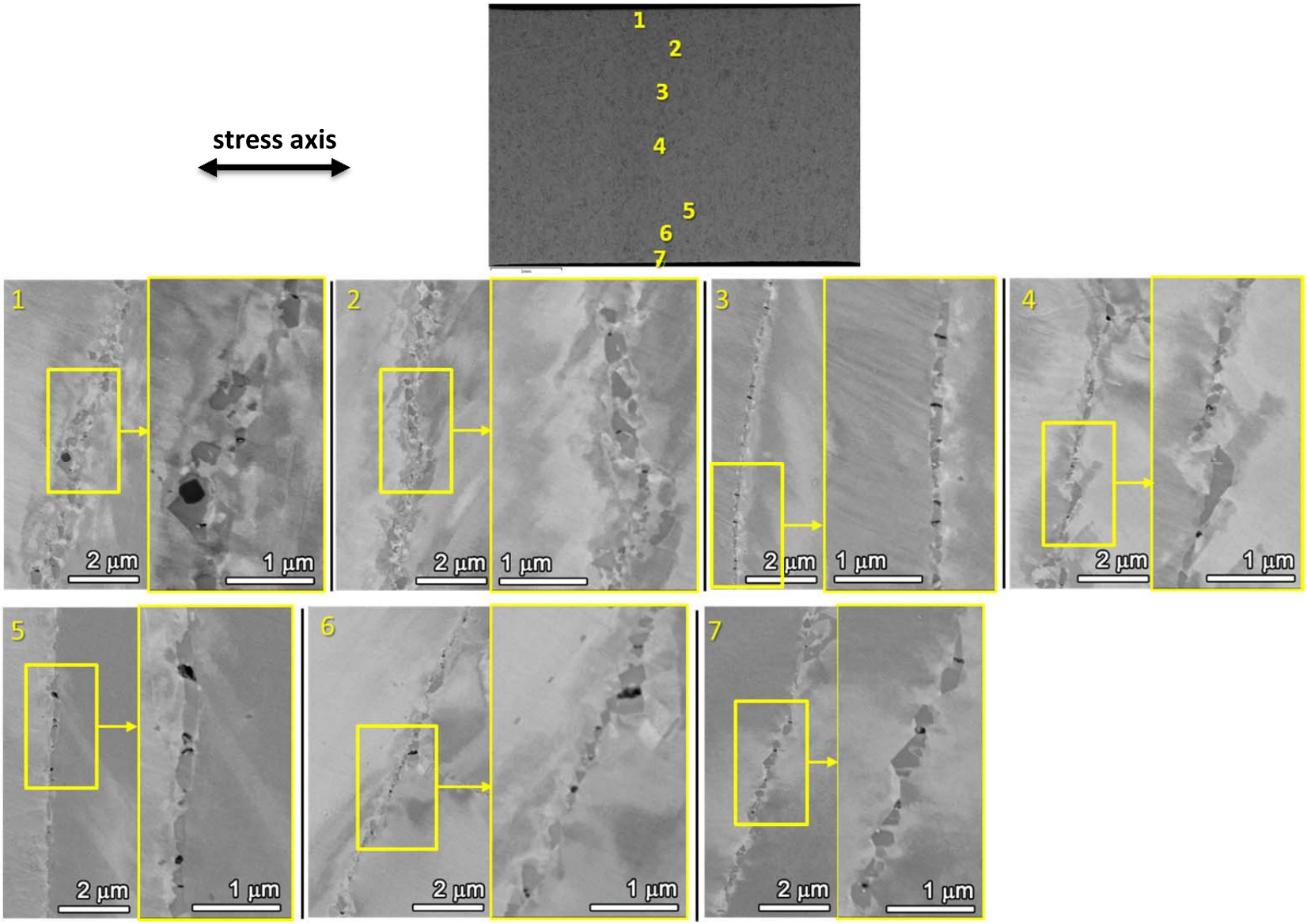

Figure 86. Morphology of GB cavities at selected sites across the gauge thickness in the ground 21%CF Valinox CRDM specimen IN029 after 9220 h of exposure.

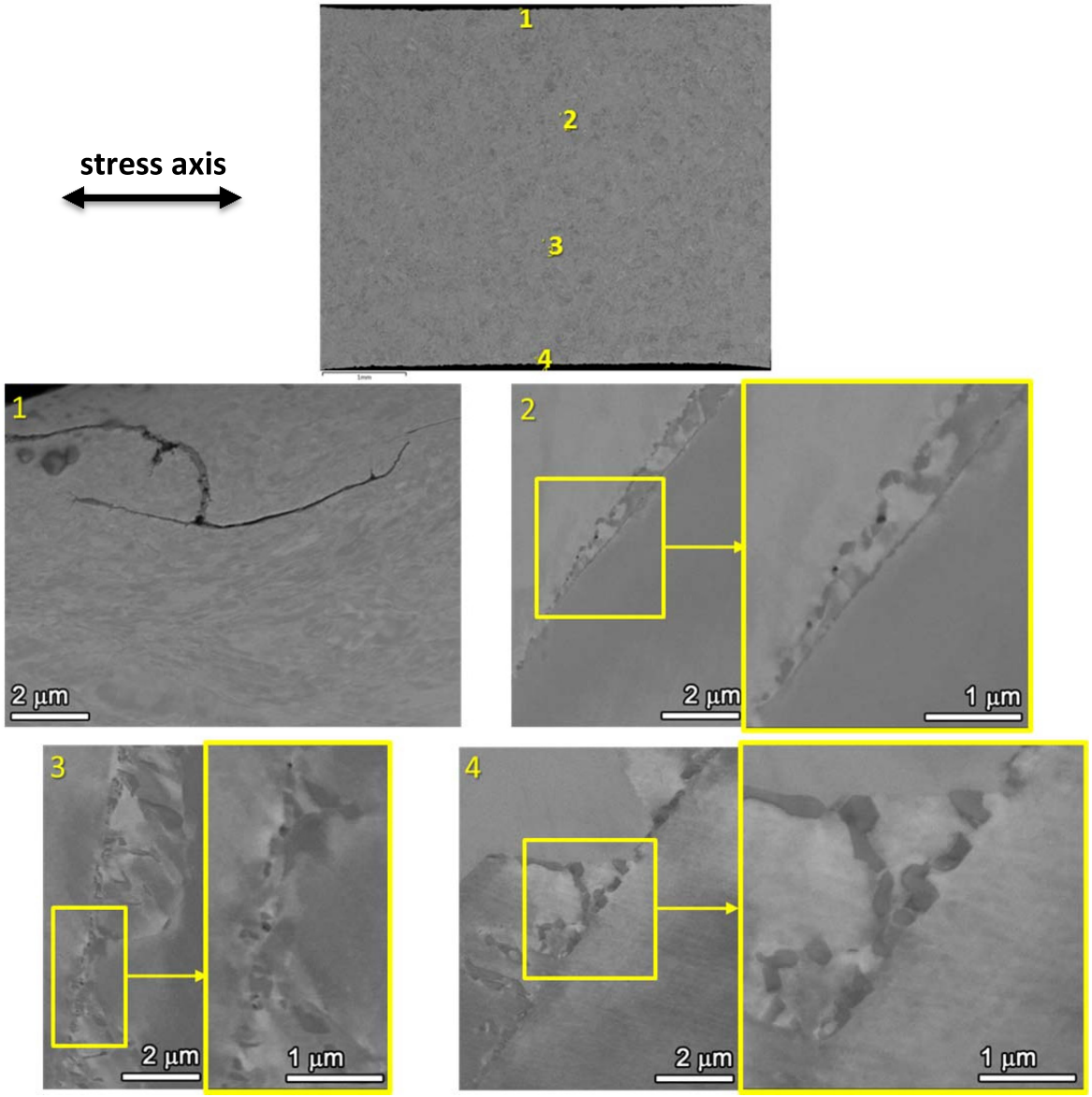

Figure 87. Morphology of GB cavities at selected sites across the gauge thickness in the ground 11.7%CF Sumitomo CRDM specimen IN067 after 7107 h of exposure.

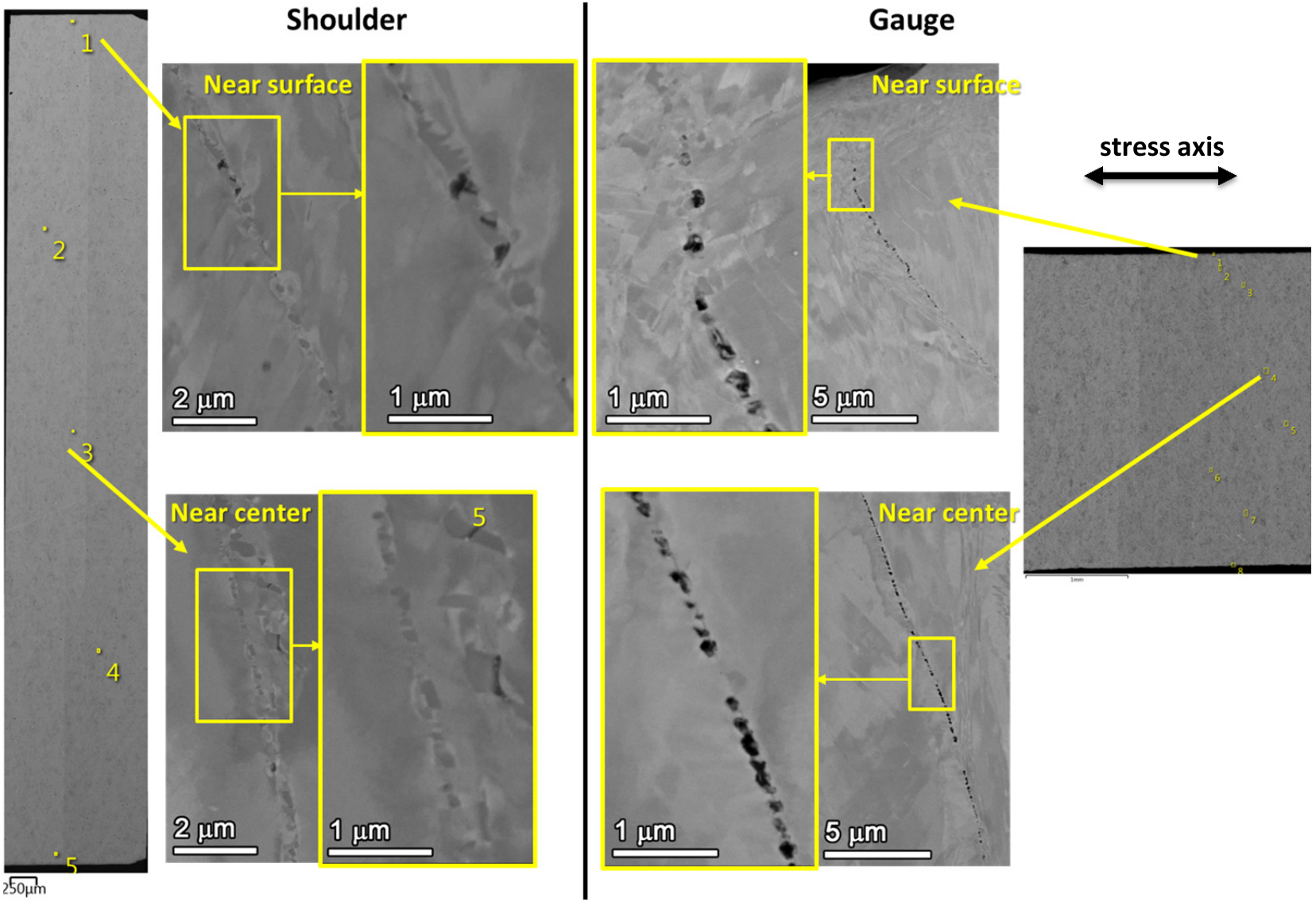

Figure 88. Morphology of the GB voids/cavities found in the shoulder (left) and the gauge (right) of the ground 31%CF Valinox CRDM specimen IN038 after 9220 h of exposure. The montage images of the shoulder and the gauge are shown at the same scale.

As noted in the microstructure chapter, the Doosan CRDM heat exhibits a very different GB carbide morphology in comparison to the other two CRDM (Sumitomo and Valinox) heats. This is also clearly illustrated in Figures 89 and 90 where GB cavities are examined at selected sites across the gauge section in the 31%CF and 21.6%CF specimens IN041 and IN032. Different from the semi-continuous elliptical GB carbides with a relatively uniform size of a few hundreds of nanometers in the Sumitomo and Valinox materials, the carbides in the Doosan heats are much more elongated, often exceeding 1μm long along the GBs with a larger spacing between one another. This seems to have resulted in a lower density of slightly larger, well-separated cavities in the highly CW specimen IN041 (Figure 89). Also instead of growing into small spheroids as in the other two CRDM heats, these cavities appear to be restricted by the facets of adjacent carbides and often exhibit a rigid triangular/rectangular shape. A decrease in the size of cavities was observed with a decrease in cold work level from 31% to 21.6% (Figure 90), but the cavities are still clearly larger than those in the other two CRDM materials at the same cold work level. Meanwhile, no significant difference in the density of cavities was found between the materials at different cold work levels. The comparison of cavity distribution and morphology between the shoulder and the gauge in the 31%CF Doosan specimen did not reveal any obvious differences (Figure 91). As a result, it is suspected that most cavities were produced by cold work prior to the test.

Post-test examinations showed less IG cracking in the 31%CF Doosan specimen as compared to the 31%CF Sumitomo and Valinox specimens (Figure 63). In addition, the size and faceted appearance of the small holes constituting the “postage stamp” GB on the surface of the 21.6%CF specimen (Figure 64) match the geometry of cavities revealed in the specimen cross-section. While the larger and well-separated GB cavities may still contributing to IG crack nucleation, their role does not appear to be as prominent as for the smaller, more continuously distributed cavities observed in the other two CRDM heats.

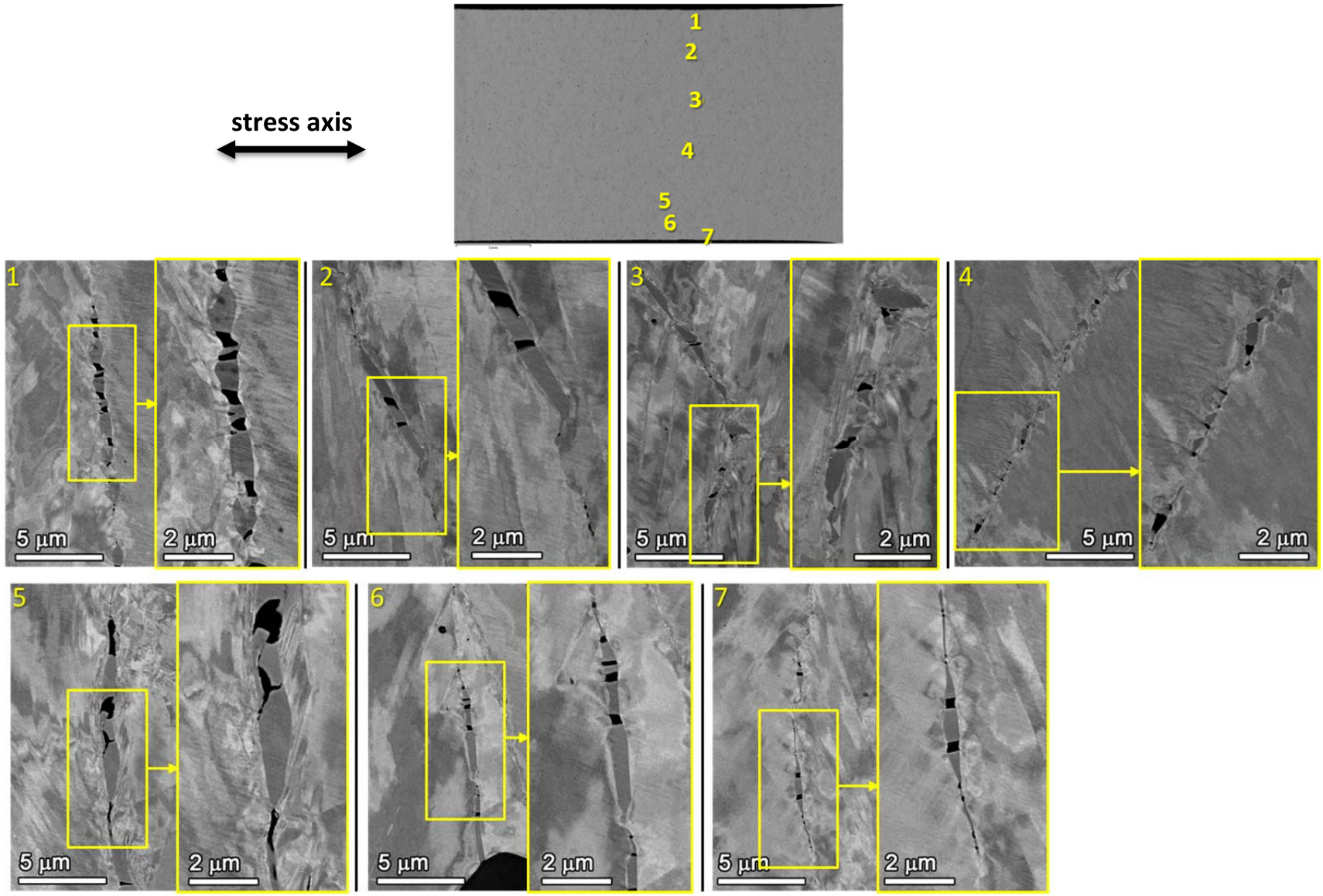

Figure 89. Morphology of GB cavities at selected sites across the gauge thickness in the ground 31%CF Doosan CRDM specimen IN041 after 9220 h of exposure.

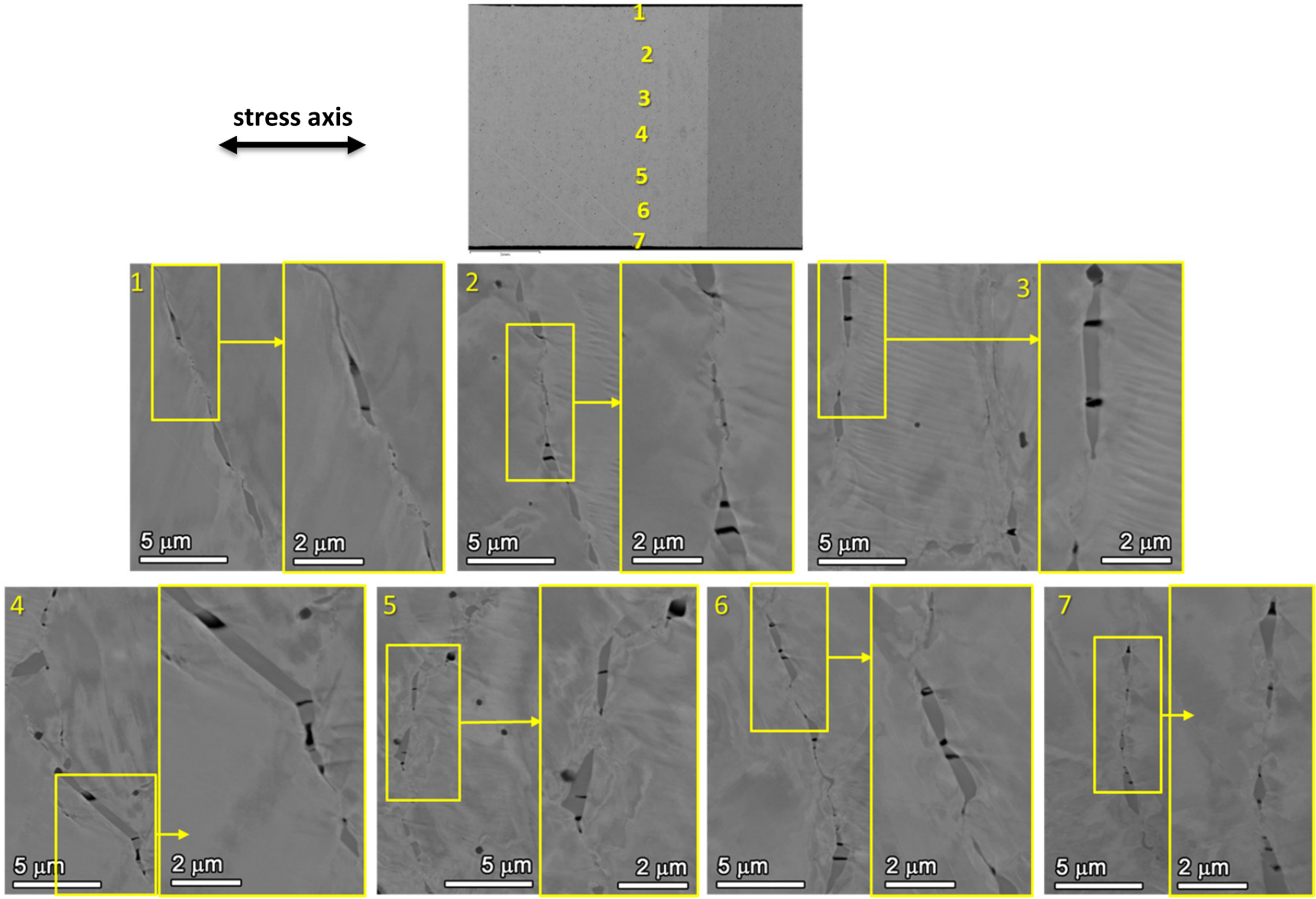

Figure 90. Morphology of GB cavities at selected sites across the gauge thickness in the ground 21.6%CF Doosan CRDM specimen IN032 after 9220 h of exposure.

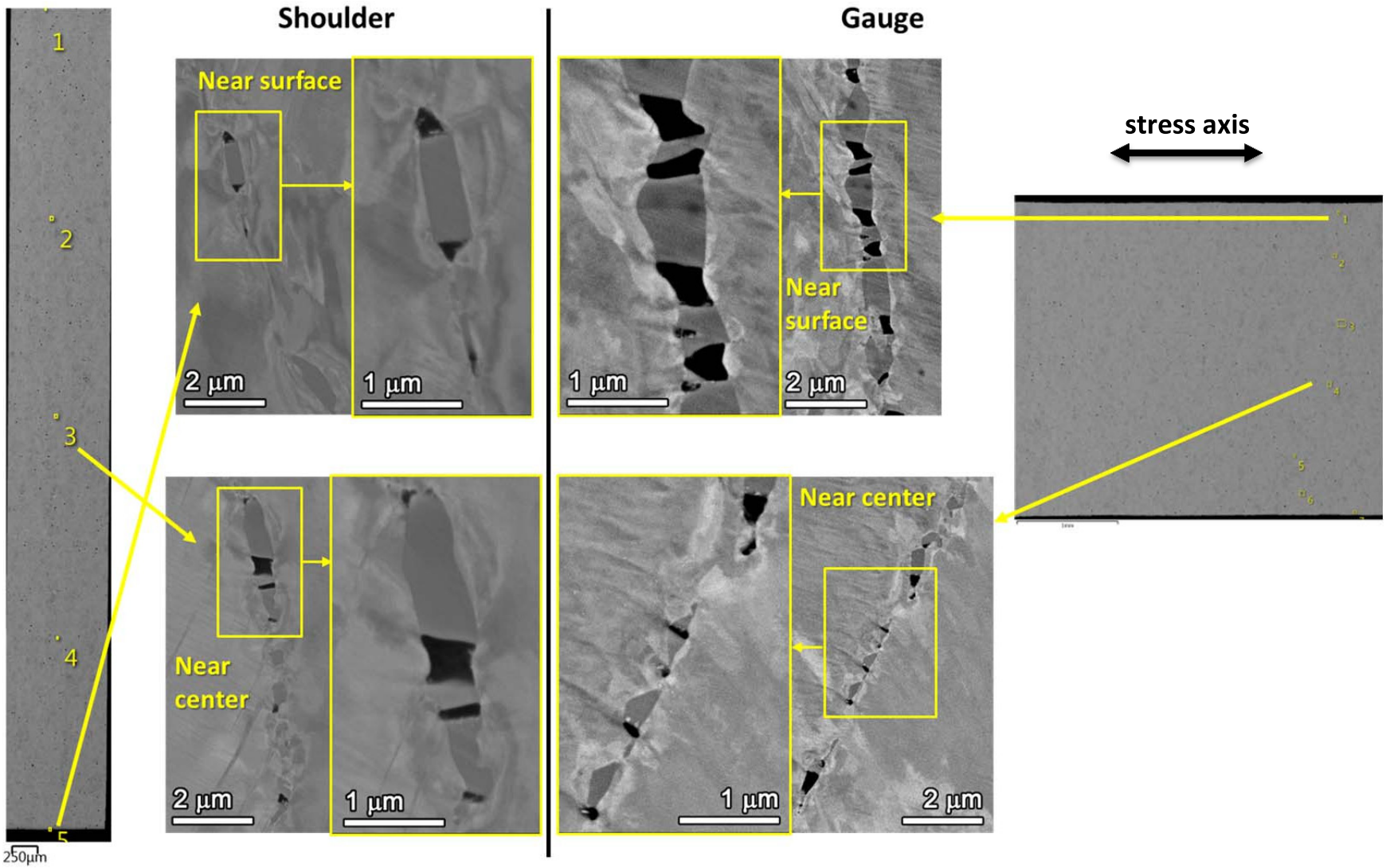

Figure 91. Morphology of the GB voids/cavities found in the shoulder (left) and the gauge (right) of the ground 31%CF Doosan CRDM specimen IN041 after 9220 h of exposure. The montage images of the shoulder and the gauge are shown at the same scale.

The GB carbides in the TK-VDM alloy 690TT plate material have comparable sizes and shapes to those observed in the Sumitomo and Valinox CRDM tubing, but are more widely spaced along high energy GBs. Consistent with this difference, a lower density of cavity aggregations are present in the 31.9%CF TK-VDM specimen IN044 in comparison to those in the 31%CF Sumitomo and Valinox specimens. In addition, GB sections with cavity aggregations are generally shorter (<10 μm) and can only be resolved at high magnifications (≥10,000X, Figure 92). Comparisons were also made for the GB cavity morphology between the shoulder and the gauge in this specimen. Similar to what was observed in the 31%CF Sumitomo and Valinox specimens, the shoulder exhibited a moderate density of small voids at IG carbide interfaces and isolated cracked carbides produced by cold work (Figure 93). There is a clear increase in the density and size of GB cavities in the gauge section indicating that the high applied stress promoted formation and growth of creep cavities at IG carbide interfaces during SCC initiation testing.

Another specimen examined in this heat was made from a block cold rolled to a 21% reduction in thickness. Although the cold working method performed on these two specimens is different, a significant decrease in the size and density of GB cavities was again observed with the decrease in cold work level from 32% to 21%. As shown in Figure 94, small isolated GB cavities were sporadically distributed in the 21%CR specimen IN061 without obvious aggregation. This cavity distribution is likely to have resulted during cold rolling with only a limited effect of the 7107 h test exposure on cavity size.

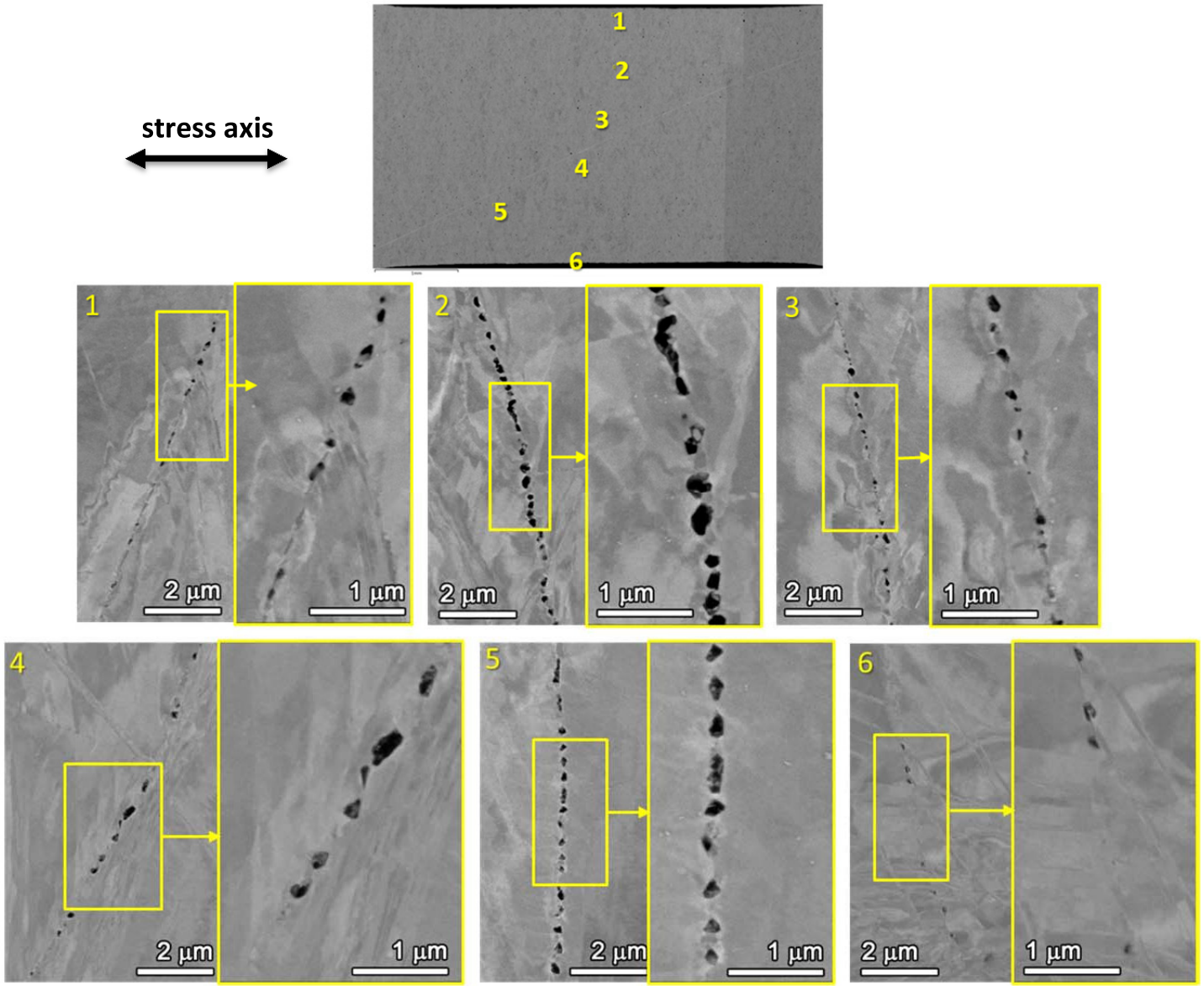

Figure 92. Morphology of GB cavities at selected sites across the gauge thickness in the ground 31.9%CF TK-VDM plate specimen IN044 after 9220 h of exposure.

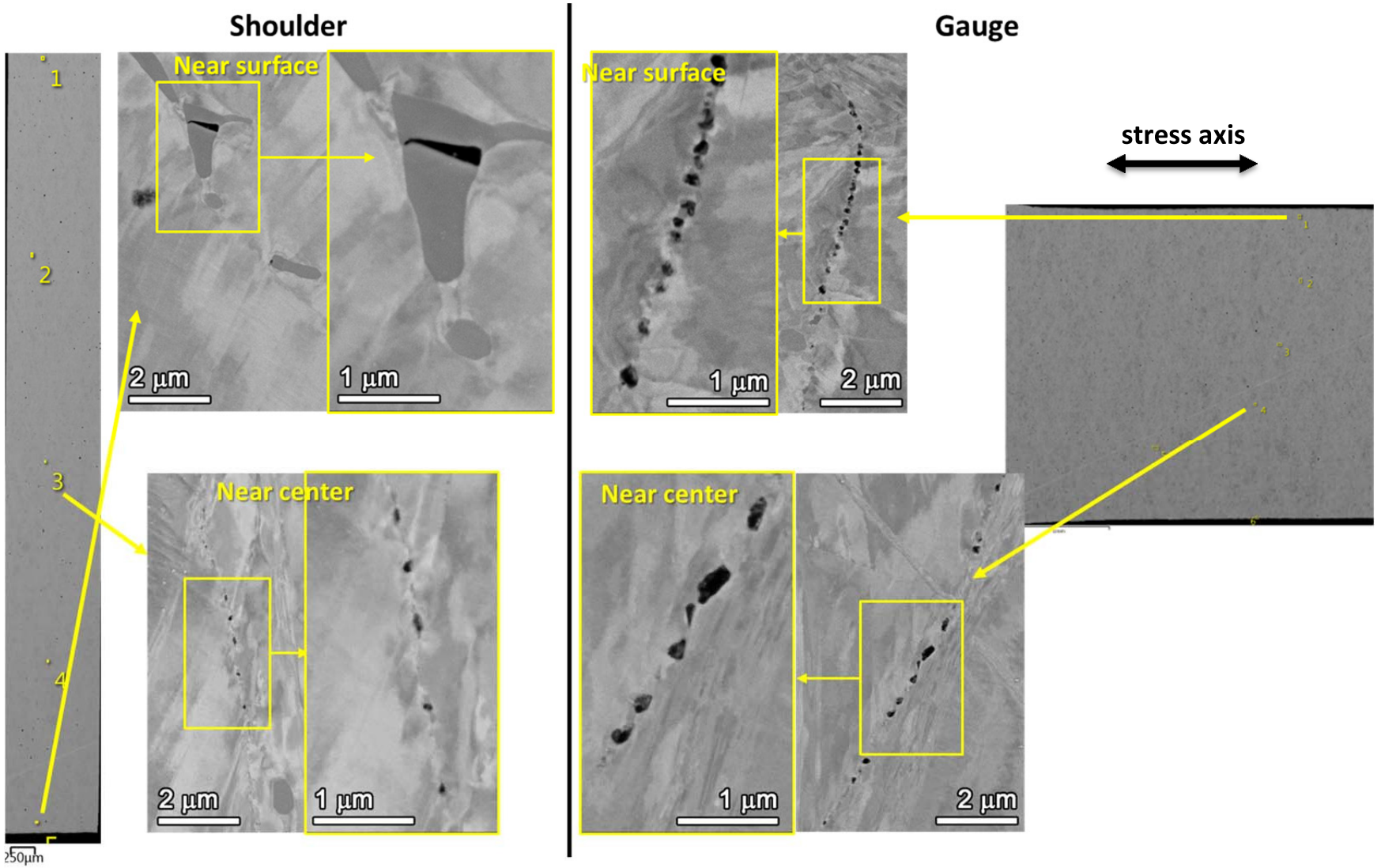

Figure 93. Morphology of the GB voids/cavities found in the shoulder (left) and the gauge (right) of the ground 31.9%CF TK-VDM plate specimen IN044 after 9220 h of exposure. The montage images of the shoulder and the gauge are shown at the same scale.

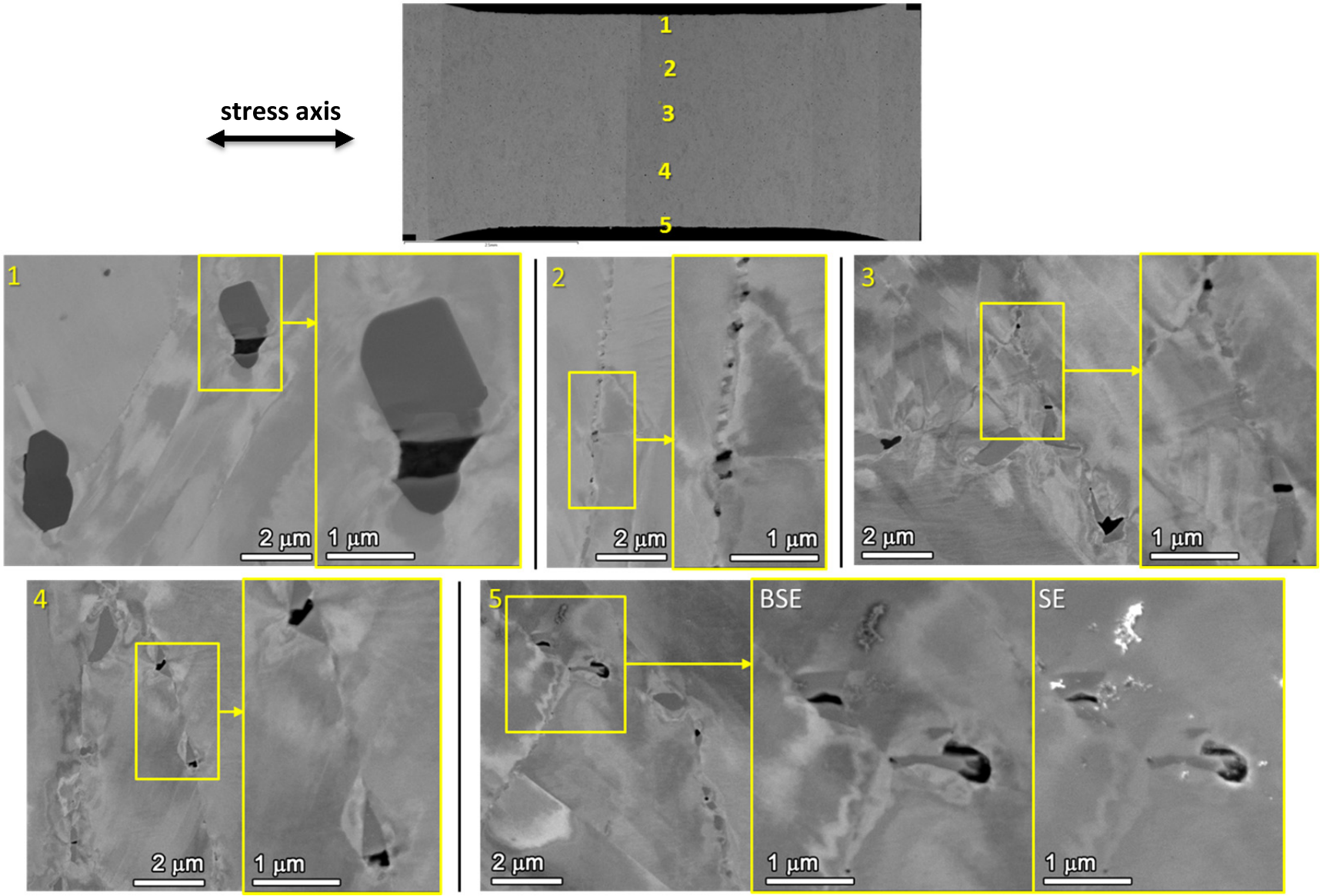

Figure 94. Morphology of GB cavities at selected sites across the gauge thickness in the ground 21%CR TK-VDM plate specimen IN061 after 7107 h of exposure.

The ANL flat bar and the GE bar materials were in the MA starting condition and their microstructures differed from the other heats in this matrix. As described earlier in this report, the ANL microstructure contained a significant number of blocky intragranular TiN particles (occasionally clustered in stringers) and a moderate density of larger GB carbides. In addition, this material was found to have the most extensive damage after cold rolling with cracked TiN, cracked carbides and voids/cavities (Figure 13). Cross-section examinations in the 26%CR ground specimen IN055 revealed many IG cavities with sizes >500 nm at GB carbide interfaces or associated with cracked carbides. The cavities often exhibited a rectangular shape apparently restricted by the faceted carbides (Figure 95). These cavities look very similar to those observed in the 31%CF Doosan CRDM specimen IN041 that also features larger, well-spaced carbides (Figure 89). Examinations in the shoulder region of the same IN055 specimen showed an almost identical distribution of GB cavities (Figure 96), which is also similar to what was observed in the 31%CF Doosan CRDM specimen IN041 (Figure 91). The early conclusion is that the GB cavity distribution after testing for 7107 hours directly results from the damage distribution present after initial cold rolling.

The other MA material tested was the GE bar heat that exhibited only isolated GBs containing carbides. In regions where carbides were present, a low density of cavities were observed at carbide interfaces or associated with cracked carbides in specimens IN058 (18.3%CF, Figure 97) and IN064 (12.4%CF, Figure 98). A few shallow cracks were discovered near the surface in both specimens, but were confined within the nanocrystalline layer produced by grinding (site 7 in Figure 97 and site 6 in Figure 98). The combination of low-to-moderate cold work, lower applied stress and limited GB carbides results in very little IG cavity formation after the test time of 7107 hours.

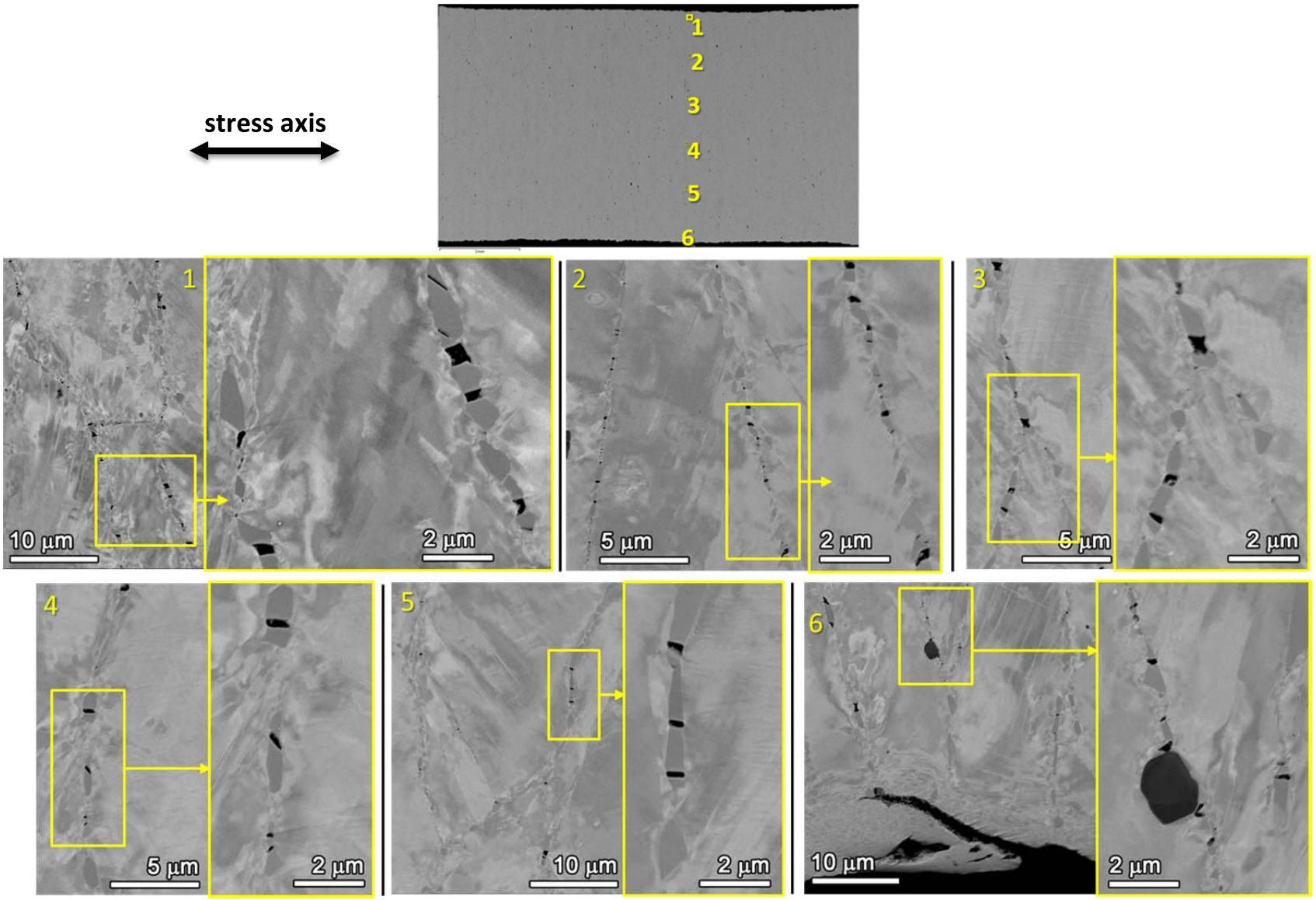

Figure 95. Morphology of GB cavities at selected sites across the gauge thickness in the ground 26%CR ANL flat bar specimen IN055 after 7107 h of exposure.

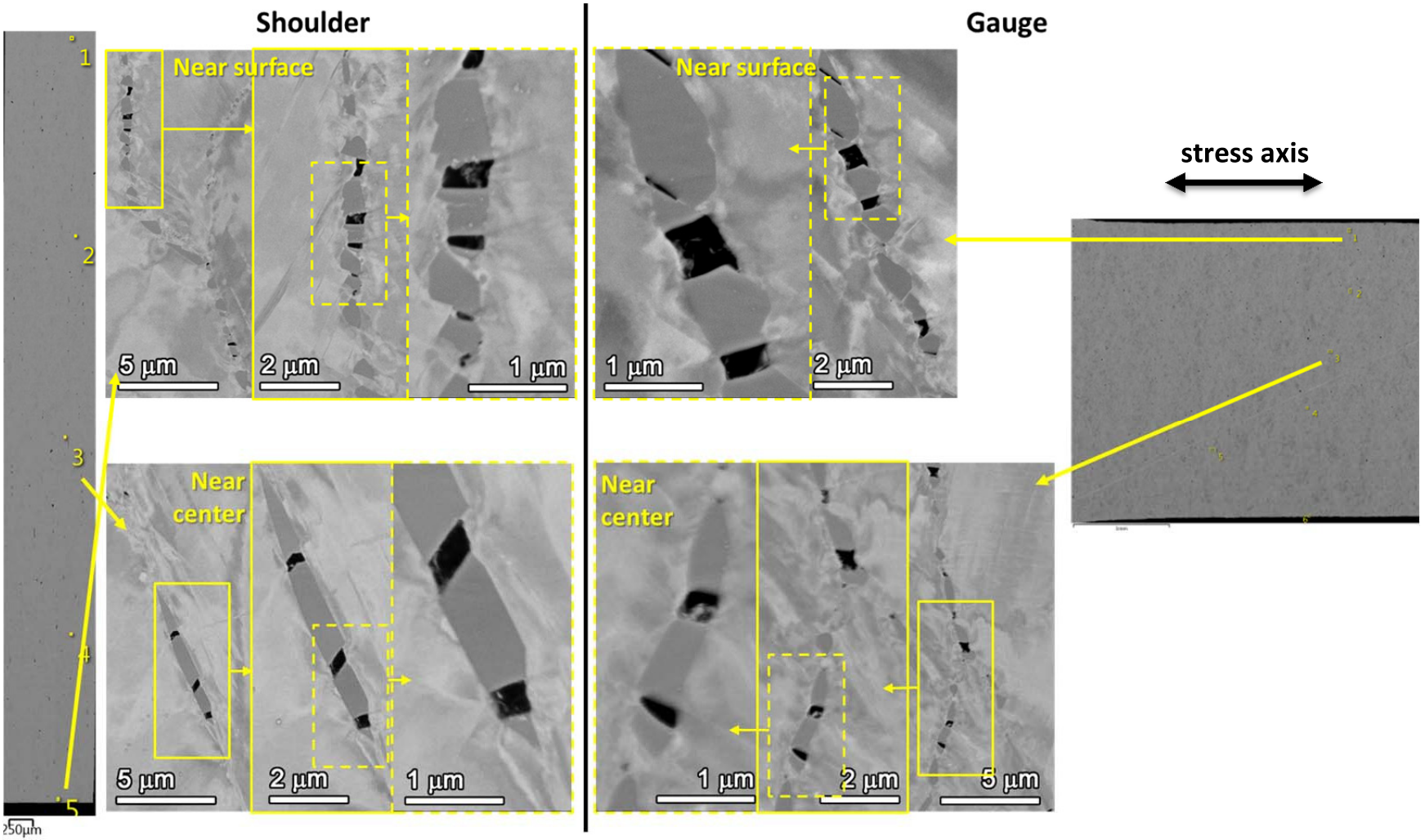

Figure 96. Morphology of the GB voids/cavities found in the shoulder (left) and the gauge (right) of the ground 26%CR ANL flat bar specimen IN055 after 7107 h of exposure. The montage images of the shoulder and the gauge are shown at the same scale.

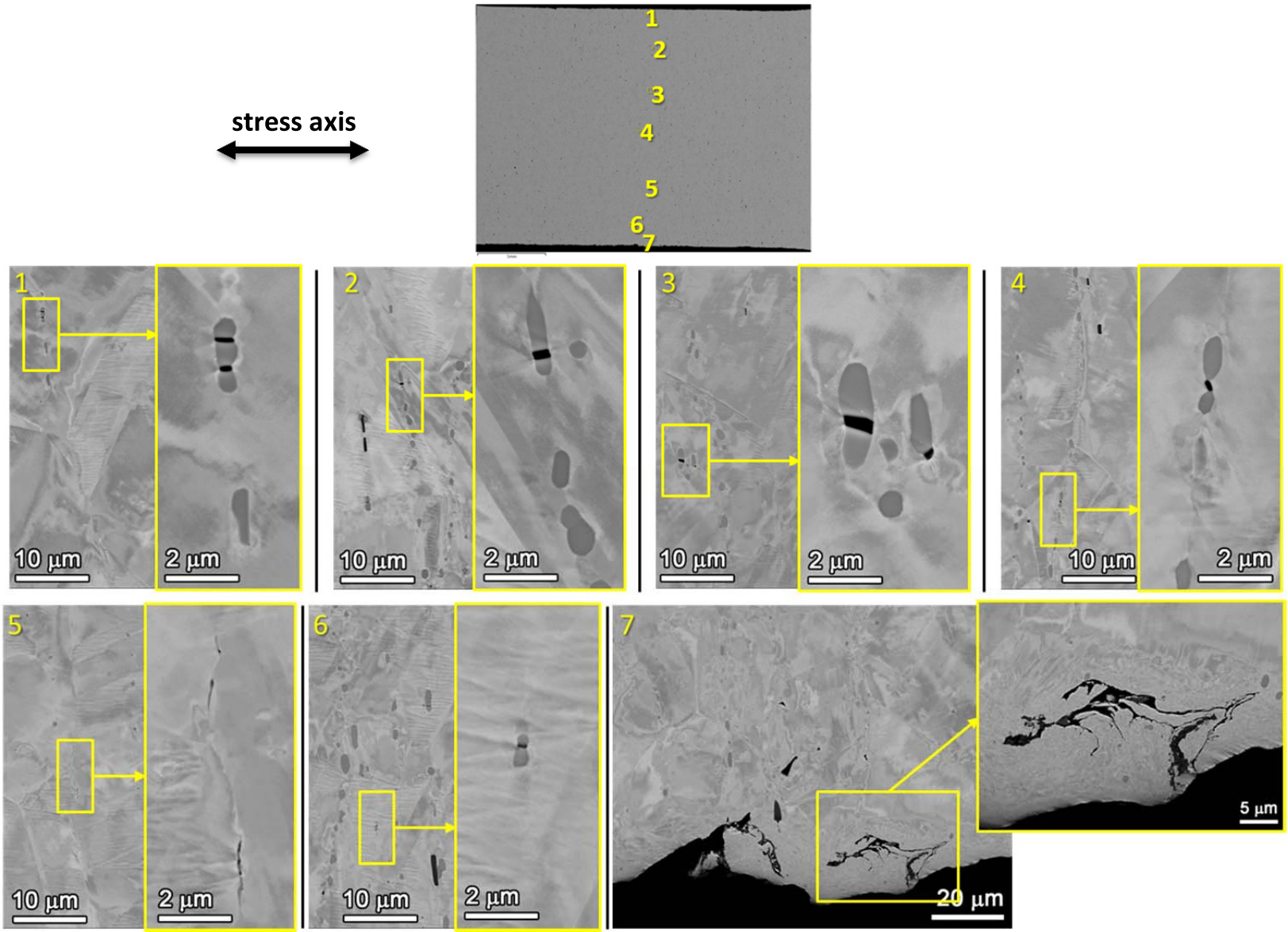

Figure 97. Morphology of GB cavities at selected sites across the gauge thickness in the ground 18.3%CF GE bar specimen IN058 after 7107 h of exposure.

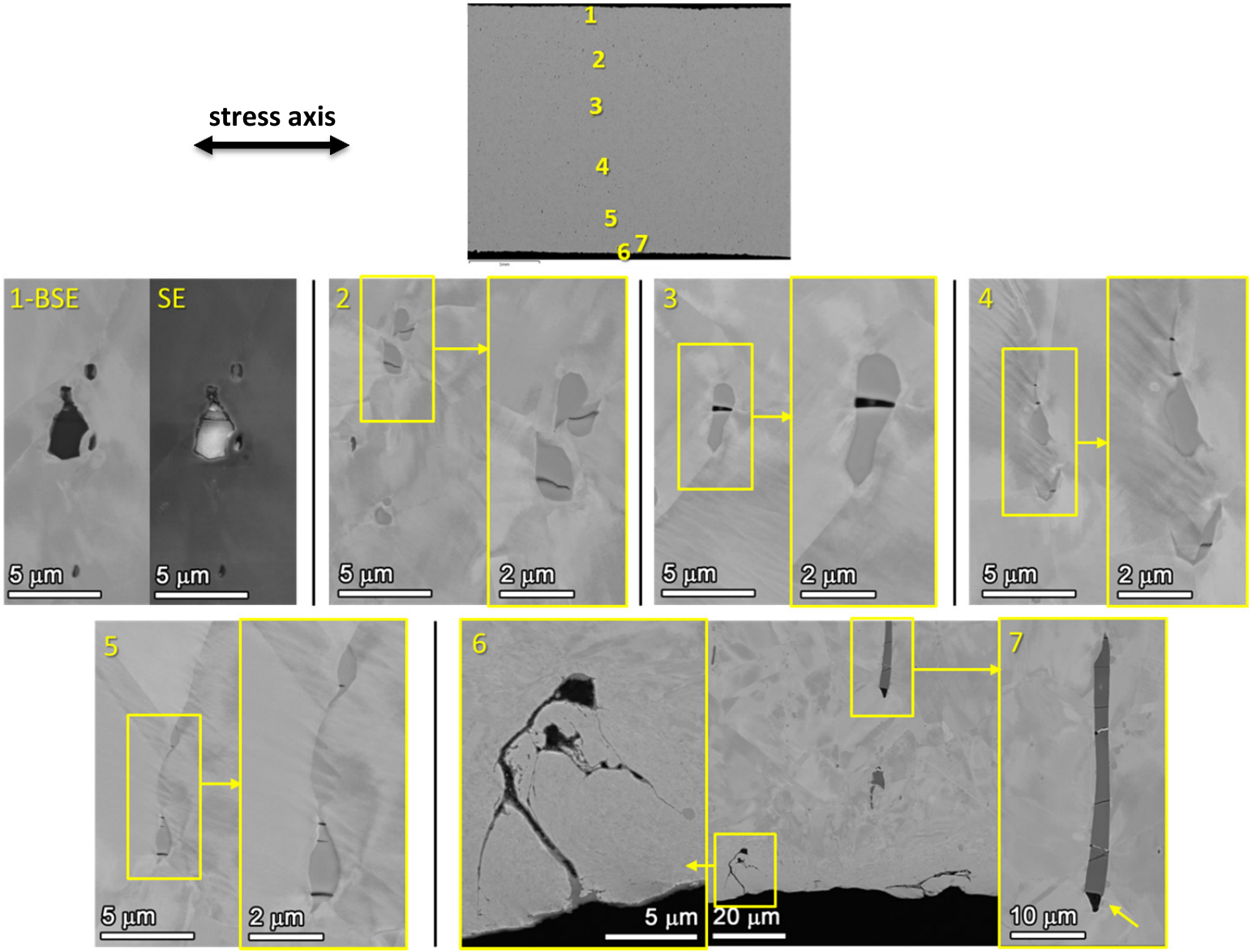

Figure 98. Morphology of GB cavities at selected sites across the gauge thickness in the ground 12.4%CF GE bar specimen IN064 after 7107 h of exposure.

Cross-section microstructural characterizations have been summarized on 13 CLT specimens (Table 11) in this section including 12 ground specimens from each heat and cold work combination, as well as the polished 31%CF Sumitomo CRDM specimen. In summary, cavities at GB carbide interfaces were clearly identified in all highly CW specimens through the entire gauge section. Similar to what was observed for cracking on specimens gauge surface, a significant decrease in the GB cavity distribution in the cross-sections has been found with decreasing cold work level in every heat. IG damage microstructures for the various ~30%CW, ~20%CW and ~12%CW specimens are presented in Figures 100, 101 and 102, respectively.

An important observation is that the starting carbide microstructure appears to have a profound impact on the formation of GB cavities. This can be clearly viewed in Figures 99 and 101, where comparisons of the GB cavity morphology are made between heats with similar cold work levels. Most extensive IG damage is clearly observed for the 31%CF Sumitomo, Valinox and TK-VDM TT materials that have the most uniform and dense GB carbide coverage. Cavities in these specimens are seen to nucleate at carbide interfaces and produce a semi-continuous distribution that is likely to link up into creep cracks as the test time progresses. These cavities usually exhibit spheroidal shapes indicative of surface energy reduction had taken place during cavity growth. An overview of the GB cavity distribution in the gauge section of the ~31%CW specimens in these three heats is displayed in Figure 102. The density of cavity aggregations (and creep cracks) in the bulk tends to scale with the density of IG cracks observed on the surface. Results show that the 31%CF Sumitomo CRDM materials exhibit the most extensive distributions of GB cavities and IG cracks followed by the 31%CF Valinox CRDM material. It is interesting that these two CRDM tubing materials represent what is commonly considered as the best alloy 690TT microstructure (very homogeneous grain structures and carbide distributions with no significant compositional banding). The Doosan alloy 690TT and ANL alloy 690MA bar materials were quite different with GB carbides that are larger, more elongated, blocky and well spaced creating a lower density of cavities that appear larger, faceted and more isolated. Even though the cavities in the 30%CW specimens with this type of microstructure can be 2-5 times larger than those observed in the Sumitomo and Valinox CRDM heats, it seems harder for these cavities to reach a semi-continuous distribution that can link up and induce IG crack formation.

The difference observed between cavity morphology in the gauge and in the shoulder in the highly CW materials also revealed a strong dependence on starting GB carbide microstructure. In the Sumitomo, Valinox and TK-VDM TT materials with semi-continuous distribution of relatively small carbides, much fewer cavities were evidenced in the shoulder region than in the gauge (Figures 83, 84, 88 and 93). These features exhibit similar spacing to the permanent damage produced by cold work prior to exposure as those shown in the first chapter. By contrast, in the TT 31%CF Doosan CRDM heat and the MA 26%CR ANL flat bar heat which feature larger and well-spaced carbides on GBs, no significant difference between the shoulder and the gauge was observed in the density of the GB cavities (Figures 91 and 96). It is still unclear how applied stress interplays with the carbide microstructures on cavity nucleation and growth in the highly-CW alloy 690 materials and more systematic quantitative analyses are needed to resolve these mechanistic issues.

Constant load SCC initiation testing was recently restarted and is continuing on 23 of the original specimens in Tables 1 and 2. The 13 CLT specimens removed for destructive examinations were replaced with additional CW alloy 690 materials including the Valinox CRDM in the solution-

annealed (SA) condition (no GB carbides) plus 31%CR or 17%CR (previously evaluated for SCC crack growth response). Other new alloy 690 materials in the specimen matrix are the 12.7%CF Sumitomo CRDM and the 31%CF Allvac heat X87N-1 materials. Finally, several new CRDM specimens were added matching existing alloy 690 conditions for the 31%CF Sumitomo and 31%CF Valinox materials. Since these two materials have revealed the highest susceptibility to GB cavity formation and IG cracking when loaded to 100%YS, the new specimens have been loaded to 90%YS) to assess the influence of applied stress. The gauge surfaces for all of the replacement specimens are in the highly polished condition enabling more effective characterization of surface damage evolution.

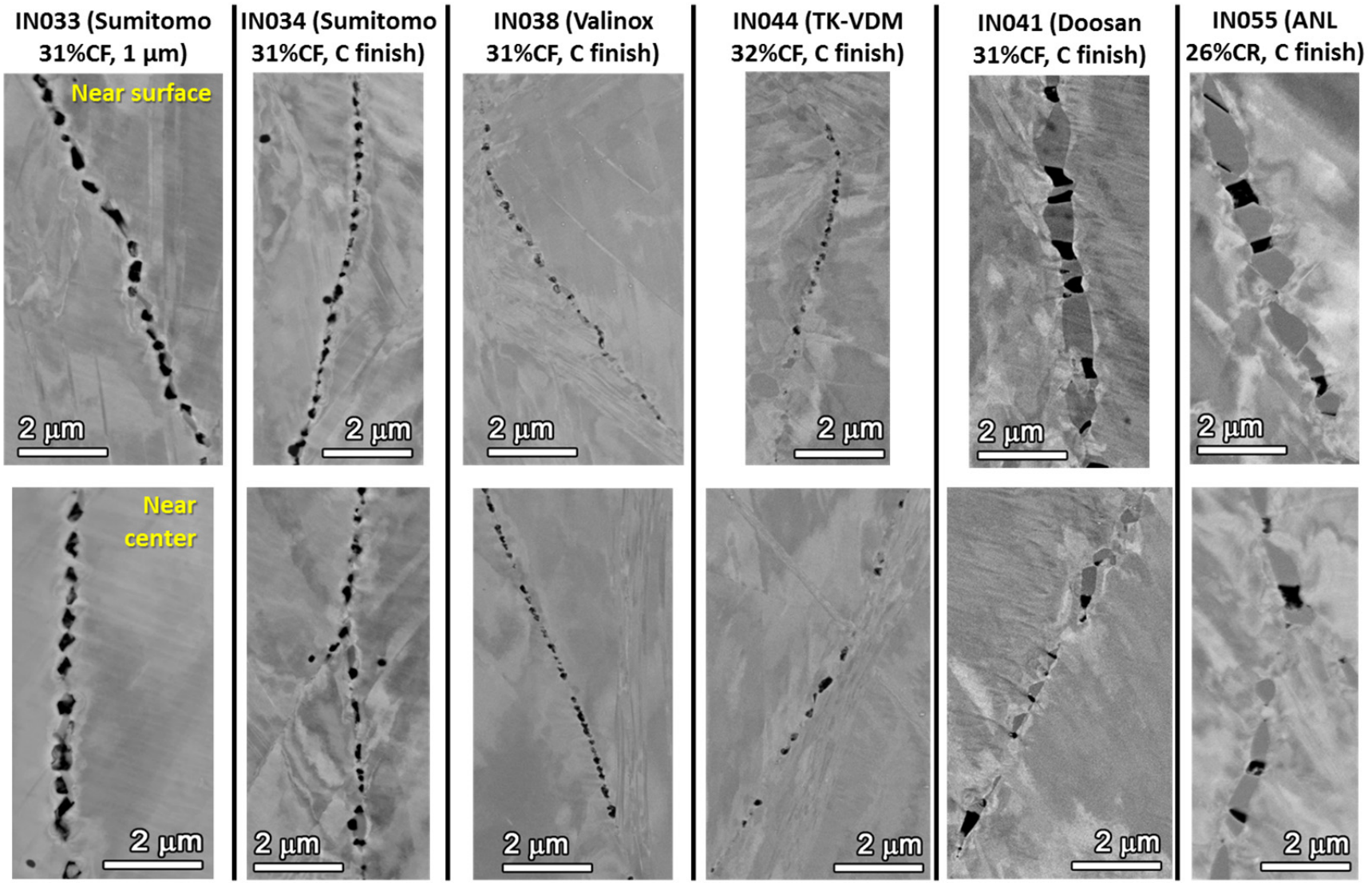

Figure 99. Heat-to-heat comparison of the cavity morphology at locations near the surface (upper row) and the center (lower row) in the gauge in ~30%CW materials.

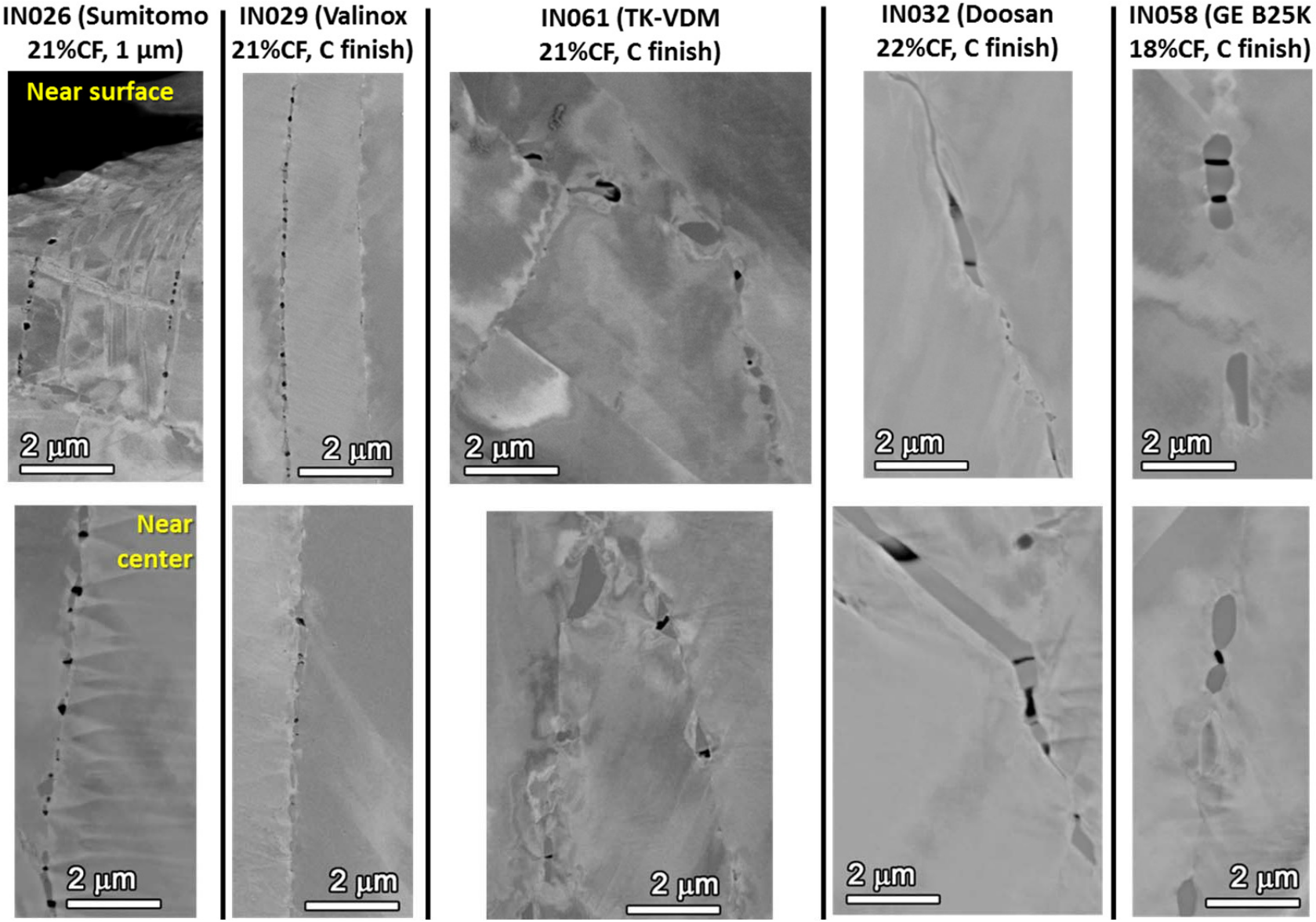

Figure 100. Heat-to-heat comparison of the cavity morphology at locations near the surface (upper row) and the center (lower row) in the gauge in ~20%CW materials.

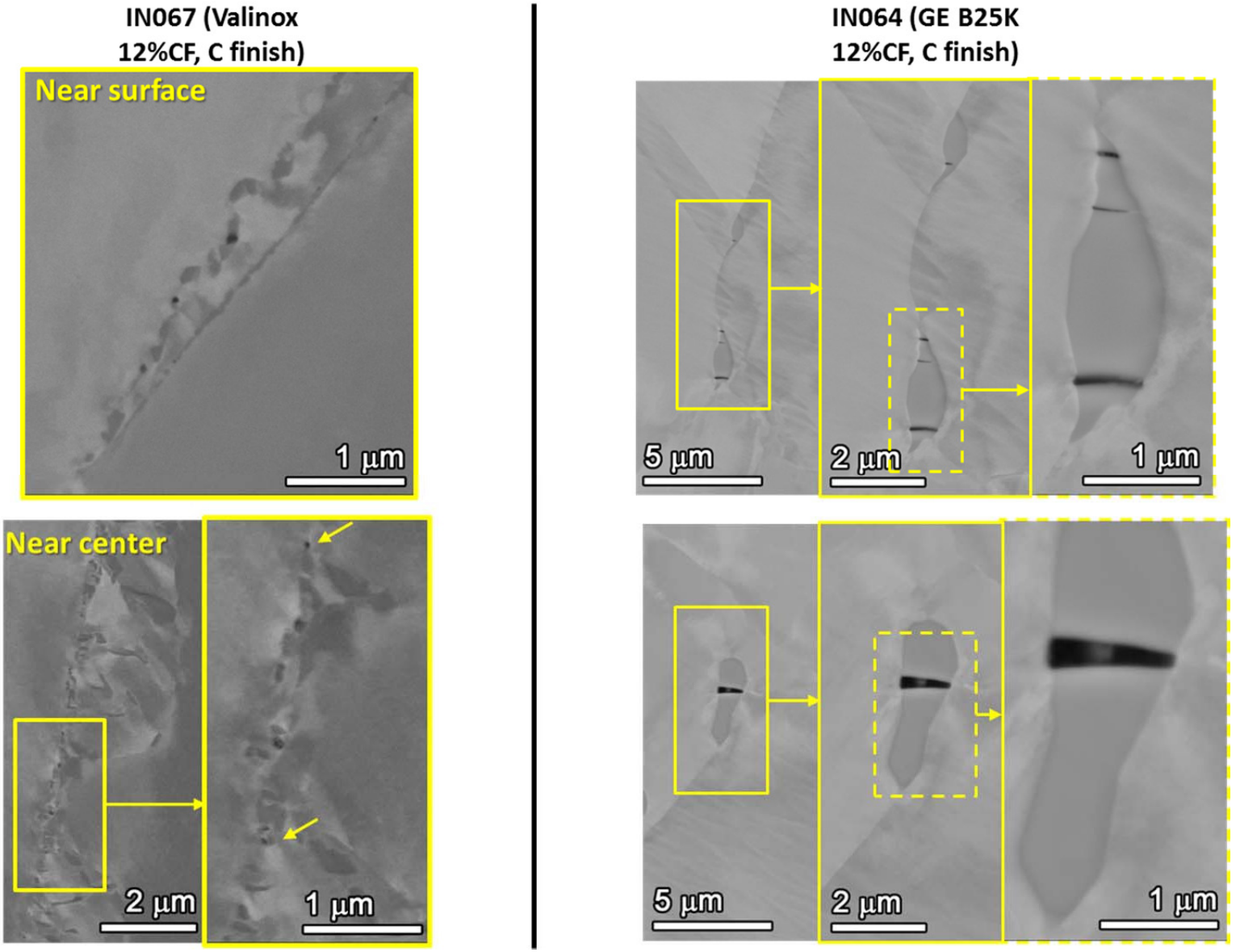

Figure 101. Heat-to-heat comparison of the cavity morphology at locations near the surface (upper row) and the center (lower row) in the gauge in ~12%CW materials.

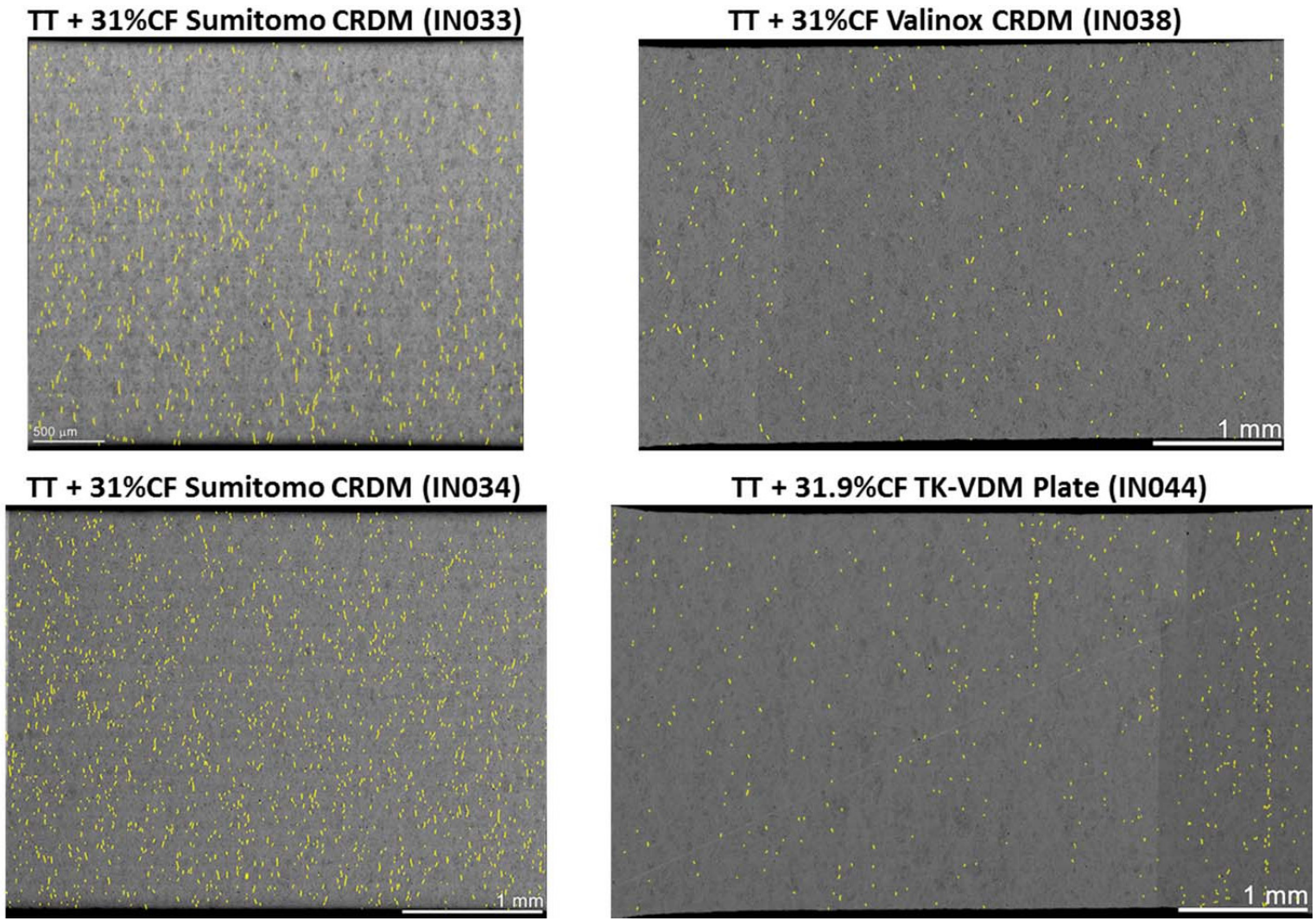

Figure 102. SEM-BSE montage images of the gauge section of four 31-32% alloy 690TT specimens with aggregations of GB cavities highlighted in yellow.

Summary and Conclusions

Recent SCC initiation testing on CW alloy 690 materials in 360°C simulated PWR primary water has been reviewed and characterizations of GB damage precursors leading to IG crack nucleation are highlighted. All BNCT and CLT tests were conducted on alloy 690 materials in the CW condition that has been shown to increase SCC susceptibility in SCC crack-growth experiments. A direct correlation is shown to exist between cavity distributions along grain boundaries reaching the surface and crack nucleation during both CLT and BNCT experiments. Preliminary observations reveal a strong effect of the %CW, applied stress and grain boundary carbide microstructure on cavity formation and IG cracking during tests in PWR primary water.

The current work builds on earlier milestone reports [1-6] that described our corrosion-structure examinations and first SCC initiation tests on both alloy 600 and alloy 690. Observations of alloy 600 initiation suggest that the mechanism to SCC initiation distills down to producing a flaw that has an SCC-relevant stress intensity to drive SCC growth. This is readily achieved in alloy 600 by stress-assisted IG attack during constant load exposure [1, 3, 6, 14, 15]. However, in alloy 690 an equivalent constant load stress corrosion-based degradation process does not appear to exist. Experimentation has revealed that due to a nonporous chromia layer formed above the GBs intersecting the surface that remained protective even after long exposures at high stresses, CW alloy 690 is extremely resistant to SCC initiation [2-5] although it can be highly susceptible to SCC growth [7-11]. Therefore, modifications to the testing approach were made to evaluate dynamic straining as a means to attempt to compromise the chromia layer and allow the possible generation of stress corrosion-based precursor cracks.

Several different straining methods were explored in previous SCC initiation experiments [2-4] on highly CW alloy 690 materials. Early tests included periodically increasing plastic deformation at moderate strain rates of ~$5x10^{-4}$ s^{-1} and cyclic loading to small plastic strains (2.5–4.5%) at slower strain rate of ~$1x10^{-7}$ s^{-1}. Post-test examinations revealed no crack initiation or only shallow transgranular cracks at slip bands that formed during plastic deformation. As a result, modifications to the testing approach were made to determine whether precursor IG cracks could be generated. This time, obvious SCC cracks were observed in a highly CW alloy 690 TT CRDM tensile specimen subjected to continuous dynamic straining to ~0.3% plastic strain at an order of magnitude slower stain rate (~$1x10^{-8}$ s^{-1}). Concurrent blunt notch tests where slow loading ramps were applied to produce 1% plastic strain using the same strain rate also resulted in DCPD-detected SCC initiation. Somewhat unexpectedly, extensive GB creep cavity formation and cracking were observed in these materials along with SCC cracks. While these tests established a means to nucleate cracks and obtain SCC initiation, and while GB cavities were suspected to play a major role in it, the specific details by which it occurred could not be explicitly determined from those tests.

The observations above led to the current round of blunt notch tests with carefully planned loading conditions and test interruptions on alloy 690TT specimens from two CRDM heats at both moderate (~21%) and high (~31%) cold work levels. Microstructural characterizations were conducted at each test interruption and at the conclusion of the test to document the evolution of GB cavity and IG crack distributions as presented in this report. The first stage of the tests consisted of a few cyclic loading ramps to 0.5% strain at a slow strain rate of $1x10^{-8}$ s^{-1}. SEM examinations afterward revealed a number of isolated IG cracks on the notch surface and GB cavities in the cross-section of all specimens, again proving that dynamic straining during the

slow cyclic loading ramps is effective in promoting cavity formation and generating precursor IG cracks in highly CW alloy 690. The tests were then continued under constant *K* loading at moderate *K* levels (36–37 MPa√m). Crack initiation was detected by DCPD at ~10400 h in the two 31%CF specimens corresponding to the significant growth of cracks. The critical role of GB cavities as precursors for IG crack nucleation and short crack growth was identified with small, closely spaced cavities reaching this surface converting into short cracks. As the test time increased for the 31%CF BNCT specimens, aggregations of GB cavities became more common in the bulk and creep cracks were formed. In contrast, the two 21%CF specimens exhibited little growth of IG cracks on the notch surface although a small, gradual increase in GB cavities was observed in the cross-sections. While these detailed characterizations reveal that GB cavities can grow under constant load conditions, it remained unclear that whether dynamic straining was required to produce this GB damage and promote SCC initiation. This aspect is of critical importance in assessing SCC initiation susceptibility of CW alloy 690 under service relevant conditions where significant dynamic straining is unlikely.

In parallel with the blunt notch experiments, long-term constant load testing was performed and continues to be performed on tensile specimens from six different alloy 690 heats with various levels of CW. For several, highly CW (~30%CW) CLT specimens loaded to their YS (~700 MPa), detailed trench observations by SEM/FIB after a total exposure of ~9220 h at 360°C revealed obvious IG cracks more than 15 μm deep but insufficient in length to cause SCC initiation. This represents the first-ever observation of IG crack nucleation for alloy 690 in PWR primary water under constant load conditions. Examinations on the cross-sections of selected specimens also showed extensive GB cavities through the entire gauge thickness showing that creep strain rates produced under constant load are sufficient to promote GB cavity formation and growth. It is important to recognize that the uniformity in size and number density of the GB cavities observed across the gauge section of many specimens suggests that this process is creep dominated. However, a clearly decreasing trend in cavity size and density was evidenced as distance from crack tips increases, indicating stress corrosion process might have promoted local cavity formation and growth once cracks were nucleated. Similar to observations on BNCT specimens, aggregations of GB cavities were directly involved in the nucleation of IG cracks at the surface. Closely spaced GB cavities were present reaching the surface before and after the crack was formed. This near-surface damage clearly evolves as a precursor to IG crack initiation in highly CW alloy 690 and appears to help promote short crack growth. It is important to note that there was significant heat-to-heat effect on IG damage evolution identified among the CRDM, bar and plate materials even in the highest CW condition (~30%). At lower levels of cold work (12-21%), specimens exhibited little or no IG precursor damage. Constant load experimentation is continuing on these and other CW alloy 690 materials particularly focused on lower cold work levels (more relevant to PWR service). In addition, new specimens are being evaluated to better understand the influence of the GB microstructure and the applied stress level on cavity formation and IG crack nucleation.

Different from the classical notion of SCC initiation, the latest results demonstrate that creep-induced GB cavity formation can occur in CW alloy 690 during long-term SCC initiation testing in high-temperature PWR primary water. Similar GB cavities have been reported in CW carbon steels and nickel-base alloys at high temperatures by other researchers [16-19] using various testing methods (e.g., slow straining, step/constant loading) and were related to increased IG cracking susceptibility. In this study, the detailed microstructural characterizations have obtained additional insights on GB cavities as crack precursors, revealing that GB cavities

provide the necessary IG damage required for IG crack nucleation at the surface and IGSCC growth. In the most susceptible highly CW materials, cavities can form and grow on GBs with a preferable orientation to the applied stress reaching a semi-continuous distribution and finally link up into IG creep cracks well before the propagation of a SCC crack from the surface. This process appeared to strongly depend on the GB microstructure, degree of cold work and applied stress. Increasing GB carbide coverage, cold work level and applied stress have all been shown to enhance IG damage during SCC initiation testing. However, it remains unclear whether GB carbides are required for cavity formation and how specific carbide morphologies or distributions influence IG damage evolution. Other critical questions are whether detrimental IG damage will develop in alloy 690 materials with lower levels of cold work and/or at low temperatures (more relevant to PWR service) and how is GB cavity evolution affected by applied stress during long-term exposure. These are key mechanistic issues that must be resolved for alloy 690. As a result, constant load and selected blunt notch tests are continuing focused on the 12-21%CW materials and the alloy 690 specimen matrix has been expanded in an attempt to isolate effects of GB carbide distributions and applied stress. High-resolution characterizations of surface and subsurface IG damage will continue to be utilized to document surface and subsurface IG damage evolution.

Acknowledgement

The authors recognize collaborative research activities funded by the Nuclear Regulatory Commission (SCC crack growth tests on alloy 690 materials), the office of Basic Energy Sciences (high-resolution grain boundary characterizations) and Rolls Royce (hardness and strain mapping on CW alloy 690 materials plus support to develop FIB techniques). These collaborations have been essential to the success of the SCC initiation research. Critical technical assistance is also recognized from Rob Seffens and Ryan Bouffioux for SCC experimentation, Clyde Chamberlin and Anthony Guzman for metallographic specimen preparation, and Nicole Overman for EBSD and hardness measurements.

References

[1] *Stress Corrosion Crack Initiation of Alloy 600 in PWR Primary Water Environments*. Pacific Northwest National Laboratory: Technical Milestone Report M3LW-13OR0403032, Light Water Reactor Sustainability Program, DOE Office of Nuclear Energy, March 2013.

[2] *Corrosion and Stress Corrosion Crack Initiation of Cold-Worked Alloy 690 in PWR Primary Water Environments*. Pacific Northwest National Laboratory: Technical Milestone Report M2LW-13OR0402035, Light Water Reactor Sustainability Program, DOE Office of Nuclear Energy, September 2013.

[3] *Stress Corrosion Crack Initiation of Cold-Worked Alloy 600 and Alloy 690 in PWR Primary Water*. Pacific Northwest National Laboratory: Technical Milestone Report M2LW-14OR0404023, Light Water Reactor Sustainability Program, DOE Office of Nuclear Energy, September 2014.

[4] *Summary of Stress Corrosion Crack Initiation Measurements and Analyses on Alloy 600 and Alloy 690*. Pacific Northwest National Laboratory: Technical Milestone Report M2LW-15OR0402034, Light Water Reactor Sustainability Program, DOE Office of Nuclear Energy, September 2015.

[5] *SCC Initiation Research on Alloy 600 and Alloy 690: Presentations at the EPRI Alloy 690 Expert Meeting*. Pacific Northwest National Laboratory: Technical Milestone Report M3LW-16OR0402032, Light Water Reactor Sustainability Program, DOE Office of Nuclear Energy, December 2015.

[6] *Mechanisms of SCC Initiation in Alloy 600: Presentations at the International Cooperative Group Meeting on Environment-Assisted Cracking*. Pacific Northwest National Laboratory: Technical Milestone Report M3LW-16OR0402033, Light Water Reactor Sustainability Program, DOE Office of Nuclear Energy, June 2016.

[7] *Pacific Northwest National Laboratory Investigation of Stress Corrosion Cracking in Nickel-Base Alloys, Volume 2*. Pacific Northwest National Laboratory: NUREG/CR-7103 Vol. 2, Nuclear Regulatory Commission, Office of Nuclear Regulatory Research, 2012.

[8] *Pacific Northwest National Laboratory Investigation of Stress Corrosion Cracking in Nickel-Base Alloys, Volume 3: Stress Corrosion Cracking of Cold-Worked Alloy 690*. Pacific Northwest National Laboratory: NUREG/CR-7103 Vol. 3, Nuclear Regulatory Commission, Office of Nuclear Regulatory Research, 2015.

[9] S. M. Bruemmer, M. J. Olszta, M. B. Toloczko and L. E. Thomas, "Linking Grain Boundary Microstructure to Stress Corrosion Cracking of Cold-Rolled Alloy 690 in Pressurized Water Reactor Primary Water", *Corrosion*, Vol.69, Iss.10, 2012, pp. 953-963.

[10] S. Bruemmer, M. J. Olszta, N. R. Overman and M. B. Toloczko, "Microstructural effects on stress corrosion cracking of cold-worked alloy 690 tubing and plate materials", in *16th International Conference on Environmental Degradation of Materials in Nuclear Power Systems - Water Reactors,* 2013, Ashville, NC, USA.

[11] S. Bruemmer, M. J. Olszta, N. R. Overman and M. B. Toloczko, "Cold work effects on stress corrosion crack growth in alloy 690 tubing and plate materials", in *17th International*

Conference on Environmental Degradation of Materials in Nuclear Power Systems - Water Reactors, 2015, Ottawa, Ontario, Canada.

[12] N. R. Overman, M. B. Toloczko, M. J. Olszta and S. M. Bruemmer, "Strain correlations in alloy 690 materials using electron backscatter diffraction and vickers hardness", in *Corrosion 2014,* 2014, San Antonio, Texas, USA: NACE International.

[13] M. J. Olszta, D. K. Schreiber, M. B. Toloczko and S. Bruemmer, "High resolution characterization of film formation and localized corrosion in alloy 690 exposed to PWR primary water", in *Corrosion 2014,* 2014, San Antonio, Texas, USA: NACE International.

[14] M. B. Toloczko, M. J. Olszta, Z. Zhai and S. Bruemmer, "Stress corrosion crack initiation measurements of alloy 600 in PWR primary water", in *17th International Conference on Environmental Degradation of Materials in Nuclear Power Systems – Water Reactors,* 2015, Ottawa, Ontario Canada.

[15] Z. Zhai, M. J. Olszta, M. B. Toloczko and S. Bruemmer, "Precursor corrosion damage and stress corrosion crack initiation in alloy 600 during exposure to PWR primary water", in *17th International Conference on Environmental Degradation of Materials in Nuclear Power Systems – Water Reactors,* 2015, Ottawa, Ontario Canada.

[16] K. Arioka, "2014 Whitney Award Lecture: Change in Bonding Strength at Grain Boundaries before Long Term SCC Initiation", *Corrosion*, Vol., 2014.

[17] K. Arioka, R. W. Staehle, T. Yamada, T. Miyamoto and T. Terachi, "Degradation of Alloy 690 After Relatively Short Times", *Corrosion*, Vol.72, Iss.10, 2016, pp. 1252-1268.

[18] T. Angeliu and G. Was, "Creep and intergranular cracking of Ni-Cr-Fe-C in 360 °C argon", *Metallurgical and Materials Transactions A*, Vol.25, Iss.6, 1994, pp. 1169-1183.

[19] T. M. Angeliu, D. J. Paraventi and G. S. Was, "Creep and Intergranular Cracking Behavior of Nickel-Chromium-Iron-Carbon Alloys in 360°C Water", *Corrosion*, Vol.51, Iss.11, 1995, pp. 837-848.